SYNTHESIS AND CHARACTERIZATON OF INORGANIC MATERIALS FOR SODIUM-ION BATTERIES

By

Rengarajan Shanmugam

A DISSERTATION

Submitted to
Michigan State University
in partial fulfillment of the requirements
for the degree of

Chemical Engineering—Doctor of Philosophy

2015

ABSTRACT

SYNTHESIS AND CHARACTERIZATION OF INORGANIC MATERIALS FOR SODIUM-ION BATTERIES

By

Rengarajan Shanmugam

Development of low-cost energy storage devices is critical for wide-scale implementation of intermittent renewable energy technologies and improving the electricity grid. Commercial devices remain prohibitively expensive or lack the performance specifications for a wider market reach. Na-ion batteries would perfectly suited for these large-scale applications as the raw materials (such as soda ash, salt, etc.) are plentiful, inexpensive and geographically unconstrained. However, extensive materials research on insertion electrodes is required for better understanding of the electrochemical and structural properties and engineering high performance Na-ion batteries. This thesis research involves exploratory study on new insertion materials with various crystallographic structure-types and extensive characterization of promising new inorganic compositions.

Tunnel-type materials, sodium nickel phosphate-Na₄Ni₇(PO₄)₆, and sodium cobalt titanate-Na_{0.8}Co_{0.4}Ti_{1.6}O₄, were investigated to capitalize on the intrinsic structural stability offered by framework materials. Sol-gel and solid-state reaction synthetic techniques were employed for inorganic powder synthesis. Galvanostatic and potentiostatic testing confirm reversible sodium insertion/de-insertion reactions albeit with inadequate electrochemical characteristics (high voltage hysteresis> 1V). Subsequent efforts involved investigating layer-structured materials supporting fast ionic transport for better electrochemical performance.

P2-sodium nickel titanate, $Na_{2/3}[Ni_{1/3}Ti_{2/3}]O_2$ (P2NT), with prismatic sodium co-ordination, was synthesized by solid-state technique. The 'bifunctional' oxide contains $Ni^{2+/4+}$ and $Ti^{4+/3+}$

redox couples with redox potentials of 3.6 V, 0.7 V vs. Na/Na⁺, respectively. This bifunctional approach would simplify electrode processing and provide cost reduction opportunities in battery manufacturing. The structural changes monitored using ex-situ XRD demonstrate a favorably broad solid-solution domain. Manganese substitution, to form P2-Na_{2/3}[Ni_{1/3}Mn_{1/3}Ti_{1/3}]O₂ (P2NMT), provides an enhanced high-current performance due to faster interfacial kinetics and accelerated charge carrier transport as shown by impedance spectroscopy and DC testing.

Structural properties of P2NT material were studied using neutron diffraction and atomisitic simulations. Rietveld refinement shows that Na_f sites have lower site occupancy than Na_e sites due to unfavorable repulsive interactions from inline transition metal atoms. Buckingham and Morse-type models accurately predicted the experimental lattice parameters. The energy landscape was explored using energy minimization runs on disordered supercells. The simulated density maps are in agreement with the experiment densities with evidence of stacking fault formation.

O3-sodium nickel titanate, Na_{0.9}[Ni_{0.45}Ti_{0.55}]O₂ (O3NT) with octahedral sodium co-ordination was synthesized by solid-state reaction technique. The influence of titanium on the poor cycleability of the O3-type electrodes was investigated. Ex-situ XRD shows two phase regions, comprised of O3+P3 phases, and a solid solution region, comprised of P3 phase. O3NT provides an excellent capacity retention of 99% for 115 cycles at C/2 rate. The good cycleability is attributed to the relative invariance of net impedance during electrode cycling using impedance spectroscopy.

ACKNOWLEDGEMENTS

I would like to recognize the valuable research guidance of my advisor Prof. Wei Lai towards my doctorate degree. I am grateful for the opportunity to do my thesis research under his mentorship and develop my professional skills. I would like to extend my thanks to Prof. Tim Hogan, Prof. Lawrence Drzal, and Prof. Jeff Sakamoto for being a part of my research committee and providing feedback on my research activities.

I would like to thank my lab mates Yuxing Wang, and Matt Klenk. I would like to acknowledge Yuxing for providing insights on research projects from a materials science perspective and support on lab equipment and facilities. It was a pleasure to share lab and office space with you guys, and engage in impromptu discussions on various scientific and non-work related topics. I acknowledge CHEMS department for providing multiple teaching assistantships and value the lecturing opportunities under the mentoring of Prof. Scott Calabrese Barton, Prof. Carl Boehlert, Maddalena Fanelli, Prof. Andre Lee and Prof. Timothy Hinds.

I appreciate the research staff at CMSC including Michael Rich and Per Askeland for providing training and valuable feedback on electron microscopy, surface area analysis, and electrospinning tools. I also thank the CAM center staff: Stanley Flegler, Carol Flegler, and Abigail Vanderberg for 7500F SEM training, sample preparations and troubleshooting. I acknowledge Prof. Richard Staples for providing training, access and inputs in XRD characterization at chemistry department, MSU.

I would like to thank all my friends for the support and making my life in graduate school exciting. Last but not the least, I am grateful for the encouragement, and emotional support of my family.

TABLE OF CONTENTS

LIST OF TABLES	5
LIST OF FIGURES	6
1. INTRODUCTION	14
1.1 Climate Change: A Major Challenge of the 21st Century	14
1.2 Sources of GreenHouse Gas Emissions	
1.3 Renewable Energy Technologies: Benefits and Issues	16
1.4 Energy Storage Technologies for Stationary Applications	19
1.4.1 Pumped Hydroelectric Storage	20
1.4.2 Compressed Air Energy Storage	20
1.4.3 Electrochemical Energy Storage	
1.4.3.1 Na/S batteries	21
1.4.3.2 Lead-acid batteries	22
1.4.3.3 Li-ion batteries	22
1.4.4 Flywheels	23
1.5 Market need for stationary sector	24
1.6 Need for Alternate Battery Chemistry	25
1.7 Rationale for investigating Na-based batteries	28
1.7.1 Na-ion vs Mg-ion batteries	28
1.7.2 Relative ease of scalability	
1.8 Insertion-based Batteries: Working Principle	30
1.9 Requisites for Intercalation-based Electrodes	31
1.10 Research Problem	
1.11 Thesis organization	34
BIBLIOGRAPHY	
2. SYNTHESIS, AND ELECTROCHEMICAL CHARAC'	redization of
NOVEL TUNNEL-TYPE SODIUM INTERCALATION N	
2.1 Introduction	
2.2 Structural features	
2.2.1 Sodium nickel phosphate: Na ₄ Ni ₇ (PO ₄) ₆	
2.2.2 Sodium cobalt titanate: Na _{0.8} Co _{0.4} Ti _{1.6} O ₄	
2.3 Inorganic Synthesis	
1 1 7	
2.3.2 Sodium cobalt titanate synthesis	
2.4 Film fabrication	
2.4.2 Casting methods	

2.5 Electrochemical characterization	52
2.5.1 Cell setup and testing	
2.5.2 Evaluation of the electrolyte and current collectors	
2.5.3 Validation of electrochemical methods using standard intercalation materials: Na _{0.7} C and LiFePO ₄	CoO_2
2.5.4 SNP Electrochemistry: Galvanostatic testing	
2.5.5 SNP Ex-situ XRD characterization	
2.5.6 SCT Electrochemistry: Potentiostatic Intermittent Titration Testing (PITT)	
2.6 Summary	
BIBLIOGRAPHY	
3. SYNTHESIS, AND ELECTROCHEMICAL CHARACTERIZATION	
P-TYPE LAYER-STRUCTURED MATERIALS: Na _{2/3} [Ni _{1/3} Mn _x Ti _{2/3-x}]O(x=0, 1/3)	
3.1 Introduction	72
3.1.1 Ionic conduction in layered materials	72
3.1.2 Literature reports on layered host materials	73
3.1.3 Materials of interest	74
3.2 Structural features	75
3.2.1 Sodium nickel titanate: P2-Na _{2/3} [Ni _{1/3} Ti _{2/3}]O ₂	75
3.2.2 Sodium nickel manganese titanate: P2-Na _{2/3} [Ni _{1/3} Mn _{1/3} Ti _{1/3}]O ₂	76
3.3 Inorganic synthesis and high-temperature processing	76
3.3.1 Sodium nickel titanate synthesis	76
3.3.2 Sodium nickel manganese titanate synthesis	79
3.3.3 Powder sintering	81
3.4 Film fabrication	
3.5 Material Characterization	
3.5.1 Voltage profile under galvanostatic testing	
3.5.1.1High-voltage cathode: Ni ^{2+/4+} redox couple	
3.5.1.2 Low-voltage anode: Ti ^{4+/3+} redox couple	84
3.5.2 Quantifying charge carrier transport processes: DC & AC Testing	86
3.5.3 Evaluating ionic transport and interfacial processes: Electrochemical impedance spectroscopy	
3.5.4 Analyzing ionic transport processes: Potentiostatic intermittent titration technique	
3.5.5 Understanding reaction mechanisms: Ex-situ XRD Testing	
3.5.6 Evaluating capacity retention	
3.5.6.1 Cycling Study	
3.5.6.2 Impedance change during cycling	
3.5.7 Rate performance testing	
3.6 Improving cathodic stability: Calcium substitution	
3.7 Improving anodic capacity: Potassium substitution	
3.8 Summary and future work	
BIBLIOGRAPHY	

4. STRUCTURAL CHARACTERIZATION OF P2-SODIUM NICKEL	
TITANATE USING EXPERIMENTAL AND COMPUTATIONAL	110
METHODS	
4.1.1 Computational methods	
4.1.2 Literature	
±	
4.2 Experimental	
4.2.1 Neutron diffraction experiments	
4.2.2 Energy calculations for many-body systems: Theory	
4.2.3 Long-range and short-range interactions	
4.2.4 Handling partial occupancy: Mean field model and Supercells	
4.2.5 Energy minimization: Optimization schemes and strategy	
4.2.6 Space group transformations.	
4.2.7 Simulation data interpretation and Pair Distribution Function (PDF) calculation	
4.3 Results and Discussion	
4.3.1 Rietveld refinement: Neutron Diffraction	
4.3.2 Interatomic potential sets: Selection and validation	
4.3.3 Energetics of disordered structures: Atomic distribution effects	
4.3.4 Energetics of ordered structures	
4.3.5 Simulated average structure	
4.3.6 Pair distribution function and probability density line-scans	
4.4 Summary and future work	
BIBLIOGRAPHY	154
5. SYNTHESIS, STRUCTURAL AND ELECTROCHEMICAL CHARACTERIZATION OF Na _{0.9} [Ni _{0.45} Ti _{0.55}]O ₂ , AN O-TYPE LAYER-STRUCTURED MATERIAL	
5.1 Introduction.	
5.1.1 O3-type materials	
5.1.2 Literature	
5.1.3 Research Strategy	
5.2 Material synthesis & electrode fabrication	
5.3 Electrochemistry	
5.3.1 Voltage-composition curves: Galvanostatic Testing	
5.3.2 Phase transitions: Ex-situ XRD	
5.3.3 Equilibrium voltage profiles and solid-state diffusivity estimation: Potentiostatic	
Intermittent Titration Technique (PITT)	170
5.3.4 Cycling study	
5.3.4.1 Capacity retention at different voltage cutoffs	
5.3.4.2 Impedance spectra evolution during cycling	
5.3.4.3 Sodium metal deactivation: Prolonged cycling	
5.3.5 Rate testing	
5.4 Summary and future work	180
BIBLIOGRAPHY	

6.	CONCLUSIONS.	
•	COLUE COLOR	······································

LIST OF TABLES

Table 1.1 Short-term and Long-term DOE targets for EES technologies (stationary applications). 25
Table 1.2 Comparison of resources and physical properties of lithium, sodium and magnesium ³⁰
Table 3.1 Theoretical capacity of P2-titanate materials based on vacancy concentration 110
Table 4.1 Interatomic potential parameters: Buckingham Core-shell model; all atomic species are taken at formal charges, Formal charge= Y_{core} + Y_{shell}
Table 4.2 Interatomic potential parameters: Morse+ LJ model
Table 4.3 Structural information of P2-NT powders: Prepared at 900 °C and tested at 15K 133
Table 4.4 Structural information of P2-NT powders: Prepared at 900 °C and tested at 300K 134
Table 4.5 Structural information of P2-NT powders: Prepared at 1000 °C and tested at 15K 134
Table 4.6 Structural information of P2-NT powders: Prepared at 1000°C and tested at 300K . 134°
Table 4.7 Transferability of Buckingham interatomic potential across binary oxides; $ \epsilon $ is the modulus percentage error in lattice parameters
Table 4.8 Transferability of Buckingham interatomic potential across ternary oxides
Table 4.9 Transferability of Morse interatomic potential across binary oxides
Table 4.10 Transferability of Morse interatomic potential across ternary oxides

LIST OF FIGURES

Figure 1.1 (a) Global carbon dioxide uptake over past decades, (b) Surface temperature anomalies; For interpretation of references to color in this and all other figures, the reader is referred to the electronic version of this thesis.
Figure 1.2 (a) Global greenhouse gas emissions, ¹² and (b) Global energy consumption in past decades. ¹³
Figure 1.3 (a) Global energy generation by sources,17 (b) Renewable energy estimated output and projections. 17
Figure 1.4 Variability in (a) solar power output and, (b) wind power output. 18
Figure 1.5 Schematic representation of (a) pumped hydroelectric system, (b) compressed air energy storage system, (c) electrochemical energy storage system with Na/S battery chemistry and (d) flywheel system. ²²
Figure 1.6 (a) Cost and efficiency comparison of different energy storage technologies; <i>hatched bars refer to the efficiency values on the secondary y-scale</i> , and (b) lifetime comparison of energy storage technologies. ²¹
Figure 1.7 Market segments for energy storage devices in the electricity grid
Figure 1.8 Energy storage technologies employed for various stationary applications. ²¹
Figure 1.9 Relative abundance chart depicting plentiful sodium element as compared to lithium. ²
Figure 1.10 Manufacturing steps for advanced batteries such as Li-ion chemistry
Figure 1.11 Working principle of an insertion/intercalation-based battery. ³⁴
Figure 1.12 Growing number of research publications on anode materials for Na-ion battery ³⁶ 34

Figure 2.1 Crystal structure of Na ₄ Ni ₇ (PO ₄) ₆ ; Pink polyhedra represents nickel octahedra, green polyhedra represents phosphate tetrahedra and yellow spheres indicate sodium atoms. Oxygen atoms are not included for clarity. ²⁶
Figure 2.2 Crystal structure of Na _{0.8} Co _{0.4} Ti _{1.6} O ₄ ; blue polyhedra represents transition metal octahedra (cobalt and titanium) and yellow spheres represent sodium atoms; oxygen atoms are omitted for clarity. ²⁵
Figure 2.3 Schematic of solid state reaction technique
Figure 2.4 XRD characterization of sodium nickel phosphate prepared by solid state reaction 45
Figure 2.5 (a) Sodium nickel phosphate powder morphology prepared by solid state reaction, and (b) Higher-magnification image of a particle showing dense morphology
Figure 2.6 Schematic of sol-gel synthesis technique
Figure 2.7 XRD characterization of sol-gel synthesized powders of sodium nickel phosphate 47
Figure 2.8 (a) Sodium nickel phosphate powder morphology prepared by sol-gel reaction, and (b) Higher-magnification image of a particle showing porous morphology
Figure 2.9 (a) XRD characterization of sodium cobalt titanate prepared by solid state reaction, and (b) SEM morphology of as-synthesized sodium cobalt titanate powders
Figure 2.10 Schematic of doctor-blade slurry casting method for fabricating battery electrodes.51
Figure 2.11 Schematic of Swagelok 3-electrode cell setup for electrochemical testing
Figure 2.12 Impedance spectroscopy curves for sodium metal SEI formation in (a) 1M NaClO4 in ethylene carbonate/dimethyl carbonate, and (b) 0.5M NaPF6 in ethylene carbonate/diethyl carbonate; 1st cycle refers to test after 4 hours open-circuit and subsequent tests
Figure 2.13 Cyclic voltammograms scanned between 1.5-4.2 V voltage window for (a) aluminum, (b) andoized aluminum, (c) stainless steel 316, and (d) titanium

Figure 2.14 (a) Cyclic voltammogram of graphite scanned between 1.5-4.2 V voltage window, and (b) oxidative voltammogram peak currents for 1 st and 10 th cycle
Figure 2.15 Voltage profile of anodized aluminum current collector tested under galvanostatic condition with 4.5V cutoff using 3-electrode setup
Figure 2.16 Voltage profiles of (a) lithium iron phosphate under galvanostatic conditions at C/10 rate demonstrating two-phase reaction between FePO ₄ and LiFePO ₄ , and (b) Na _{0.7} CoO ₂ showing complex voltage steps and plateaus due to multiple phase transitions
Figure 2.17 Sodium nickel phosphate tested under galvanostatic conditions with discharge cut-off voltage of (a) 1.5 V in 1st cycle, and (b) 0.8 V
Figure 2.18 Ex-situ XRD characterization of SNP electrode film at different state-of-charge, Mylar film and wax (used for sticking the electrode to the holder base)
Figure 2.19 (a) Voltage curve of sodium cobalt titanate from PITT with C/50 current limit, 100 mV step potential tested at 70 °C using 0.5M NaPF6 in EC/DEC electrolyte, and (b) Discharge capacity and faradaic efficiency with cycle number
Figure 2.20 (a) Voltage profile of sodium cobalt titanate tested under at C/100 rate using 1M NaClO4 in EC/DMC electrolyte at room temperature, and (b) Ex-situ XRD of SCT at pristine, 20% charged and discharged state.
Figure 3.1 Schematic of the transition metal slab in layered oxide depicting charge carrier pathways in (a) P2-NT, and (b) P2-NMT through formation of percolating network; red, blue and orange spheres denote nickel, titanium, and manganese atoms, respectively
Figure 3.2 Crystal structure of Na _{2/3} [Ni _{1/3} Ti _{2/3}]O ₂ ; blue spheres refer to transition metals (nickel and titanium), yellow spheres refer to sodium atoms Oxygen atoms are not included for clarity.
Figure 3.3 XRD characterization of sodium nickel titanate prepared by solid state reaction from micron-sized precursors fired for 12 hours duration; The dominant peaks of the impurity and target phases are indexed.
Figure 3.4 XRD characterization of P2-NT material prepared by solid state reaction from wet-milled nano-sized precursors fired at (a) 800 °C, and (b) 900 °C, SEM morphology of powders prepared from (c) micron-sized precursors, and (d) nano-sized precursors

Figure 3.5 (a) XRD comparisons of sodium nickel titanate and sodium nickel manganese titanate powders prepared by solid state reaction, (b) and SEM powder morphology
Figure 3.6 (a) Surface morphology of sintered pellets of (a) $P2-Na_{2/3}[Ni_{1/3}Ti_{2/3}]O_2$, and (b) $P2-Na_{2/3}[Ni_{1/3}Mn_{1/3}Ti_{2/3}]O_2$.
Figure 3.7 Cathodic voltage profile under galvanostatic testing rate of C/50 rate for (a) P2-NT material with cutoff of 4.2 V and, (b) P2-NT material with cutoff of 4.5 V, (c) P2-NMT material with cutoff of 4.2 V and, (d) P2-NMT material with cutoff of 4.5 V
Figure 3.8 Anodic voltage profile of sodium nickel titanate under galvanostatic testing of C/5 rate with 0.2 V cutoff voltage.
Figure 3.9 (a) Electrical equivalent circuit model representing physical processes in a mixed electronic-ionic conductors with blocking electrodes, (b) Limiting model for high-frequency AC signal, and (c) Limiting model for DC signal. ²⁸
Figure 3.10 Electrical testing of P2-NMT sintered pellet: (a) High-frequency AC impedance spectra in temperature range of 383-423 K with 10 K increments, and (b) Current decay response upon applying a potential of 200 mV at a 383 K
Figure 3.11 Total effective conductivity (ionic and electronic) and electronic conductivity curves as a function of temperature from AC impedance and DC testing
Figure 3.12 Electrical equivalent circuit model depicting sodium ion transport processes (within liquid electrolyte, across surface films, across the interface, and bulk solid state diffusion) of the composite electrode; where Re is the electrolyte resistance, Rsf is the surface film resistance, CPE _{st} is the constant phase element due to surface films, CPE _{ct} is the constant phase element due to the double layer, and Z _w is the semi-infinite Warburg diffusional element
Figure 3.13 Nyquist plot of P2-NT (blue) and P2-NMT (yellow) electrodes scanned between frequency range of 5 MHz to 10 mHz with inset showing high-frequency depressed semicircles at voltage of (a) 3.4 V vs. Na/Na ⁺ , (b) 3.8 V vs. Na/Na ⁺ , and (c) 4.2 V vs. Na/Na ⁺
Figure 3.14 Potential dependence of (a) charge transfer resistance and double layer capacitance, and (b) surface film resistance and surface film capacitances
Figure 3.15 Linear fitting of Zreal vs. $\omega^{-0.5}$ curves using planar diffusion model to obtain Warburg prefactor

Figure 3.16 Voltage profile under potentiostatic intermittent titration technique using C/100 current limitation for (a) cathodic P2-NT with 5 mV voltage step, and (b) cathodic P2-NMT with 5 mV voltage step, and (c) anodic P2-NT with 15 mV voltage step; inset in cathodic curves depict electrode precycling at C/10 rate.
Figure 3.17 (a) Linear fitting of current transients from potentiostatic intermittent titration technique at different electrode potentials with current limitation of C/100 for cathodic P2-NT electrode, (b) linear fitting of P2-NMT electrode under identical conditions, and (c) variation of apparent chemical diffusion co-efficient with electrode potential as calculated from potentiostatic intermittent titration technique and impedance spectroscopy
Figure 3.18 Ex-situ XRD of electrode films: (a) sodium nickel titanate cathode charged till 4.2 V with inset showing the evolution of 160 reflection, (b) sodium nickel titanate cathode charged to 4.5 V, (c) sodium nickel manganese titanate cathode charged till 4.2 V, and (d) sodium nickel titanate anode charged to 0.2 V with inset showing evolution of 16° reflection; all potentials are measured with respect to Na/Na ⁺
Figure 3.19 Capacity retention study with 4.2 V upper voltage cutoff for (a) cathodic sodium nickel titanate at C/10 rate, (b) cathodic sodium nickel manganese titanate electrodes tested at C/5 rate and (c) anodic sodium nickel titanate tested at C/5 rate
Figure 3.20 (a) Nyquist impedance spectroscopy plot of sodium nickel manganese titanate electrode scanned in frequency range of 5 MHz to 10 mHz after charging to 4.2 V, (b) variation of impedance resistive parameters, and (c) capacitive parameters during cycling
Figure 3.21 High-current rate testing of (a) cathodic sodium nickel titanate powders with micronand nano-sized powders, (b) cathodic sodium nickel titanate and sodium nickel manganese titanate electrodes with 4.2 V cutoff, and (c) anodic sodium nickel titanate with cutoff voltage of 0.2 V.
Figure 3.22 (a) XRD characterization of 5% and 20% calcium substituted sodium nickel titanate prepared by solid-state reaction at 900 °C, and (b) EDS mapping of 5% sodium nickel titanate powders to check calcium distribution
Figure 3.23 XRD characterization of powders to synthesize (a) sodium deficient compositions with $x=0.67,\ 0.55$ and 0.50 at firing temperature of 1000 °C for 20 h duration, and (b) Na _{2/3-y} K _y [Li _{1/3} Ti _{2/3}]O ₂ for y=0, 0.05, 0.10 and 0.15 prepared at firing temperature of 800°C for 20 h 110
Figure 4.1 Variation of interaction energy for Buckingham and Morse interatomic potentials for

Figure 4.2 Unit cell transformation from space group 194 to 63
Figure 4.3 Space group transformation to generate in-plane ordered structure
Figure 4.4 Space group transformation to generate through-plane ordered structure
Figure 4.5 Rietveld refinement of P2-NT powders prepared at 900 °C and characterized at (a) 15K, bank 1, (b) 15K, bank 4, (c) 300K, bank 1, and (d) 300K, bank 4; red point indicates experimental data, green curve indicates simulated structure, and pink curve indicates difference curve; bank 1, bank 2 includes diffraction data in the d-spacing range of 0-2.2 Å, and 1.1-8 Å, respectively 132
Figure 4.6 Rietveld refinement of P2-NT powders prepared at 1000 °C and characterized at (a) 15K, bank 1, (b) 15K, bank 4, (c) 300K, bank 1, and (d) 300K, bank 4
Figure 4.7 3D nuclear density map using Rietveld refined 900 °C, 15K structure (a), {100} planar density describing sodium (b), transition metal (c) and oxygen atoms (d) with minimum and maximum saturation levels at 0 and 5 Å ⁻³ ; atomic species legend is included on the right-side of 3D density map
Figure 4.8 Crystal structure of (a) cubic sodium oxide (Na ₂ O), (b) cubic nickel oxide (NiO), (c) tetragonal titanium oxide (TiO ₂), (d) rhombohedral nickel titanium oxide (NiTiO ₃), (e) monoclinic sodium titanate-I (Na ₂ Ti ₃ O ₇), and (f) monoclinic sodium titanate-II (Na ₂ Ti ₆ O ₁₃); yellow, grey, red, and blue spheres represent sodium, nickel, oxygen, and titanium, respectively. colored polyhedra represent transition metals co-ordinated with oxygen atoms, sodium are left unbonded for clarity. 40-45
Figure 4.9 (a) Buckingham potential energy distribution curve, (b) Morse potential energy distribution curve, (c) probability distribution histogram of randomized structures with equal atomic distribution between layers using Buckingham potential, and (d) probability distribution histogram of randomized structures with equal atomic distribution between layers using Morse potential
Figure 4.10 Probability distribution histogram for (a) unequal sodium distribution using Buckingham potential, (b) unequal sodium distribution using Morse potential, (c) unequal transition metal distribution using Buckingham potential, and (d) unequal transition metal distribution using Morse potential
Figure 4.11 Probability distribution histogram for completely randomized structures using (a) Buckingham potential, and (b) Morse potential

Figure 4.12 Energy distribution curve for ordered and disordered structures using Morse potential
Figure 4.13 Simulated sodium probability density maps in (a) 3D using Buckingham potential and (b) 3D using Morse potential, (c) 2D along using Buckingham potential, and (d) 2D using Morse potential; selected 2D cut-sections are parallel to {100} planes; minimum and maximum saturation levels set at 0 and 5 Å ⁻³
Figure 4.14 Simulated probability density maps for (a) sodium atoms in 3D using Buckingham potential and (b) sodium atoms in 3D using Morse potential, (c) sodium atoms in 2D using Buckingham potential, (d) sodium atoms in 2D using Morse potential; 2D cut-sections are parallel to {100} planes; minimum and maximum saturation levels set at 0 and 5 Å ⁻³
Figure 4.15 2D oxygen density maps using (a) Buckingham potential, and (b) Morse potential; 2D cut-sections are parallel to {100} planes; minimum and maximum saturation levels set at 0 and 5 Å-3.
Figure 4.16 (a) Experimental pair distribution function using Buckingham potential, (b) experimental pair distribution function using Morse potential, (c) normalized probability density between Na _f and Na _e sites on the 'ab' plane comparing simulations with experiments, and (d) normalized probability density between four different Na _f -Na _e locations using Buckingham potential
Figure 5.1 (a) Rietveld refinement of O3NT powders prepared by solid-state reaction at 1000 °C for 10 hours firing duration with inset figure showing powder morphology, (b) SEM morphology of composite film electrode showing O3NT particles embedded in a carbon network formed by conductive additive, and (c) EDS mapping of powders showing elemental distribution of carbon and titanium; refinement was performed with lab powder diffraction dataset using TOPAS software by Bruker Corporation. 163
Figure 5.2 Voltage-composition curve of O3-Na _{0.9} [Ni _{0.45} Ti _{0.55}]O ₂ under galvanostatic conditions of C/50 rate with (a) 4.2 V cutoff, and (b) 4.5 V cutoff; negative 'x' value during the 1 st charging cycle is due to side reactions
Figure 5.3 Crystal structure of (a) O3 phase with octahedral co-ordination of sodium, and (b) P3 phase with prismatic co-ordination of sodium demonstrating the different oxygen stacking sequence
Figure 5.4 Ex-situ XRD characterization of O3NT phase at different sodium content; 'un' refers to the unidentified phase formed due to moisture intercalation of the low-sodium content phases.

Figure 5.5 Rietveld refinement of O3NT electrode (Na _x [Ni _{0,45} Ti _{0.55}]O ₂) prepared by electrochemical sodium extraction with (a) 'x'=0.52, and (b) 'x'=0.39; refinement performed using TOPAS software from Bruker Corporation, insert figures depict sodium co-ordination environment and Na-O bond lengths.
Figure 5.6 (a) Voltage profile of O3-Na _{0.9} [Ni _{0.45} Ti _{0.55}]O ₂ using Potentiostatic Intermittent Titration Technique (PITT) with C/100 current and 4.2 V voltage limit, (b) Voltage profile using PITT with C/100 current and 4.5 V voltage limit, (c) current transient linear fitting with 4.2 V limit, and (d) current transient linear fitting with 4.5 V limit
Figure 5.7 Solid-state diffusion co-efficient of sodium ions in O3NT material using potentiostatic intermittent titration testing
Figure 5.8 Capacity study of O3-Na _{0.9} [Ni _{0.45} Ti _{0.55}]O ₂ material: (a) 4.0 V charging limit, (b) 4.2 V charging limit, (c) 4.4 V charging limit, and (d) Variation of charging capacity with different cut-off voltage limit
Figure 5.9 (a) Nyquist plot of O3NT electrodes charged to 4.2 V during cycling, (b) Bode plots of O3NT electrodes charged to 4.2 V during cycling, (c) Variation of electrolyte resistance (R _e), surface film resistances (Rsf1 and Rsf2), and charge transfer resistance (Rct) during cycling, and (d) Variation of double layer capacitance (Cdl) and surface film capacitances (Csf1 and Csf2).
Figure 5.10 Variation of peak counter electrode potential with cycle number during galvanostatic cycling measured against Na/Na ⁺ reference electrode; ideally the measured voltage would be zero at the counter electrode as it has the same chemical potential as the reference electrode 178
Figure 5.11 Rate performance testing of O3-Na _{0.9} [Ni _{0.45} Ti _{0.55}]O ₂ material with 4.2 V cut-off voltage (a) capacity retention, and (b) voltage profiles

1. INTRODUCTION

1.1 Climate Change: A Major Challenge of the 21st Century

The amount of atmospheric carbon dioxide has substantially increased over the past two decades and was estimated to be at 395 ppm in 2014 (Figure 1.1a). 1,2 The increasing amount of carbon dioxide along with other anthropogenically produced greenhouse gases (methane, nitrous oxide, fluorinated gases, etc.) has led to the warming of the climate system. Global climate change is anticipated to result in a number of deleterious effects such as higher surface temperatures-land and oceanic (Figure 1.1b)³, elevation of mean sea level, acidification of the ocean and alteration, natural weather patterns (including precipitation, drought, etc.). 1,3-6 Even though these harmful effects are widely recognized, there are significant hurdles to reduce gas emissions due to the complex interplay between climate change, ecology, and economy. 7-11

International agencies such as United Nations Framework Convention on Climate Change (UNFCC) and Intergovernmental Panel on Climate Change (IPCC) have been striving to achieve a global collective consensus on emission reductions. Climate change has become one of the prime challenges of the 21st century and advancing and developing alternate green technology solutions is of paramount importance.

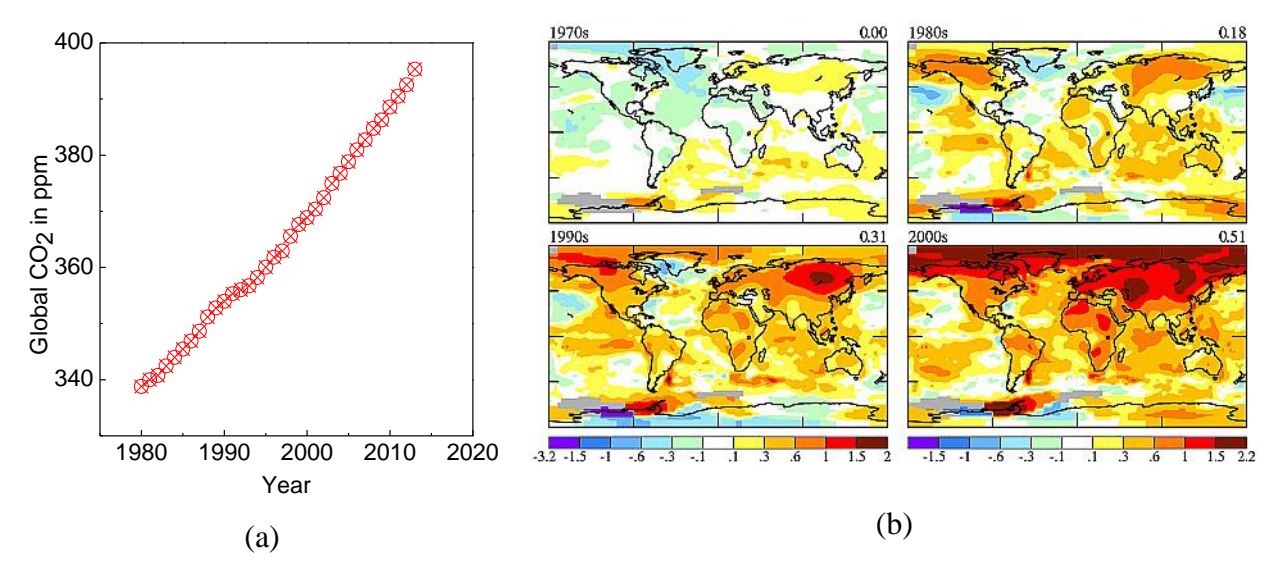


Figure 1.1 (a) Global carbon dioxide uptake over past decades, (b) Surface temperature anomalies;³ For interpretation of references to color in this and all other figures, the reader is referred to the electronic version of this thesis.

1.2 Sources of GreenHouse Gas Emissions

The combustion of fossil fuels (coal, natural gas and oil) for energy generation is the largest contributor (26%) of global (Greenhouse gases) GHG emissions (Figure 1.2a) based on estimates by U.S. Environmental Protection Agency (EPA). The global energy usage has grown substantially as shown in Figure 1.2b and the currently at 530 Quadrillion Btu in 2012 based on estimates by U.S. Energy Information Administration (EIA). In the light of ever-growing energy needs in the modern society, developing improved low-carbon renewable sources (wind and solar) and wide-scale integration of these technologies are vital for generating clean and sustainable energy. The unavailability of cheap, high-performance energy storage devices is considered a major setback for increasing the adoption of renewable energy sources. 14-16

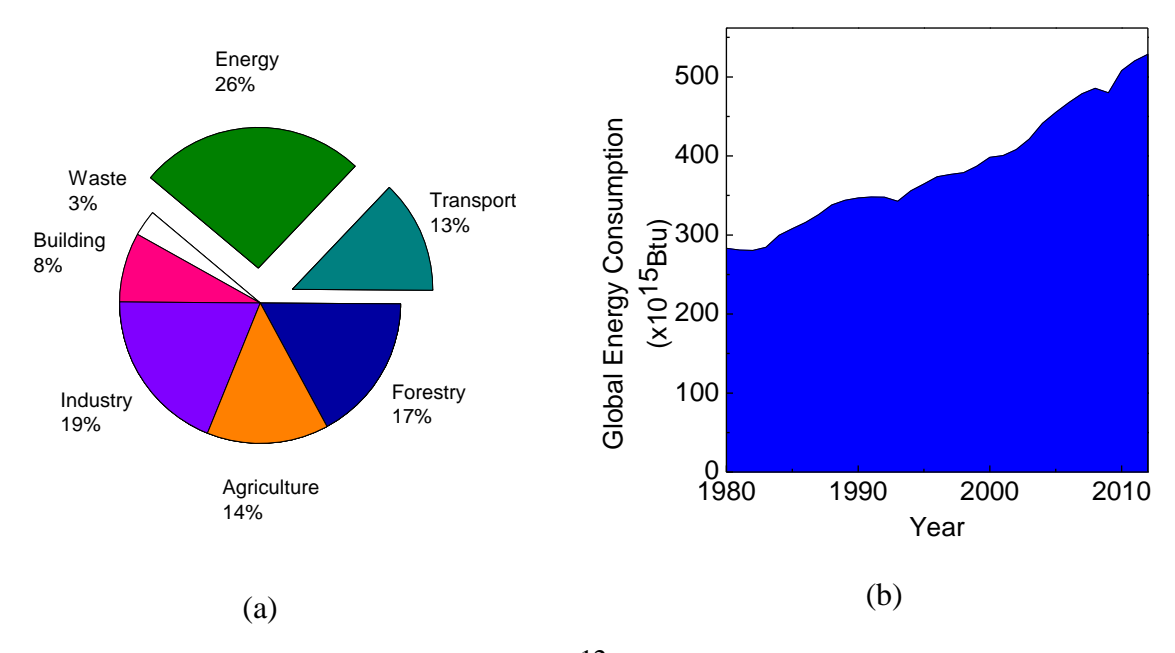


Figure 1.2 (a) Global greenhouse gas emissions, ¹² and (b) Global energy consumption in past decades. ¹³

EPA reports transportation sector to be a significant emissions contributor at 13% (Figure 1.2). 12 Emission reductions in this sector are addressed by government regulations stipulating increased automobile fuel efficiencies spurring the advancement of hybrid and fully electric drivetrains that incorporate energy storage devices (batteries).

1.3 Renewable Energy Technologies: Benefits and Issues

Renewable energy sources such as wind, solar, geothermal, etc. are extensively developed as viable alternative sources of clean energy with minimal carbon footprint. Widespread deployment of renewable energy technologies would provide the following benefits:

Achieve compliance with emission standards to combat global climate change
 provides capacity addition to meet the ever-increasing energy demands of the society

- ii. Reduce dependence on depleting non-renewable fossil fuel reserves and provide economic stability by locally producing energy and cut down on oil imports
- iii. Provide a cleaner environment without air or water pollution by zero-emissions operation
- iv. Decentralize electricity grids and potentially aid in creating self-sufficient/off-grid homes and communities

Despite these advantages, renewables accounted for a paltry 19% of the global energy production in 2012 (Figure 1.3a).¹⁷ Nevertheless, the electricity output from renewables has shown a promising rising trajectory (Figure 1.3b), and is anticipated to increase further.¹⁷

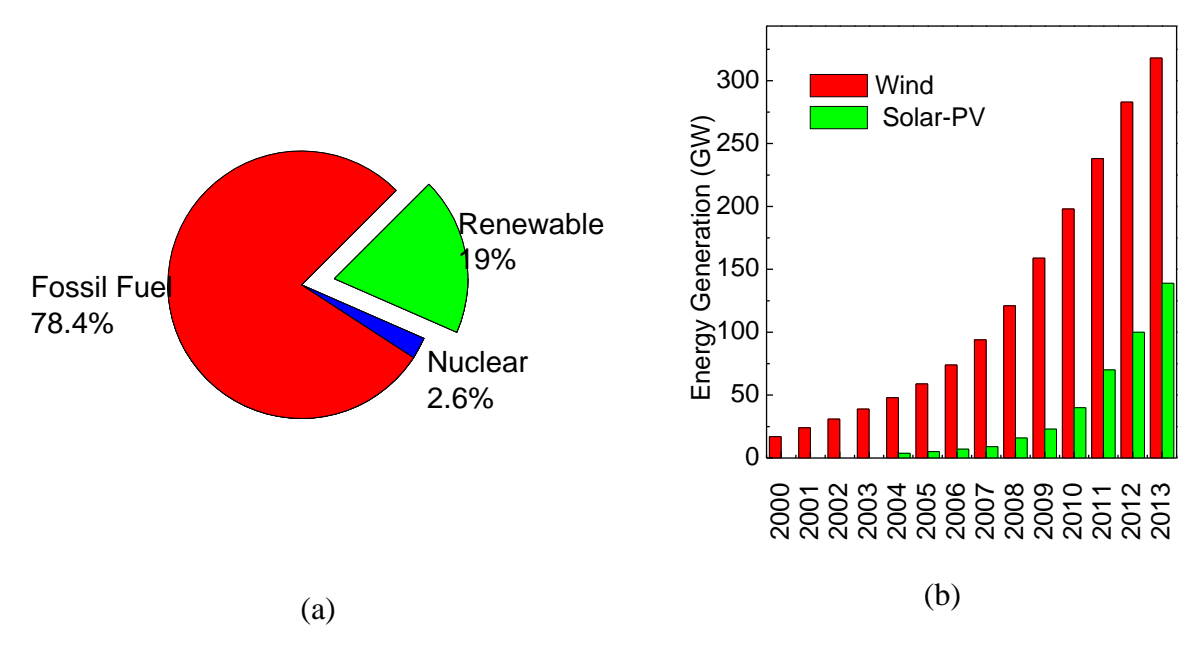


Figure 1.3 (a) Global energy generation by sources,17 (b) Renewable energy estimated output and projections. ¹⁷

Renewable technologies, such as solar and wind, are highly intermittent and this poses challenges while catering to the complex electricity demands of the end-consumers. For instance, solar energy has significant variations in the electricity output depending on factors like day/night

cycle, cloud cover, sun positioning, etc. as shown in Figure 1.4a. ¹⁸ Temporally and geographically uneven wind flow patterns can lead to unpredictable power output from wind energy technology (Figure 1.4b). ¹⁸ For instance, Germany, with large investments in renewable sources (as a consequence of the 'Energiewende' plan) has had 200,000 blackouts in 2011 due to unreliable power generation further substantiating the intermittency issue. ¹⁹

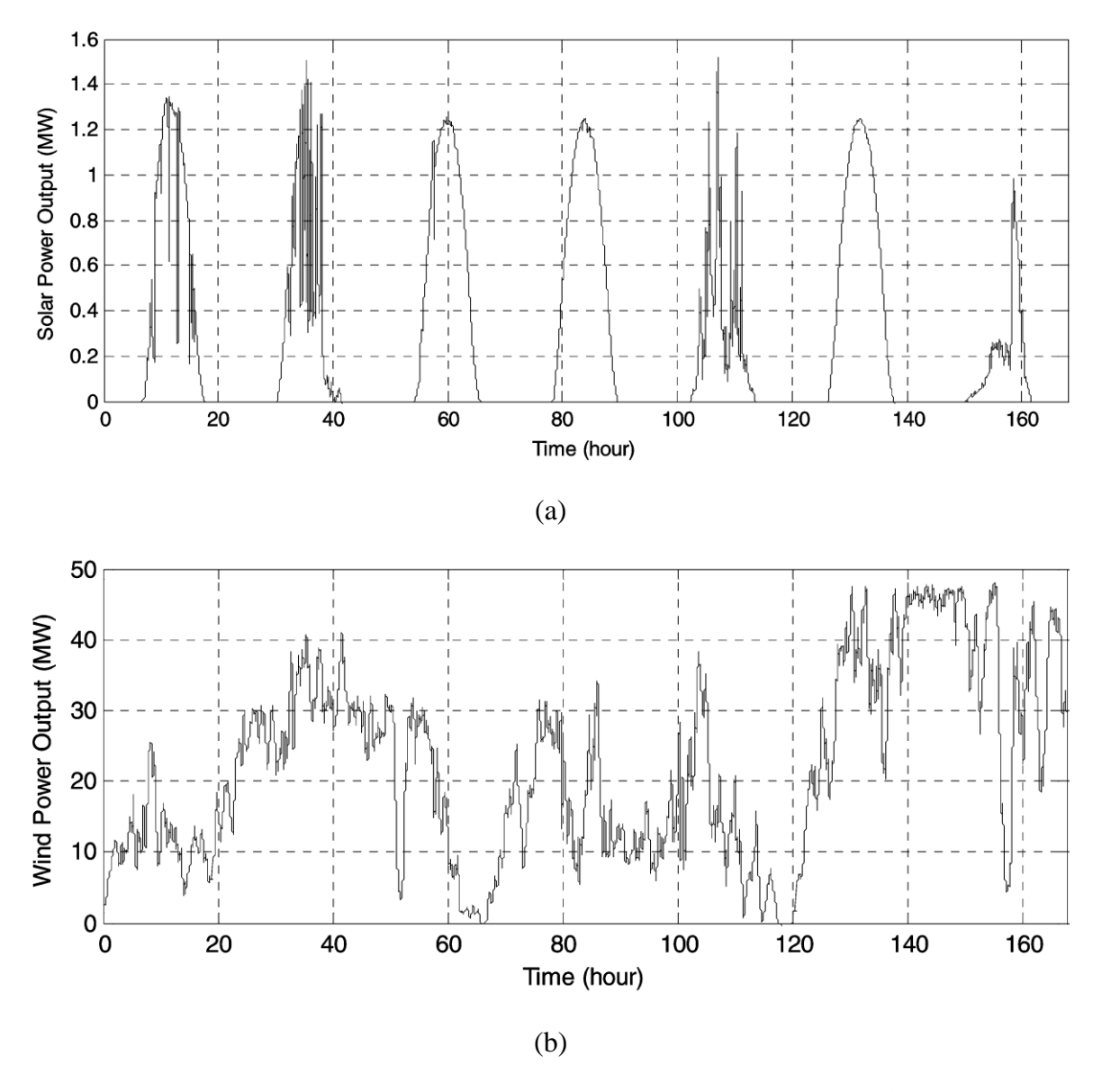


Figure 1.4 Variability in (a) solar power output and, (b) wind power output. ¹⁸

Energy storage devices can act as a buffer by storing excess energy during times of surplus generation and provide the stored energy during times of lean generation (termed as 'time-shifting'). Development of low-cost, long-life energy storage devices would help reduce the variability in renewable throughput and improve overall reliability. In addition to being vital cogs for renewables technologies, large-scale energy storage devices can be beneficial to the conventional electricity grid by

- i. Providing load leveling for traditional power plants (coal, natural gas and nuclear) and improve the overall efficiency by permitting optimal constant capacity operation (no rampup or ramp-down cycles and eliminates the need for inefficient 'peaker' plants)
- ii. Enhancing the power quality by voltage and frequency regulation
- iii. Improving grid reliability by reducing power outages and acting as a backup system

1.4 Energy Storage Technologies for Stationary Applications

Different energy storage technologies have been developed and commercialized for stationary applications and includes

- i. Pumped Hydroelectric Storage (PHS)
- ii. Compressed Air Energy Storage (CAES)
- iii. Electrochemical Energy Storage (EES)
- iv. Flywheels (FW)

While PHS, CAES and FW technologies harness mechanical conversion processes, EES utilizes chemical conversion methods. A schematic of working mechanisms of these storage technologies is illustrated in Figure 1.5.

1.4.1 Pumped Hydroelectric Storage

PHS operates by pumping water to an elevated reservoir (from ground level) and running it through a turbine to extract the stored potential energy (Figure 1.5a). PHS is currently the largest energy storage method and provides 99% of the net global capacity (127 GW). This is because PHS provides a means for large capacity installations at low operational costs (Figure 1.6a). The stored energy scales linearly with mass (or volume) of stored water and elevation difference (E_P=mgh, where 'E_P' is the potential energy, 'm' is the mass, 'g' is the acceleration due to gravity, 'h' is the potential head). PHS supports long lifetime (13,000 cycles) as depicted in Figure 1.6b. However, constructing new PHS facilities requires specific geographical locations such as hilly terrains and accessible large water bodies. Hence, hydroelectric technology is mostly constructed near river canyons with proper topographical features and rock formations. Consequently, it is becomes geographically constrained and suitable only for large-capacity installations.

1.4.2 Compressed Air Energy Storage

CAES operates by compressing gasses into enclosed spaces (caverns, special rock formations, abandoned oil mines, etc.) as illustrated in Figure 1.5b. It has a net installed capacity of 440 MW, three orders of magnitude lower than PHS. CAES provides comparable lifetime (13,000 cycles) to PHS. However, like PHS this technology also requires specific geographic formations (to avoid pressure losses to surroundings). Another approach has been make use of high-pressure tanks but this limits the scale of the application due to technological limitations and increases installation costs. ²⁰

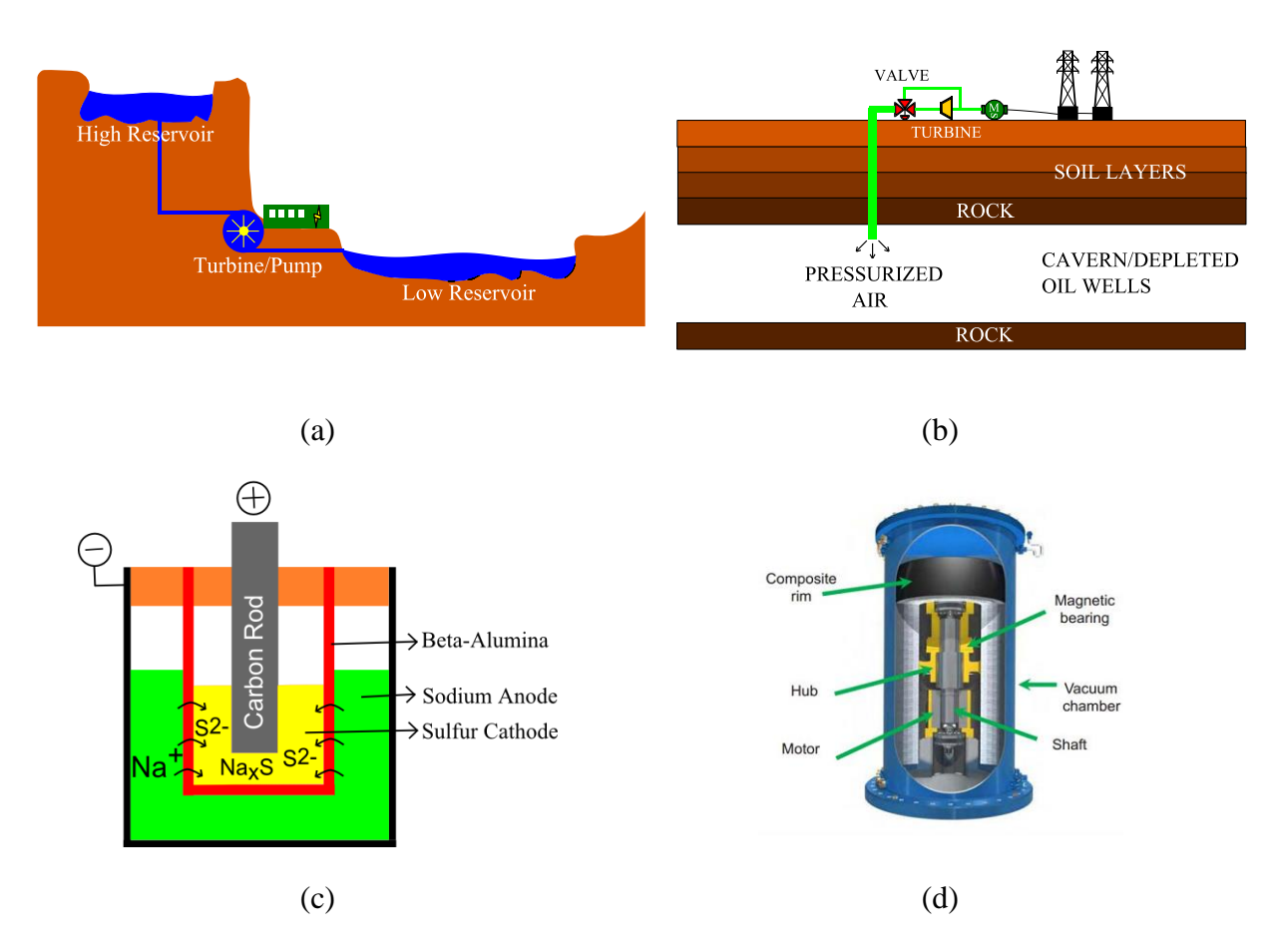


Figure 1.5 Schematic representation of (a) pumped hydroelectric system, (b) compressed air energy storage system, (c) electrochemical energy storage system with Na/S battery chemistry, and (d) flywheel system. ²²

1.4.3 Electrochemical Energy Storage

1.4.3.1 Na/S batteries

Na/S batteries (EES) operate with molten sodium and sulfur as the active components using an electrochemical setup as illustrated in Figure 1.5c. The modular design allows for easy installation anywhere using scalable battery packs. However, these devices have a shorter lifetime (4500 cycles) and higher installation costs (\$535/kWh) than PHS and CAES as shown in Figure 1.6a and b.²¹ The high temperature operation using super reactive molten elements poses challenges in

material selection and engineering fail-safe mechanisms. In 2011, NAS batteries designed by The Tokyo Electric Power Company caught fire due to leakage issues.

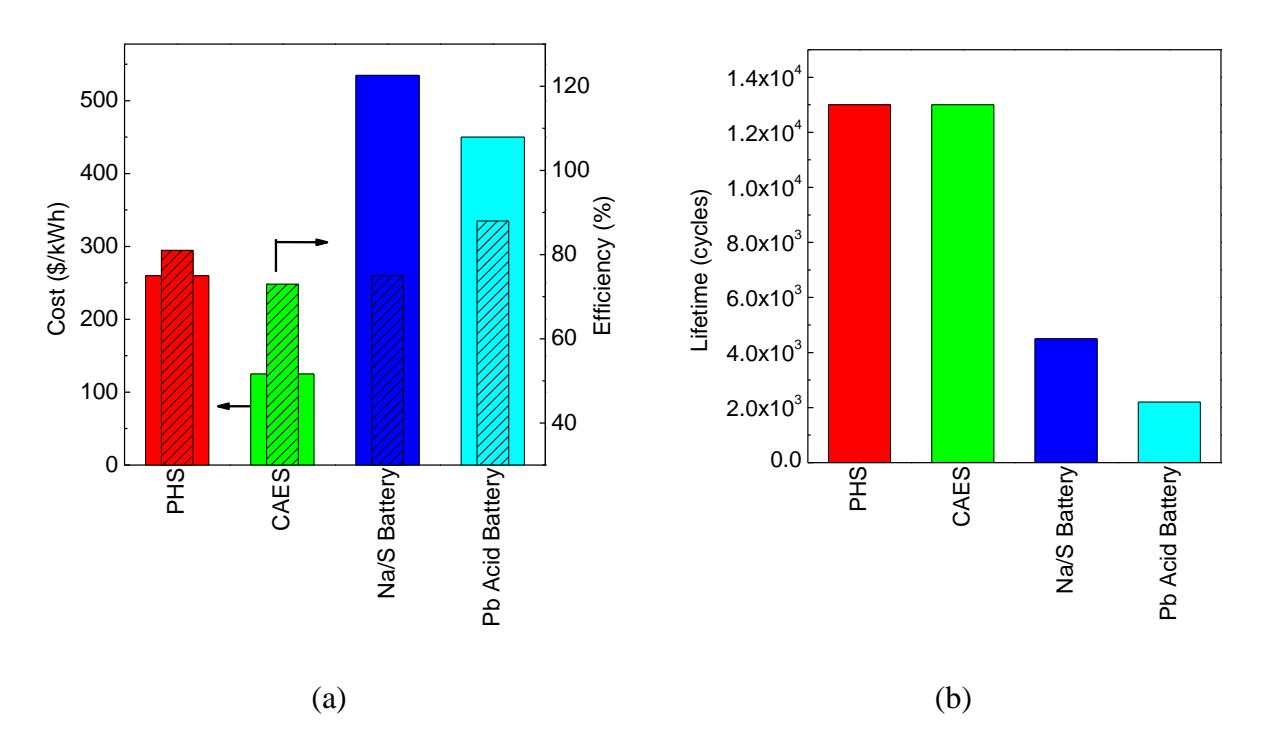


Figure 1.6 (a) Cost and efficiency comparison of different energy storage technologies; *hatched bars refer to the efficiency values on the secondary y-scale*, and (b) lifetime comparison of energy storage technologies.²¹

1.4.3.2 Lead-acid batteries

Lead Acid Batteries (LABs) offers a relatively low-cost EES solution (\$450/kWh) using a well-established battery technology and largely used for small-scale backup for homes and businesses as Uninterrupted Power Supply (UPS) devices. However, they have a short cycle life (2200 cycles) which adds to the routine replacement costs for applications requiring long lifetime.

1.4.3.3 Li-ion batteries

Li-ion batteries (LIBs) offer high-energy density as they are based on highly electropositive and light weight lithium as an active component. LIB demonstrations have been made for relatively

small-scale frequency regulation and renewables applications so far with good efficiency (90%). However, they remain fairly expensive for bulk energy storage. Safety issues due to lithium dendritic plating, electrolyte decomposition due to overcharging, etc. can arise if used beyond the recommended operating specifications and in-built circuits coupled with sensors actively monitor individual cell voltages (within a pack). These circuits help avoid overcharging, and temperature abnormalities that can potentially lead to battery failures. ²³ It is anticipated that high-volume manufacturing of larger LIB packs for automotive drivetrains would lead to cost-reductions and enable increased usage in stationary sectors.

1.4.4 Flywheels

Flywheels work by converting electrical energy into kinetic energy in the form of angular momentum of a spinning rotor as illustrated in Figure 1.5d. At a smaller scale, they are extensively employed in automobiles to transfer the energy from the power stroke to idle strokes of a combustion cycle and help level-out the power output. Stationary applications require high operational efficiency and this is typically attained by spinning the rotors inside low-pressure chambers to minimize frictional losses.

Since kinetic energy scales non-linearly with angular velocity ($E_k=1/2*I*v^2$, where ' E_k ' is the kinetic energy, 'I' is the moment of inertia and 'v' is the angular velocity), it is beneficial to run these devices at high rotational speeds. However, faster spinning can lead to higher inertial stresses and subsequent device failure.²⁴ State-of-the-art flywheels have been engineered to operate for around 100,000 cycles. However, high costs (\$8300/kWh) restrict flywheels to frequency regulation-related applications.

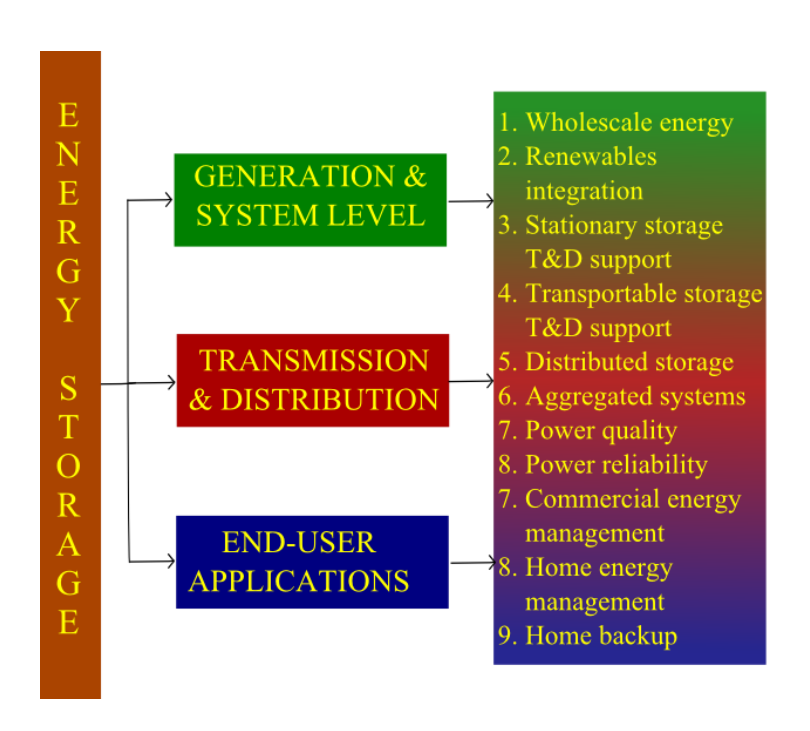


Figure 1.7 Market segments for energy storage devices in the electricity grid.

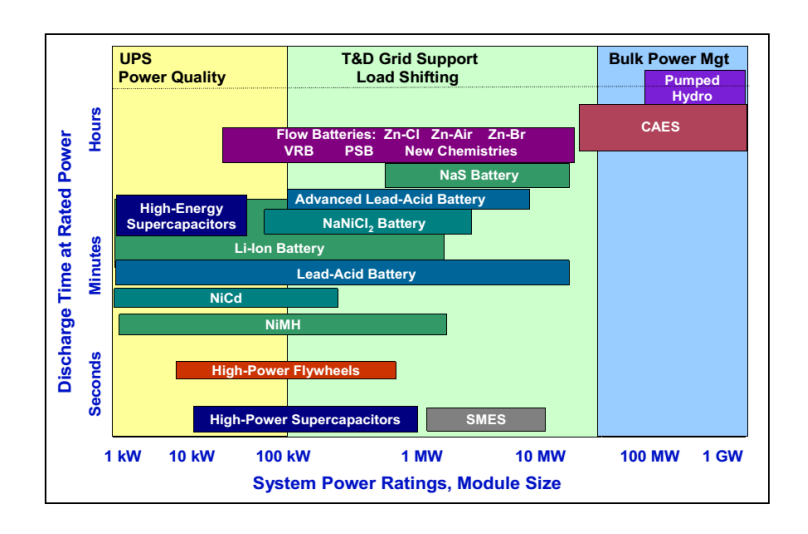


Figure 1.8 Energy storage technologies employed for various stationary applications.²¹

1.5 Market need for stationary sector

The grid sector can be partitioned into three segments: generation, transmission and distribution and end-user (Figure 1.7) and EES can be implemented in various levels shown in Figure 1.8. A

single EES technology is incapable of addressing the performance specifications and cost demands for all these segments in the grid sector. Hence, a multitude of technology solutions address the varied needs and EES technologies primarily compete for mid-scale T&D and small-scale enduser applications.

LIBs perform fairly well but are limited by high installation costs while the cheaper LABs do not offer good cycle-life characteristics. Thus, there is a market demand for a cost-effective EES technology in the stationary sector that can fill-in this gap between LIBs and LABs. The newly researched alternate battery chemistries are anticipated to address this market need by having comparable performance to LIBs while still being relatively inexpensive. The Department of Energy (DOE) target specifications for EES devices are less than \$150/kWh cost, at least 80% faradaic efficiency and minimum cycle-life of 5000, as shown in Table 1.1. Current EES devices do not meet these specifications and the newly researched alternate chemistries are anticipated to enable development of low-cost, highly-efficient, long-life devices.

Table 1.1 Short-term and Long-term DOE targets for EES technologies (stationary applications). ²⁵

Product Specification	Short-term Target	Long-term Target	
Cost	<\$250/kWh	<\$150/kWh	
Efficiency	>75%	>80%	
Cycle life	4000	5000	

1.6 Need for Alternate Battery Chemistry

Alternate battery chemistries, such as sodium and magnesium-based technologies, rely on earthabundant natural resources. Cost-reductions are targeted by relying on widely available, inexpensive raw materials. It is expected that these low-cost devices would help overcome the critical barrier for EES technologies into entering the various grid segments. Higher atomic weight species like sodium and magnesium can be utilized for these applications since the grid sector does not place a large premium on attaining high specific energy (Wh/kg).

By 2100, the global lithium consumption by the transportation sector run in entirety by electric vehicles (with 90% recycling) is predicted to be 20 Mt. On the other hand, optimistic estimates for available lithium resource is 39 Mt. ²⁶ In this best-case scenario, the demand for lithium mineral would be barely sufficient to meet the needs of automotive sector while omitting other potential applications like grid storage. ²⁷ The relative abundance of sodium is significantly higher than that of lithium minerals as shown in Figure 1.9. It is estimated that the available sodium resources in earth's crust and oceans exceeds lithium resources by 3 and 5 orders of magnitude, respectively as seen from Table 1.2. Commercially, sodium is extracted from brine solutions (NaCl) using Solvay process, an important industrial method, to produce soda ash (Na₂CO₃). Due to significance of soda ash to chemical industries (annual production of 11.6 MT), its monthly production rate is utilized as one of the economic indicators by the Federal Reserve Board. ²⁸ Considering the enormity of the grid sector applications that scarcely utilizes batteries at the present, it is prudent to design a battery chemistry based on a cheap, mass-manufactured chemical commodity.

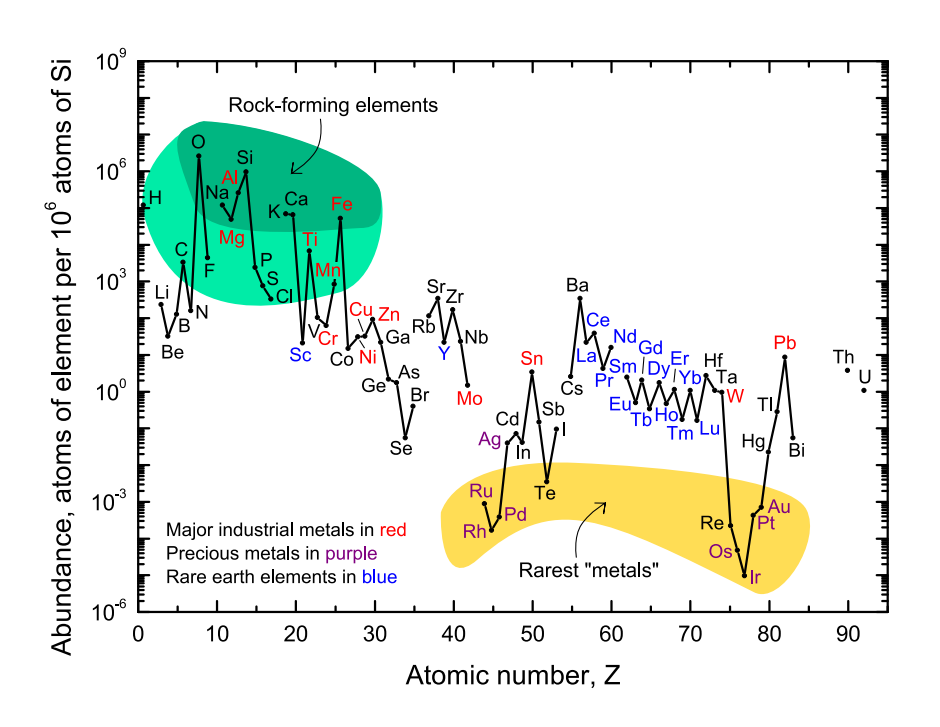


Figure 1.9 Relative abundance chart depicting plentiful sodium element as compared to lithium. 29

Table 1.2 Comparison of resources and physical properties of lithium, sodium and magnesium³⁰

Property	Lithium	Sodium	Magnesium
Crustal Abundance (ppm)	20	23,600	23,300
Oceanic Abundance (mg/L)	0.1	10,800	1,290
Resources (MT)	40	Unlimited	Unlimited
Redox Potential (V) vs. SHE	-3.04	-2.71	-2.37
Atomic Mass (amu)	6.941	22.999	24.305
Atomic Radii (pm)	76	102	72
Ionic Charge	1+	1+	2+

Additionally, the majority of the lithium resources are restricted to few countries and geopolitics can potentially become an issue for ramping up production levels. However, sodium resources have a more uniform global distribution (Table 1.2) and mineral costs would not be affected by geopolitical issues as much. Due to cheap and wide-scale mineral availability, sodium-based batteries offer the considerable potential for developing low-cost EES. This new EES technology

would help in product diversification of EES methods, potentially fill-in the market gap between LIBs and LABs and enable greater deployment of EES in various segments of the grid sector.

1.7 Rationale for investigating Na-based batteries

1.7.1 Na-ion vs Mg-ion batteries

Sodium- and magnesium-based chemistries are highly researched as alternate battery chemistries for grid storage sector. ³¹⁻³³ In terms of resource availability, both sodium and magnesium are fairly abundant in earth's crust as shown in Table 1.2. The standard reduction potential of sodium is closer to lithium (300 mV) than magnesium (600 mV). The more electropositive character of sodium than magnesium would permit building higher voltage cells with the former. Higher cell voltage translates to fewer cells/pack to achieve the product specification stack-level voltage and subsequently reduces failure modes owing to individual cell variability. Having fewer cells to monitor can also reduce the complexity in control systems at the pack level.

Additionally, the divalent magnesium ions is known to suffer from extremely slow solid-state diffusion due to strong interactions between magnesium ions and the host anions (larger coulombic attractive forces). Hence, it is desirable to use monovalent intercalant species such as sodium to reduce the polarizing interactions and obtain reasonable fast solid-state diffusivity, essential for practical applications. The room temperature and intercalation-based operation of sodium-ion chemistries would eliminate the potential safety issues that are usually associated with high-temperature Na/S batteries.

1.7.2 Relative ease of scalability

The high-volume manufacturing practices of building large lithium battery packs (~50 kWh) are currently being optimized and this scaling effect is expected to produce marked cost-savings for transportation sector. A conventional battery manufacturing process is shown in Figure 1.10.

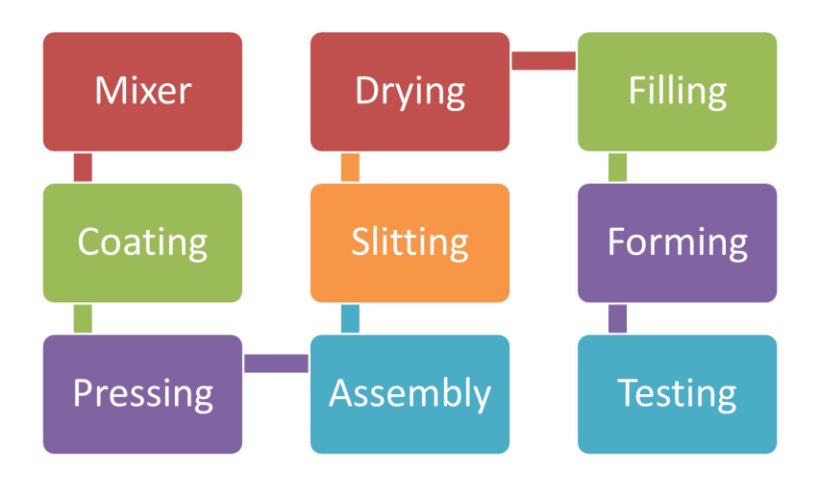


Figure 1.10 Manufacturing steps for advanced batteries such as Li-ion chemistry.

Existing LIB plants can be modified to manufacture sodium-based batteries without the need for new equipment or facility upgrades. The dryroom conditions currently used for LIBs would be suitable for sodium battery manufacturing. This transition can be performed by incorporating few key changes to the existing process modules as follows:

- Replace lithium-based active powders with sodium-based active powders in the 'mixer' module to fabricate sodium intercalation electrodes
- ii. Optimize electrolyte slurry viscosity and film thickness to specification levels in the 'coating' module to prepare electrode films of desired quality
- iii. Replace lithium-based salt with sodium-based salt in the 'filling' module to allow for relatively fast sodium ionic conduction in the non-aqueous electrolytes

iv. Change organic solvent (linear and cyclic carbonate) type and ratios in the 'filling' module to suit the requirements for sodium batteries

By this relatively straightforward approach, the key cost saving measures of LIBs can be readily transferred to sodium-chemistries. This would also advance technology development from labscale research to building device prototypes to mass manufacturing in a fairly rapid fashion.

1.8 Insertion-based Batteries: Working Principle

Insertion/Intercalation-based batteries function on the fundamental principle of a galvanic cell; electric current generated by two spontaneous, spatially separated redox reactions is utilized for doing external work. The redox reactions in insertion batteries are facilitated by transition metal species that occupy specific crystallographic sites in an inorganic material. So, when the oxidation state of the transition metal changes, the concentration of the intercalant species gets modified by electrochemical ion exchange process to maintain overall charge neutrality.

Thus, when using intercalation electrodes are utilized as anode and cathode, the intercalant species gets shuttled between them through the electrolyte media that allows for only ion transport. This 'rocking-chair' mechanism is illustrated in Figure 1.11 using lithium/sodium as the intercalant species, and LiCoO₂/NaCoO₂ as electrode materials.

Insertion/removal of intercalant species in the host electrode framework can lead to changes in physicochemical and structural properties and even phase transformations. For attaining long cycle-life, the intercalant species needs to be shuttled between the two electrodes for at least a few 1000 cycles while accommodating concomitant lattice stresses. Intercalation-based batteries that use solid-solution mechanisms do have electrodes undergo phase changes and typically offer excellent cycle life compared to other battery mechanisms (such as alloying). This is because the

host electrode materials retain their original structure fairly well and hence their intercalation capacity remains reasonably stable. Cycle life is a key performance specification for stationary applications and this research is focused only on intercalation-based materials.

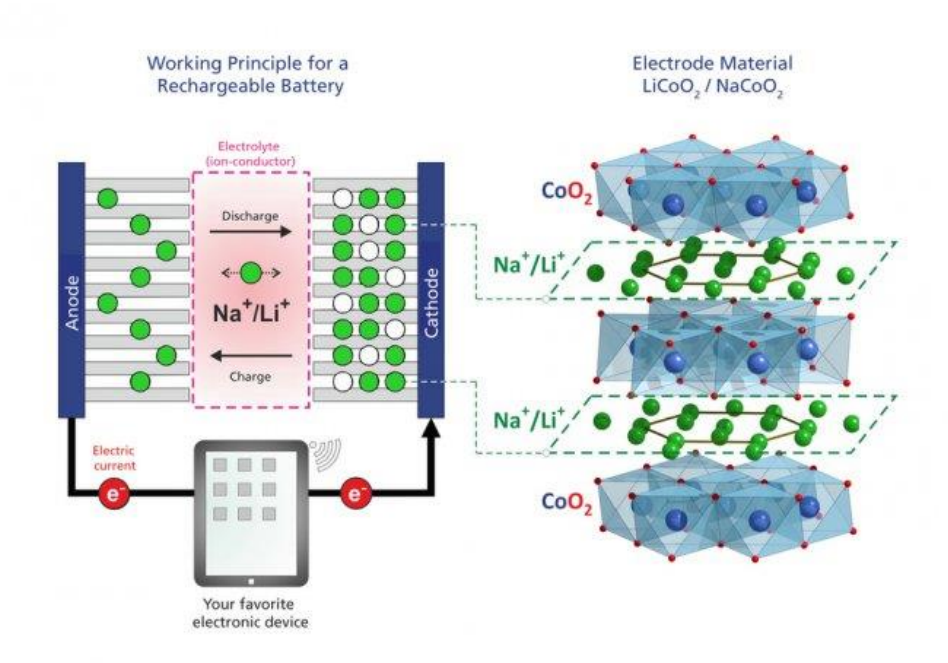


Figure 1.11 Working principle of an insertion/intercalation-based battery.³⁴

1.9 Requisites for Intercalation-based Electrodes

Designing high-performance, intercalation-type battery materials requires selecting electrodes with the following essential properties:

i. High electronic conductivity: Intercalation reactions involve exchange of intercalant species and a concomitant redox reaction. Materials with high electronic conductivity would facilitate faster electron/hole hopping to the electrode-electrolyte interface where electrochemical reactions occur.

- ii. **High ionic conductivity:** Intercalant species needs to diffuse fairly rapidly within the host material so that they can reach the electrode-electrolyte interface. This requires materials with inter-connected channels/tunnels where the intercalant species can reside.
- iii. **Fast interfacial kinetics:** The interfacial reaction that occurs at the electrode/electrolyte interface allows needs to have fast heterogeneous reaction kinetics.
- iv. **High redox potential:** The redox potential of the electrode is directly proportional to the free energy of the formation between product (de-intercalated state for anode) and reactant (intercalated state for anode) as given by the Nernst equation (under electrochemical equilibrium): $\Delta G = G_{Pdt} G_{Rct} = -nFE$, where ' ΔG ' refers to the Gibb's free energy for the reaction, ' G_{Pdt} ' and ' G_{Rct} ' are the free energy of the product and reactant, respectively, 'n' is the number of electrons transferred during the redox reaction, 'F' is Faraday's constant and 'E' is the standard reduction potential
- v. **Structural stability:** Preserving the structure of the host materials during intercalation/de-intercalation is essential to retain the intercalant crystallographic sites. Significant changes in structure (phase transitions) can lead to loss of available intercalation sites and consequently poor charge storage capability. For instance, a material transforming from crystalline to amorphous would completely lose charge-storage capability due to intercalation mechanisms.
- vi. **Stable Solid Electrolyte Interface (SEI):** Insertion-electrodes typically operate in highly oxidizing and reducing conditions. Current Li-ion battery electrolytes rely on kinetic barriers to limit the thermodynamically favored reduction reactions at the anode (graphite). Formation of a stable, compact, electrically insulating and ionically conducting SEI as a passivation layer is essential to limit the side-reactions and attain stable capacity retention.³⁵ Finding suitable

electrolyte chemistries that can support different electrode materials by forming a stable SEI is one of the key challenges for realizing practical Na-ion chemistry devices.

1.10 Research Problem

Driven by the potential for stationary applications, Na-ion batteries has become a highly researched area in the recent years as highlighted by the rapidly growing number of research publications as shown in Figure 1.12. 31,32,36-38

Identification and characterization of new, high-performance functional materials that can support reversible sodium intercalation/de-intercalation reactions remains one of the key challenges in Na-ion battery field. Exploratory research of new inorganic host materials forms the cornerstone for advanced batteries and can possibly open up new avenues for different application areas. This thesis research embarks on an exploratory research to identify potentially new inorganic host electrodes and characterize promising electrode candidates. The research goals include shortlisting promising compositions and increasing the understanding of material and electrochemical properties that would eventually lead to device prototyping and product commercialization.

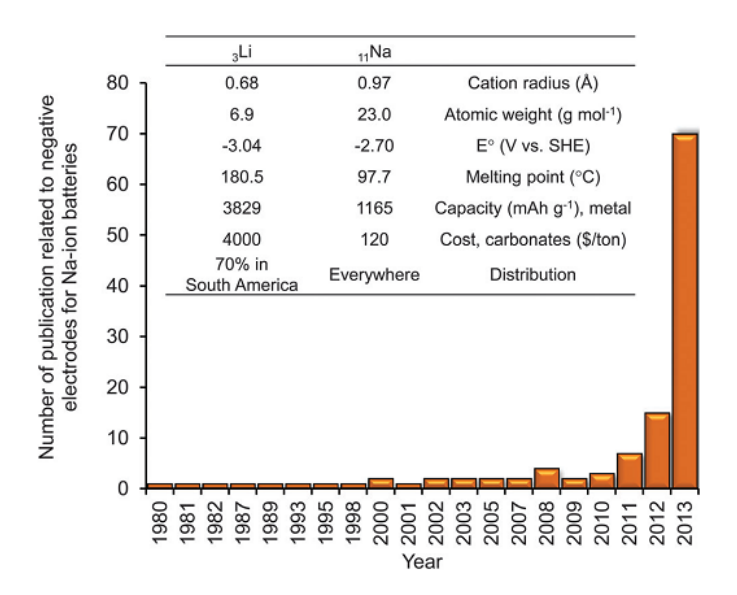


Figure 1.12 Growing number of research publications on anode materials for Na-ion battery.³⁶

1.11 Thesis organization

The second chapter of this dissertation begins with evaluating sodium metal SEI in different electrolytes and passivation study of current collectors. Thereafter, it discusses about the exploratory study of novel tunnel-type electrode materials: sodium nickel phosphate (Na₄Ni₇[PO₄]₆) and sodium cobalt titanate (Na_{0.8}Co_{0.4}Ti_{1.6}O₄). The synthetic strategies and electrochemical characterization of these materials are elaborated.

The third chapter elaborates the characterization of sodium nickel titanate (P2-Na_{2/3}[Ni_{1/3}Ti_{2/3}]O₂) with prismatic co-ordination of sodium atoms. We evaluate the electrochemistry of this novel layer-structured material by selectively activating nickel and titanium redox couples. The bottleneck physicochemical processes are evaluated using impedance spectroscopy and the role of manganese substitution (P2-Na_{2/3}[Ni_{1/3}Mn_{1/3}Ti_{1/3}]O₂) on the electrical, ionic and electrochemical properties of these compositions are studied.

The fourth chapter discusses the structural characterization of sodium nickel titanate (P2) using experimental (neutron diffraction) and computational methods (atomistic simulations). Rietveld refinement provides average structural information while force field models simulate average and local structural details. Computational methods were utilized to develop atomic density maps and the simulated structural patterns were found to be consistent with the experimental results.

The fifth chapter covers synthesis, structural and electrochemical characterization of sodium nickel titanate material (O3-Na_{0.9}[Ni_{0.45}Ti_{0.55}]O₂) with octahedral co-ordination of sodium atoms. We investigate the stabilizing influence of titanium atoms to mitigate poor capacity retention of O3-type electrode materials and perform cycling-coupled-impedance studies, step-potential electroanalytical testing, and ex-situ XRD characterization.

BIBLIOGRAPHY

BIBLIOGRAPHY

- 1. Alley, R. *et al.* Summary for policymakers. Climate Change 2007: The Physical Science Basis. *Cambridge Univ. Press*
- 2. Tans, P. & Keeling, R. http://www.esrl.noaa.gov/gmd/ccgg/trends/. (2014).
- 3. Hansen, J., Ruedy, R., Sato, M. & Lo, K. Global Surface Temperature Change. *Rev. Geophys.* **48**, 1–29 (2010).
- 4. Tett, S. F. B., Stott, P. A., Allen, M. R., Ingram, W. J. & Mitchell, J. F. B. Causes of twentieth-century temperature change near the Earth's surface. *Nature* **399**, 569–572 (1999).
- 5. Liverman, D. From Uncertain to Unequivocal. *Environ. Sci. Policy Sustain. Dev.* **49,** 28–32 (2007).
- 6. Dessler, A. & Parson, E. *The science and politics of global climate change*. (Cambridge University Press, 2010).
- 7. Thomas, C. D. et al. Extinction risk from climate change. *Nature* **427**, 145–8 (2004).
- 8. Araújo, M. B. & Rahbek, C. Ecology. How does climate change affect biodiversity? *Science* (80-.). **313**, 1396–7 (2006).
- 9. Thuiller, W. Climate change and the ecologist. *Nature* **448**, 1–3 (2007).
- 10. Stern, N. What is the Economics of Climate Change? World Econ. 7, 1–10 (2006).
- 11. Tol, R. S. J. The Economic Effects of Climate Change. *J. Econ. Perspect.* **23**, 29–51 (2009).
- 12. Inventory of U.S. Greenhouse Gas Emissions and Sinks: 1990-2013, Executive Summary. Annu. Rep. 1–27 (2013).
- 13. International Energy Statistics. http://www.eia.gov/cfapps/ipdbproject/iedindex3.cfm?tid=44&pid=44&aid=2&cid=ww, &syid=1980&eyid=2012&unit=QBTU (2015).
- 14. Beaudin, M., Zareipour, H., Schellenberglabe, A. & Rosehart, W. Energy storage for mitigating the variability of renewable electricity sources: An updated review. *Energy Sustain. Dev.* **14**, 302–314 (2010).
- 15. Denholm, P., Ela, E., Kirby, B. & Milligan, M. *The Role of energy storage with renewable electricity generation*. (2010).

- 16. Barnhart, C. J. & Benson, S. M. On the importance of reducing the energetic and material demands of electrical energy storage. *Energy Environ. Sci.* **6**, 1083 (2013).
- 17. REN21, Global Status Report 2014 (Renewable Energy Policy Network for the 21st Century); available at www.ren21.net/Portals/0/documents/e-paper/GSR2014/index.html.
- 18. Teleke, S., Baran, M. E., Bhattacharya, S. & Huang, A. Q. Rule-Based Control of Battery Energy Storage for Dispatching Intermittent Renewable Sources. *IEEE Trans. Sustain. Energy* **1**, 117–124 (2010).
- 19. Schiermeier, Q. Germany's Energy Gamble. *Nature* **496**, 156–158 (2013).
- 20. Hadjipaschalis, I., Poullikkas, A. & Efthimiou, V. Overview of current and future energy storage technologies for electric power applications. *Renew. Sustain. Energy Rev.* **13**, 1513–1522 (2009).
- 21. Electricity Energy Storage Technology Options; EPRI White Paper. (2010).
- 22. http://energystorage.org/energy-storage/technologies/flywheels.
- 23. Smart, M. C. & Ratnakumar, B. V. Effects of Electrolyte Composition on Lithium Plating in Lithium-Ion Cells. *J. Electrochem. Soc.* **158**, A379–A389 (2011).
- 24. Tzeng, J., Emerson, R. & Moy, P. Composite flywheels for energy storage. *Compos. Sci. Technol.* **66**, 2520–2527 (2006).
- 25. *Grid Energy Storage: Executive summary; U.S. DOE.* (2013).
- 26. Gruber, P. W. et al. Global Lithium Availability. J. Ind. Ecol. 15, 760–775 (2011).
- 27. Tarascon, J.-M. Is lithium the new gold? *Nat. Chem.* **2,** 510 (2010).
- 28. http://minerals.usgs.gov/minerals/pubs/commodity/soda_ash/.
- 29. Rare Earth Elements- Critical Resources for High Technology; USGS Fact Sheet 087-02. (2002).
- 30. CRC Handbook of Physics and Chemistry, 77th Edition.
- 31. Slater, M. D., Kim, D., Lee, E. & Johnson, C. S. Sodium-Ion Batteries. *Adv. Funct. Mater.* **23,** 947–958 (2013).
- 32. Palomares, V. *et al.* Na-ion batteries, recent advances and present challenges to become low cost energy storage systems. *Energy Environ. Sci.* **5**, 5884–5901 (2012).

- 33. Levi, E., Gofer, Y. & Aurbach, D. On the Way to Rechargeable Mg Batteries: The Challenge of New Cathode Materials. *Chem. Mater.* **22**, 860–868 (2010).
- 34. http://neutronsources.org/news/scientific-highlights/towards-sodium-ion-batteries-understanding-sodium-dynamics-on-a-microscopic-level.html.
- 35. Peled, E., Golodnitsky, D. & Penciner, J. Handbook of Battery Materials. (2011).
- 36. Dahbi, M., Yabuuchi, N., Kubota, K., Tokiwa, K. & Komaba, S. Negative electrodes for Na-ion batteries. *Phys. Chem. Chem. Phys.* **16**, 15007 (2014).
- 37. Pan, H., Hu, Y.-S. & Chen, L. Room-Temperature Stationary Sodium-Ion Batteries for Large-Scale Electric Energy Storage. *Energy Environ. Sci.* **6**, (2013).
- 38. Ellis, B. L. & Nazar, L. F. Sodium and sodium-ion energy storage batteries. *Curr. Opin. Solid State Mater. Sci.* **16**, 168–177 (2012).

2. SYNTHESIS, AND ELECTROCHEMICAL CHARACTERIZATION OF NOVEL TUNNEL-TYPE SODIUM INTERCALATION MATERIALS

2.1 Introduction

Tunnel-type inorganic battery materials can be classified into two structural categories: polyanion-and spinel-based. Polyanion-based electrode materials have tetrahedrally co-ordinated polyanionic functional groups (XO₄)ⁿ⁻, where 'X' can be P, Si, W, Mo or As, as a distinct structural feature. Some of the well-studied polyanionic materials include LiMPO₄(M-Fe, Mn, Ni, Co), Li₂MSiO₄ (M- Fe, Mn), LiMSO₄F (M- Co, Ni), etc.¹⁻⁶ These materials possess covalently bonded oxygen atoms that provide excellent charging stability (especially at high potentials) and improved thermal stability.^{1,7} Hence, these polyanionic materials are intrinsically safer, an important feature for large-scale grid storage applications.

Additionally, suitable selection of polyanion functional groups allows for selective tuning of the redox potential of the transition metal species. For instance, the transition metal in NASICON-structured materials have shown a wide range of redox potential values solely based on the type of polyanion framework. The bonding nature of the polyanion groups affect the ionicity of the transition metal-oxygen bonds and hence alters the redox potential.

For Na-ion batteries, polyanionic materials such as Na₂MPO₄F (M- Fe, Mn), Na₂MP₂O₇ (M-Fe, Co, Mn, Cu), NaFePO₄, Na₃M₂(PO₄)₃ (M- V, Ti), Na₃M₂(PO₄)₂F₃ (M- Ti, Fe, V) have shown promise. ¹¹⁻¹⁹ In this section, Sodium nickel phosphate (SNP), with stoichiometry Na₄Ni₇(PO₄)₆, is investigated as a potential tunnel-type electrode to take advantage of the structural stability of these classes of materials.

Spinels, with general stoichiometry AB₂O₄, have been shown to possess attractive intercalation/de-intercalation properties using compositions such as LiMn₂O₄ and Li₁[Li_{0.33}Ti_{1.67}] O4.²⁰⁻²⁴ This piqued our interest in exploring similar prototypical structures with sodium as intercalant species with spinel-related host framework. However, spinel structures are not favorable for sodium-based quaternary oxides due to the large-size of the sodium atoms for the tetrahedral '8a' sites. Instead, they form calcium ferrite-based prototypical structures with single or double tunnels depending that allows for a longer Na-O bond.²⁵ Sodium cobalt titanate (SCT), with stoichiometry Na_{0.8}Co_{0.4}Ti_{1.6}O₄, has calcium ferrite-type structure and is investigated as an alternative tunnel-type electrode candidate.

This chapter discusses about synthesis and electrochemistry of two tunnel-type materials with compositions Na₄Ni₇(PO₄)₆ (polyanionic-based) and Na_{0.8}Co_{0.4}Ti_{1.6}O₄ (calcium ferrite-based). Both these tunnel-type materials contain electrochemically-inert units, in the form of phosphate tetrahedra and titanium octahedra, which interconnect to form a relatively stable host-framework with possibly improved structural stability. Sodium ion conduction would occur in the in 3-D interconnected tunnels that lie within the host framework.

2.2 Structural features

2.2.1 Sodium nickel phosphate: Na₄Ni₇(PO₄)₆

Previously, the crystal structure of Na₄Ni₇(PO₄)₆ was refined using X-ray diffraction with single-crystals grown by flux method.²⁶ Space group 'Cm' was found to provide the best fit for the experimental diffraction dataset and nickel and phosphorus were assigned octahedral and tetrahedral co-ordination, respectively. The structure is comprised of a 'Ni layer' containing interconnected nickel octahedra and phosphorus tetrahedra lying parallel to the 'ab' plane. These

'Ni-layers' are in-turn linked by corner-shared phosphorus polyhedra resulting in parallel tunnels/cavities that hosts sodium atoms (Figure 2.1). The presence of continuous tunnels and unoccupied sodium sites in this phosphate material provides the feasibility for reasonably facile solid-state sodium ion transport. We anticipate that the phosphate units between the 'Ni-layers' would act as 'linking pillars' rendering structural stability by keeping the layers together during electrochemical de-sodiation.

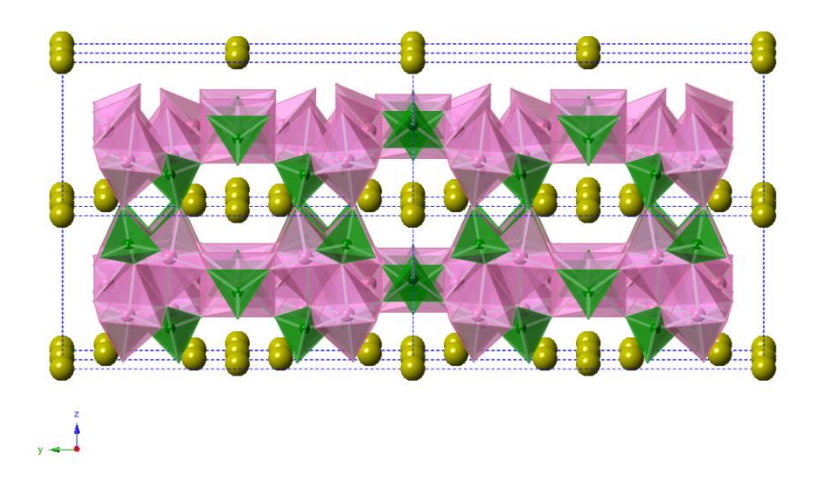


Figure 2.1 Crystal structure of Na₄Ni₇(PO₄)₆; *Pink polyhedra represents nickel octahedra, green polyhedra represents phosphate tetrahedra and yellow spheres indicate sodium atoms. Oxygen atoms are not included for clarity.* ²⁶

2.2.2 Sodium cobalt titanate: Na_{0.8}Co_{0.4}Ti_{1.6}O₄

 $Na_{0.8}M_{0.4}Ti_{1.6}O_4$ was reported to crystallize with space group Pnma.²⁵ The studied composition, $Na_{0.8}Co_{0.4}Ti_{1.6}O_2$, has edge-shared groups of four transition metal octahedra (blue polyhedra) forming 'Z-shaped' chains that run parallel to the b-axis infinitely as shown in Figure 2.2. It is likely that these quaternary oxides support facile sodium ion transport due to their low activation energy (1.1 eV) for sodium hopping and unusually high sodium thermal vibrational parameter (U_{22}) .^{25,27}

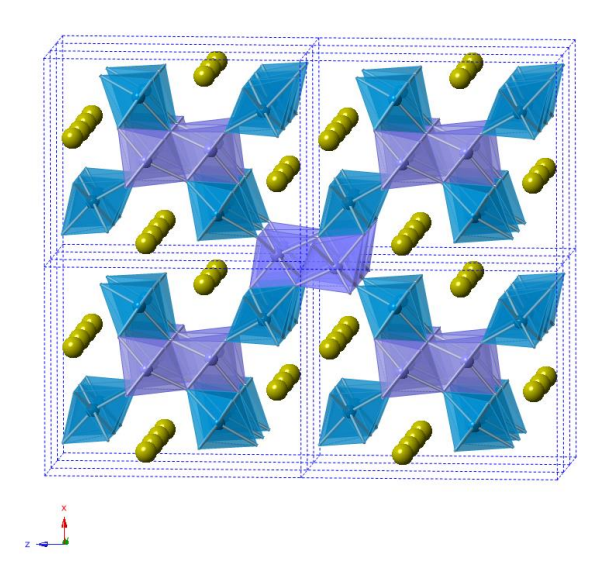


Figure 2.2 Crystal structure of Na_{0.8}Co_{0.4}Ti_{1.6}O₄; blue polyhedra represents transition metal octahedra (cobalt and titanium) and yellow spheres represent sodium atoms; oxygen atoms are omitted for clarity. ²⁵

2.3 Inorganic Synthesis

The synthetic conditions for the quaternary oxide phases were optimized to yield powders of desirable morphology for fabrication of composite, porous electrode films. Battery electrodes typically consists of powders with relatively small-sized particles (preferably in the length-scale of 100s of micrometer to nanometers) to avoid potential transport limitations. High-temperature powder processing can lead to particle sintering and this should be avoided.

2.3.1 Sodium nickel phosphate synthesis

Previous report of SNP synthesis was carried out by slow cooling of high temperature melts (1150°C) to obtain single crystals for diffraction studies.²⁶ We developed a solid state synthetic method to produce phase-pure powders at a much lower temperature.

The precursors Na₂CO₃ (S4132, Sigma-Aldrich, 99.5%), NiO (399523, Sigma-Aldrich, 99%) and NH₄H₂(PO₄)₂ (204005, Sigma-Aldrich, 99.999%) were dry milled in the target stoichiometry

using a high-energy SPEX mill (8000M Mixer/Mill, SPEXSamplePrep) with steel balls inside a hardened steel vial. The homogenized powders were fired with an alumina crucible (CoorsTM high-alumina crucible, Sigma-Aldrich) inside a box furnace (CWF-1300, Carbolite and Lindberg blue M, Thermo-scientific models) to provide sufficient thermal energy for activating the reaction and enabling faster diffusion, as typical in solid-state reaction technique. The overall synthesis schematic is illustrated in Figure 2.3.



Figure 2.3 Schematic of solid state reaction technique.

Powder X-ray diffraction experiments were performed using Bruker Da-vinci D8 Diffractometer with copper X-ray source at the Center for Materials Characterization, Department of Chemistry, Michigan State University. Crystalline, phase-pure powders were obtained by heating the powders to 900°C for 10 h duration as revealed by the X-Ray Diffraction (XRD) patterns that show sharp, intense peaks and a good match with the database standard (ICSD reference code: 84-0845) as seen in Figure 2.4.

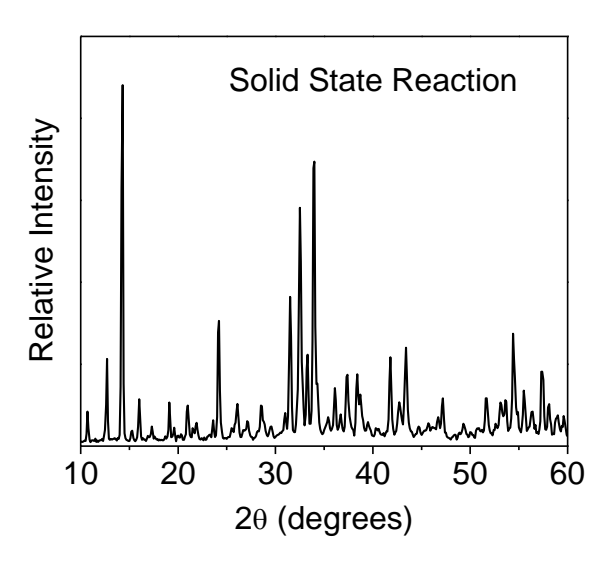


Figure 2.4 XRD characterization of sodium nickel phosphate prepared by solid state reaction.

The powder morphology was analyzed using JEOL-7500F ultra-high resolution SEM equipment at the Center for Advanced Microscopy (CAM), MSU. Conductive-adhesive backed carbon tape (Ted Pella, Inc.) is placed on top of an aluminum stub and inorganic powders are sprinkled on top. The powders are gently tapped-off to dislodge excess powder accumulation. Typically, the powders are coated with a thin, sputtered gold film (~10-20 nm) to mitigate charging issues that can occur due to the interaction between electron gun and sample powders. The 7500F SEM is operated under ultra-high vacuum mode at sample chamber pressure of 96 μPa. The SEM images showed that the as-synthesized powders consisted of large (>100 μm), dense particles that are not ideal for electrochemical characterization. The individual particles did not have any visible pores and appears sintered (Figure 2.5a and b). Attempts were made to prepare smaller-sized powders by wet-chemistry methods.

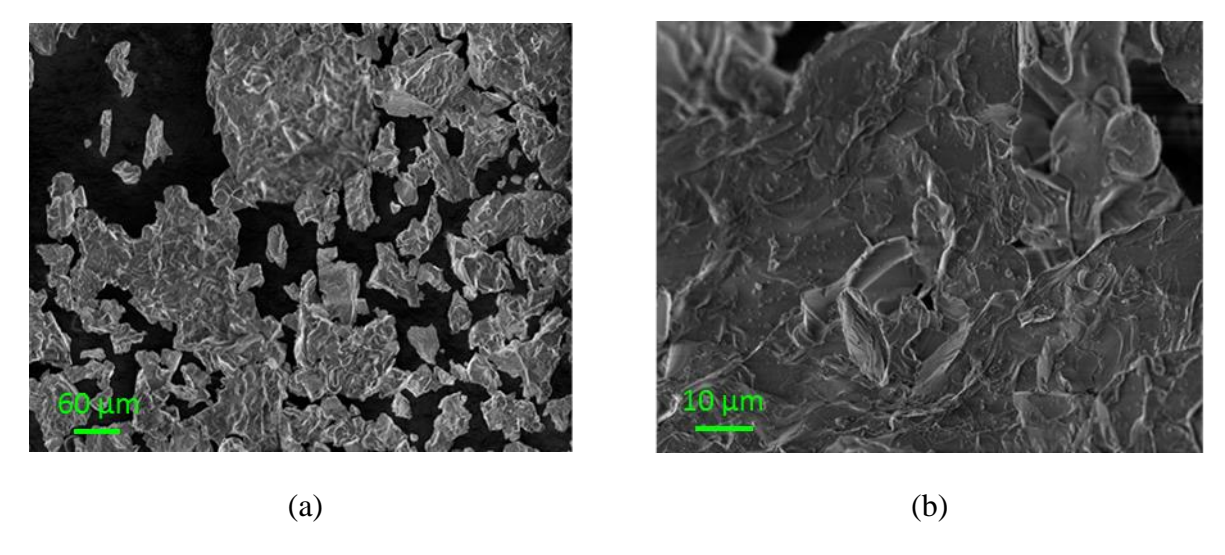


Figure 2.5 (a) Sodium nickel phosphate powder morphology prepared by solid state reaction, and (b) Higher-magnification image of a particle showing dense morphology.

Sol-gel synthesis facilitates atomic-level mixing by incorporating all the metallic species in a gel network. ²⁸⁻³⁰ Having chemical homogeneity at an atomic-scale typically enables reduction of phase formation temperature and consequently helps to avoid undesired particle agglomeration and sintering. Water soluble precursors such as CH₃COONa (S8750, Sigma-Aldrich, 99%), Ni(CH₃COO)₂.4H₂O (72225, Sigma-Aldrich, 99%) and NH₄H₂(PO₄)₂ (204005, Sigma-Aldrich, 99.999%) were utilized while citric acid (36664, Alfa-Aesar, 99.5%) functioned as the chelating agent and nitric acid (438073, Sigma-Aldrich, 70%) served to maintain acidic pH. Evaporation of water resulted in the formation of transparent green gels as shown in Figure 2.6. The green gel was firing at 800°C to burn the organic components (mostly from citric acid) and promote phase formation and this leads to the formation of yellow powders.

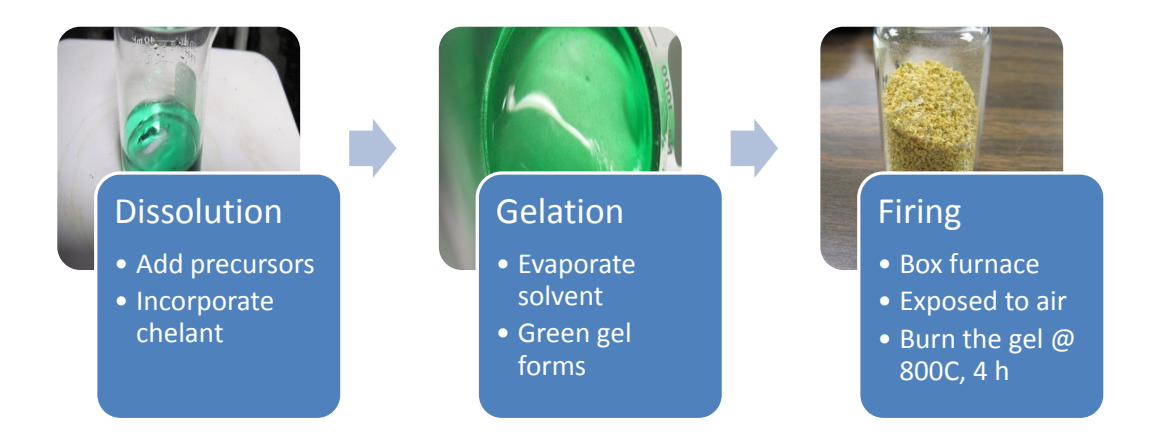


Figure 2.6 Schematic of sol-gel synthesis technique.

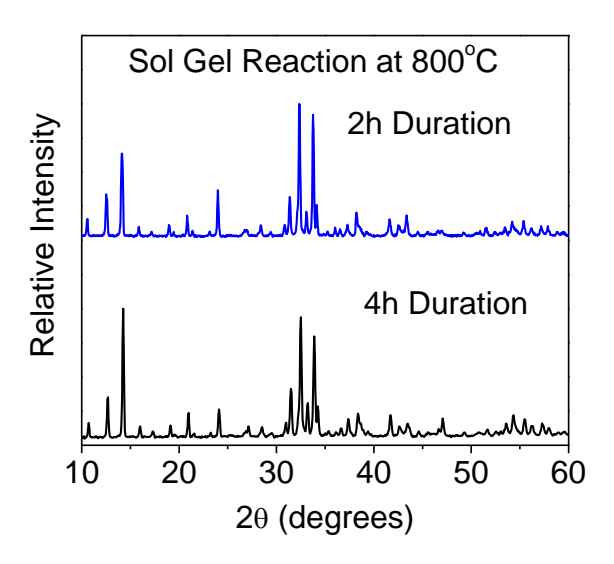


Figure 2.7 XRD characterization of sol-gel synthesized powders of sodium nickel phosphate.

XRD patterns confirm the formation of the target phase when firing duration is at least 4 hours (ICSD reference code: 84-0845). It was found that reducing the synthesis duration to 2 hours results in an impurity phase formation (NaNiPO₄, ICSD reference code: 34-1446), as shown in Figure 2.7. The sol-gel powders had a smaller particle size (~15 µm) than the powders prepared

by solid-state reaction due to the lower firing temperature enabled by chemical homogeneity at atomic-scale. The SEM images, in Figure 2.8, show relatively large primary particles comprising of partially sintered secondary particles. The latter were found to be $\sim 1~\mu m$ in diameter and are interconnected to form an extensive pore network through which the liquid electrolyte can possibly permeate and facilitate faster ion diffusion.

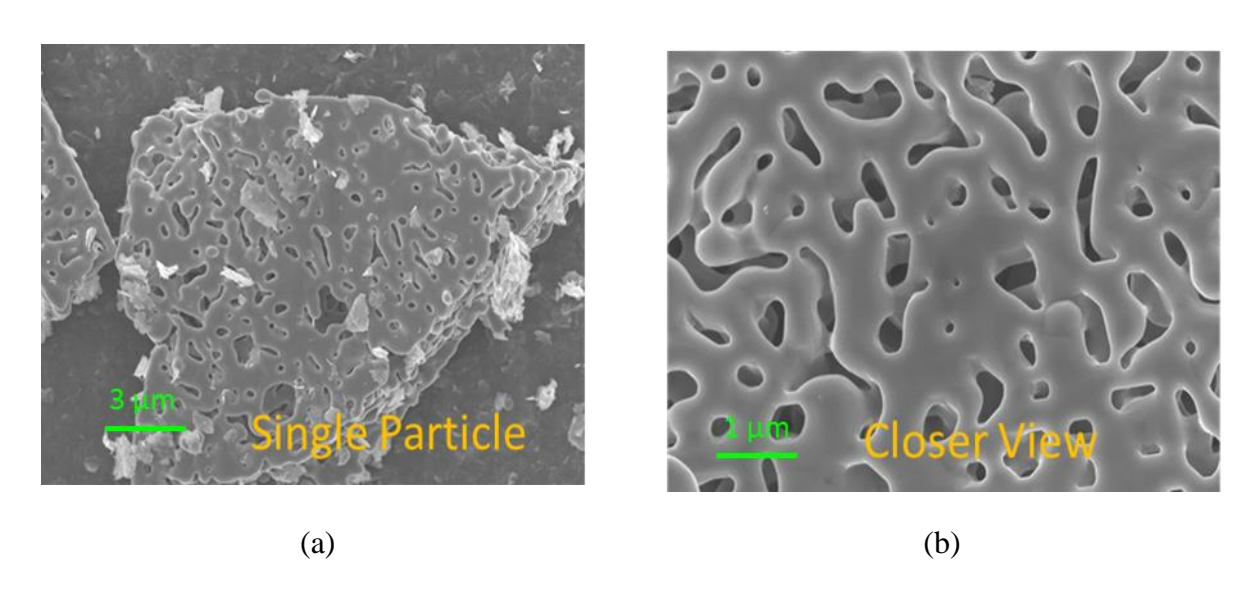


Figure 2.8 (a) Sodium nickel phosphate powder morphology prepared by sol-gel reaction, and (b) Higher-magnification image of a particle showing porous morphology.

2.3.2 Sodium cobalt titanate synthesis

SCT was synthesized by solid-state reaction method using NaNO₃ (S5506, Sigma-Aldrich, 99%), Co(CH₃COO)₂ (208396, Sigma-Aldrich, 99.5%), and TiO₂ (248576, Sigma-Aldrich, 99%, Anatase phase) as starting precursors. The precursors were wet milled using high-energy SPEX mill with steel balls as grinding media and 2-propanol as solvent. The well-mixed slurry was dried using an IR lamp in a glass petri dish and the dried powders were fired in a box furnace at 900°C for 10 hours. Na-Co-Ti-O composition with calcium-ferrite prototype structure is not reported in the ICSD database. XRD patterns, in Figure 2.9a, of the synthesized powders shows excellent

match with Na_{0.79}[Fe_{0.8}Ti_{1.6}]O₄ (ICSD reference code: 87-1550), that is isostructural with calciumferrite double tunnel structure. Since replacing cobalt in place of iron did not change the space group Pnma, we propose that the prepared powders retain the tunnel structure.

The as-synthesized powders were found to be ~3 µm sized rods as primary particles that appeared non-porous. The particles do not show any evidence of sintering (Figure 2.9b) while maintaining good crystallinity suggesting that the synthetic conditions are fairly close to optimal conditions. Hence, no attempts were made to prepare the powders by sol-gel method since the research objective was to have a fairly straightforward synthetic protocol (to enable scalability and cost effectiveness).

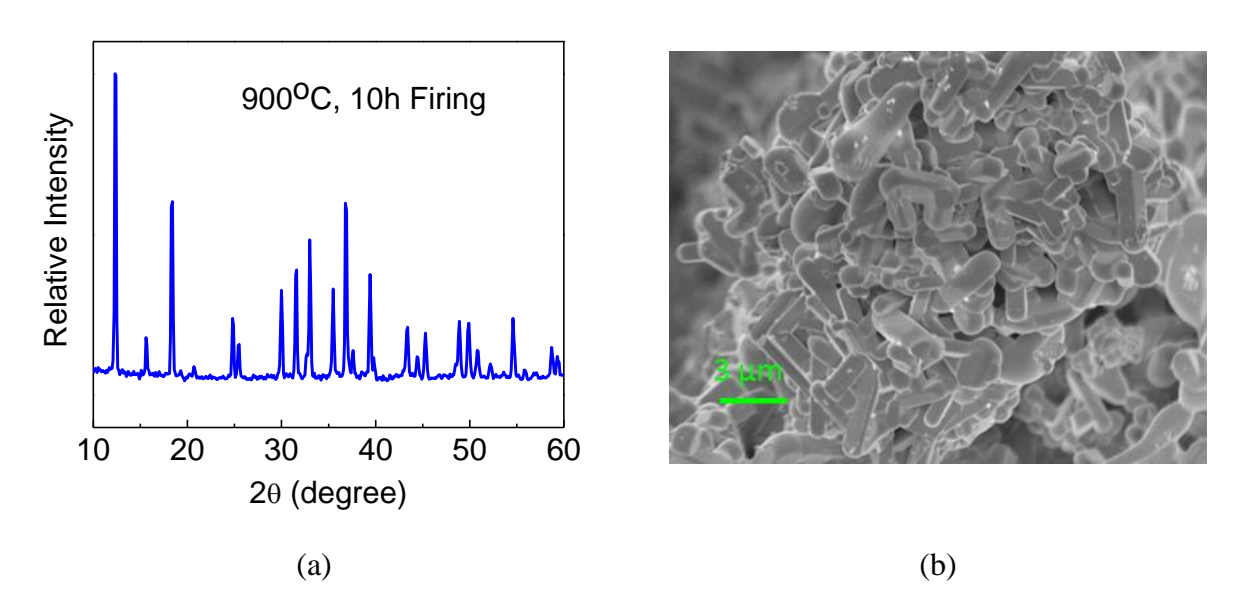


Figure 2.9 (a) XRD characterization of sodium cobalt titanate prepared by solid state reaction, and (b) SEM morphology of as-synthesized sodium cobalt titanate powders.

2.4 Film fabrication

2.4.1 Substrate selection

Highly-conductive metal substrates (or current collectors), typically aluminum (MTI Corp., EQ-bcaf-15u-280) and copper (MTI Corp., EQ-bccf-25u), are utilized for backing the active components of the electrode films. In commercial devices, these substrates carry the current from individual electrodes to the cell terminals. The prerequisite properties for substrates include good electrochemical stability (oxidizing environment for cathodes and reducing conditions for anodes), suitable chemical stability with active components (oxide materials, lithium metal, sodium metal, etc.), excellent electrical conductivity (to avoid ohmic losses), good thermal conductivity (for heat dissipation) and sufficient mechanical properties (to withstand thermal vibrations, mechanical impacts typical during battery operation).

Aluminum substrate is utilized for casting the cathode films as it provides excellent electrical conductivity and remains stable in highly oxidizing cathodic conditions (due to passivation films). However, phase diagrams suggest that aluminum forms binary alloys such as AlLi, Al₂Li₃, Al₄Li₉³¹ with lithium metal and hence is not a suitable substrate for lithium battery anodes. Aluminum substrates can be used for Na-ion batteries as it does not alloy with sodium metal. The low-cost and light-weight aluminum substrates are expected to provide energy density gains and cost reduction opportunities at pack-level battery configurations.

2.4.2 Casting methods

The as-synthesized powders are cast into a porous, composite electrode for electrochemical characterization. The film electrode is comprised of the active powders (quaternary oxides), conductive carbon (Super C65, Timcal, USA), and polyvinylidene fluoride (44080, Alfa-Aesar) in

80:10:10 weight ratio. The active powders and conductive carbon are dispersed thoroughly in a viscous solution made from dissolving polyvinylidene fluoride in N-Methyl-2-pyrrolidone (L03595, Alfa-Aesar) solvent using high-energy ball milling. The wet slurry is casted onto the aluminum substrate using an adjustable film applicator (doctor-blade, EQ-Se-KTQ-100, MTI Corp.) and film coater (MSK-AFA-III, MTI Corp.) after selecting the desired film thickness and setting the traverse speed at 10 mm/s. Suction is created by an oil-free vacuum pump (Model no. 9901K64, standard pump with maximum vacuum of 26" Hg, McMaster-Carr) to the aluminum vacuum chuck and this secures the aluminum foil/substrate in place. A schematic of film fabrication is illustrated in Figure 2.10. The film is dried using an IR lamp overnight to ensure that the solvent gets removed completely. The prepared electrodes are punched into 0.5" diameter discs using a hollow-punch (Mayhew tools, 66000) and transferred to MBraun labmaster-SP glovebox (with <1 ppm O₂ and <1 ppm H₂O) to minimize exposure to moisture and carbon dioxide.

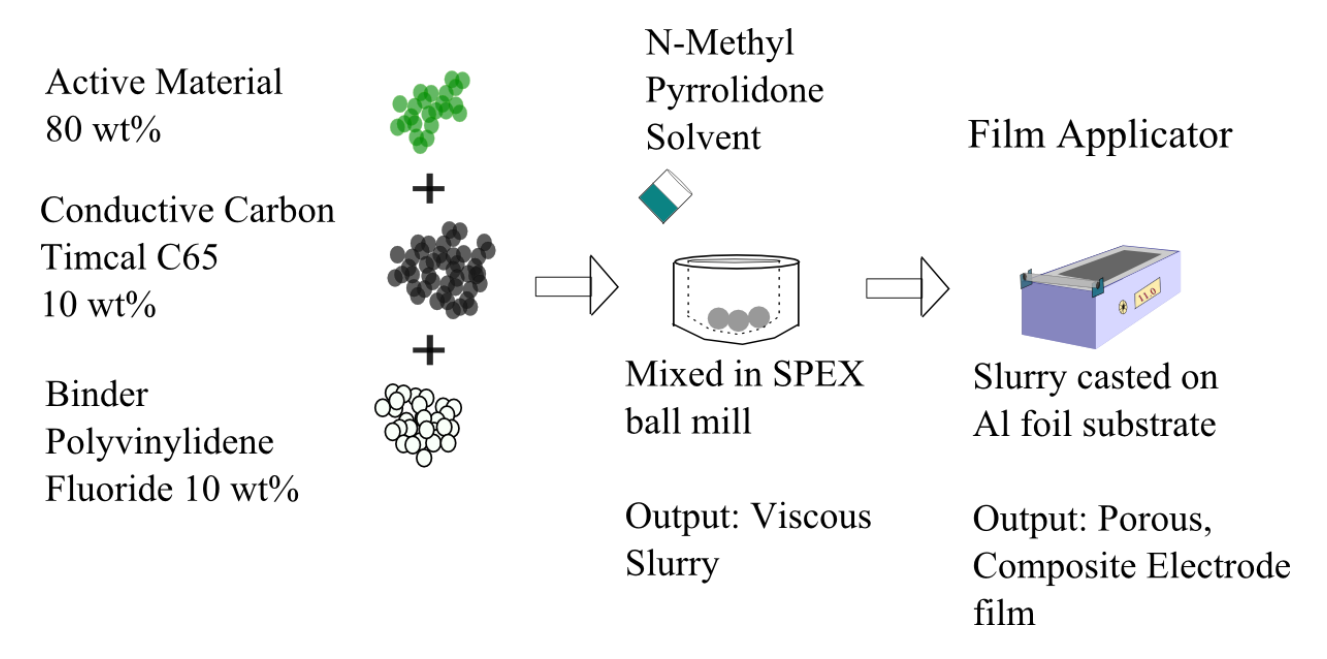


Figure 2.10 Schematic of doctor-blade slurry casting method for fabricating battery electrodes.

2.5 Electrochemical characterization

2.5.1 Cell setup and testing

Electrochemical testing is performed in 3-electrode configuration which includes working electrode, counter electrode and a reference electrode. Working electrode consists of an electrode disk (0.5" diameter) that is backed by aluminum rod serving as current terminals (equivalent to plate terminals in commercial packs). The counter and reference electrodes are prepared by cutting soft sodium ingots into thin slices with a knife, punching the slices into a circular disks and pressing the disks against a copper rod with Teflon tape and manual press. The three electrodes are inserted into the three legs of a Swagelok tube fitting (PFA-grade, Swagelok Inc.,) while inserting a polyethylene separator between the rods to avoid cell shorting. Figure 2.11 depicts electrode arrangement in cell assembly. The cell assembly is performed inside glovebox and Swagelok assembly ensures hermetic sealing of cell components. Cell testing is carried out using Biologic Potentiostat VSP300 and SP200 models outside the glovebox. The accuracy of the potentiostats was periodically tested using standard dummy cells from Biologic.

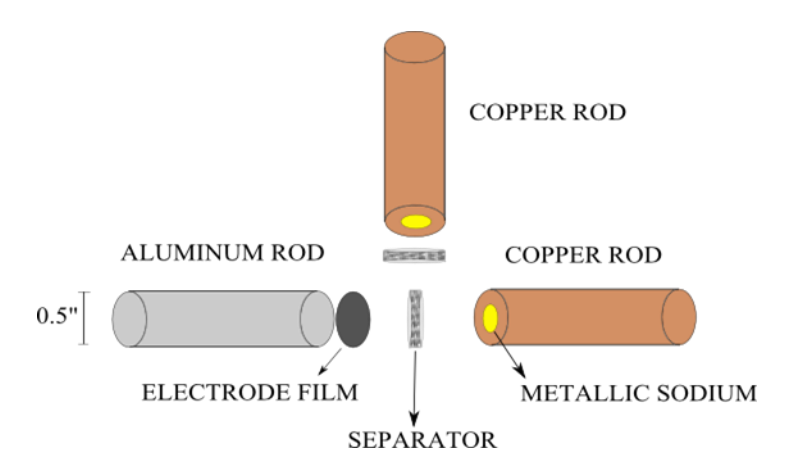


Figure 2.11 Schematic of Swagelok 3-electrode cell setup for electrochemical testing.

2.5.2 Evaluation of the electrolyte and current collectors

Sodium metal is frequently used in lab-scale half-cell tests due to the unavailability of commercial high-performance sodium-based anodes as counter electrodes. We tested the electrochemistry of Na₂Ti₃O₇, a reported low-voltage anode (E^o=0.3 V vs. Na/Na⁺ for Ti^{4+/3+}) for Na-ion batteries.³² However, the performance of the electrodes fabricated using the commercial powders (401307, Sigma-Aldrich) were found to be unsatisfactory with reversible capacity of only ~10% of theoretical. XRD testing revealed the commercial powders to contain a significant amount of Na₂Ti₆O₁₃ impurity phase in addition to the target Na₂Ti₃O₇ phase. Hence, further attempts were focused on finding a suitable electrolyte combination that can potentially work with the reactive sodium metal for the scope of preliminary electrochemical testing. The stability of sodium metal (282065, Sigma-Aldrich) in two electrolytes 1M NaClO₄ in EC/DMC (50/50 vol%) and 0.5M NaPF₆ in EC/DEC (50/50 vol%) were evaluated using impedance spectroscopy. The dry sodium metal sticks packed in nitrogen atmosphere is opened and stored inside the glovebox atmosphere. During cell assembly the outer regions of the stick are removed to discard the white coating (possibly oxide) and cut into ~3-5 mm slices using a steel knife. The thin slides are placed between two separator pieces and manually pressed (with Dayton ½ ton Arbor press). The pressed-slices are punched into disks with a hollow punch manually.

Symmetric cells were assembled using two sodium metals that were affixed to copper metal rods in 2-electrode configuration. Impedance tests were carried out by applying a sinusoidal voltage perturbation of 10 mV amplitude over the open-circuit potential in a frequency range of 1 MHz to 1 mHz. The spacing between the sodium metal pieces was maintained at 4.6 cm (1.8") and the space between the rods was filled-in with surplus electrolyte solution. The 1st impedance

test (black curve) was performed after 4 hours of open-circuit condition and subsequent tests every 2 hours.

Impedance spectrum reflects the evolution of the Solid Electrolyte Interface (SEI) on sodium metal surface over time without any significant polarization from open circuit conditions. Similar analysis has been reported for lithium metal SEI formation.³³ Perchlorate-based electrolyte exhibits a single semi-arc in the initial cycles that can be attributed to passivation films formed due to the degradation of organic solvents as shown in Figure 2.12a.

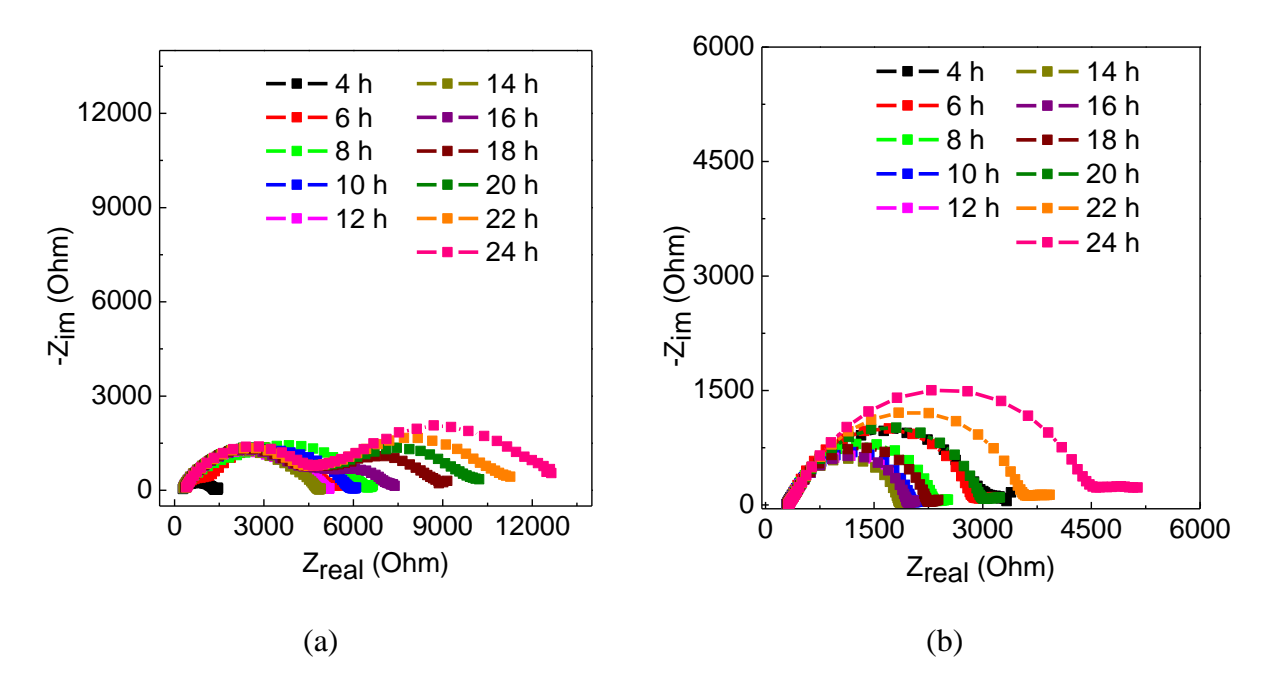


Figure 2.12 Impedance spectroscopy curves for sodium metal SEI formation in (a) 1M NaClO4 in ethylene carbonate/dimethyl carbonate, and (b) 0.5M NaPF6 in ethylene carbonate/diethyl carbonate; 1st cycle refers to test after 4 hours open-circuit and subsequent tests.

Prolonged exposure results in the formation of a 2nd arc related to the formation of a secondary passivation film. The increasing film resistance is due to continuous incorporation of the electrolyte degradation components and subsequent increase in film thickness. Fluorine-based

electrolyte shows a smaller single-arc over the tested time-duration and the film resistance increase is more gradual as seen in Figure 2.12b. We attribute this effect to the formation of a more stable passivation film involving fluorine-related species such as sodium fluoride as previously reported with a fluorinated solvent.³⁴ The electrolyte resistance did not change significantly under these test conditions as the cell-configuration was flooded and the byproducts did not accumulate to a significant extent.

These impedance spectra were obtained under steady-state open circuit conditions to investigate the reactivity of sodium metal under open circuit conditions. The nature of the passivation films would change during actual cell operation that includes current perturbation. Also, during galvanostatic testing, sodium metal plating is visually observed to be in the form of dendritic powders. These dendrites lose eventually contact with sodium metal due to poor adhesion and results in loss of partial deactivation (at the counter electrode). During long-time cycling tests, these dendrites also potentially pose concerns of cell shorting through the separator. Significant electrolyte optimizations are further required to address these issues and further technology commercialization.

Current collectors and solvent species can typically get oxidized during the electrochemical testing of the inorganic materials and this can result in contamination of the electrolyte. Electrolyte contamination can lead to additional redox contributions, complex interactions with studied active components and should be avoided.

Electroanalytical techniques such as cyclic voltammetry are routinely employed to define the operable voltage window. This technique involves scanning over the desired voltage window at a predefined scan-rate (mV/s) and measuring the current response. A distinct current increase would

be noticeable corresponding to the electrochemical reactions of solvent species and current collectors. Using multiple scans, we can investigate the suppression capability (corrosion resistance) of the surface passivation films that typically form in the first cycle for various materials. Different substrates such as aluminum, anodized aluminum, stainless steel (grade 316), titanium and graphite were evaluated for their electroanalytical response as shown in Figure 2.13 and Figure 2.14. The substrates were 0.5" in diameter to fit the Swagelok assembly and typically around 3-4 inches long. The anodized aluminum (hard anodized 6061 Al rod, McMaster-Carr) has a black insulating oxide coating on the rod circumference while the end cut-sections have exposed aluminum metal (to provide electrical contact to electrode films). The oxide coating has excellent corrosion resistance and is left intact to minimize the electrolyte contact with bare aluminum surface. The rods were polished with 600 grit sanding sheets (polished finish grade, McMaster-Carr) to obtain a fresh metal surface with smooth finish while removing surface impurities. Subsequently, they were subjected to ultrasonication (using Branson, 3510 sonicator) in 2propanol solution for ~15 minutes to dislodge any residual metal powders from prior sanding step and air-dried before cell-assembly.

The 1st cycle cyclic voltammogram of aluminum exhibits a peak current of 54 μ A during the oxidative scan and this gets reduced substantially (10th cycle peak current ~ 6 μ A) in the subsequent cycles due to surface passivation that limits further reactions. Anodized aluminum rod shows much lower peak current (9.9 μ A) in the 1st cycle due to lower exposed metal surface contacting the electrolyte. It also has a strong passivation effect during subsequent cycles (10th cycle peak current-0.7 μ A).

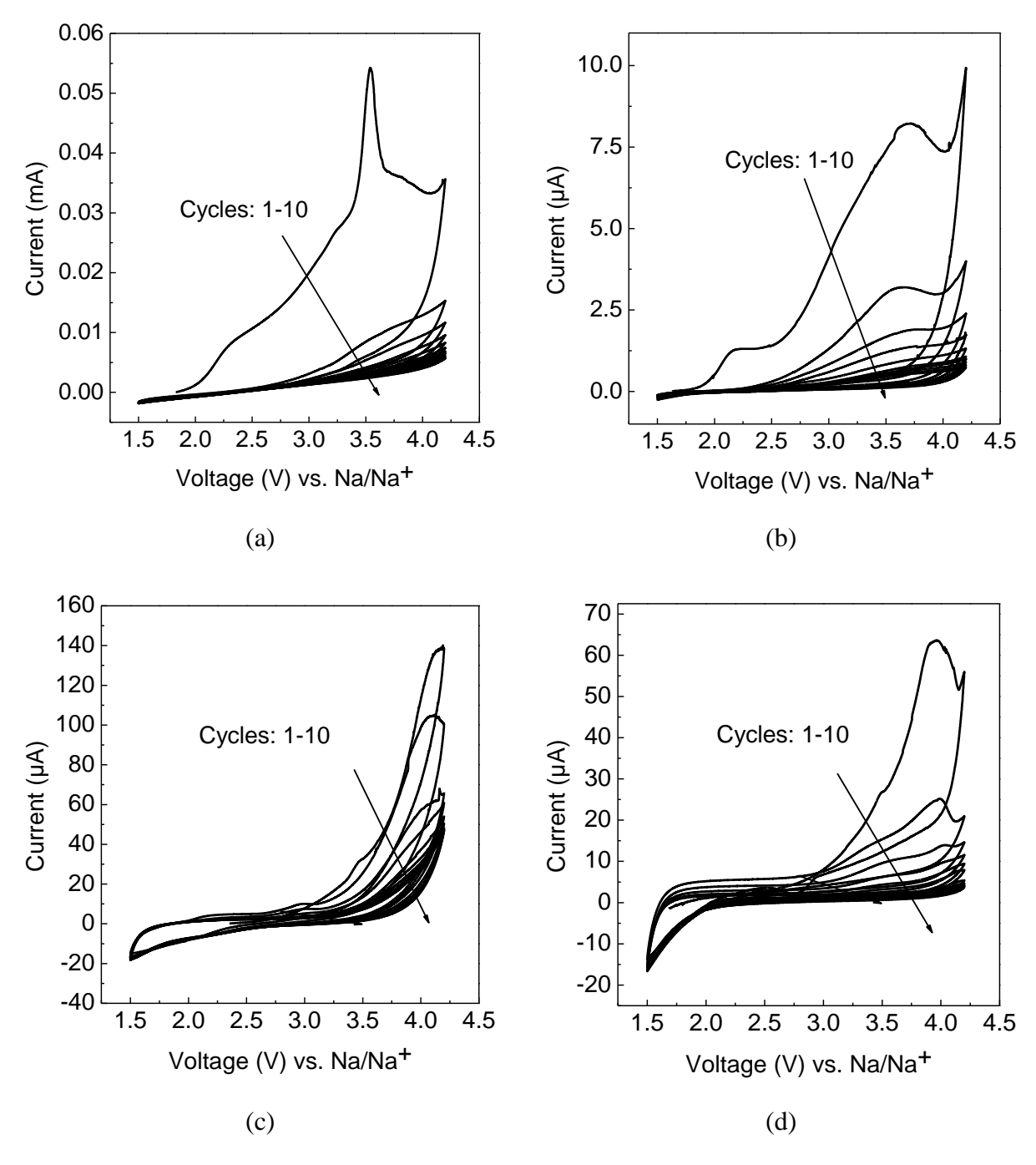


Figure 2.13 Cyclic voltammograms scanned between 1.5-4.2 V voltage window for (a) aluminum, (b) andoized aluminum, (c) stainless steel 316, and (d) titanium.

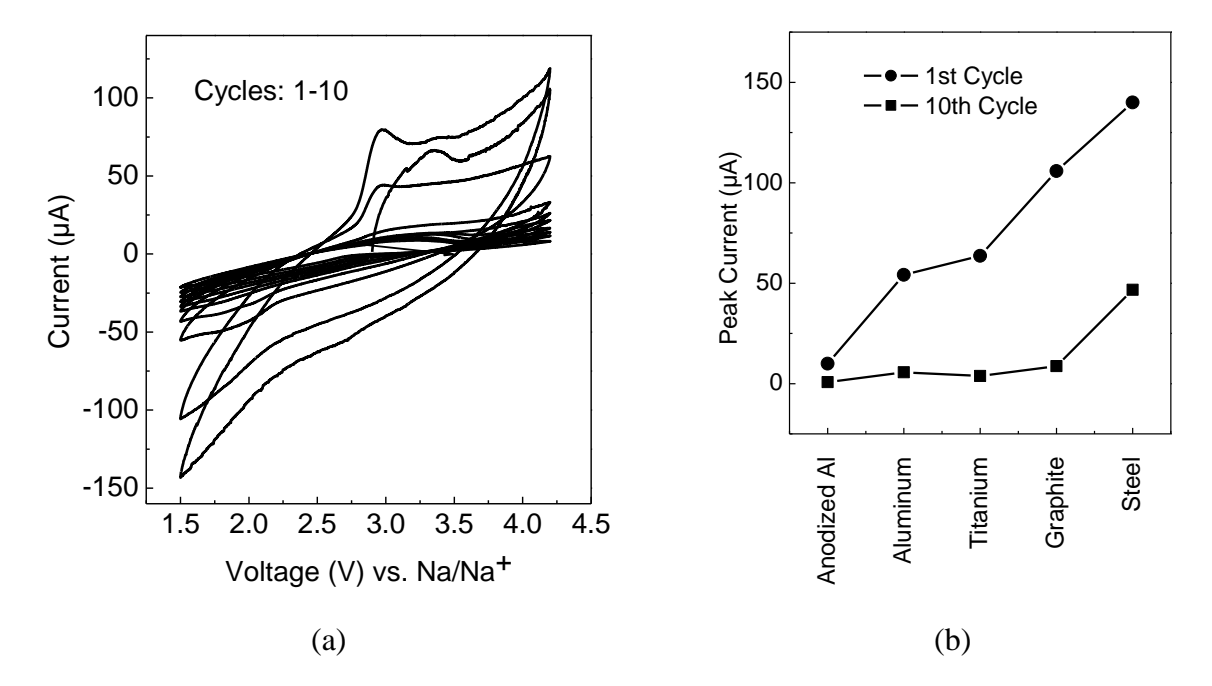


Figure 2.14 (a) Cyclic voltammogram of graphite scanned between 1.5-4.2 V voltage window, and (b) oxidative voltammogram peak currents for 1st and 10th cycle.

Stainless steel (grade 316), titanium and graphite have 1^{st} cycle peak current values of 140 μ A, 64 μ A, and 106 μ A respectively. Like aluminum, these materials also show a tendency towards passivation as evidenced by peak current reduction as shown in Figure 2.14b. For further testing, only anodized aluminum is utilized as current collector as it exhibited superior oxidative stability compared to the remaining materials.

We also tested the anodized aluminum rod under galvanostatic conditions that are typically used in battery electrode testing. The galvanostatic results are in accord with cyclic voltammetric studies. At $23.6 \,\mu\text{A/cm}^2$ current density, the upper voltage limit of $4.5 \,\text{V}$ is reached in 6 min during which aluminum passivation occurs. Subsequently, voltage profiles are steeper as further oxidation reactions are not supported readily and the rods can be considered to be fairly inert under the test conditions (Figure 2.15).

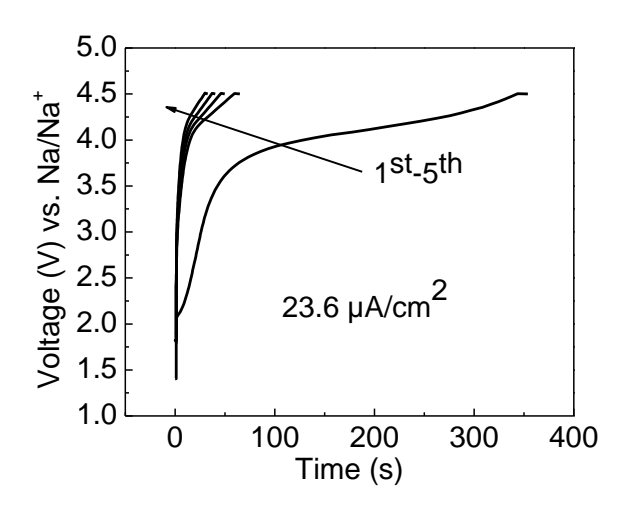


Figure 2.15 Voltage profile of anodized aluminum current collector tested under galvanostatic condition with 4.5V cutoff using 3-electrode setup.

2.5.3 Validation of electrochemical methods using standard intercalation materials: Na_{0.7}CoO₂ and LiFePO₄

In order to validate the experimental methods for film fabrication and cell assembly, well-studied materials such as LiFePO₄ and Na_{0.7}CoO₂ were tested. The goal was to ensure that the experimental results are consistent with the literature reports.

LiFePO₄ powders were synthesized by dry milling Li₂CO₃, NH₄H₂PO₄ and Fe(C₂O₄).2H₂O (from Sigma-Aldrich) with 10 wt% carbon mixture (equal proportions of sucrose and Ketjen Black, AkzoNobel) and firing the precursors in a tube furnace with argon atmosphere at 600°C for 6 hours duration. This modified procedure was adopted from literature results suggesting that the incorporation of carbon additives improves electrochemical performance.³⁵ The as-synthesized powders were comprised of <100 nm sized particles that are interconnected by a carbon network. Na_{0.7}CoO₂ was synthesized by straightforward solid-state reaction method in a box furnace. Materials were subject to electrochemical testing using 3-electrode cell assembly.

Figure 2.16a shows the charge/discharge curves for LiFePO₄ electrodes using lithium metal as counter and reference electrodes and LiPF₆-based commercial electrolyte from MTI Corp. (EQ-LBC3051C). A flat-voltage profile at 3.4 V vs. Li/Li⁺ is observed demonstrating the activity of Fe^{2+/3+} redox couple accompanied by a two phase reaction (involving LiFePO₄ and FePO₄ phases) matching the literature reports.^{2,35,36} The discharge capacity values are 74% of the theoretical capacity (170 mAh/g) at C/10 rate.

Na_{0.7}CoO₂ electrodes were tested with sodium metal as counter and reference electrodes and 0.5 M NaPF₆ in EC/DMC electrolyte (50/50 vol%). The complex voltage steps and plateau, in Figure 2.16b are attributable to single/bi-phasic domains and vacancy ordering as previously reported.³⁷ These results provide a good confidence on our experimental design as they replicate the literature reports fairly accurately.

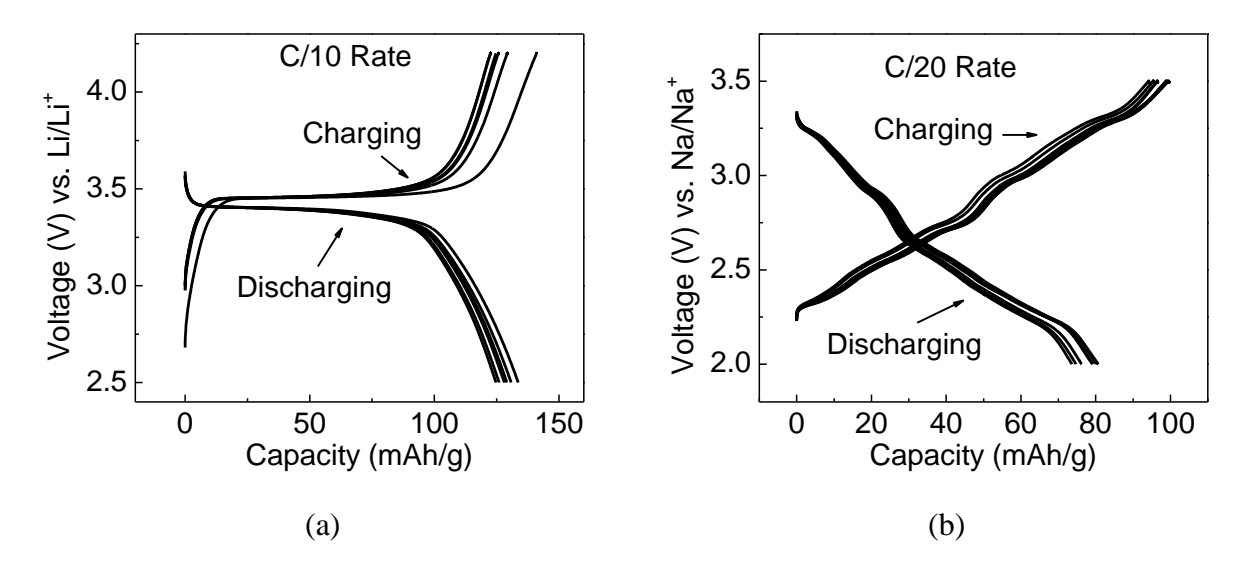


Figure 2.16 Voltage profiles of (a) lithium iron phosphate under galvanostatic conditions at C/10 rate demonstrating two-phase reaction between FePO₄ and LiFePO₄, and (b) Na_{0.7}CoO₂ showing complex voltage steps and plateaus due to multiple phase transitions.

2.5.4 SNP Electrochemistry: Galvanostatic testing

SNP has a theoretical capacity of 106 mAh/g for complete sodium de-intercalation (x=4) from the structure [Na₄Ni₇(PO₄)₆ to Ni₇(PO₄)₆]. The sodium de-intercalation/intercalation reactions supported by Ni^{2+/4+} redox couple can be represented in Equation 2.1.

$$Na_4Ni_7^{II}[PO_4]_6 \leftrightarrow Na_{4-x}Ni_{7-x/2}^{II}Ni_{x/2}^{IV}[PO_4]_6 + xNa^+ + xe^-$$
 2.1

Galvanostatic charge/discharge studies are executed to get an improved understanding of the reversibility of the redox reactions. Studied electrolytes include 1M NaClO₄ in Ethylene Carbonate/Dimethyl Carbonate (EC/DMC) and 0.5 M NaPF₆ in Ethylene Carbonate/Diethyl Carbonate (EC/DEC) solutions in voltage window between 3.2 and 4.2 V.

During charging, there is an initial rapid voltage rise to 2.8 V vs. Na/Na⁺ after which the voltage curve shows a gradual sloping profile, as depicted in Figure 2.17a. Prolonged charging results in continued extraction of sodium ions resulting in concomitant generation of additional Ni⁴⁺ states. Complete sodium de-intercalation could be achieved after which the voltage starts to rise due to electrolyte oxidation reactions to support the current. The current direction was reversed to induce reduction of Ni⁴⁺ species but this resulted in a significant voltage polarization with very little sodium intercalation with voltage cutoff limited to 1.5 V. Lowering the voltage cutoff to 0.8 V leads to a long voltage plateau which cannot be accounted for by just considering sodium intercalation reactions. It is likely that in addition to sodium intercalation, there is considerable amount of electrolyte reduction reactions, possibly catalyzed by SNP particles. Nevertheless, the subsequent charging cycle provides ~50% theoretical capacity at a lower electrode potential (~2.0 V vs. Na/Na⁺) in Figure 2.17b. The voltage profile remains in the same regime for further cycles and the difference between the first and second cycle can possibly be accounted for by local re-

organization effects (not captured by XRD discussed in the next section). Future studies to increase the understanding of voltage hysteresis effect (1 V) and electrocatalytic reduction of organic solvents are required to improve the energy density and arrest capacity fade.

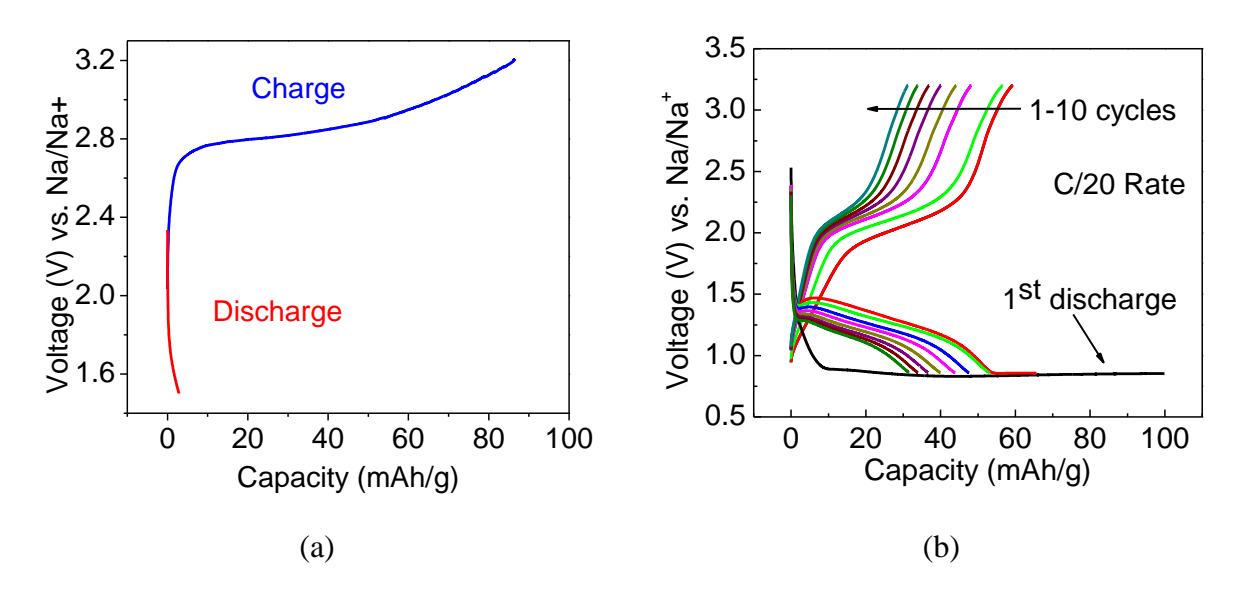


Figure 2.17 Sodium nickel phosphate tested under galvanostatic conditions with discharge cutoff voltage of (a) 1.5 V in 1st cycle, and (b) 0.8 V.

2.5.5 SNP Ex-situ XRD characterization

Ex-situ XRD testing is utilized to characterize the film electrodes at various sodium contents. This helps in detecting electrochemically-driven phase transitions and analyzing the crystallinity of the studied battery materials. The film electrodes are subjected allowed to reach different charge/discharge voltages under galvanostatic conditions to achieve various sodium intercalation contents inside the electrochemical setup. After passing charge and allowing for equilibration (typically 2 hours), the cell is disassembled to obtain the electrodes and the film is washed with DMC solvent to remove any residual salt components inside the glovebox. The washed film is dried under ambient conditions and transferred to a vial for XRD characterization. The film is mounted on Bruker sample holder and secured using wax. Mylar tape is placed over the sample

holder and a seal mechanism limits air exposure during the characterization. Inclusion of wax and Mylar does lead to unwanted bumps and peaks in the XRD patterns (Figure 2.18) and there were found not to overlap with the main peaks of the target SNP phase.

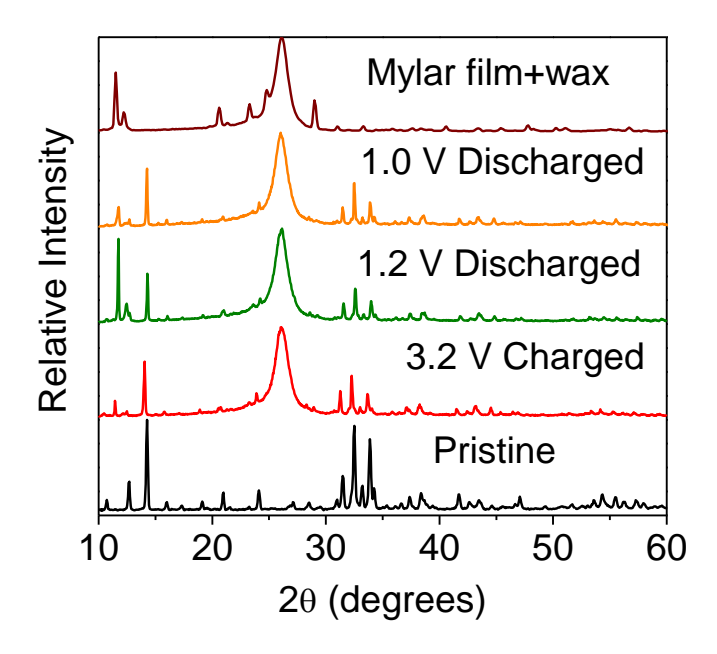


Figure 2.18 Ex-situ XRD characterization of SNP electrode film at different state-of-charge, Mylar film and wax (used for sticking the electrode to the holder base).

We found that the 3.2 V charged electrode peaks are identical to those of pristine powders demonstrating that the SNP material retains the same crystal structure even after complete sodium de-intercalation, as shown in Figure 2.18. We attribute this structural stability to the 'pillaring' effect of phosphate functional groups, typical of polyanionic materials. The electrodes subjected to deep discharge of 1.2 and 1.0 V also have comparable patterns indicating that the redox reactions occurring at those potential regions are not due to the formation of metallic nickel species (conversion-type mechanisms). We demonstrate that the reaction mechanism that provides charge storage capability is due to the desired intercalation-type mechanisms. Since SNP has a relatively

low redox potential (~2 V) and only a modest reversible capacity (~ 50 mAh/g), we focused our attempts to investigate different structural types for our exploratory research.

2.5.6 SCT Electrochemistry: Potentiostatic Intermittent Titration Testing (PITT)

PITT involves scanning the electrode potential over the working range (upper and lower cutoff voltages) with voltage steps and allowing for current relaxation (C/50) during each step. The relaxation step allows the material to approach close-to equilibrium conditions. For complete sodium de-intercalation (x=0.8), the theoretical capacity is calculated to be 117 mAh/g. Sodium intercalation/de-intercalation reactions due to $Co^{2+/4+}$ redox couple can be represented in Equation 2.2.

$$Na_{0.8}[Co_{0.4}^{II}Ti_{1.6}^{IV}]O_2 \leftrightarrow Na_{0.8-x}[Co_{0.4-x/2}^{II}Co_{x/2}^{IV}Ti_{1.6}^{IV}]O_2 + xNa^+ + xe^-$$
 2.2

SCT was tested using 0.5 M NaPF₆ in 50/50 vol% EC/DEC electrolyte in a 3-electrode cell assembly. The 1st charging voltage profile slopes gradually between 3.6 and 4.2 V and remains fairly identical for next two cycles as shown in Figure 2.19a. The discharge profile also follows a sloping profile with a large initial voltage polarization. The symmetric nature of the charging and discharging curves suggests reversible sodium intercalation/de-intercalation reactions. The capacity retention was also found to be fairly stable in the tested 3 cycles and the faradaic efficiency improves to 86% in the 3rd cycle (Figure 2.19b). However, there is a large voltage hysteresis of 1.4 V between charge and discharge curves even while testing the cell at 70°C.

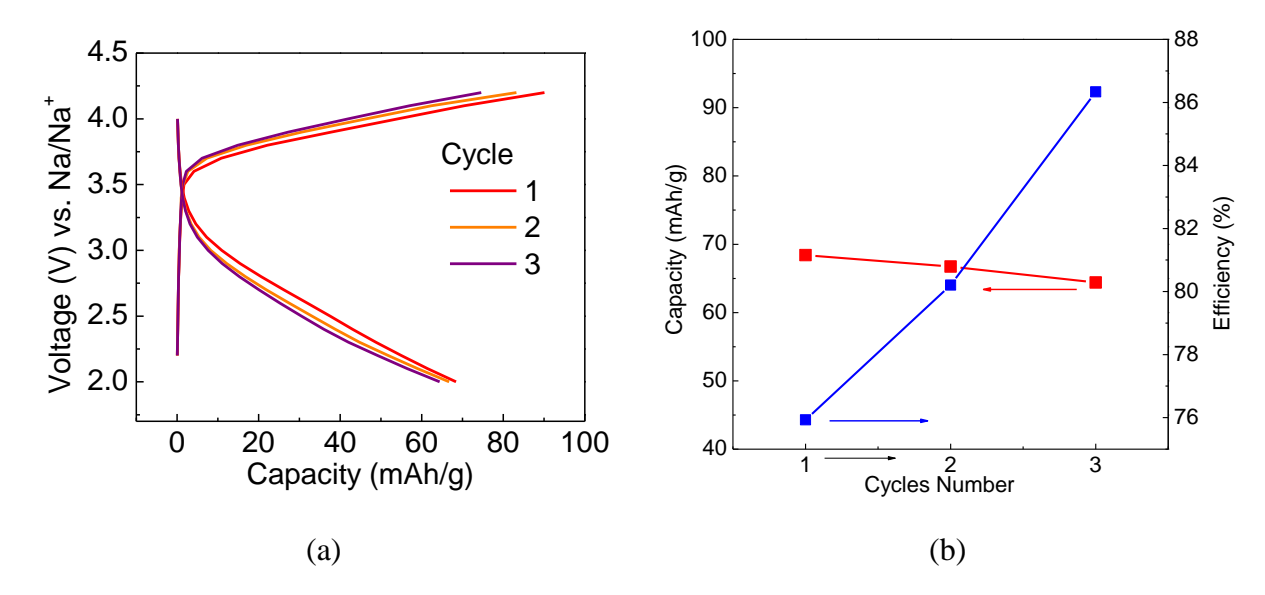


Figure 2.19 (a) Voltage curve of sodium cobalt titanate from PITT with C/50 current limit, 100 mV step potential tested at 70 °C using 0.5M NaPF6 in EC/DEC electrolyte, and (b) Discharge capacity and faradaic efficiency with cycle number.

SCT was also evaluated with 1M NaClO₄ in EC/DMC electrolyte using slow-rate galvanostatic testing of C/100 at room temperature. The voltage hysteresis increases to 1.6 V for room-temperature testing suggesting a thermally activated limiting process (Figure 2.20a). We also show that the hysteresis is not related to the nature of solvent and is inherent to the studied material. In Figure 2.20b, Ex-situ XRD results confirm that the SCT pristine peak positions are fairly comparable to those of partial charged (20%) and discharged films. The absence of additional peaks indicates that there is not a tendency towards phase transformations. The partially deintercalated electrode has slightly different peak intensities and suggesting the possibility of sodium redistribution amongst the remaining vacant sites.

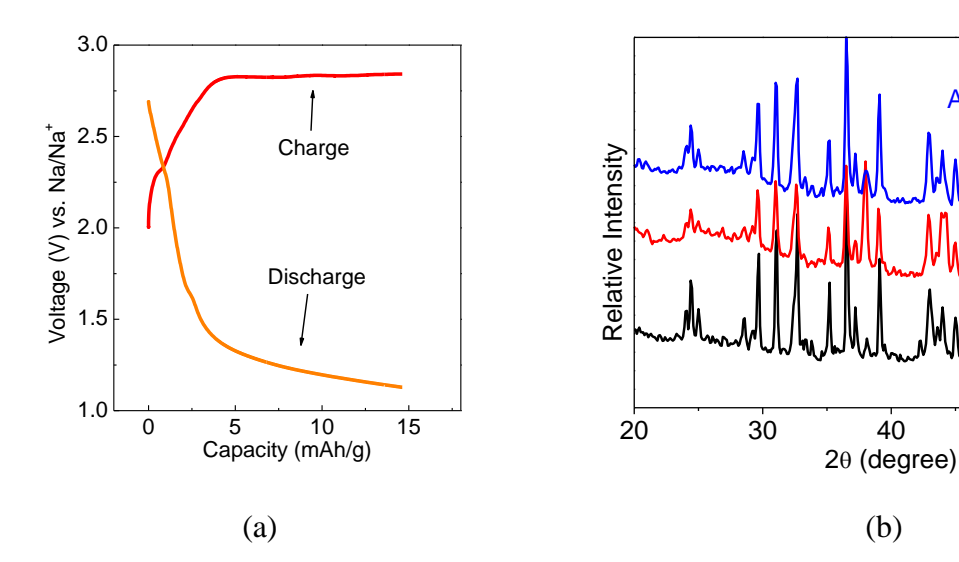


Figure 2.20 (a) Voltage profile of sodium cobalt titanate tested under at C/100 rate using 1M NaClO4 in EC/DMC electrolyte at room temperature, and (b) Ex-situ XRD of SCT at pristine, 20% charged and discharged state.

After discharge

50

60

We hypothesize that the hysteresis phenomenon is related to relatively slow diffusion of sodium ions in the tunnels and further improvements can be realized by grain-size reduction (nano-scale) by chimie douce synthetic methods. The scope of this exploratory research was to identify potential inorganic materials that can possibly sustain relatively facile sodium intercalation/de-intercalation reactions using micron length-scale particles. The reported tunnel-type materials does show promise in terms of structural stability (after sodium de-intercalation) but their electrochemistry is fairly constrained by diffusional limitations. We initiated the study of novel layer-structured, bimetallic transition metal oxides, with the general composition Na_xM_yM'_{1-y}O₂ as suitable sodium intercalation electrodes in the subsequent chapters.

2.6 Summary

In this chapter, two tunnel-type materials Na₄Ni₇(PO₄)₆ and Na_{0.8}Co_{0.4}Ti_{1.6}O₂ were explored as potential sodium intercalation electrode materials. These framework materials were anticipated to

possess good stability based on structural connectivity and reasonable sodium transport through the 3-D tunnels. Phase-pure, crystalline powders of these two compositions were successfully synthesized by solid-state reaction and sol-gel techniques as demonstrated by the characteristic XRD peak sets. SNP shows a sloping charging voltage profile at 2 V and discharge profile at 1.25 V with a noticeable voltage hysteresis. These reactions were confirmed to be due to topotactic exchange of sodium intercalant without any phase change. SCT was also found to be electrochemically active with charging and discharging voltage profile at 3.7 and 2.5 V, respectively when tested at 70°C. The large voltage hysteresis is predicted to be due to slow-diffusion of sodium. These materials show promise in terms of structural stability as no phase change was evident upon sodium removal. However, to mitigate voltage hysteresis, future research needs to focus on developing improved chimie douce methods for nano-sizing the particles without particle sintering.

BIBLIOGRAPHY

BIBLIOGRAPHY

- 1. Gong, Z. & Yang, Y. Recent advances in the research of polyanion-type cathode materials for Li-ion batteries. *Energy Environ. Sci.* **4,** 3223 (2011).
- 2. Padhi, A. K., Nanjundaswamy, K. S. & Goodenough, J. B. Phospho-olivines as Positive-Electrode Materials for Rechargeable Lithium Batteries. *J. Electrochem. Soc* **144**, 1188–1194 (1997).
- 3. Nytén, A., Abouimrane, A., Armand, M., Gustafsson, T. & Thomas, J. O. Electrochemical performance of Li2FeSiO4 as a new Li-battery cathode material. *Electrochem. commun.* **7**, 156–160 (2005).
- 4. Guo, H. *et al.* Optimum synthesis of Li2Fe1–xMnxSiO4/C cathode for lithium ion batteries. *Electrochim. Acta* **55**, 8036–8042 (2010).
- 5. Choi, D. *et al.* LiMnPO4 nanoplate grown via solid-state reaction in molten hydrocarbon for Li-ion battery cathode. *Nano Lett.* **10**, 2799–805 (2010).
- 6. Weker, J. N., Li, Y., Shanmugam, R., Lai, W. & Chueh, W. C. Tracking Non-Uniform Mesoscale Transport in LiFePO 4 Agglomerates During Electrochemical Cycling. *ChemElectroChem* (2015). doi:10.1002/celc.201500119
- 7. Xu, B., Qian, D., Wang, Z. & Meng, Y. S. Recent progress in cathode materials research for advanced lithium ion batteries. *Mater. Sci. Eng. R* **73**, 51–65 (2012).
- 8. Nanjundaswamy, K. S. *et al.* Synthesis, redox potential evaluation and electrochemical characteristics of NASICON-related-3D framework compounds. *Solid State Ionics* **92**, 1–10 (1996).
- 9. Padhi, A. K., Nanjundaswamy, K. S., Masquelier, C. & Goodenough, J. B. Mapping of Transition Metal Reclox Energies in Phosphates with NASICON Structure by Lithium Intercalation. *J. Electrochem. Soc.* **144**, 2581–2586 (1997).
- 10. Masquelier, C., Padhi, A. K., Nanjundaswamy, K. S. & Goodenough, J. B. New Cathode Materials for Rechargeable Lithium Batteries: The 3-D Framework Structures Li 3Fe2(XO4)3(X=P, As). *J. Solid State Chem.* 228–234 (1998).
- 11. Gopalakrishnan, J. & Rangan, K. K. V2(PO4)3: A Novel NASICON-Type Vanadium Phosphate Synthesized by Oxidative Deintercalation of Sodium from Na3V2(O4)3. *Chem. Mater.* **4**, 745–747 (1992).
- 12. Gover, R., Bryan, A., Burns, P. & Barker, J. The electrochemical insertion properties of sodium vanadium fluorophosphate, Na3V2(PO4)2F3. *Solid State Ionics* **177**, 1495–1500 (2006).

- 13. Palomares, V., Casas-Cabanas, M., Castillo-Martínez, E., Han, M. H. & Rojo, T. Update on Na-based battery materials. A growing research path. *Energy Environ. Sci.* **6**, 2312 (2013).
- 14. Lim, S. Y., Kim, H., Shakoor, R. A., Jung, Y. & Choi, J. W. Electrochemical and Thermal Properties of NASICON Structured Na3V2(PO4)3 as a Sodium Rechargeable Battery Cathode: A Combined Experimental and Theoretical Study. *J. Electrochem. Soc.* **159**, A1393–A1397 (2012).
- 15. Chihara, K., Kitajou, A., Gocheva, I. D., Okada, S. & Yamaki, J. Cathode properties of Na3M2(PO4)2F3 [M = Ti, Fe, V] for sodium-ion batteries. *J. Power Sources* **227**, 80–85 (2013).
- 16. Barpanda, P. *et al.* Sodium iron pyrophosphate: A novel 3.0V iron-based cathode for sodium-ion batteries. *Electrochem. commun.* **24,** 116–119 (2012).
- 17. Palomares, V. *et al.* Na-ion batteries, recent advances and present challenges to become low cost energy storage systems. *Energy Environ. Sci.* **5**, 5884 (2012).
- 18. Slater, M. D., Kim, D., Lee, E. & Johnson, C. S. Sodium-Ion Batteries. *Adv. Funct. Mater.* **23,** 947–958 (2013).
- 19. Huili, P., And, H. Y.-S. & Liquan, C. Room-Temperature Stationary Sdoium-Ion Batteries for Large-Scale Electric Energy Storage. *Energy Environ. Sci.* (2013). doi:10.1039/C3EE40847G
- 20. Thackeray, M. M. Spinel Electrodes for Lithium Batteries. *J. Am. Ceram. Soc* **82,** 3347–3354 (1999).
- 21. Shenouda, A. Y. & Murali, K. R. Electrochemical properties of doped lithium titanate compounds and their performance in lithium rechargeable batteries. *J. Power Sources* **176**, 332–339 (2008).
- 22. Nakahara, K., Nakajima, R., Matsushima, T. & Majima, H. Preparation of particulate Li4Ti5O12 having excellent characteristics as an electrode active material for power storage cells. *J. Power Sources* **117**, 131–136 (2003).
- 23. Yao, X. L. *et al.* Comparisons of graphite and spinel Li1.33Ti1.67O4 as anode materials for rechargeable lithium-ion batteries. *Electrochim. Acta* **50**, 4076–4081 (2005).
- 24. Xiao, X., Lu, J. & Li, Y. LiMn2O4 microspheres: Synthesis, characterization and use as a cathode in lithium ion batteries. *Nano Res.* **3,** 733–737 (2010).
- 25. Mumme, W. G. & Reid, A. F. Non-stoichiometric Sodium Iron Titanate, NaxFexTi2-xO4, 0.90> x >0.75. *Acta Crystallogr. B* **24**, 625–631 (1968).

- 26. Moring, J. & Kostiner, E. The Crystal Structure of Na4Ni7(PO4)6. *J. Solid State Chem.* **62,** 105–111 (1986).
- 27. Kuhn, A. *et al.* Study of the Conductivity of Nax-del FexTi2-xO4 (x=0 . 875 ,del<0.40). *J. Solid State Chem.* **173**, 168–173 (1998).
- 28. Kakihana, M. "Sol-gel" Preparation of High Temperature Superconducting Oxides. *J. Sol-Gel Sci. Technol.* **6,** 7–55 (1996).
- 29. Liu, H., Wu, Y. P., Rahm, E., Holze, R. & Wu, H. Q. Cathode materials for lithium ion batteries prepared by sol-gel methods. *J. Solid State Electrochem.* **8,** 450–466 (2004).
- 30. Fu, L. J. *et al.* Electrode materials for lithium secondary batteries prepared by sol–gel methods. *Prog. Mater. Sci.* **50**, 881–928 (2005).
- 31. Hamon, Y. *et al.* Aluminum negative electrode in lithium ion batteries. *J. Power Sources* **97-98**, 185–187 (2001).
- 32. Senguttuvan, P., Rousse, G., Seznec, V., Tarascon, J.-M. & Palacín, M. R. Na2Ti3O7: Lowest Voltage Ever Reported Oxide Insertion Electrode for Sodium Ion Batteries. *Chem. Mater.* **23**, 4109–4111 (2011).
- 33. Thevenin, J. Passivation films on lithium electrodes: An approach by means of impedance spectroscopy. *J. Power Sources* **14**, 45–52 (1985).
- 34. Komaba, S. *et al.* Fluorinated Ethylene Carbonate as Electrolyte Additive for Rechargeable Na Batteries. *ACS Appl. Mater. Interfaces* **3**, 4165–4168 (2011).
- 35. Croce, F. *et al.* A Novel Concept for the Synthesis of an Improved LiFePO4 Lithium Battery Cathode. *Electrochem. Solid-State Lett.* **5,** A47–A50 (2002).
- 36. Huang, H., Yin, S.-C. & Nazar, L. F. Approaching Theoretical Capacity of LiFePO4 at Room Temperature at High Rates. *Electrochem. Solid-State Lett.* **4,** A170–A172 (2001).
- 37. Berthelot, R., Carlier, D. & Delmas, C. Electrochemical investigation of the P2–NaxCoO2 phase diagram. *Nat. Mater.* **10**, 74–80 (2011).

3. SYNTHESIS, AND ELECTROCHEMICAL CHARACTERIZATION OF P-TYPE LAYER-STRUCTURED MATERIALS: Na_{2/3}[Ni_{1/3}Mn_xTi_{2/3-x}]O₂ (x=0, 1/3)

3.1 Introduction

3.1.1 Ionic conduction in layered materials

Layer-structured oxide materials have a general formula of A_xMO_2 ($0 \le x \le 2$), where 'A' is the alkali intercalant species and 'M' is the transition metal species. These material classes are classified as 'O3', 'T1', 'P2', 'P3' structures based on the oxygen stacking sequence as given by Delmas notation where the 'O', 'T' and 'P' refers to octahedra, tetrahedra and prismatic coordination of the alkali atoms, and the numeric character denotes the number of alkali layers per unit cell.¹⁻³

The alkali atoms that sandwich the transition metal layers provide a shielding effect for the close-packed oxygen layers. Hence, structures with lower 'x' have larger alkali layer spacing due to higher repulsive interactions and these structures have larger A-O bond length (prismatic coordination). The relatively large sodium atoms adopt P-type or O-type configuration while the smaller lithium atoms prefer O-type or T-type configuration environments.

As the number of vacant sites increases in the order of 'P'>'O'>'T', sodium-layered oxides generally have higher vacancy concentration (more non-stoichiometric) than lithium-layered oxides. Non-stoichiometric ('x'<1) sodium-layered oxide containing high vacancy concentration, support fast-ion mobility by means of the conventional 'vacancy hopping' mechanism. This conduction mechanism is operative in lithium-layered oxides, as well.⁴ The fast-ion mobility is these material classes is of particular interest for Na-intercalation electrodes as they overcome the

large-size effects. Hence, P-type sodium-layered materials are considerable attractive candidates as host electrodes for Na-ion batteries.

3.1.2 Literature reports on layered host materials

LiCoO₂ (LCO), with O3-layered structure (α -NaFeO₂ prototype), has been instrumental in the commercialization of Li-ion Batteries (LIBs) for electronics applications. However, LCO is limited by high cost and moderate capacity (\sim 140 mAh/g). Strategies for next-generation layered materials include elemental substitution to form Li[Ni_{1-x}Co_x]O₂, Li[Ni_{1/3}Mn_{1/3}Co_{1/3}]O₂ and similar oxides and structural stabilization to form xLi₂MnO₃.(1-x)LiMO₂ to improve the electrochemical properties. ⁵⁻⁸

The electrochemistry of NaCoO₂ has been extensively studied and reversible sodium intercalation/de-intercalation has been demonstrated. However, the complex interplay between Na⁺/vacancy ordering at the sodium sites and charge ordering in the transition metal sites results in a complex voltage profile that includes a number of steps and plateau. Formation of various single-phase and biphasic domains is undesirable for practical applications as these often lead to poor electrochemical performance. By introducing two or more transition metal species with different valence states, it is anticipated that the complex ordering processes would get disrupted possibly resulting in solid-solution type behavior. Some of the studied quaternary oxides containing aliovalent transition metals include $Na_xNi_{1/3}Mn_{2/3}O_2$, $Na_xFe_{1/2}Mn_{1/2}O_2$, $Na_{0.45}Ni_{0.22}Co_{0.11}Mn_{0.66}O_2$, $Na_{0.85}(Li_{0.17}Ni_{0.21}Mn_{0.64})O_2$. $^{10-15}$

3.1.3 Materials of interest

This study explores the potential of titanium-based aliovalent quaternary oxide with the composition Na_{2/3}[Ni_{1/3}Ti_{2/3}]O₂. The beneficial role of the inert titanium matrix in enhancing the structural stability of lithium quaternary oxides for cathode applications is largely known. ¹⁶⁻¹⁸ This work unravels Ti-induced stability mechanisms for sodium intercalation cathodes. Like other P2 compositions, the excellent ionic conductivity of sodium nickel titanate (P2-NT) has been documented previously. ¹⁹

The presence of two different transition metals (nickel and titanium) with significantly different redox potentials offers the possibility of achieving 'bi-functionality'. Nickel and titanium redox couples can be selectively activated making this composition suitable as cathode and anode. Using a 'bi-functional' material, the existing 'dual-line' manufacturing processes (separate for anodes and cathodes) can be substituted with a 'single-line' manufacturing to provide significantly lower capital and operating costs. Using a single material would also eliminate any cross-contamination issues between anode and cathode in manufacturing.

Electronic conduction in d-block transition metal oxides occurs by polaron hopping mechanisms involving charge carrier movement between localized potential wells. ²⁰⁻²³ The relative ease of ionization and the distribution of the transition metal species determines the charge carrier concentration and the polaron hopping length, respectively. The ionization energies of Ni^{2+/3+}, Mn^{4+/5+}, and Ti^{4+/5+} are 17, 21, and 56 eV, respectively. ²⁴ For P2-NT material, charge-carrier motion is anticipated to occur mostly between the nickel states since titanium has high ionization energy. However, since the nickel concentration is relatively low, this hopping process

might not be readily favored as seen in Figure 3.1a. Inclusion of manganese in the transition metal layer to form sodium nickel manganese titanate (P2-NMT) material would increase the intrinsic charge carrier concentration and provide additional transport pathways by forming a percolating network as shown in Figure 3.1b. This chapter delves into evaluating the electrical and electrochemical properties of these novel electrode compositions.

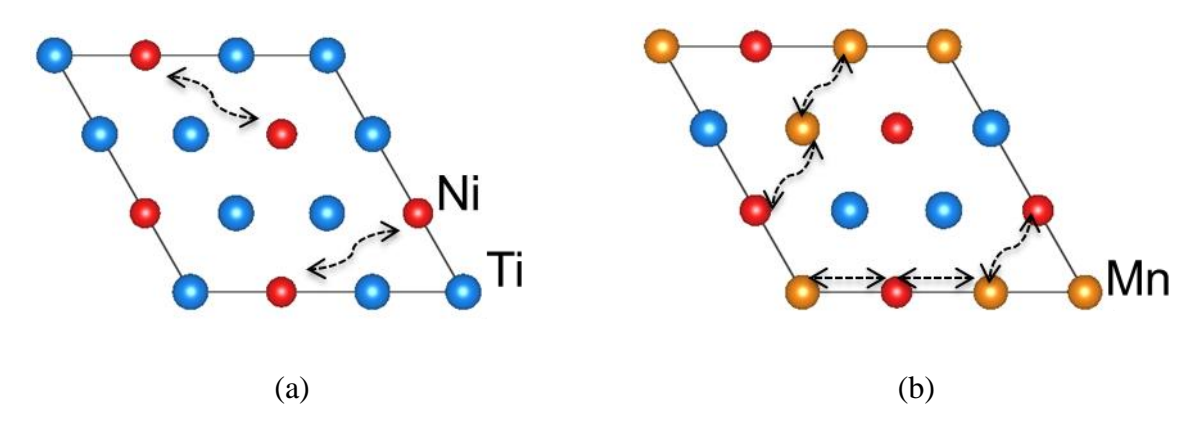


Figure 3.1 Schematic of the transition metal slab in layered oxide depicting charge carrier pathways in (a) P2-NT, and (b) P2-NMT through formation of percolating network; red, blue and orange spheres denote nickel, titanium, and manganese atoms, respectively.

3.2 Structural features

3.2.1 Sodium nickel titanate: P2-Na_{2/3}[Ni_{1/3}Ti_{2/3}]O₂

P2-NT phase was reported to crystallize in a disordered layered structure with space group P6₃/mmc (space group 194).^{3,19} The studied material has the same prototype structure as the well-reported Na_{0.7}CoO₂ material.²⁵ The oxygen stacking has been found to be in 'ABBA' sequence with sodium atoms occupying two different crystallographic sites: '2b' (Na_f site) and '2d' (Na_e site). It was reported that Na_f and Na_e are not energetically equivalent and the former has lower site occupancy by virtue of its larger repulsive interactions with the transition metals. Figure 3.2 shows the location of two sodium layers per unit cell and hence this structure can be represented

by Delmas notation as 'P2'. The complete accounting of the XRD reflections by the 194 space group led to the suggestion that the transition metal atoms are randomly distributed at the '2a' site. ¹⁹

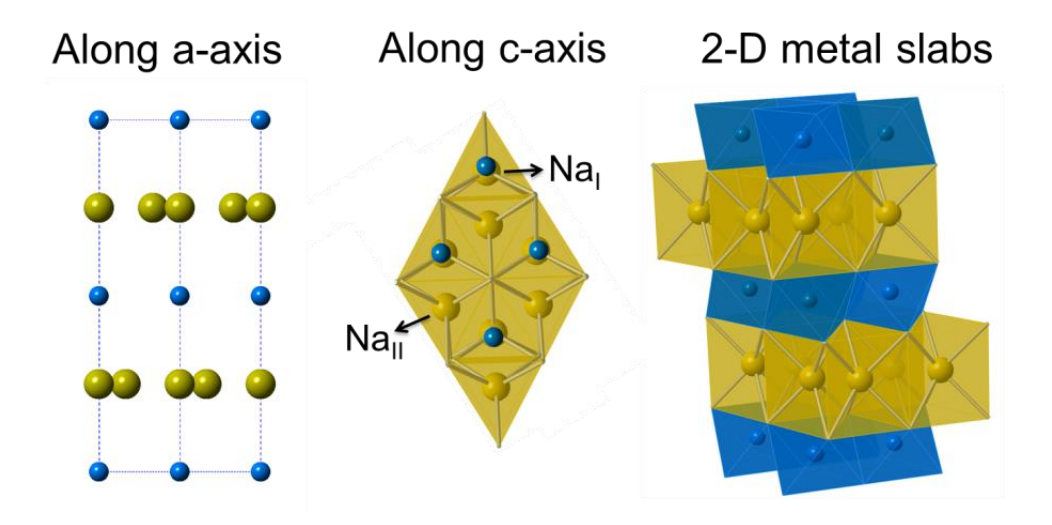


Figure 3.2 Crystal structure of $Na_{2/3}[Ni_{1/3}Ti_{2/3}]O_2$; blue spheres refer to transition metals (nickel and titanium), yellow spheres refer to sodium atoms Oxygen atoms are not included for clarity.

3.2.2 Sodium nickel manganese titanate: P2-Na_{2/3}[Ni_{1/3}Mn_{1/3}Ti_{1/3}]O₂

The substitution of manganese to partially replace titanium atoms at the '2a' sites forms a solid solution composition with the parent phase, P2-NT. Hence, P2-NMT has the same crystal structure as P2-NT phase, shown previously in Figure 3.2 with random distribution of manganese. This allows for retaining the excellent sodium conduction pathways of the P2 phase while potentially improving the electrical transport properties in the transition metal layer.

3.3 Inorganic synthesis and high-temperature processing

3.3.1 Sodium nickel titanate synthesis

The precursors were Na₂CO₃ (≥99.5%), NiO (micron powder, 99%; <50 nm powder, 99.8%), and

TiO₂ (micron powder, 99%; 21 nm powder, ≥99.5%). For a typical synthesis of 10 g of powder, 4.6 g of Na₂CO₃, 2.5 g of NiO, and 5.4 g of TiO₂ were used. Na₂CO₃ of 10 wt% excess were added to compensate the sodium oxide evaporation during high-temperature processing. Both micronand nano-sized NiO and TiO₂ were employed to compare the effect of particle size on the ease of synthesis and the electrochemical properties. Micron-sized precursors were subjected to dry-milling using SPEX SamplePrep 8000M mixer/mill. Nano-sized precursors were mixed in a jar mill with 2-propanol as solvent. After uniform mixing and solvent removal at 120°C, the powders were fired at 900 °C in a box furnace exposed to air.

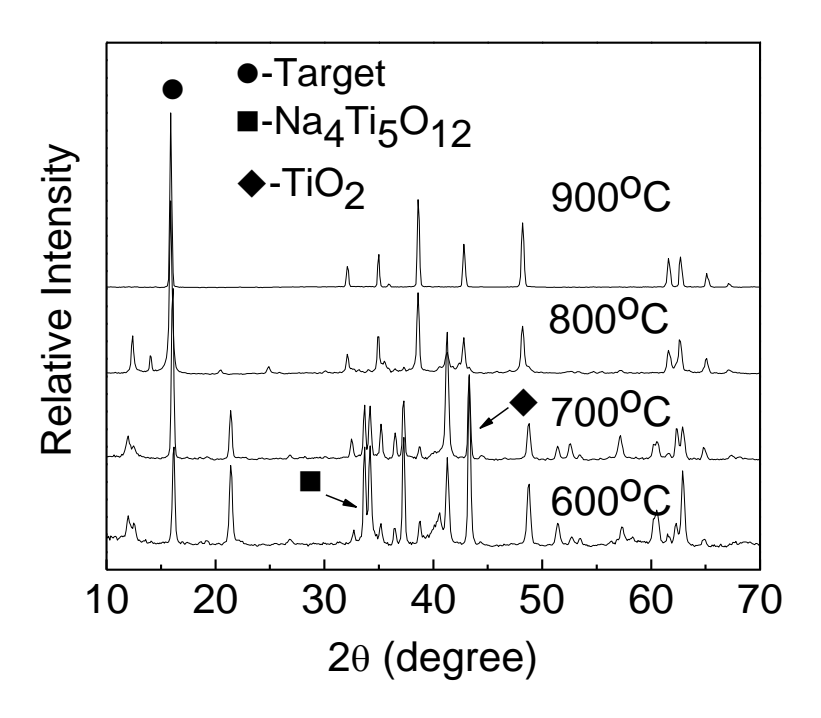


Figure 3.3 XRD characterization of sodium nickel titanate prepared by solid state reaction from micron-sized precursors fired for 12 hours duration; The dominant peaks of the impurity and target phases are indexed.

The XRD patterns of the micron-sized precursor powders fired for 12 hours duration at different temperatures are shown in Figure 3.3. Powders fired at 600 °C had considerable amount of

unreacted TiO_{0.9} phase (ICSD reference code: 78-0720) and Na₄Ti₅O₁₂ (ICSD reference code: 52-1814) impurity phase along with the target Na_{2/3}[Ni_{1/3}Ti₂₃]O₂ phase (ICSD reference code: 48-0164). As the calcination temperature is increased to 700 and 800 °C, a reduction in the amount of unreacted TiO₂ and impurity phase is observed. It was found that heating to 900 °C is essential to obtain phase-pure powders with these precursor powders and processing conditions.

When using nano-precursors, the fired powders were matched with the target phase without unreacted components as shown in Figure 3.4a. even when calcined at a lower temperature of 800 °C. However, a small impurity peak was detected at 41° and this could not be reasonably matched with any binary or ternary Na-Ni-Ti-O oxide components in ICSD database. Attempts to eliminate this impurity by prolonging the synthesis duration to 20 and 36 hours were not successful. Completely pure target phase could only be formed at a slightly higher temperature of 900 °C when heated for at least 2 hours and further electrochemical testing was performed using these powders, as depicted in Figure 3.4b.

The SEM images of the as-prepared P2-NT powders are shown in Figure 3.4c and d. Synthesis from micron-sized precursors results in fairly spherical particles that are roughly 5-10 μ m in diameter. Nano-sized precursors yielded finer powders with particles less than 5 μ m due to reduced heating duration. Nano-precursors provide pure phase powders, with smaller particle size, in shorter synthesis due to shorter diffusional length and facile reaction kinetics.

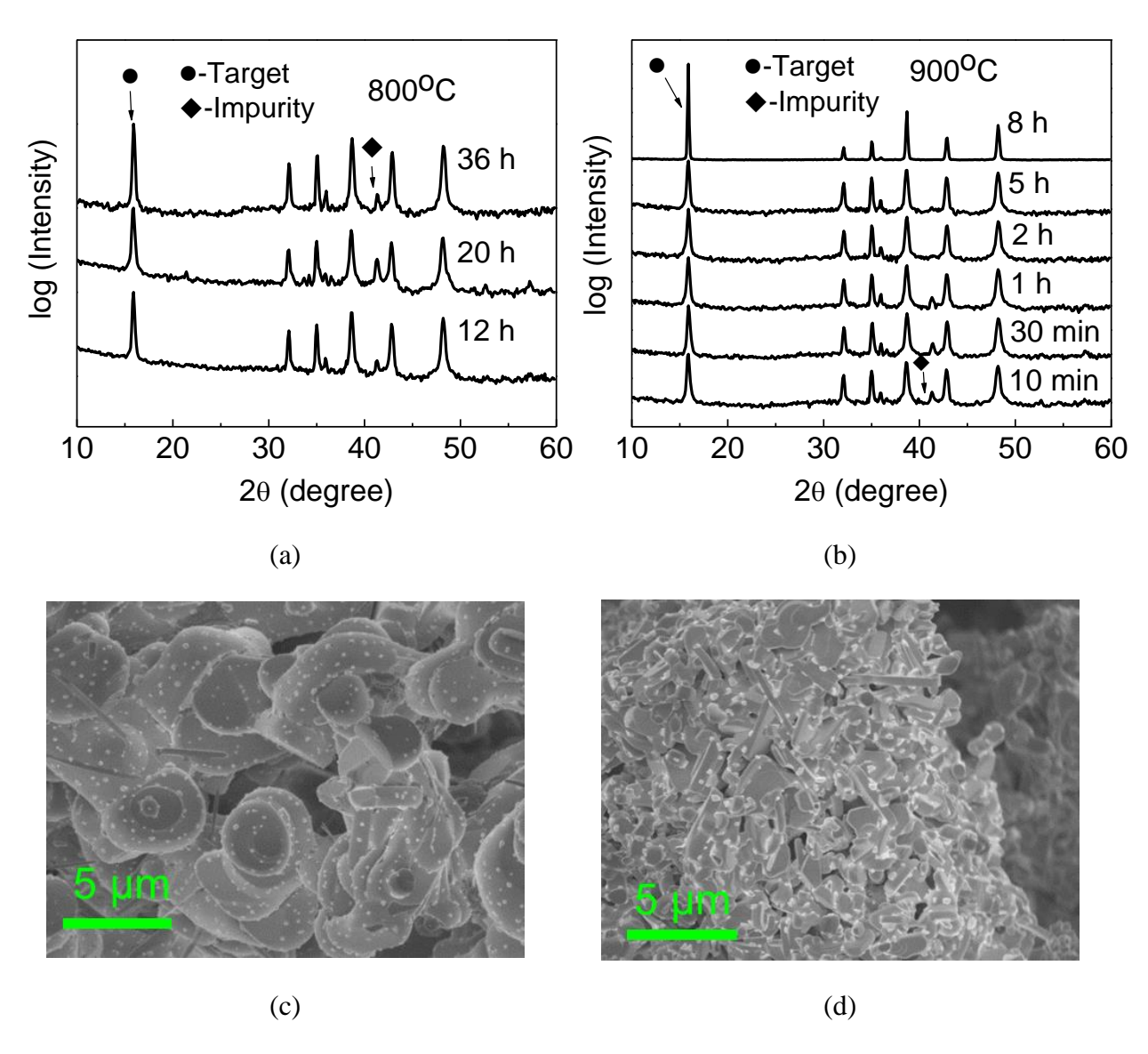


Figure 3.4 XRD characterization of P2-NT material prepared by solid state reaction from wetmilled nano-sized precursors fired at (a) 800 °C, and (b) 900 °C, SEM morphology of powders prepared from (c) micron-sized precursors, and (d) nano-sized precursors.

3.3.2 Sodium nickel manganese titanate synthesis

The precursors consisting of stoichiometric amounts of Na₂CO₃ (\geq 99.5%), NiO (micron powder, 99%), TiO₂ (micron powder, 99%) and MnO₂ (\geq 99%) were dry-milled using high-energy SPEX mill and subsequently fired at 900 °C for 12 hours duration. XRD of P2-NT and P2-NMT phases

have identical patterns as both structures have the same space group (194) suggesting solid solution formation with manganese occupying the octahedral '2a' sites (Figure 3.5a).

The prepared P2-NMT powders were found to be agglomerates of micron-sized particles as shown in Figure 3.5b. For the purposes of this study, the valency of nickel, manganese and titanium are taken as 2+, 4+, and 4+, respectively, based on the synthetic conditions and literature reports for isostructural materials. 3,10,19

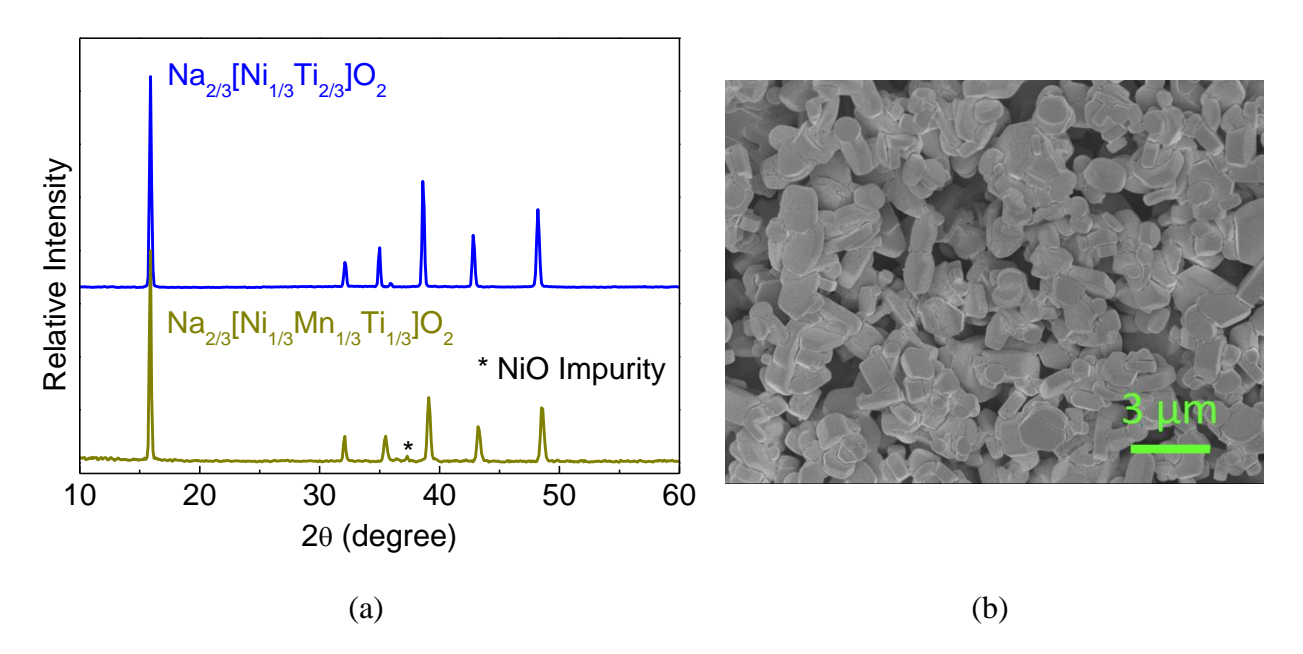


Figure 3.5 (a) XRD comparisons of sodium nickel titanate and sodium nickel manganese titanate powders prepared by solid state reaction, (b) and SEM powder morphology.

The surface area of the as-synthesized powders were measured using the Brunauer-Emmett-Teller (BET) method with Micromeritics ASAP 2020 instrument employing krypton as the adsorbate gas. The powders were subjected to a degassing step where the powders were preheated in a sample holder under low-pressure conditions to eliminate any physisorbed water and volatile adsorbed components. The BET surface area of the P2-NT (micron-sized precursors), P2-NT

(micron-sized precursor) and P2-NMT (micron-sized precursor) powders were estimated to be 0.58, 1.30 and 0.78 m²/g, respectively. This translates to an average particle size of 1.33 μm and 0.97 μm for P2-NT and P2-NMT, respectively, which is used subsequently for diffusion coefficient calculations.

3.3.3 Powder sintering

The as-prepared oxide powders were cold-pressed at a pressure of 2 MPa and sintered at a temperature of 1000 °C for 10h to obtain a dense pellet. The surface morphology of the P2-NT and P2-NMT pellets are depicted in Figure 3.6. Both pellets appear to have sintered without any visible surface pores. Quantitative estimates of the pellet densities were obtained using the Archimedes method with 2-Propanol as solvent. The P2-NT and P2-NMT pellets were measured to have relatively high density values of 93 and 89%, respectively, substantiating the SEM-morphology observations. The sintered pellets were pasted with gold contacts on both sides for further electrical measurements (DC and impedance spectroscopy testing). The sintered pellets were 2.3 mm thick and 12.6 mm in diameter.

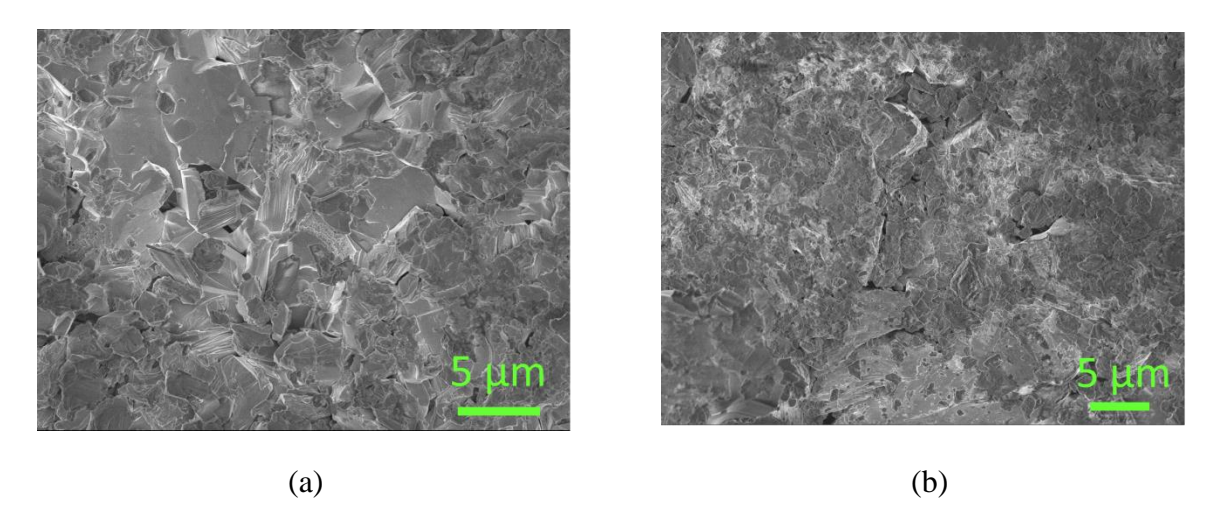


Figure 3.6 (a) Surface morphology of sintered pellets of (a) P2-Na_{2/3}[Ni_{1/3}Ti_{2/3}]O₂, and (b) P2-Na_{2/3}[Ni_{1/3}Mn_{1/3}Ti_{2/3}]O₂.

3.4 Film fabrication

The previously established protocols (chapter 2) were followed for fabricating the porous, composite electrode films with P2-NT and P2-NMT as active components. The film contains 80:10:10 weight ratio of active component, polymeric binder and conductive carbon. The punched film electrodes were transferred to a glovebox to reduce exposure to atmospheric water vapor and carbon dioxide.

3.5 Material Characterization

3.5.1 Voltage profile under galvanostatic testing

3.5.1.1High-voltage cathode: Ni^{2+/4+} redox couple

Sodium de-intercalation/intercalation in P2-NT would initiate the Ni^{2+/4+} redox couple and the theoretical capacity is estimated to be 181 mAh/g for complete sodium content range ($0 \le x \ge 2/3$, $Na_{2/3}[Ni_{1/3}Ti_{2/3}]O_2 \leftrightarrow Na_0[Ni_{1/3}Ti_{2/3}]O_2$). The redox reactions can be represented as

$$Na_{2/3}[Ni_{1/3}^{II}Ti_{2/3}]O_{2} \leftrightarrow Na_{2/3-x}[Ni_{1/3-x/2}^{II}Ni_{x/2}^{IV}Ti_{2/3}]O_{2} + xNa^{+} + xe^{-} \qquad 3.1$$

P2-NMT would have identical reaction as Equation 3.1 in the cathodic regime activating only the nickel redox couple with manganese remaining inert at valency of 4+ in the studied voltage range. The theoretical capacity of this phase is calculated to be 176.6 mAh/g assuming complete sodium exchange.

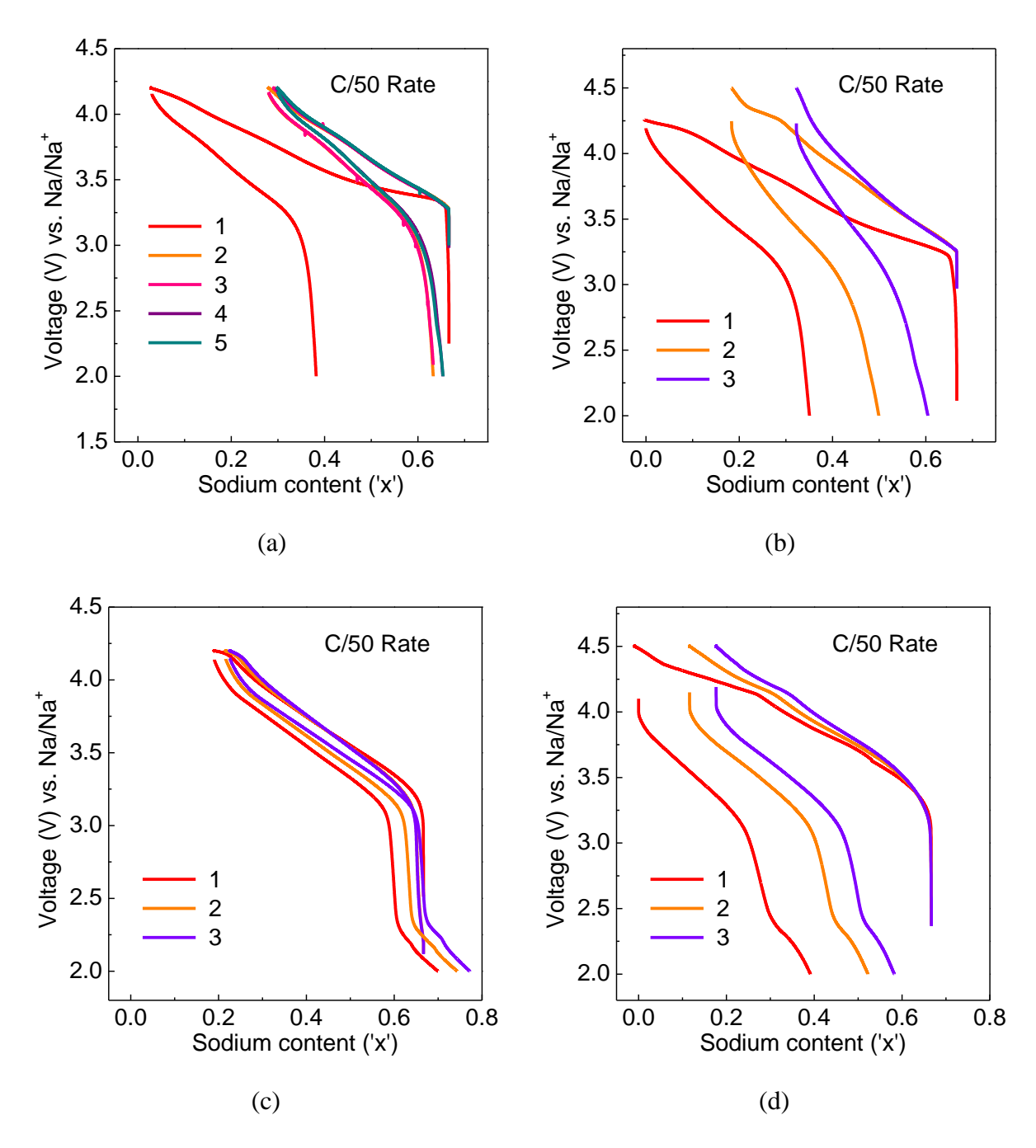


Figure 3.7 Cathodic voltage profile under galvanostatic testing rate of C/50 rate for (a) P2-NT material with cutoff of 4.2 V and, (b) P2-NT material with cutoff of 4.5 V, (c) P2-NMT material with cutoff of 4.2 V and, (d) P2-NMT material with cutoff of 4.5 V.

Figure 3.7 illustrates the voltage profile of P2-NT and P2-NMT phases under galvanostatic conditions of C/50 rate. In P2-NT, the first charge/discharge curve has a large irreversible capacity

and substantial voltage hysteresis due to electrolyte side reactions.²⁶ During the subsequent cycles, the voltage gap gets significantly diminished and the material exhibits good reversibility. The voltage profile appears sloping and does not involve multiple steps and plateau indicative of solid solution reaction mechanism when cycled till 4.2 V. However, a significant voltage hysteresis is noticeable upon increasing the charging voltage to 4.5 V. Additionally, a voltage plateau is observed at around 4.2 V corresponding to possibly a two phase reaction. Operating in the multiphasic domains contributes to poor reversibility as seen from Figure 3.7b.

P2-NMT exhibits excellent reversible sodium intercalation/de-intercalation reactions as illustrated in Figure 3.7c.²⁷ The voltage curves are sloping with very small voltage gap and good faradaic efficiency. Unlike P2-NT, the first charge/discharge cycle does not have a significant irreversible capacity showing that P2-NMT does not favor electrolyte oxidation as much as P2-NT. With high charging cutoff voltage of 4.5 V, a voltage plateau appears at around 4.2 V and this contributes to large voltage hysteresis and poor reversibility Figure 3.7d). The high redox potential (E°~3.7 V vs. Na/Na⁺) of these materials makes them attractive as high-voltage sodium intercalation cathodes.

3.5.1.2 Low-voltage anode: Ti^{4+/3+} redox couple

Titanium redox couple in P2-NT is activated by filling-in the vacant sodium sites in the pristine composition. This is made feasible by the presence of unusually high number of of vacant sites in this non-stoichiometric oxide. The sodium intercalation reaction can be represented by Equation 3.2.

$$Na_{2/3}[Ni_{1/3}Ti_{2/3}^{IV}]O_2 + xNa^+ + xe^- \leftrightarrow Na_{2/3+x}[Ni_{1/3}Ti_{2/3-x}^{IV}Ti_x^{III}]O_2$$
 3.2

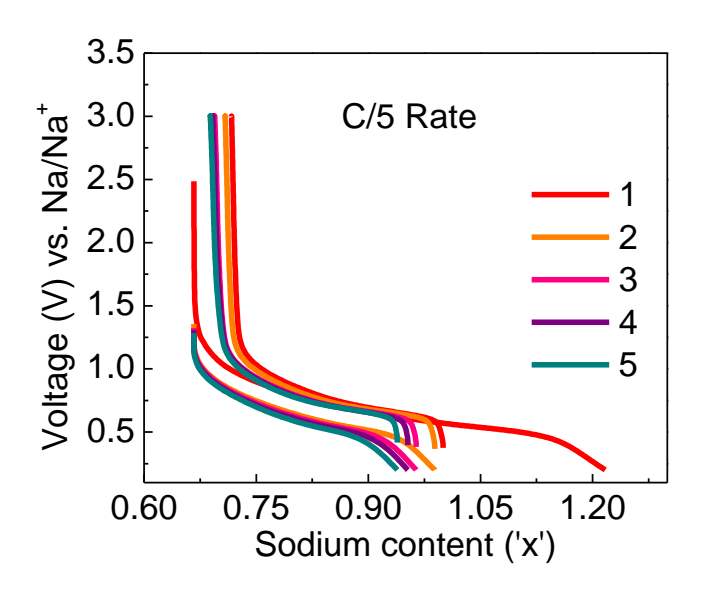


Figure 3.8 Anodic voltage profile of sodium nickel titanate under galvanostatic testing of C/5 rate with 0.2 V cutoff voltage.

During the 1st cycle charging curve, the amount of intercalated sodium is higher than the theoretical capacity (corresponding to 'x'=1) due to irreversible side reactions occurring at highly reductive potentials (E~0.2 V vs. Na/Na⁺), as shown in Figure 3.8. It is anticipated that these degradation reactions are promoted by conductive carbon additive and P2-NT active particles. Nevertheless, the intercalated sodium ions could be extracted in the subsequent discharge cycle indicating that these degradation reactions do not form a blocking surface film. During the subsequent cycles, very little side reaction is observed with full realization of the theoretical capacity in the studied voltage window. The voltage gap between the charge and discharge curves is relatively small even at high charging currents of C/5 indicating that this composition has excellent reversibility in the anodic regime. Ti^{4+/3+} redox couple was found to have a low reduction potential (E°=0.7 V vs. Na/Na⁺) and hence this phase shows promise as low-voltage, intercalation-based anode.

P2-NT has been shown to demonstrate reversible sodium intercalation/de-intercalation reactions using Ni^{2+/4+} and Ti^{4+/3+} redox couples with E^o values of 3.7, and 0.7 V, respectively. This composition can be utilized as a 'bi-functional' electrode due to the large separation in redox potentials of transition metal species in the same composition. The 'bi-functionality' feature allows for the design of 3 V battery devices using the same material as anode and cathode and is anticipated to provide substantial cost-reduction in capital and operating costs by switching over to 'single-line' manufacturing without cross-contamination issues.

3.5.2 Quantifying charge carrier transport processes: DC & AC Testing

The electrical response of mixed conducting pellets with ion-blocking metal electrodes (gold) can be represented using a circuit model that accounts for the two charge carrier transport mechanisms, i.e. electronic and ionic, as illustrated in Figure 3.9a. The ionic conduction rail has circuit elements to account for the resistance to ion hopping within individual grains (R_{ion}), resistance to ion hopping across grains with different orientations (R_{gb}), capacitive contribution at the grain boundary (C_{gb}) and intercalation capacitance (C_{int}). The electronic conduction rail is simplified to a single resistive element with ohmic response (R_{eon}). A capacitive element accounting for the pellet geometric capacitance effects (C_{geom}) by passes the electronic and ionic conduction rails.²⁸

Given that the tested pellets are reasonably thick (2.3 mm), the geometric capacitance rail is ignored as it correlates inversely with the separation distance as given by the expression: $C = \varepsilon_o \varepsilon_r A/d$; where 'C' is the capacitance, ' ε_r ' is the relative permittivity of the pellet, ' ε_o ' is the permittivity of vacuum, 'A' is the pellet cross-sectional area, and 'd' is the pellet thickness.

At the high-frequency limit, the interfacial capacitance and grain boundary capacitance become shorted as the impedance of capacitive elements correlate inversely with AC signal frequency as

given by the expression: $Z_C = 1/j\omega C$, where ' Z_c ' refers to the capacitive impedance, and ' ω ' refers to the angular frequency. Hence, the equivalent circuit gets reduced to Figure 3.9b. At the DC limit (ω =0), all capacitance elements offer very high impedance and the equivalent circuit is reduced to just the electronic conduction rail as shown in Figure 3.9c.

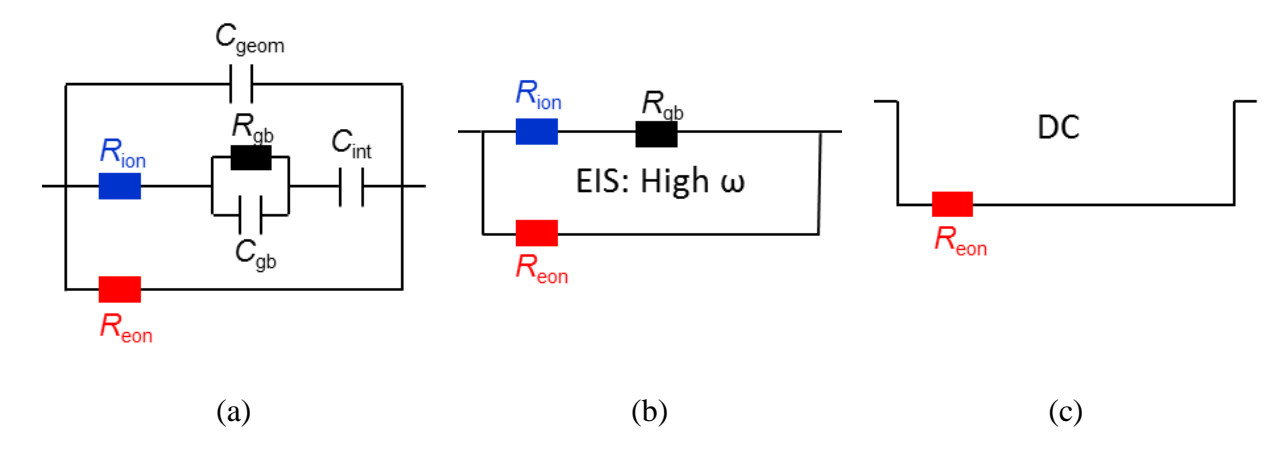


Figure 3.9 (a) Electrical equivalent circuit model representing physical processes in a mixed electronic-ionic conductors with blocking electrodes, (b) Limiting model for high-frequency AC signal, and (c) Limiting model for DC signal. ²⁸

The total conductivity due to all charge carriers (ions and electrons) is estimated from the high frequency intercept of the impedance curves. For the impedance measurement, the impedance curves gets smaller (total conductivity increases) with rising temperature due to an overall enhancement of charge carrier transport processes as shown in Figure 3.10a.

For DC testing, Figure 3.10b. shows the measured current response after applying a step potential of 200 mV. There is an initial capacitive decay and steady state current is attained at longer durations that is related to the steady-state supply of charge carriers. The data is fitted with an exponential curve to extrapolate the steady state current and subsequently obtain electronic conductivity values at different temperatures.

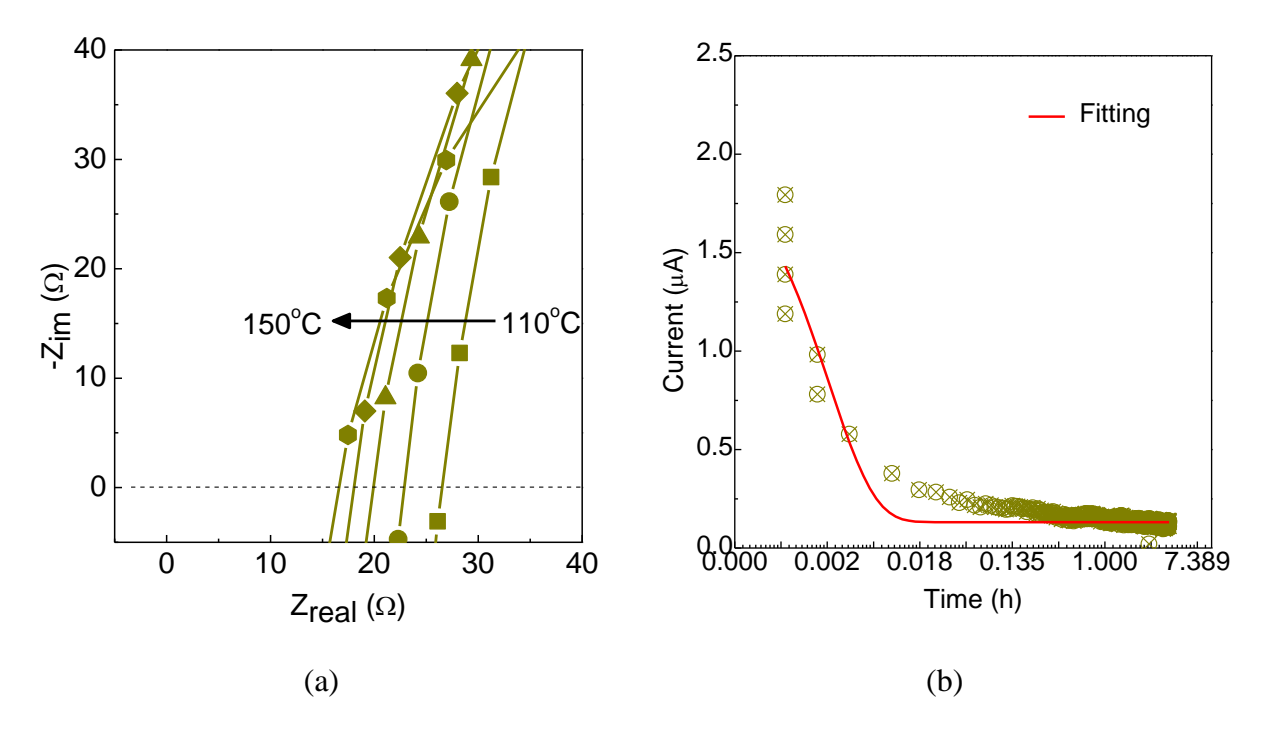


Figure 3.10 Electrical testing of P2-NMT sintered pellet: (a) High-frequency AC impedance spectra in temperature range of 383-423 K with 10 K increments, and (b) Current decay response upon applying a potential of 200 mV at a 383 K.

The total conductivity curves and the electronic conductivity curves obey Arrhenius temperature relation (Figure 3.11). The total conductivity is around 4 orders magnitude higher than the electronic conductivity for both phases. This shows that sodium ions are the dominant charge carriers for these layered materials.

The electronic conductivity of P2-NMT (1.21×10^{-7} S/cm at 110 °C) is higher than P2-NT (3.96×10^{-8} S/cm at 110 °C) with E_a values of 0.574 eV and 0.862 eV, respectively. The charge carrier transport is demonstrated to show a significant improvement by manganese incorporation by providing a percolation network in the transition metal layer. It is also found that P2-NMT has total conductivity of 8.28×10^{-3} S/cm (at 110 °C) with activation energy (E_a) of 0.279 eV while P2-

NT has total conductivity of 4.89×10^{-3} S/cm (at 110 °C) with E_a of 0.296 eV. Manganese addition improves ion transport rate by a factor of 1.7.

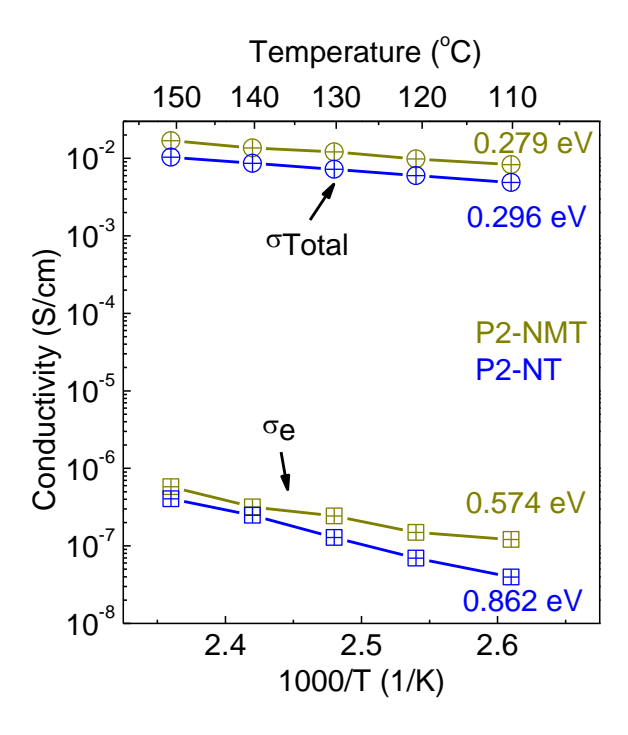


Figure 3.11 Total effective conductivity (ionic and electronic) and electronic conductivity curves as a function of temperature from AC impedance and DC testing.

Nevertheless, the intrinsic electronic conductivity values of both materials are still relatively low and this needs to be addressed (using strategies such as aliovalent doping, elemental substitution, reducing the particle size etc.) to achieve improved electron transport and subsequently better electrochemical properties at high currents. As the conductivities curves follow an Arrhenius correlation and the conductivity values are small, it is likely that there is only a small overlapping of the conduction bands and charge transport is facilitated by hopping of small polarons between localized potential wells (between the 3d transition metal species). A similar conductivity trend was reported for P3-Na_{0.6}[Ni_{0.6}Co_{0.4}]O₂ but with much higher electronic

conductivity values ($\sigma_e > 10^{-2}$ S/cm at 270 K) facilitated by the faster electron hopping via cobalt and nickel atoms. ²⁹

3.5.3 Evaluating ionic transport and interfacial processes: Electrochemical impedance spectroscopy

Electrochemical impedance spectroscopy (EIS) is utilized as a quantitative tool to isolate various sodium-ion transport processes in the composite electrode that have widely separated time constants. It has been demonstrated that the basic electrical circuit elements such as resistors, capacitors and their modified combinations have similar mathematical formulation as physical, chemical and electrochemical processes. For instance, the ion transport in electrolytes can be represented by Equation 3.3 which takes the same mathematical form as an ohmic resistor

$$i_i = Z_i e C_i u_i E = \sigma_i E = E / R_i$$
 3.3

where 'i_i' is the ionic current due to species i, 'Z_i' is the charge of species i, 'e' is the charge of an electron, 'C_i' is the concentration of species i, 'u_i' is the mobility of species i, 'E' is the electric field, ' σ_i ' is the partial conductivity due to species i, and 'R_i' is the ohmic resistance.

Interfacial charge transfer reactions can be represented by a resistive circuit element (referred as charge transfer resistance, 'Rct') and are inversely correlated to the equilibrium exchange current density, 'i₀' as described by Equation 3.4.

$$R_{ct} = RT/nFi_o 3.4$$

where 'R' is the molar gas constant, 'T' is the temperature, 'n' is the number of electrons transferred, and 'F' is the Faraday's constant.

These circuit elements are applied for emulating the multi-time scale physicochemical processes and interpreting impedance spectra data. Assigning different parameters to various physicochemical processes permits identification of the bottleneck processes. However, several circuit models can provide a good match to the experimental spectra and the selected model needs to have reasonable physical meaning for accurate interpretation. This requires a priori knowledge of the basic processes for a given system and state-of-the-art models for similar materials.

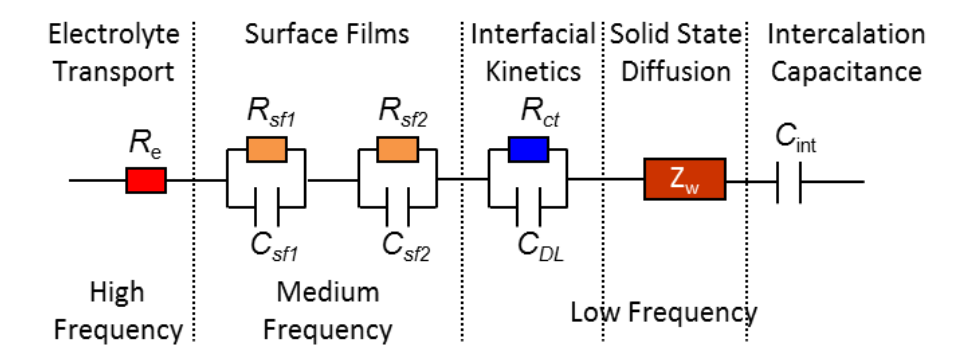


Figure 3.12 Electrical equivalent circuit model depicting sodium ion transport processes (within liquid electrolyte, across surface films, across the interface, and bulk solid state diffusion) of the composite electrode; where Re is the electrolyte resistance, Rsf is the surface film resistance, CPE_{sf} is the constant phase element due to surface films, CPE_{ct} is the constant phase element due to the double layer, and Z_w is the semi-infinite Warburg diffusional element.

The impedance curves of Na-intercalation electrodes are analyzed using an analogous circuit model developed previously to interpret lithium intercalation phenomenon in graphite and lithium transition metal oxides³⁰⁻³² as depicted in Figure 3.12. Nyquist plots of P2-NT and P2-NMT electrodes display the following features: two over-lapping semi-circles in the high frequency domain, one semi-circle in the medium frequency domain and a small diffusion tail at the low frequency domain (depending on the electrode potential) as seen in Figure 3.13. The semi-circles at the high and medium frequency region are attributed to the relatively fast transport of sodium

ions through the surface films at the film/electrolyte interface (at active material and sodium metal), coupled with film capacitance. These surface films can be formed on the pristine material due to interaction with atmospheric CO_2 or decomposition of electrolyte constituents during sodium intercalation/de-intercalation and have been reported for intercalation materials.³⁰ The capacitance has been modeled using a constant phase element (CPE) to account for the depressed semi-circles formed possibly due to surface heterogeneities. The effective capacitance (C) is calculated using the relation, $C=Q^{1/\alpha}R^{(1/\alpha-1)}$; where 'Q' and ' α ' are the CPE fitting parameters and 'R' is the resistance fitting parameter.

The low frequency semi-circle is assigned to the interfacial charge transfer of sodium ions (R_{ct}), coupled with capacitance (C_{ct}) at the electrode/surface film interface. The analysis of the impedance spectra was performed using Zview impedance analysis software (Scribner Associates Inc., Southern Pines, NC). Non-linear Least Square fitting (NLLS) provides a good fitting of the experimental data as seen in Figure 3.13. The linear tail region in the low frequency region is attributed to diffusion phenomenon discussed subsequently.

The C_{ct} is measured to be in the order of few mF, much higher than the film capacitance (10^{-4} - 10^{-6} F) as seen in Figure 3.14a. The true surface areas of the porous electrode particles are much higher than the geometric area and hence we get these high capacitance values. The film capacitance values are in the range of μ F as they correspond to surface film/electrolyte interface as seen in Figure 3.14b.

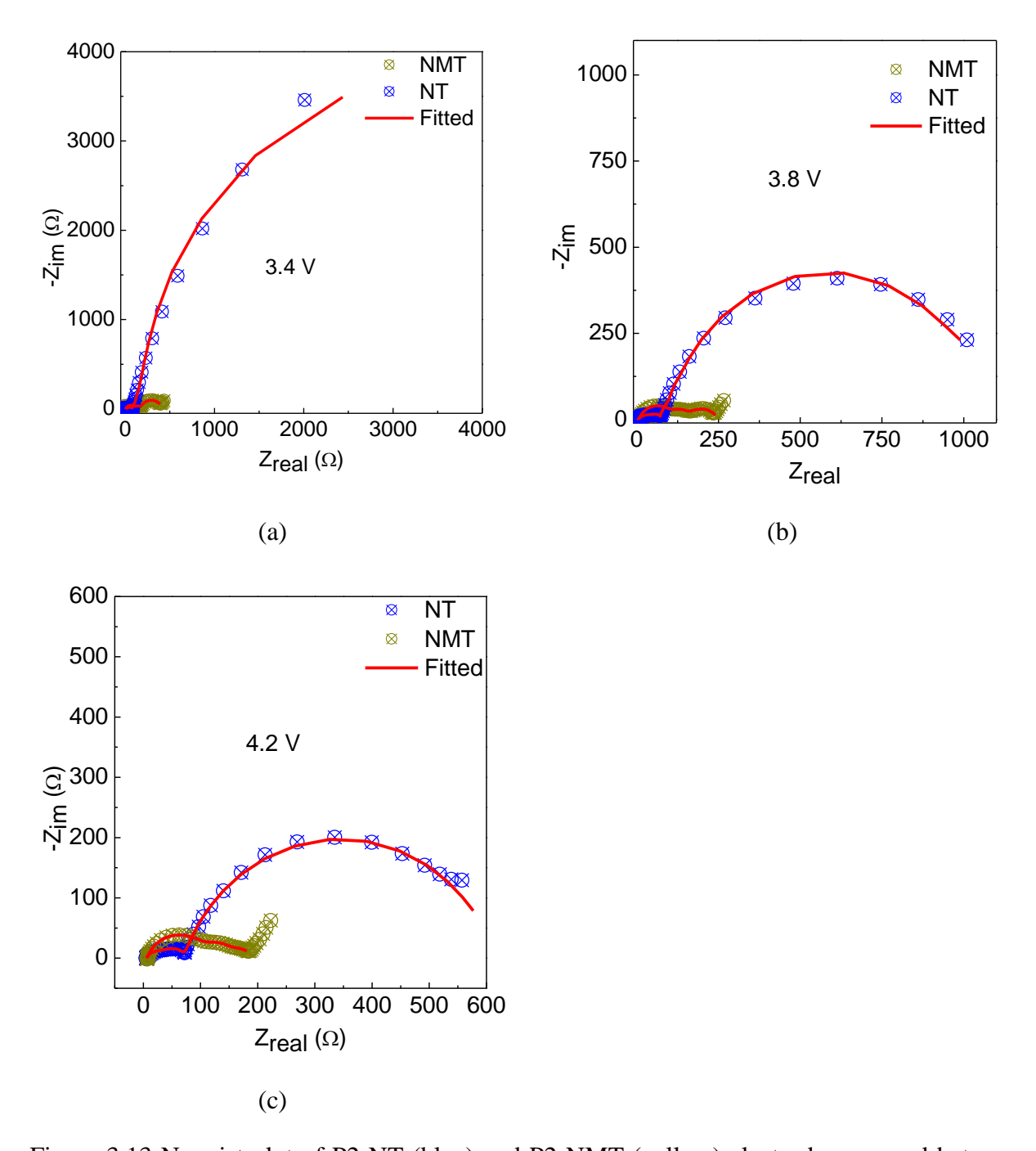


Figure 3.13 Nyquist plot of P2-NT (blue) and P2-NMT (yellow) electrodes scanned between frequency range of 5 MHz to 10 mHz with inset showing high-frequency depressed semicircles at voltage of (a) $3.4~V~vs.~Na/Na^+$, (b) $3.8~V~vs.~Na/Na^+$, and (c) $4.2~V~vs.~Na/Na^+$.

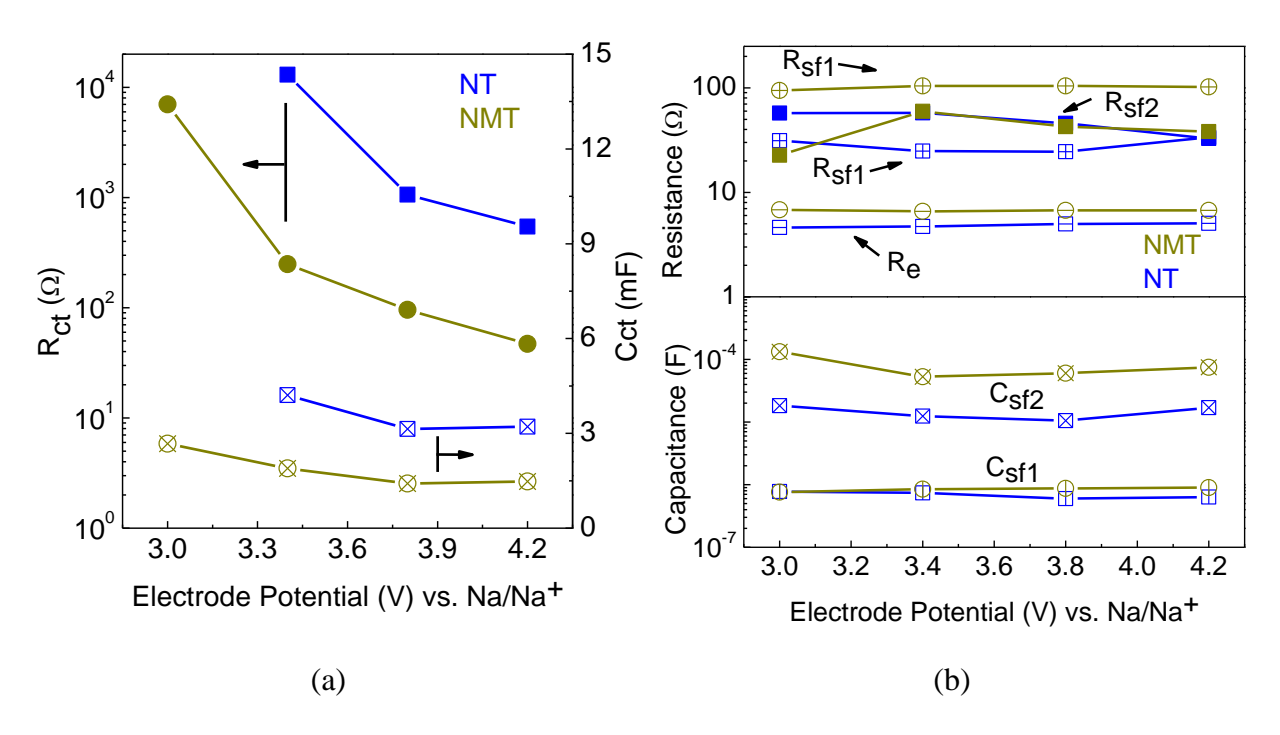


Figure 3.14 Potential dependence of (a) charge transfer resistance and double layer capacitance, and (b) surface film resistance and surface film capacitances.

Figure 3.14a shows that the interfacial charge transfer resistance (R_{ct}), for both P2-NT and P2-NMT, has a strong dependence on electrode potential and decreases by several orders of magnitude as the electrode potential increases from 3.0 to 4.2 V. At highly oxidative potentials, the increased amount of Ni⁴⁺/Ni²⁺ states allows for enhanced mobility of the charge carriers (between these multivalent states) resulting in faster interfacial kinetics. Similar strong correlation of interfacial kinetics with electrode potential has been previously observed for Li_{1-x}CoO₂ electrodes. Also, it is found that the R_{ct} of P2-NMT is considerably smaller than P2-NT over the complete range of measured electrode potentials indicating that the former material supports faster interfacial transfer than the latter. This trend aligns with the polaron attributed electronic conductivity boasting mechanism discussed previously. The associated double-layer capacitance values (C_{ct}) remains fairly independent of the electrode potentials and is comparable for both materials. This is

anticipated as the electrode surface area does not change significantly during sodium deintercalation. The electrolyte resistance is invariant with electrode potential as the concentration of sodium ions is constant. The surface film resistances (R_{sl1} and R_{sf2}) and surface film capacitances (C_{sf1} and C_{sf2}) are largely invariant with electrode potential suggesting that these films are fairly stable and do not change significantly in their chemical make-up/composition (that can affect the dielectric constant) and film thickness in the high voltage region.

The solid state diffusion of sodium ions within the active particles contributes to the Warburg response in the low frequency domain as seen by the characteristic linear response in the Nyquist plots (45° tails) depicted in Figure 3.13b and c (seen distinctly for P2-NMT). We make use of the conventional planar diffusion model, typically used to simulate intercalation electrodes, to interpret the experimental data. The imaginary and real components of the impedance can be expressed as Equation 3.5 and Equation 3.6:

$$-Z_j = \frac{V_m dE dx}{AF\sqrt{2\widetilde{D}}} \omega^{-1/2} = A_W \omega^{-1/2}$$
3.5

$$Z_{real} = \frac{V_m dE dx}{AF\sqrt{2\widetilde{D}}} \omega^{-1/2} = A_W \omega^{-1/2}$$
 3.6

where ' Z_j ' is the imaginary impedance, ' Z_{real} ' is the real impedance, ' V_m ' is the molar volume, 'dEdx' is the slope of the voltage-composition curve, 'A' is the surface area of the electrode, 'F' is the Faraday constant, ' \widetilde{D} ' is the chemical diffusion co-efficient, ' ω ' is the angular frequency, and ' A_w ' is the Warburg pre-factor.

The Warburg pre-factor (A_W) is estimated from linear fitting of the experimental data as shown in Figure 3.15 The average of A_W from the real and imaginary part of impedance was used to obtain the apparent chemical diffusion coefficient of sodium ions in the host materials.

The impedance curves of P2-NT (all measured voltages) and P2-NMT at 3.0 V do not show a distinctive diffusion tail (within the measured frequency domain) and hence are not considered for further analysis. This is because the slow interfacial kinetics overshadows the diffusion process. The measured 'D' values for P2-NMT, from EIS, are reasonably high (Mean D=9.1×10⁻¹³ cm²/s), as typical of intercalation electrodes. Further discussion of the diffusion co-efficients is provided in the subsequent electroanalytical section.

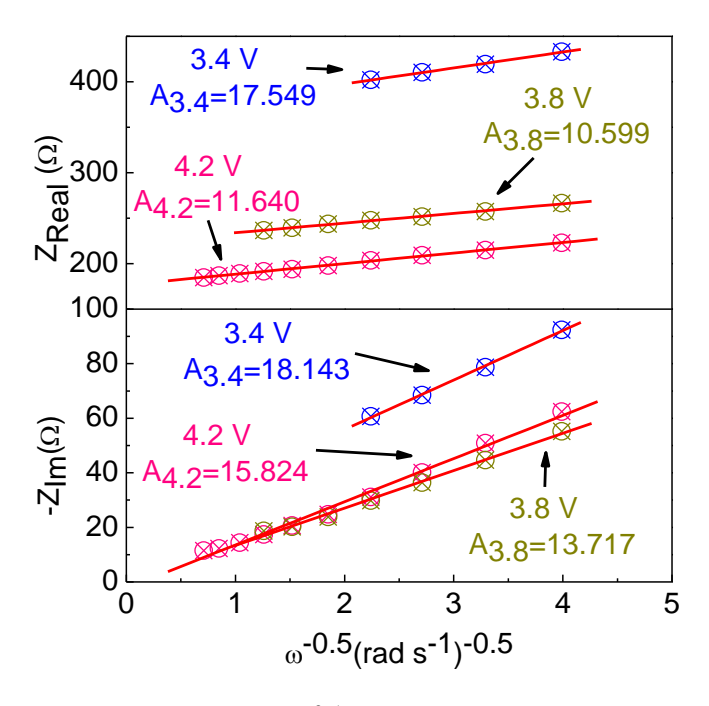


Figure 3.15 Linear fitting of Zreal vs. $\omega^{\text{-0.5}}$ curves using planar diffusion model to obtain Warburg prefactor.

3.5.4 Analyzing ionic transport processes: Potentiostatic intermittent titration technique

Potentiostatic Intermittent Titration technique (PITT) provides a complimentary method to evaluate the diffusional properties of the studied materials. Low limitation currents of C/100 were imposed to approach close-to-equilibrium conditions. The electrodes were subjected to initial precycling at C/10 rate before the PITT experiments (as depicted in inset of Figure 3.16a and b). The voltage profiles of P2-NT and P2-NMT materials are fairly comparable to galvanostatic testing. P2-NT has a solid solution behavior evidenced by the sloping voltage trend when cycled with voltage limit of 4.2 V. It has a low faradaic efficiency as the low limiting current values feed the irreversible side reactions. P2-NMT has sloping voltage profile till 4.1 V after which a plateau is noticed.

The PITT voltage profile of P2-NT material in the anodic regime (Figure 3.16c) has significantly large irreversible capacity loss compared to the galvanostatic testing. The increase in side reactions at slower charging rate suggests that these side reactions are catalyzed chemically at these reductive potentials rather than electrochemical mechanisms. Long-time approximation method is used to extract diffusional information from PITT measurements. Kinetic limitations, that are noticeable in the impedance analysis, are overcome by using a relatively long relaxation time (current drops to C/100) between the incremental steps. The expression for current transient upon impressing a constant potential is given by Equation 3.7.

$$I(t) = \frac{2Q'\widetilde{D}}{L^2} exp\left(\frac{-\pi^2\widetilde{D}t}{4L^2}\right)$$
3.7

where I(t) is the measured current transient, Q' is the charge passed during the incremental potential step, \widetilde{D} is the chemical diffusion co-efficient, L is the diffusion length scale, and t is the time taken for relaxation.

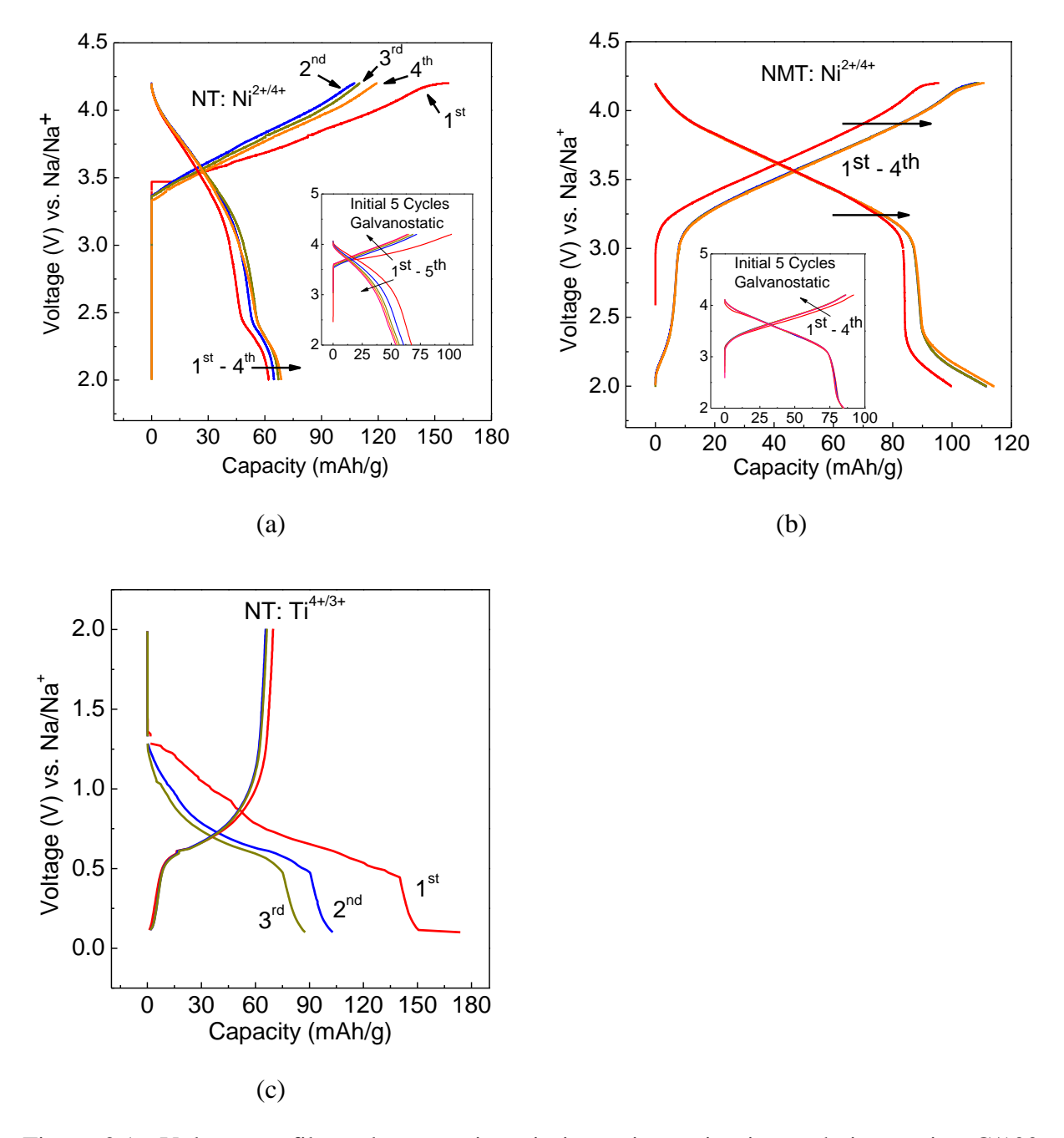


Figure 3.16 Voltage profile under potentiostatic intermittent titration technique using C/100 current limitation for (a) cathodic P2-NT with 5 mV voltage step, and (b) cathodic P2-NMT with 5 mV voltage step, and (c) anodic P2-NT with 15 mV voltage step; inset in cathodic curves depict electrode precycling at C/10 rate.

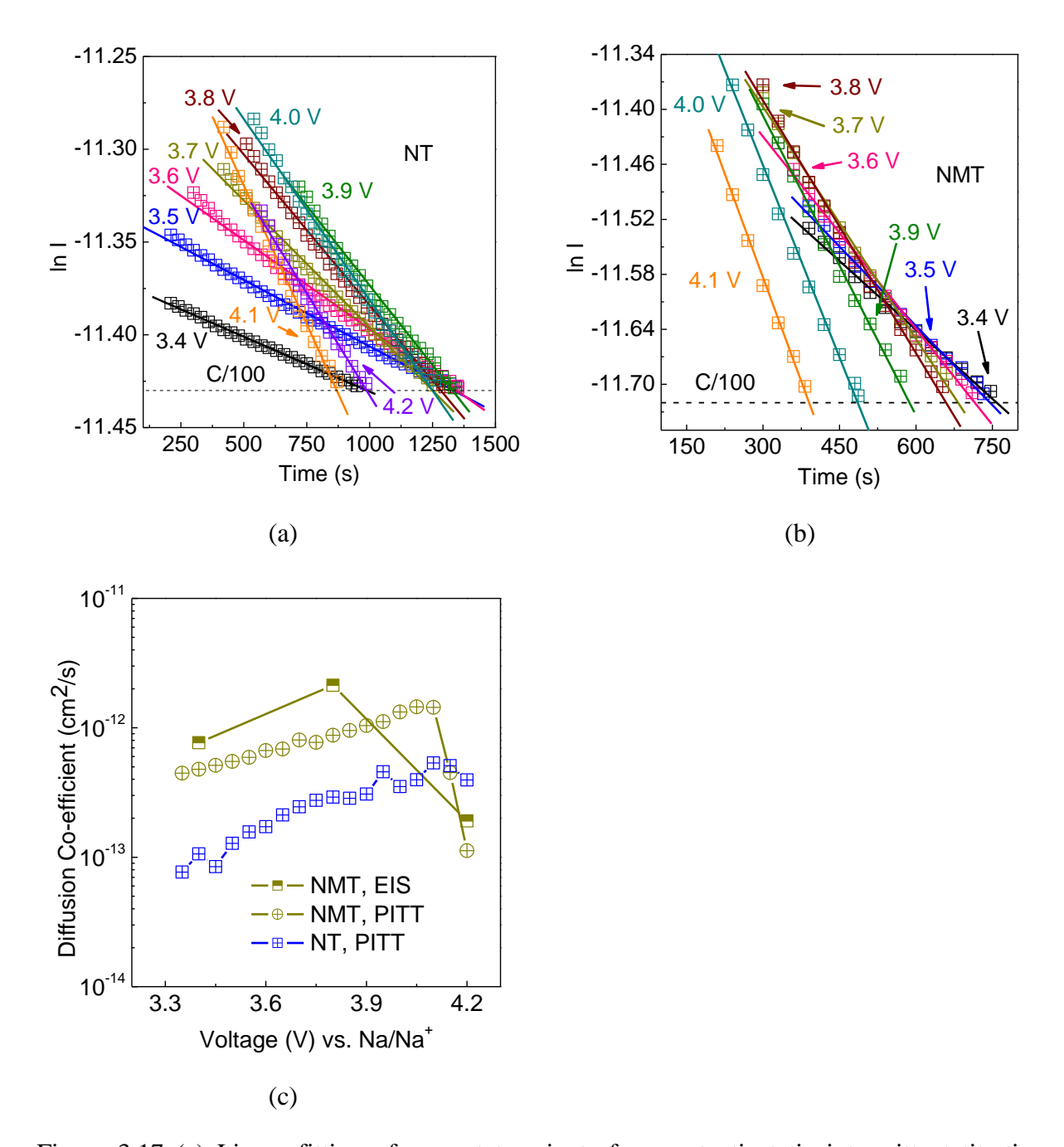


Figure 3.17 (a) Linear fitting of current transients from potentiostatic intermittent titration technique at different electrode potentials with current limitation of C/100 for cathodic P2-NT electrode, (b) linear fitting of P2-NMT electrode under identical conditions, and (c) variation of apparent chemical diffusion co-efficient with electrode potential as calculated from potentiostatic intermittent titration technique and impedance spectroscopy.

Figure 3.17a and b displays the linearity of the experimental data for both NT and NMT materials validating the use of this PITT model and the slope is used to estimate the diffusion coefficients. The estimated 'D' values are reasonably high (10⁻¹²-10⁻¹³ cm²/s) and comparable to EIS estimates. The diffusivity of P2-NMT increases with voltage and falls off at 4.2 V as evident from the PITT and EIS estimations in Figure 3.17c. P2-NT also follows a similar rising trend with voltage. This can be rationalized by the fact that sodium diffusivity increases due to the creation of additional sodium vacancies. However, it is likely that the low concentration of sodium ions charge carriers leads to diffusivity drop at high voltages. The diffusivity dip of P2-NMT also gets convoluted by the presence of additional phases that form at high charging voltage leading to breakdown of current-transient model assumptions.

3.5.5 Understanding reaction mechanisms: Ex-situ XRD Testing

Ex-situ XRD testing on the P2-NT film electrodes at different stages of charging shows that the material retains its P2-layered structure during sodium removal as shown in Figure 3.18a. The dominant peak at 2θ of 16° starts to shift towards lower angles indicating that the structure starts to expand along the c-direction (inset in Figure 3.19a). As sodium content decreases in these P2 materials, the oxygen atoms in the adjacent layers start experiencing increased repulsive interactions contributing to the expansion along the c-axis. A solid-solution reaction mechanism till charging voltage of 4.2 V without any phase change is confirmed by the XRD results. However, when the charging voltage is increased to 4.5 V, an unidentified phase possibly related to O-type structure forms (Figure 3.18b) and this phase change responsible for poor reversibility in the high voltage region.

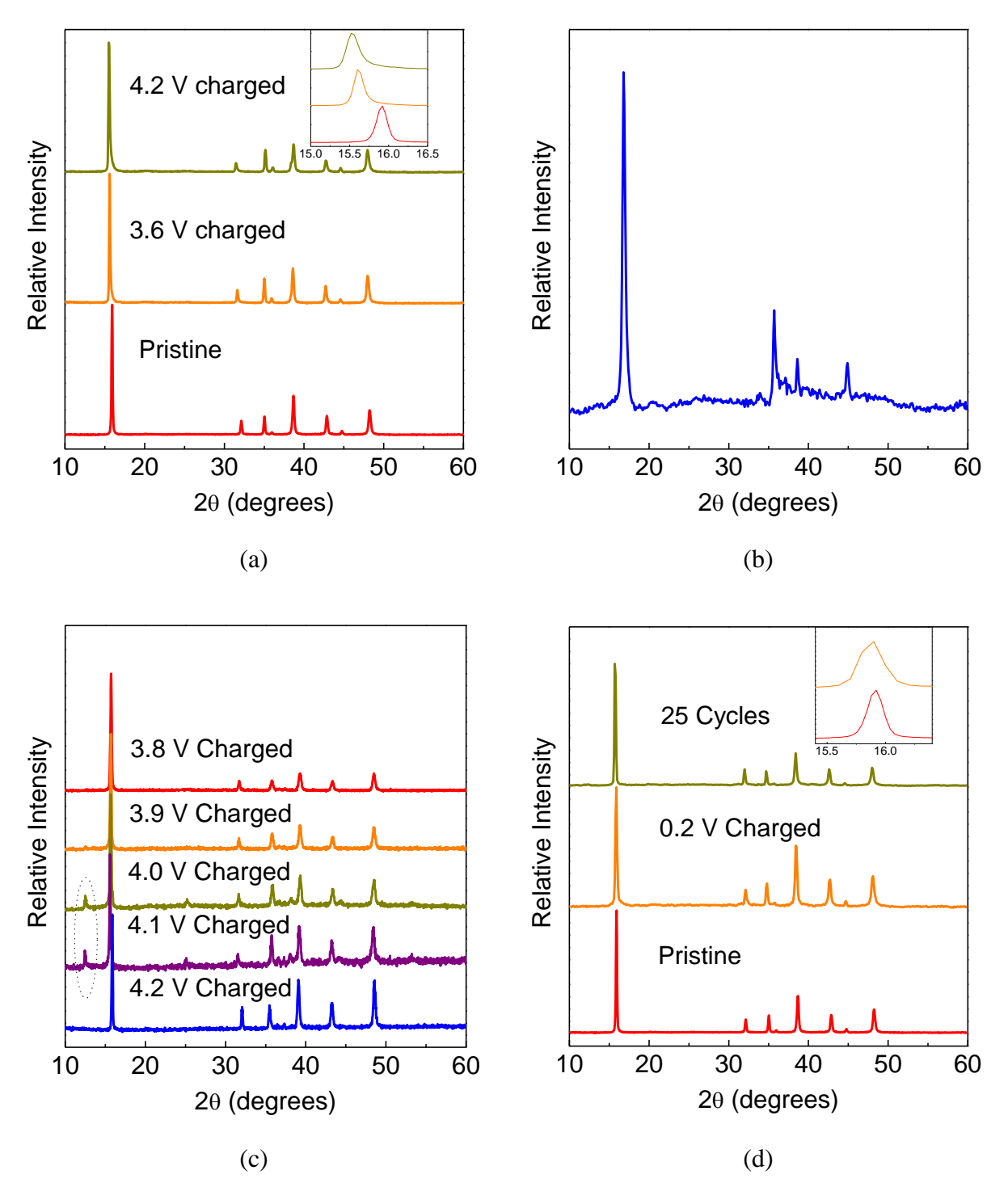


Figure 3.18 Ex-situ XRD of electrode films: (a) sodium nickel titanate cathode charged till 4.2 V with inset showing the evolution of 160 reflection, (b) sodium nickel titanate cathode charged to 4.5 V, (c) sodium nickel manganese titanate cathode charged till 4.2 V, and (d) sodium nickel titanate anode charged to 0.2 V with inset showing evolution of 16° reflection; all potentials are measured with respect to Na/Na⁺.

P2-NMT also demonstrates a solid-solution mechanism till charging voltage of 4.0 V where the pristine phase peaks are retained as seen from Figure 3.18c. Removing further sodium leads to formation of a low-angle peak at 12.5°. During subsequent sodium intercalation, this peak vanishes and the film returns to its initial state suggesting good reversibility. This is possibly due to sodium ordering processes along the c-direction.

P2-NT electrode in the anodic regime appears fairly stable without the formation of any metallic components (such as nickel, titanium) confirming that the low-voltage reactions are due to intercalation mechanism as shown in Figure 3.18d. Very little change in peak positions (16°) suggests that the lattice parameters of the fully intercalated phase is fairly comparable to that of the pristine phase. The XRD pattern of the cycled electrode also remains identical to the pristine phase suggesting that the material does not degrade significantly during the electrochemical cycling.

3.5.6 Evaluating capacity retention

3.5.6.1 Cycling Study

Capacity retention during repeated charge/discharge cycles is essential to designing long-life battery devices. However, it is found that the repeated intercalation/de-intercalation processes contributes causes mechanical strain effects as a result of host-intercalant interactions leading to capacity fade. Other fade mechanisms include electrolyte degradation, dissolution of active materials, defect formations, etc.³⁶ The cycling study in this research work is limited to half-cell testing that poses inherent limitations due to sodium dendritic formation.

In the cathodic regime, the faradaic efficiency of the P2-NT phase is poor in the initial few cycles and it improves subsequent cycling. The discharge capacity is found to be fairly stable

during the tested 30 cycles as shown in Figure 3.19a P2-NMT phase has an initial stabilization period of 10 cycles after which it shows excellent charge retention with no loss in discharge capacity between 11th and 50th cycle. Figure 3.19b illustrates that the faradaic efficiency of NMT phase is fairly close to 100%. The initial stabilization phase is attributed to electrolyte side reactions. The excellent capacity retention of the P2 materials in cathodic regime, even in half-cell testing, is due to the very small volume expansion as reported for similar structures.³⁷ Since the material does not undergo significant strain during sodium exchange processes, the active particles remain fairly intact and contribute to good cycling performance. These compositions show promise for designing long-life, intercalation host electrodes.

In the anodic regime, P2-NT phase shows a continuous capacity fade as observed in Figure 3.19c. Considering that the XRD patterns of the cycled electrode remained identical to the pristine phase, this capacity fade is not associated with bulk structural changes that would lead to loss of crystallinity. We predict that this is due to electrolyte degradation at the low potentials that gets catalyzed by nickel atoms in this P2 composition. Recently a lithiated P2 phase with identical prototypical structure has been shown to have excellent capacity retention.³⁷ Future work would need to focus on identifying electrolyte degradation components using spectroscopic characterization techniques. This would isolate the solvent component that is responsible for the fade mechanism and enable development of better electrolyte combinations.

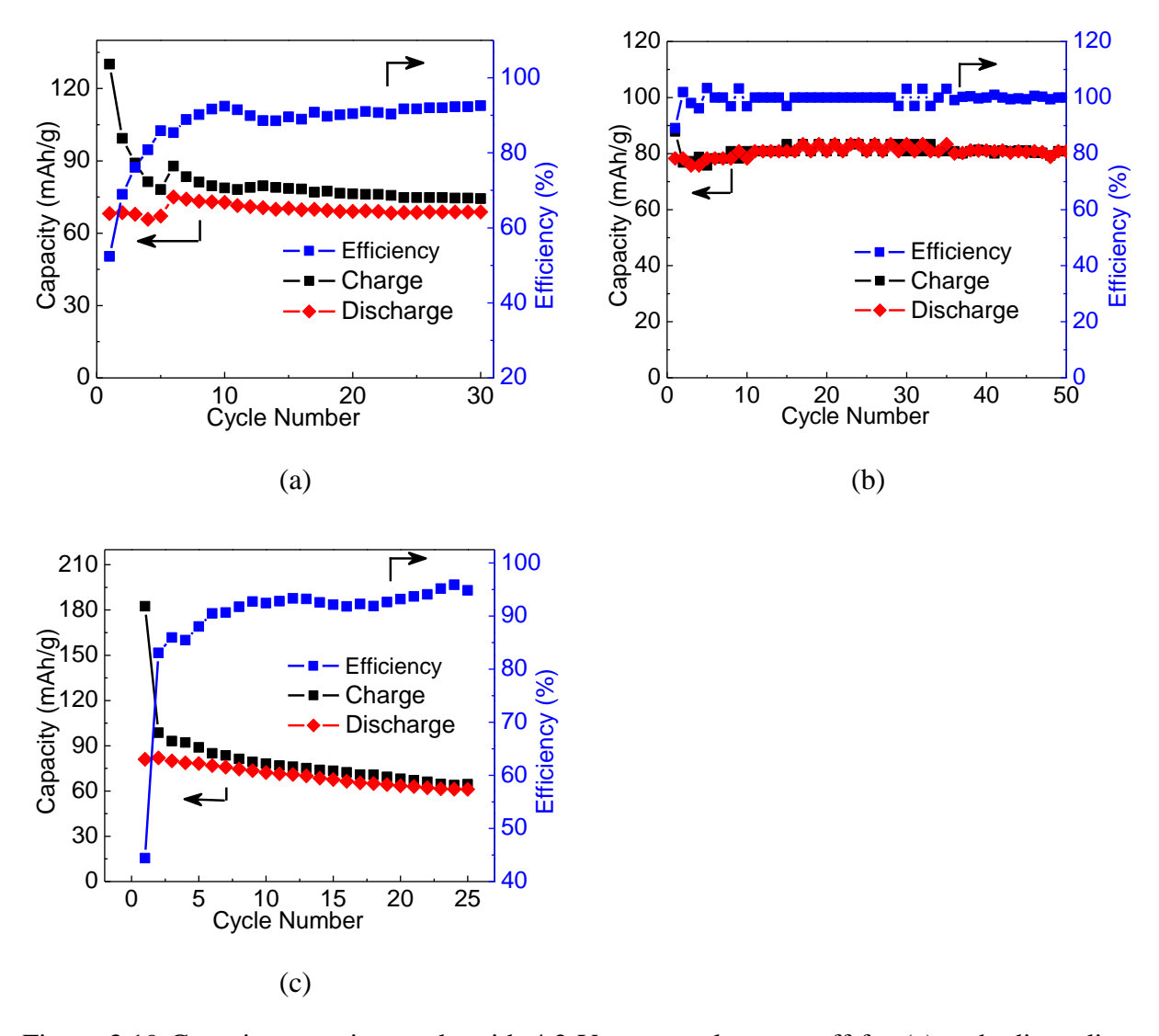


Figure 3.19 Capacity retention study with 4.2 V upper voltage cutoff for (a) cathodic sodium nickel titanate at C/10 rate, (b) cathodic sodium nickel manganese titanate electrodes tested at C/5 rate, and (c) anodic sodium nickel titanate tested at C/5 rate.

3.5.6.2 Impedance change during cycling

Impedance spectra of P2-NMT phase was analyzed during the cycling test after the charging the electrodes to 4.2 V as shown in Figure 3.20a. The curves remain fairly consistent suggesting that the underlying physicochemical processes are identical for the pristine and cycled electrode.

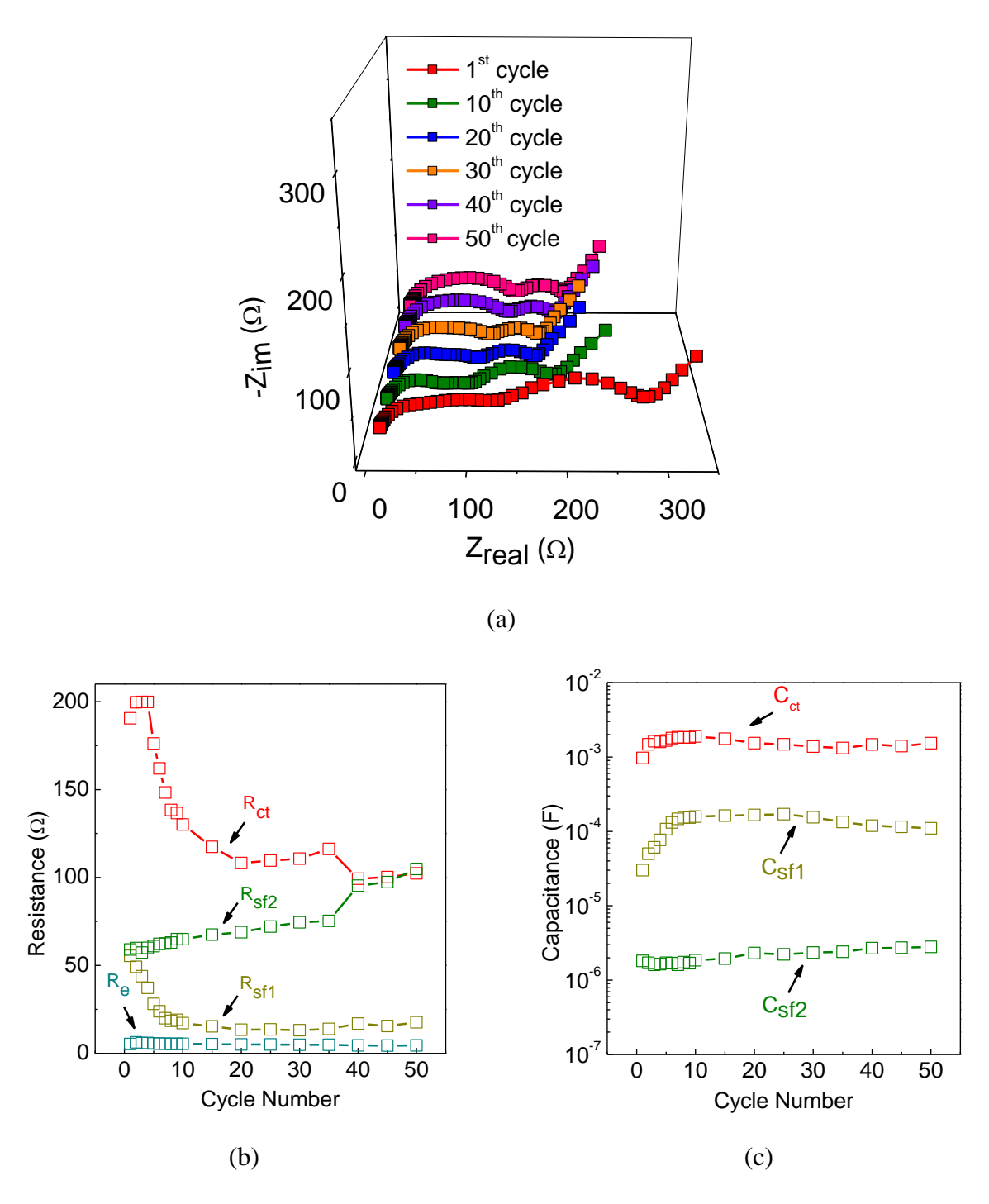


Figure 3.20 (a) Nyquist impedance spectroscopy plot of sodium nickel manganese titanate electrode scanned in frequency range of 5 MHz to 10 mHz after charging to 4.2 V, (b) variation of impedance resistive parameters, and (c) capacitive parameters during cycling.

The electrolyte resistance, from the high-frequency intercept, was found to be invariant during the electrode cycling as shown in Figure 3.20b. Even though the electrolyte composition is not optimized and sodium metal still reacts with the solvent, those effects did not affect the ionic conductivity considerably. The interfacial charge transfer resistance, after the initial stabilization period, remains invariant. The surface film resistances show only minor fluctuations during the testing. The invariant double-layer capacitance can be correlated to the stable surface area of the active particles, while the invariant surface film capacitance correlates to insignificant change to the dielectric properties of the surface films (Figure 3.20c). These suggests that the side reactions get arrested after the initial cycles and a relatively stable passivation film (SEI) gets formed at the electrode/electrolyte interface.

3.5.7 Rate performance testing

Cathodic P2-NT material prepared from nano-sized precursors provides capacity values of 81 mAh/g, 77 mAh/g, 68 mAh/g, 34 mAh/g, and 9 mAh/g at C/20, C/10, C/5, 1C, and 2C rates, respectively, as shown in Figure 3.21a. Cathodic P2-NT material prepared from micron-sized precursors yielded capacity values of 60 mAh/g, 53 mAh/g, 45 mAh/g, 17 mAh/g and 3 mAh/g at C/20, C/10, C/5, 1C and 2C, respectively. The cathodic P2-NT powders with smaller particle size delivers higher capacity values due to shorter charge-carrier transport length scales.

It was also found that P2-NMT material (micron-sized precursors) provides capacity values of 90 mAh/g, 80 mAh/g, 65 mAh/g, 54 mAh/g and 40 mAh/g at C/20, C/10, C/5, 1C and 2C, respectively (Figure 3.21b). Under identical processing and calcination conditions, P2-NMT phase clearly has improved capacity retention and is more suitable for high power applications. As discussed in the previous sections, this capacity boast with manganese substitution is attributed to accelerated interfacial kinetics of sodium ion transfer at the electrode/electrolyte interface,

relatively unhindered electron hopping facilitated between manganese and nickel sites, and higher diffusivity of sodium ions as demonstrated from EIS, DC measurements and PITT analysis.

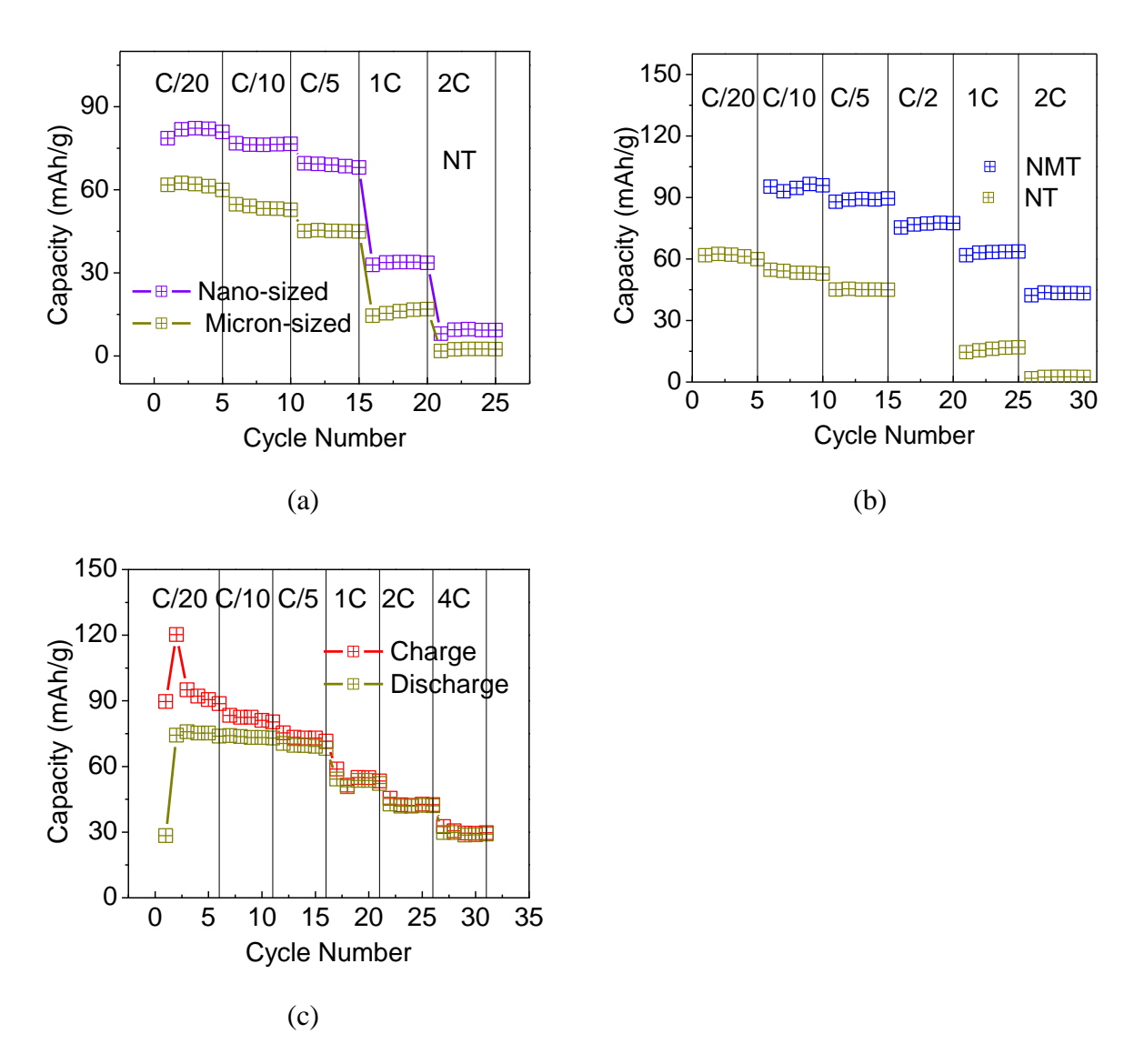


Figure 3.21 High-current rate testing of (a) cathodic sodium nickel titanate powders with micron- and nano-sized powders, (b) cathodic sodium nickel titanate and sodium nickel manganese titanate electrodes with 4.2 V cutoff, and (c) anodic sodium nickel titanate with cutoff voltage of 0.2 V.

.

Anodic P2-NT furnishes capacity values of 75 mAh/g, 73 mAh/g, 70 mAh/g, 53 mAh/g, 43 mAh/g, and 30 mAh/g at charging rates of C/20, C/10, C/5, 1C, 2C, and 4C respectively (Figure

3.21c). These values are significantly better than those in the cathodic region for the same composition. The improved rate performance in the anodic region is due to the presence of large number of titanium atoms, i.e. 2/3 of Ti compared to 1/3 of Ni, forming a percolating network leading to enhanced electron conduction (due to $Ti^{4+/3+}$) in the transition metal layer.

3.6 Improving cathodic stability: Calcium substitution

During charging, the sodium content becomes reduced in the layered host materials and this leads to excessive unfavorable repulsive interactions and phase change. This limits the electrochemical window and also leads to loss of reversible capacity. The scope of this preliminary study was to potentially stabilize the layered oxides using calcium substitution. Calcium is anticipated to occupy the sodium layer and provide structural stability at high charging voltages.

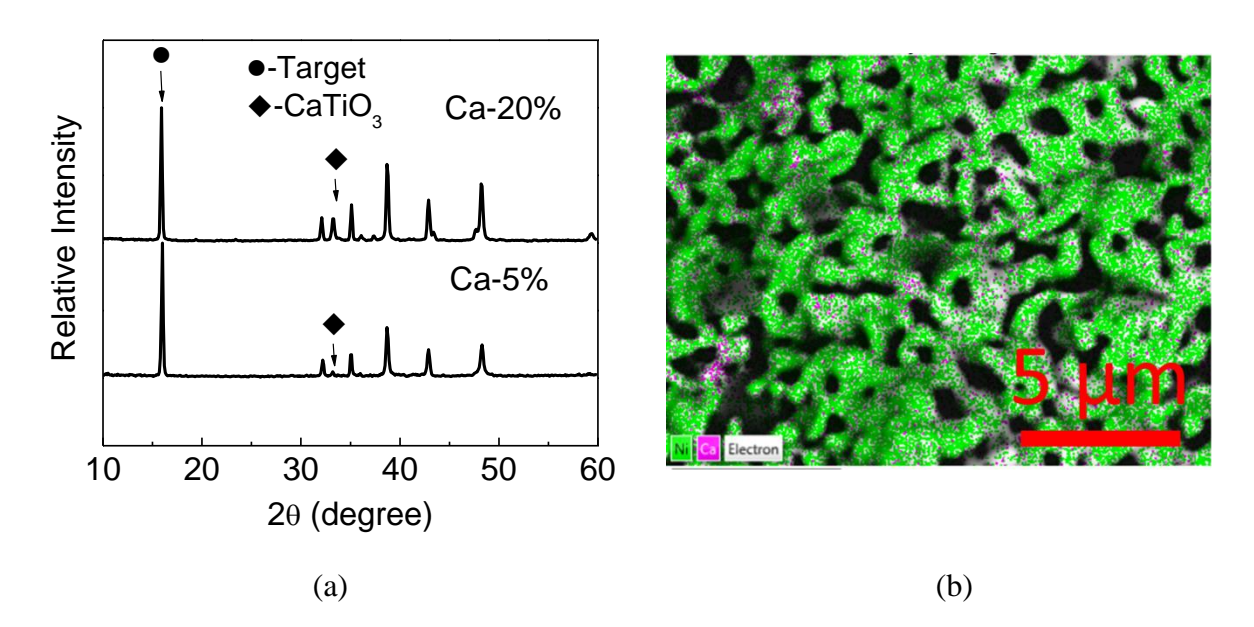


Figure 3.22 (a) XRD characterization of 5% and 20% calcium substituted sodium nickel titanate prepared by solid-state reaction at 900 °C, and (b) EDS mapping of 5% sodium nickel titanate powders to check calcium distribution.

Sodium was partially replaced with calcium to prepare target compositions of [Na_{0.53}Ca_{0.07}][Ni_{0.33}Ti_{0.67}]O₂ (20% calcium substituted) and [Na_{0.63}Ca_{0.02}][Ni_{0.33}Ti_{0.67}]O₂ (5% calcium substituted). The stoichiometric precursors consisting of Na₂CO₃, nano-NiO, nano-TiO₂ and CaO (99.9%) were wet milled as discussed before and fired at 900 °C.

The XRD patterns of 20% Ca-substituted material indicated that the calcium did not get incorporated in the layered structure and formed a perovskite secondary phase with composition CaTiO₃ (ICSD reference code: 88-0790) as seen in Figure 3.22a. The powders prepared with a lower 5% calcium content also displayed the characteristic perovskite peaks. EDS mapping was performed on the 5% calcium-powders to check the overall distribution of calcium as seen purple spots in Figure 3.22b. Nickel distribution is overlayed as an internal standard.

The calcium distribution is found to be fairly uniform without significant enrichment due to perovskite particles. This suggests the possibility of low-level calcium substitution or perovskite phase forming a thin coating on all the particles. Since we did not have a solid evidence for calcium forming a solid solution, these powders were not electrochemically characterized. Nevertheless, a recent research study supports the concept of calcium-attributed stabilization in isostructural $Na_{0.7}CoO_2$ with significantly improved capacity retention.³⁸

3.7 Improving anodic capacity: Potassium substitution

The anodic capacity of the P2-NT phase is limited by the number of available vacant sites in the structure; 1 mole of Na_{2/3}[Ni_{1/3}Ti_{2/3}]O₂ has 1/3 unoccupied '2b' and '2d' sites limiting the theoretical capacity to 90 mAh/g. Recently, a lithiated P2 phase, Na_{2/3}[Li_{1/3}Ti_{2/3}]O₂, was found to have excellent electrochemical properties in the anodic regime.³⁷ For these P2 non-stoichiometric

materials, even a modest increase in vacancy concentration would provide a significant boast to the sodium intercalation capacities as seen from Table 3.1.

Table 3.1 Theoretical capacity of P2-titanate materials based on vacancy concentration.

Composition	Vacancy (1-x)	Theoretical capacity (mAh/g)	Molar mass (g/mol)
Na _{0.67} [Li _{0.33} Ti _{0.67}]O ₂	0.33	105.9	86.0
Na _{0.55} [Li _{0.18} Ti _{0.82}]O ₂	0.45	141.9	85.0
Na _{0.5} [Li _{0.17} Ti _{0.83}]O ₂	0.50	158.5	84.5

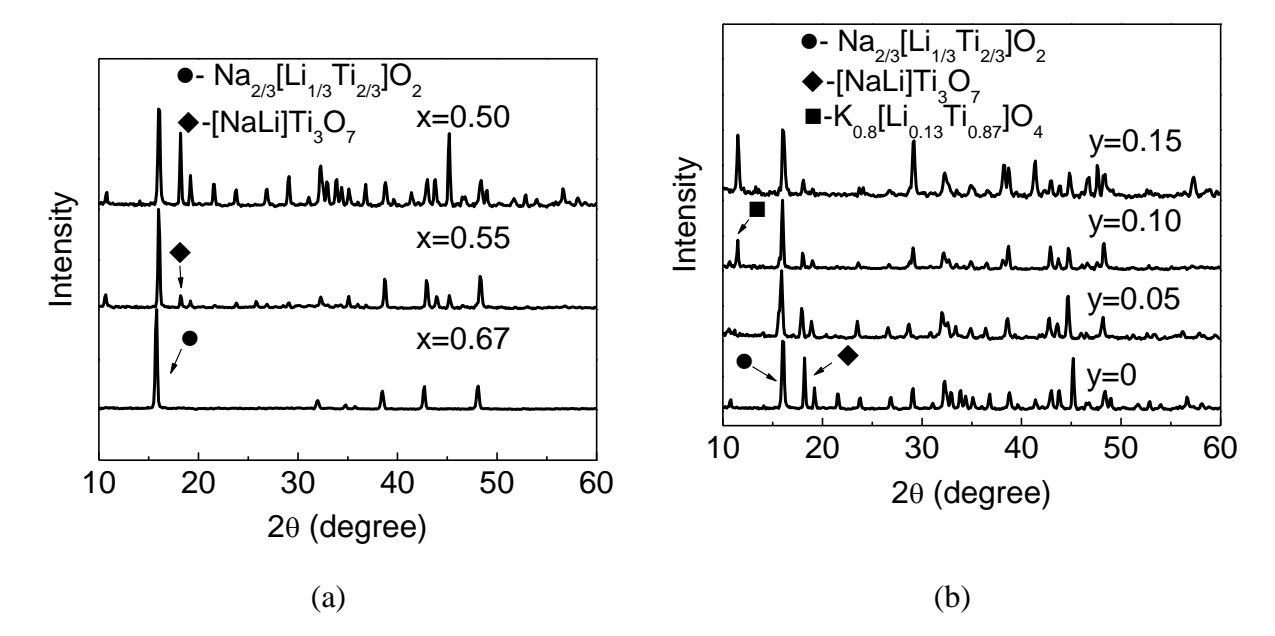


Figure 3.23 XRD characterization of powders to synthesize (a) sodium deficient compositions with x=0.67, 0.55 and 0.50 at firing temperature of 1000 °C for 20 h duration, and (b) $Na_{2/3-y}K_y$ [Li_{1/3}Ti_{2/3}]O₂ for y=0, 0.05, 0.10 and 0.15 prepared at firing temperature of 800°C for 20 h.

Solid-state synthetic technique was utilized to prepare the aforementioned low sodium content phases with theoretical capacity of \sim 158 mAh/g, i.e. 75% higher than the pristine phase. The pristine lithiated phase (x=0.67) was successfully prepared with solid-state synthesis technique by firing the precursor powders at 1000 °C for net duration for 20 hours; the calcined powders were

ground after heating for 10 hours to promote powder homogeneity and fired for additional 10 hours. Figure 3.23a confirms that the prepared powders of the pristine phase were phase-pure.

Sodium deficient phases (x=0.55 and x=0.50) were prepared by identical methods but resulted in the formation of [NaLi]Ti₃O₇ impurity phase (ICSD reference: 52-0690). This is due to structural destabilization due to increased alkali layer spacing. Samples were prepared with potassium contents of 0, 0.05, 0.1, and 0.15 by firing at 1000°C.

Potassium is studied as a potential stabilizer due to large A-O bond length and its preference for prismatic co-ordination. Solid-state synthetic method was utilized to prepare potassium substituted compositions, $[Na_{0.5-x}K_x][Li_{0.17}Ti_{0.83}]O_2$ (x=0.05, 0.10, and 0.15). However, it was found that potassium does not show solubility in the studied material and tunnel-type impurity phase, with $K_{0.8}[Li_{0.13}Ti_{0.87}]O_4$ prototype structure, (ICSD reference: 89-5420) formed under the synthetic conditions as shown in Figure 3.23b.

Attempts to quench the powders rapidly from 1000°C to room temperature to possibly freeze the meta-stable low-sodium content phases yielded identical impurity phases. It is likely that the formation of the sodium deficient structures with large interlayer spacing is unfavorable, especially with solid-state reaction conditions involving high thermal energy.

3.8 Summary and future work

In this chapter, titanate-based layer-structured quaternary oxide, sodium nickel titanate, is investigated as a novel sodium intercalation electrode. The solid-state synthetic methods were optimized using micron-sized and nano-sized precursors to prepare phase-pure powders with different particle morphologies. We studied the electrochemical properties of P2-NT phase and demonstrated its potential as a 'bi-functional' electrode material. We anticipate that this 'bi-

functional' approach of using the same material as anode and cathode would provide substantial cost benefits in large-scale battery manufacturing and reduce device cost. Electrochemical testing shows the activation of nickel redox couple between 'x'=2/3-1/3 with reversible sodium intercalation/de-intercalation reactions in a solid-solution regime with a high redox potential of 3.7 V. On the other hand, titanium activation between 'x'=2/3-1 provides a low redox potential of 0.7 V. The rate performance in the anodic region is better than the cathodic region due to higher amount of titanium in the transition metal layer. The cathodic P2-NT phase yields good capacity retention while the anodic P2-NT phase has a capacity fade during cycling. This continuous capacity loss is attributed to catalytic breakdown of electrolyte components at low potentials and requires further spectroscopic characterization to understand degradation mechanisms.

In the cathodic regime, we have shown that manganese incorporation has a positive effect on the transport and electrochemical properties. We have demonstrated improved capacity retention at high currents, and achieved good cycleability. These performance gains are attributed to the following mechanisms: faster transport of charge-carriers (electron/holes and Na-ions) leading to higher electronic and ionic conduction, and accelerated interfacial reaction kinetics as shown by EIS, PITT and DC measurements. P2-NT and P2-NMT phases have a dominant sodium transport mechanism and ionic conductivity is 5 orders of magnitude higher than electronic conductivity. Further improvements need to target achieving metallic-type conductivity by elemental substitution. EIS illustrated that interfacial resistance has a strong dependence on electrode potential and decreases by several orders of magnitude at low sodium content due to the formation of more Ni⁴⁺ states. We report a high sodium diffusion co-efficient in the range of 10⁻¹²-10⁻¹³ cm²/s. Impedance-coupled-cycling study showed that P2-NMT has excellent capacity retention due to fairly stable charge transfer resistance, surface film resistance and film capacitances.

Attempts to improve the stability of P2-NT phases using calcium substitution (20%) were unsuccessful due to the formation of stable perovskite-structured calcium impurity phases during material synthesis. We did not observe solid evidence of solid solution formation with calcium even at lower substitutional level of 5%. It was identified that the anodic capacity can be improved substantially by utilizing sodium deficient compositions ($Na_x[Ni_{1/3}Ti_{2/3}]O_2$ where x<2/3). These highly non-stoichiometric phases were found to be unstable and could not be synthesized under traditional solid-state routes. Efforts to stabilize these phases that contain high vacancy concentration by incorporating larger potassium metal in the alkali layer results in phase separation with tunnel-type impurity oxides. Soft chemistry routes are often utilized to prepare metastable phases and it is likely that these potassium substituted phases can be synthesized under milder conditions.³⁹

BIBLIOGRAPHY

BIBLIOGRAPHY

- 1. Delmas, C., Fouassier, C. & Hagenmuller, P. Structural classification and properties of the layered oxides. *Physica* **99B**, 81–85 (1980).
- 2. Johnson, C. S. *et al.* Structural Characterization of Layered LixNi0.5Mn0.5O2(0<x< 2) Oxide Electrodes for Li Batteries. *Chem. Mater.* 2313–2322 (2003).
- 3. Shin, Y. & Yi, M. Preparation and structural properties of layer-type oxides NaxNix/2Ti1-x/2O2. *Solid State Ionics* **132**, 131–141 (2000).
- 4. Bouwman, P., Boukamp, B. A., Bouwmeester, H. J. M. & Notten, P. H. L. Structure-related intercalation behaviour of LiCoO2 films. *Solid State Ionics* **152-153**, 181–188 (2002).
- 5. Rougier, A., Nazri, G. A. & C., J. Vibrational Spectroscopy and Electrochemical Properties of LiNi0.7Co03O2 Cathode Material for Rechargeable Lithium Batteries. *Ionics (Kiel).* **3**, 170–176 (1997).
- 6. Kim, H.-S., Kim, K., Moon, S.-I., Kim, I.-J. & Gu, H.-B. A study on carbon-coated LiNi1/3Mn1/3Co1/3O2 cathode material for lithium secondary batteries. *J. Solid State Electrochem.* **12**, 867–872 (2008).
- 7. Choi, J. & Manthiram, A. Role of Chemical and Structural Stabilities on the Electrochemical Properties of Layered LiNi1/3Mn1/3Co1/3O2 Cathodes. *J. Electrochem. Soc.* **152**, A1714–A1718 (2005).
- 8. Thackeray, M. M. *et al.* Li2MnO3-stabilized LiMO2 (M = Mn, Ni, Co) electrodes for lithium-ion batteries. *J. Mater. Chem.* **17**, 3112 (2007).
- 9. Berthelot, R., Carlier, D. & Delmas, C. Electrochemical investigation of the P2–NaxCoO2 phase diagram. *Nat. Mater.* **10,** 74–80 (2011).
- 10. Lee, D. H., Xu, J. & Meng, Y. S. An advanced cathode for Na-ion batteries with high rate and excellent structural stability. *Phys. Chem. Chem. Phys.* **15**, 3304–12 (2013).
- 11. Lu, Z. & Dahn, J. R. In Situ X-Ray Diffraction Study of P2-Na2/3Ni1/3Mn2/3O2. *J. Electrochem. Soc.* **148**, A1225–A1229 (2001).
- 12. Komaba, S. *et al.* Study on the Reversible Electrode Reaction of Na1-xNi0.5Mn0.5O2 for a Rechargeable Sodium-Ion Battery. *Inorg. Chem.* **51**, 6211–6220 (2012).
- 13. Yabuuchi, N. *et al.* P2-type Na(x)[Fe(1/2)Mn(1/2)]O2 made from earth-abundant elements for rechargeable Na batteries. *Nat. Mater.* **11,** 512–7 (2012).

- 14. Buchholz, D., Chagas, L. G., Winter, M. & Passerini, S. P2-type layered Na0.45Ni0.22Co0.11Mn0.66O2 as Intercalation Host Material for Lithium and Sodium Batteries. *Electrochim. Acta* (2013). doi:10.1016/j.electacta.2013.02.109
- 15. Kim, D. *et al.* Enabling Sodium Batteries Using Lithium-Substituted Sodium Layered Transition Metal Oxide Cathodes. *Adv. Energy Mater.* **1,** 333–336 (2011).
- 16. Fujimoto, K., Ikezawa, K. & Ito, S. Charge–discharge properties of a layered-type Li(Ni,Co,Ti)O 2 powder library. *Sci. Technol. Adv. Mater.* **12,** 054203 (2011).
- 17. Kam, K. C., Mehta, a., Heron, J. T. & Doeff, M. M. Electrochemical and Physical Properties of Ti-Substituted Layered Nickel Manganese Cobalt Oxide (NMC) Cathode Materials. *J. Electrochem. Soc.* **159**, A1383–A1392 (2012).
- 18. Tang, H., Zhao, F., Chang, Z., Yuan, X.-Z. & Wang, H. Synthesis and Electrochemical Properties of High Density LiNi0.8Co0.2-xTixO2 for Lithium-Ion Batteries. *J. Electrochem. Soc.* **156**, A478–A482 (2009).
- 19. Shin, Y.-J., Park, M.-H., Kwak, J.-H., Namgoong, H. & Han, O. H. Ionic conduction properties of layer-type oxides. *Solid State Ionics* **150**, 363–372 (2002).
- 20. Kabi, S. & Ghosh, A. Polaron conduction in Lix[Ni1/3Mn1/3Co1/3]O[2 $-\delta$] (x=1, 0.9 and δ =0, 0.05) cathodes. *J. Appl. Phys.* **107**, 103715 (2010).
- 21. Rao, M. C., Begum, S. M., Reddy, E. S. & Hussain, O. M. Electrical conduction behavior of LiNixCo1-xO2 thin films. *AIP Conf. Proc.* **613**, 613–614 (2012).
- 22. Zhuang, Q. *et al.* An Electrochemical Impedance Spectroscopic Study of the Electronic and Ionic Transport Properties of Spinel LiMn 2 O 4. *J. Phys. Chem. C.* **114**, 8614–8621 (2010).
- 23. Singh, R. S., Ansari, T. H., Singh, R. A. & Wanklyn, B. M. Electrical conduction in NiTiO3 single crystals. *Mater. Chem. Phys.* **40**, 173–177 (1995).
- 24. *CRC Handbook of Physics and Chemistry. CRC Handb. Phys. Chem.* 10–197 (CRC Press, 2013).
- 25. Zandbergen, H. W., Foo, M., Xu, Q., Kumar, V. & Cava, R. J. Sodium ion ordering in NaxCoO2: Electron diffraction study. *Phys. Rev. B* **70**, 024101 (2004).
- 26. Shanmugam, R. & Lai, W. Na2/3Ni1/3Ti2/3O2: "Bi-Functional" Electrode Materials for Na-Ion Batteries. *ECS Electrochem. Lett.* **3,** A23–A25 (2014).
- 27. Shanmugam, R. & Lai, W. Study of Transport Properties and Interfacial Kinetics of Na2/3[Ni1/3MnxTi2/3-x]O2 (x = 0,1/3) as Electrodes for Na-Ion Batteries. *J. Electrochem. Soc.* **162**, A8–A14 (2014).

- 28. Huggins, R. A. Simple Method to Determine Electronic and Ionic Components of the Conductivity in Mixed Conductors: A Review. *Ionics (Kiel)*. **8,** 300–313 (2002).
- 29. Saadoune, I., Maazaz, A., Menetrier, M. and & Delmas, C. On the NaxNi0.6Co0.4O2 System: Physical and Electrochemical Studies. *J. Solid State Chem.* **117**, 111–117 (1996).
- 30. Aurbach, D. *et al.* Common Electroanalytical Behavior of Li Intercalation Processes into Graphite and Transition Metal Oxides [Q/It"]'. *J.Electrochem. Soc* **145**, 3024–3034 (1998).
- 31. Levi, M. D. *et al.* Solid-State Electrochemical Kinetics of Li-Ion Intercalation into Li 1-x CoO 2: Simultaneous Application of Electroanalytical Techniques SSCV, PITT and EIS. *J. Electrochem. Soc.* **146**, 1279–1289 (1999).
- 32. Levi, M. D., Lu, Z. & Aurbach, D. Application of finite-diffusion models for the interpretation of chronoamperometric and electrochemical impedance responses of thin lithium insertion V 2 O 5 electrodes. *Solid State Ionics* **143**, 309–318 (2001).
- 33. Hirschorn, B. *et al.* Determination of effective capacitance and film thickness from constant-phase-element parameters. *Electrochim. Acta* **55**, 6218–6227 (2010).
- 34. Lai, W. & Haile, S. M. Impedance Spectroscopy as a Tool for Chemical and Electrochemical Analysis of Mixed Conductors: A Case Study of Ceria. *J. Am. Ceram. Soc.* **88,** 2979–2997 (2005).
- 35. Lai, W. & Ciucci, F. Small-Signal Apparent Diffusion Impedance of Intercalation Battery Electrodes. *J. Electrochem. Soc.* **158**, A115–A121 (2011).
- 36. Zhang, D. *et al.* Studies on capacity fade of lithium-ion batteries. *J. Power Sources* **91,** 122–129 (2000).
- 37. Wang, Y. *et al.* A zero-strain layered metal oxide as the negative electrode for long-life sodium-ion batteries. *Nat. Commun.* **4**, 1–7 (2013).
- 38. Han, S. C. *et al.* Ca-doped NaxCoO2 for improved cyclability in sodium ion batteries. *J. Power Sources* **277**, 9–16 (2015).
- 39. Gopalakrishnan, J. Chimie Douce Approaches to the Synthesis of Metastable. *Chemistry* (*Easton*). (1995).

4. STRUCTURAL CHARACTERIZATION OF P2-SODIUM NICKEL TITANATE USING EXPERIMENTAL AND COMPUTATIONAL METHODS

4.1 Introduction

4.1.1 Computational methods

Computer simulations based on static lattice, molecular dynamics and ab-initio calculations provide compelling insights on material characteristics such as defect energetics, order/disorder phenomenon, ionic conduction pathways, migration activation energies, etc. 1–7 These methods often provide information that are not readily accessible by conventional experiments and hence have become a vital part of battery materials research. Other modeling methods based on constitutive equations (transport modeling) operate at a much larger length-scale and are very useful for predicting macroscopic physicochemical properties required for optimizing cell design and configurations in commercial devices. 8–11 This chapter deals with utilizing static calculations for structural studies of inorganic materials as our research goal was to understand material properties at an atomic length-scale.

Classical static lattice calculations, also referred as atomistic simulations, employed in this study are excellent for studying a large ensemble of atoms as they are computationally inexpensive. This feature facilitates the exploration of a broad energy landscape for non-stoichiometric, disordered materials that possess a wide gamut of possible configurations due to the typically high vacancy concentration. Parallel optimization of multitudes of structural configurations can be readily performed with high-throughput atomistic simulations which would otherwise be impractical with first-principles calculations and molecular dynamics study. With this methodology, the most energetically favorable structural configurations in a given energy

landscape can be shortlisted for further investigation with molecular dynamics or ab-initio studies that demand more computational resources. We extend the applicability of these classical simulation approaches to titanate-based material chemistries for Na-ion batteries.

4.1.2 Literature

The energetics of sodium/vacancy ordering at different sodium contents (x) in P2-Na_xNbS₂ have been studied using Density Functional Theory (DFT) calculations and atomistic simulations. ¹² The formation of transition metal ordered superlattice has been suggested for Na_xNi_{x/2}Mn_{1-x/2}O₂. ¹³ Atomistic simulations predicted a low activation energy of 0.32 eV for sodium hopping in NaFePO₄ along [010] direction. ⁵ A 1-D curved trajectory between sodium sites was proposed to facilitate fast sodium ion conduction in this polyanionic material. At low sodium contents, first principles calculations predicted the O2 phase to be energetically more favorable than P2 phase (25 meV lower) in P2-Na_x[Ni_{1/3}Mn_{2/3}]O₂ and validated experimentally. ¹⁴ It was also shown that the P2 phase has lower activation energy for sodium transport than the O2 phase and hence promotes faster sodium ion diffusion.

4.1.3 Scope of current work

Titanium based layered quaternary oxides ($Na_x[M_{1-y}Ti_y]O_2$) have been demonstrated to have attractive sodium intercalation/de-intercalation with good capacity retention, high cathodic redox potential (E=3.7 V vs. Na/Na⁺ for Ni²⁺⁴⁺ species) and low anodic redox potential (E=0.7 V vs. Na/Na⁺ for Ti^{4+/3+} species). In this study, the average and local structural properties and the energetics of atomic distribution in P2-Na_{2/3}[Ni_{1/3}Ti_{2/3}]O₂ (P2-NT) are investigated using interatomic potential based atomistic simulations and neutron diffraction experiments.

4.2 Experimental

4.2.1 Neutron diffraction experiments

For the neutron diffraction study, P2-NT phase powders were prepared solid state reaction by firing SPEX-milled Na₂CO₃, NiO and TiO₂ precursor powders at 900 °C and 1000 °C, as described in chapter 3. Sodium volatility losses at the high temperature firing conditions were compensated by adding 10% excess sodium. After synthesis, the titanate powders were immediately transferred to glove box kept at inert argon atmosphere to limit potential air exposure effects. The powders were sealed in vanadium cans to minimize air exposure during storage and shipping to neutron diffraction facility. The neutron diffraction experiments were performed in beamline 11A of POWGEN diffractometer facility at Spallation Neutron Source (SNS) of Oak Ridge National Lab (ORNL). Rietveld refinement was performed using EXPGUI-GSAS software.^{21,22}

4.2.2 Energy calculations for many-body systems: Theory

The internal energy of a many-body ensemble contains contribution from multiple nuclei and electrons. Static lattice calculations simplify this system by assuming that the electronic contributions can be effectively included within individual atoms by suitable force-field models. Hence, these calculations are more approachable at the expense of inaccuracies for systems with strongly correlated electronic interactions. For 'N' atoms, the total energy can be partitioned into a series expansion as Equation 4.1.

$$U_{net} = \sum_{i}^{n} U_{i} + \frac{1}{2} \sum_{i}^{n} \sum_{i}^{n} U_{ij} + \frac{1}{6} \sum_{i}^{n} \sum_{i}^{n} \sum_{k}^{n} U_{ijk} + \cdots$$

$$4.1$$

where the first term represents the one-body interactions due to externally imposed fields, the second term represents two-body interactions depending on governing equations (short-range and long-range) that typically includes species charge and separation distance, and the third term includes three-body interactions. The higher order terms are typically truncated as they become negligible.

In this work, this series is truncated to include only up to the 2nd order interactions as typical for transition metal oxides. Also, this study does not invoke electric field effects as we are interested in equilibrium material properties and hence the first self-interaction term is also neglected. However, it should be noted that in real devices, these materials do operate under dynamic conditions with electric field gradients.

4.2.3 Long-range and short-range interactions

The two-body interactions are classified into long-range and short-range. The long-range interactions were expressed by Coulombic law to define forces between the point charges as given by Equation 4.2.

$$U_{ij}^{Coulombic} = q_i q_j / 4\pi \epsilon r_{ij}$$
 4.2

where ' U_{ij} ' is the interaction energy, 'q' is the ionic charge, ' r_{ij} ' is the separation of the ions and ' ϵ ' is the permittivity of the medium. Ewald summation method is used as the de-facto standard for calculating the Coulombic energy of the periodic crystal by splitting the energy component into short-range zone for evaluation in real-space and long-range zone for evaluation in Fourier space. Such calculations based on Madelung potential have been in use in the field computational chemistry for several decades. The net atomic charges were taken as formal charges since they were found to provide satisfactory results.

Some of the commonly reported short-range, two-body interaction models include the Harmonic potential, Born potential, Buckingham potential, Lennard-Jones potential, Morse potential, etc. The parameters for these potential models are generally derived empirically by fitting the model with lattice parameters, elastic properties, dielectric properties, phonon dispersion curves and quantum mechanically derived energy hypersurface. After a thorough literature survey of different interatomic potential models and potential parameters for various oxide materials (with different structural classes including layered, olivine, spinel, perovskite, etc.), two force-field models based on Buckingham- and Morse-type potentials were found to work fairly well for the P2-NT phase. These are mathematically expressed in the form of Equation 4.3 and 4.4.

$$U_{ij}^{Buckingham} = Ae^{-r_{ij}/\rho} - C/r_{ij}^6$$
 4.3

$$U_{ij}^{Morse} = D_e[(1 - e^{-a(r - r_0)})^2 - 1]$$
 4.4

where 'A' refers to Buckingham pre-exponent repulsive parameter, 'p' refers to Buckingham well depth parameter, 'C' refers to Buckingham attractive parameter, 'De' is Morse bond dissociation parameter, 'a' is Morse force-constant parameter and 'ro' is Morse equilibrium bond length parameter. The Buckingham model includes an attractive term to describe bonding effects that hold atoms together in a molecule and repulsive term to describe electron cloud repulsion effect that occur when the separation distances reach subatomic values. Morse model is an anharmonic extension of the symmetric harmonic bond model and is frequently used for covalently bonded materials with high vibrational energies accounted for by the exponential term. The interatomic potential parameters for the two models are listed in Table 4.1and Table 4.2.

For the Buckingham potential, the model parameters for Ti-O interactions were based on a defect study of anatase phase.³ Dipole polarizations are incorporated using the standard Dick-Overhauser approach employing a core-shell model to represent the coupling between valence electrons and core shell electrons. Typically, the core is positively charged and shell is negatively charged and they are linked by a harmonic spring with predefined stiffness (spring constant- k_{cs}).²⁵ The core and shell start out at the same positions for all the atoms and they are allowed to reorganize to different co-ordinates (within an allowable limit) to account for polarizability effects. This core-shell concept also takes care of covalent contributions as the valence electrons become more shared in covalent bonds. Titanium-oxygen bonds have a non-negligible covalent character (~30%) and hence both these atomic species are treated with a core-shell approach.²⁶ The remaining atoms, nickel and sodium, are considered as non-polarizable (highly ionic).

The Morse potential parameters were obtained from a previous study that works for a wide range of oxide and silicate material.²⁷ Lennard-Jones (LJ) repulsive interaction is also included in the Morse potential to avoid prevent atoms from reaching unreasonably short atomic separations. Additional shells are not utilized for Morse potential as they already account for covalent bond character. These short-range interaction potentials were defined to apply within a spherical zone with a cut-off radius of 12 Å for any given atomic pair while the long-range forces act for the whole studied zone. The variation of the interaction energy as a function of atomic separation is shown in Figure 4.1. It is apparent that these short range interatomic potentials provide an energy penalty at extremely short interatomic distances.

Table 4.1 Interatomic potential parameters: Buckingham Core-shell model; all atomic species are taken at formal charges, Formal charge= $Y_{core} + Y_{shell}$

Interactions	A (eV)	ρ (Å)	C (eV Å ⁶)
Na-O	1663.28	0.2900	0
Ni-O	932.61	0.3170	0
Ti-O	5111.70	0.2625	0
O-O	12420.50	0.2215	29.07

 Core-Shell parameters

 Species
 k (eV Å -²)
 Y (e)

 Ti
 314
 -0.1

 O
 31
 -2.8

Table 4.2 Interatomic potential parameters: Morse+ LJ model

	Morse Potential									
Interactions	D _{ij} (eV)	a _{ij} (Å ⁻²)	r _o (Å)							
Na-O	0.0234	1.76	3.01							
Ni-O	0.0294	2.68	2.50							
Ti-O	0.0242	2.25	2.71							
O-O	0.0424	1.38	3.62							
Le	nnard-Jones Pote	ntial (12-6)								
Interactions	A	В	C							
Na-O	5	0	0							
Ni-O	22	0	0							
Ti-O	1	0	0							
O-O	3	0	0							

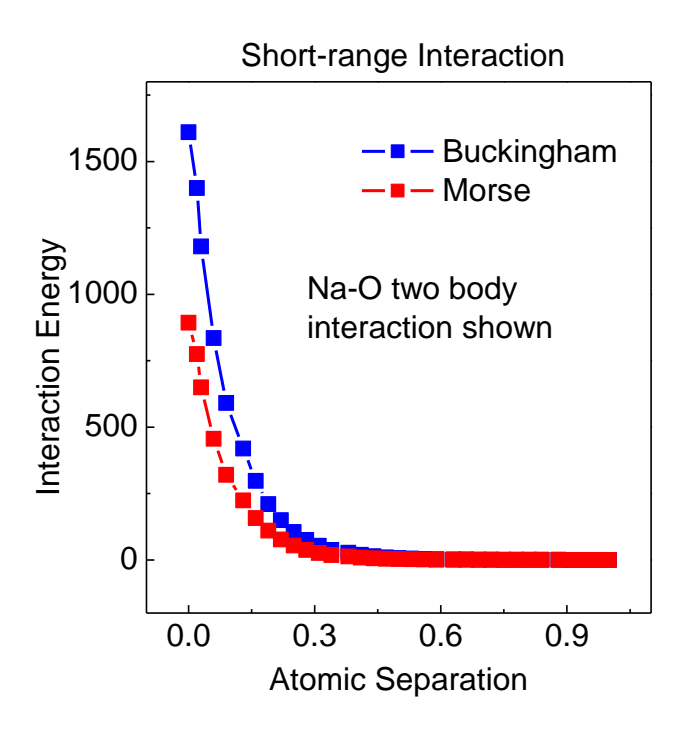


Figure 4.1 Variation of interaction energy for Buckingham and Morse interatomic potentials for Na-O two-body interactions.

4.2.4 Handling partial occupancy: Mean field model and Supercells

The studied oxide material has structural disorder in the transition metal and sodium sites; nickel and titanium occupy identical '2a' Wyckoff site position while sodium atoms partially occupy '2b' and '2c' Wyckoff site position. Mean field model is invoked to apply partial occupancy for any given crystallographic site to accommodate this structural disorder. The relative atomic interactions (short-range and long-range) are scaled based on the partial occupancy values for all atomic species. Traditionally, this approximation works fairly well for predicting macroscopic properties as the averaged crystallographic structure tends to be a reasonable representative. We utilize this methodology to predict the structural properties of the oxide material, at the scale of a unit cell, to validate the interatomic potential models. However, local structural effects cannot be

predicted due to the averaging effect and this can become an influential factor in fast ionic conductors.

3x2x1 supercell structures containing stoichiometric number of atoms were investigated for the local structural study. These studies are not limited by mean field approximation as the supercell structures do not contain partial occupancies and thereby allows for extracting potential local structural details that would otherwise be inaccessible by conventional simulation methods. However, a proper statistically relevant study requires investigating a large number of possible structural configurations. A total of 2000 randomized structures were sampled to yield statistically relevant results. Parallel structural optimization runs were performed using General Utility Lattice Program (GULP) code with random structures (.gin format) generated by a MATLAB script. ^{28,29} Specific details of atomic distribution in the random structural assignment and their results will be discussed further.

4.2.5 Energy minimization: Optimization schemes and strategy

GULP code is employed to find the energy minimum of the complex energy hypersurface in disordered materials. Taylor series expansion is applied to the internal energy and the first and second derivatives, also referred to as gradient vector (g) and Hessian matrix (H), respectively, are computed. Non-linear multivariate optimization is performed using Broyden-Fletcher-Goldfarb-Shanno (BFGS) scheme which includes the conjugate gradient method for faster descent to the energy minimum. The BFGS scheme is essentially a modified Newton-Raphson method that is suitable for solving large systems. During each optimization step, atoms are subject to a small displacement from their initial positions and energy values are computed. Subsequent direction of

descent and step size are decided to reach the energy minimum. Successive iterations ensures that the final optimized structure reaches the stationary point in the energy hypersurface.

However, certain initial structures might be too far from the energy minimum or get stuck in local potential wells. These factors can likely prevent proper convergence using the BFGS optimization schemes. To mitigate this effect, a large number of configurations are sampled so that at least a modest number of initial structures start out at favorable locations to reach energy minimum.

During the energy minimization, all atomic cores and their corresponding shells are relaxed simultaneously to reach the energy minimum in a 1-step method. A 2-step method with only shell relaxation in the 1st step followed by relaxation of all cores and shells in the 2nd step was also performed. The premise was that this permits pre-allotment of the polarization effects before the energy minimization step. However, the results from the 2-step method were found to be comparable to the 1-step method at the cost of additional computational time and were not considered further.

4.2.6 Space group transformations

For the disordered simulation study, the unit cell is transformed from 194 space group (P6₃/mmc) to 63 subgroup (Cmcm) using PowderCell2.4 software. ³⁰ The transformed structure is referred to as 'pseudocubic' and is depicted in Figure 4.2.

194 Space group: Hexagonal 63 Space group: Orthorhombic

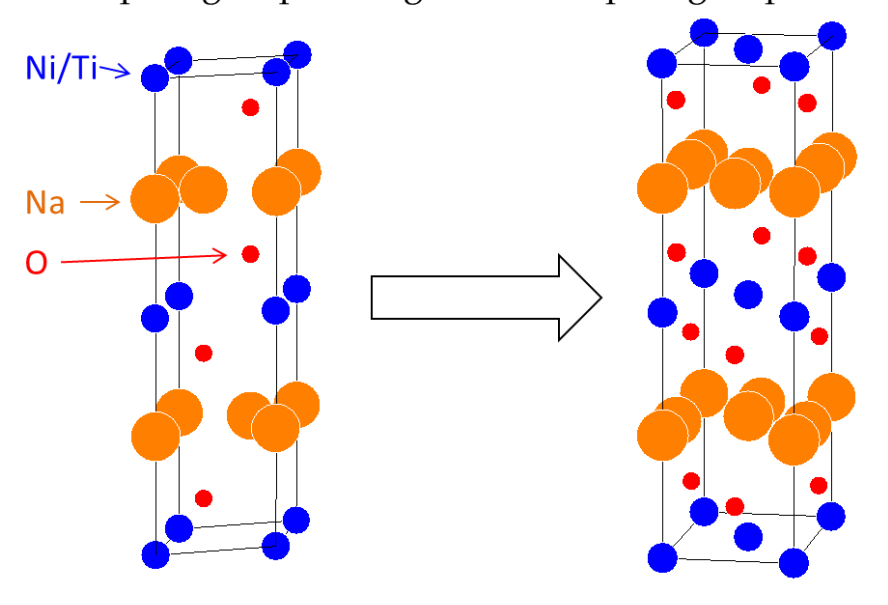


Figure 4.2 Unit cell transformation from space group 194 to 63.

This transformation allows for independent definition of the lattice parameters and consequently easier scaling of the supercells helps reduce computational time. Energy minimization were done on 3x2x1 pseudocubic supercells. (a'=8.9 Å, b'=10.3 Å, and c=11.1 Å)

In-plane ordered structures were generated by transformation from 194 space group to 193 subgroup. Due to the splitting of the transition metal sites, the transformed structure has a distinct in-plane ordering pattern as shown in Figure 4.3. The ordered hexagonal structure is further converted to a pseudocubic structure (space group 63) as before. The single crystallographic site ('2a') for transition metal atoms in 194 space group gets split into two distinct Wyckoff positions: '4a' and '8e' in the pseudocubic unit cell. No randomization is required for the transition metal atoms as they have determined site positions. Disorder in introduced in the two sodium metal sites: '4c', and '8g' by randomizing sodium distribution. Simulation study involves 1x3x1 ordered supercells (lattice parameters: a'=8.9 Å, b'=15.4 Å, and c=11.1 Å).

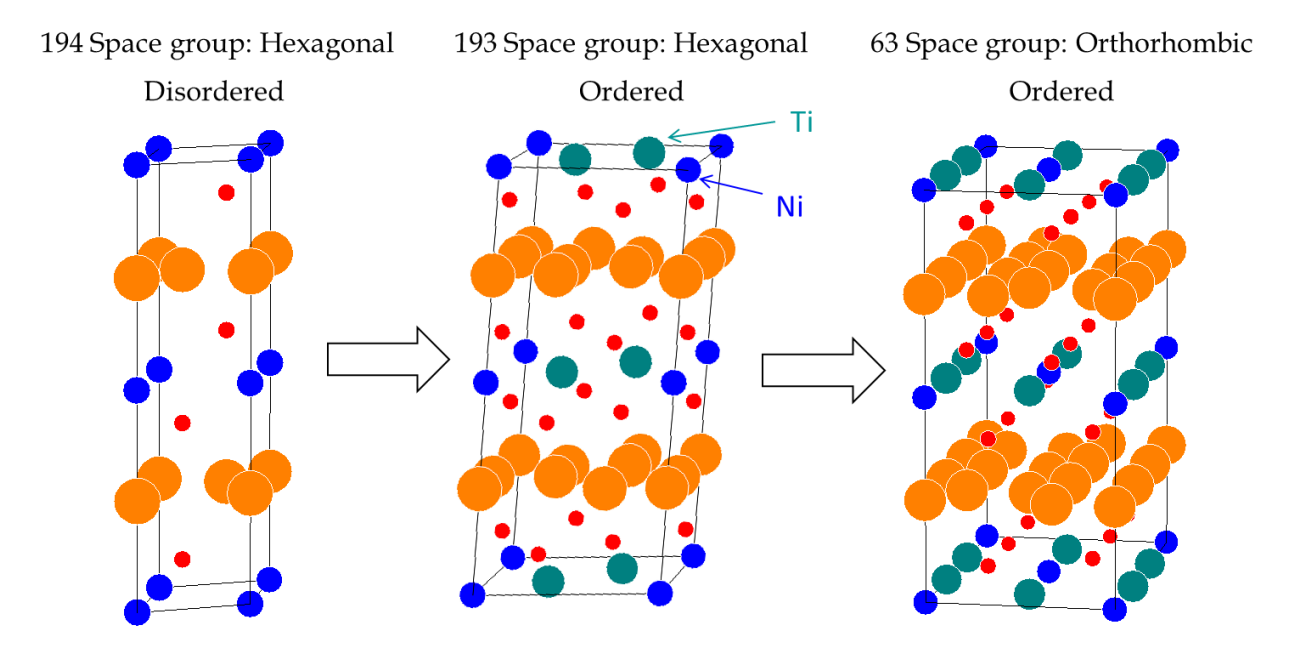


Figure 4.3 Space group transformation to generate in-plane ordered structure.

Through-plane ordering of the transition metal atoms was performed by the transforming the unit cell axis as $[(a \ b \ c) \rightarrow (a \ b \ 3c)]$ without changing the space group (194) as shown in Figure 4.4. This results in a periodic ordering pattern with two layers of titanium alternating between two layers of nickel atoms. This ordered structure is further transformed to pseudocubic structure, as well. Energy optimization runs were carried out with 3x2x1 ordered supercells (a'=8.9 Å, b'=10.3 Å, and c'=33.4 Å).

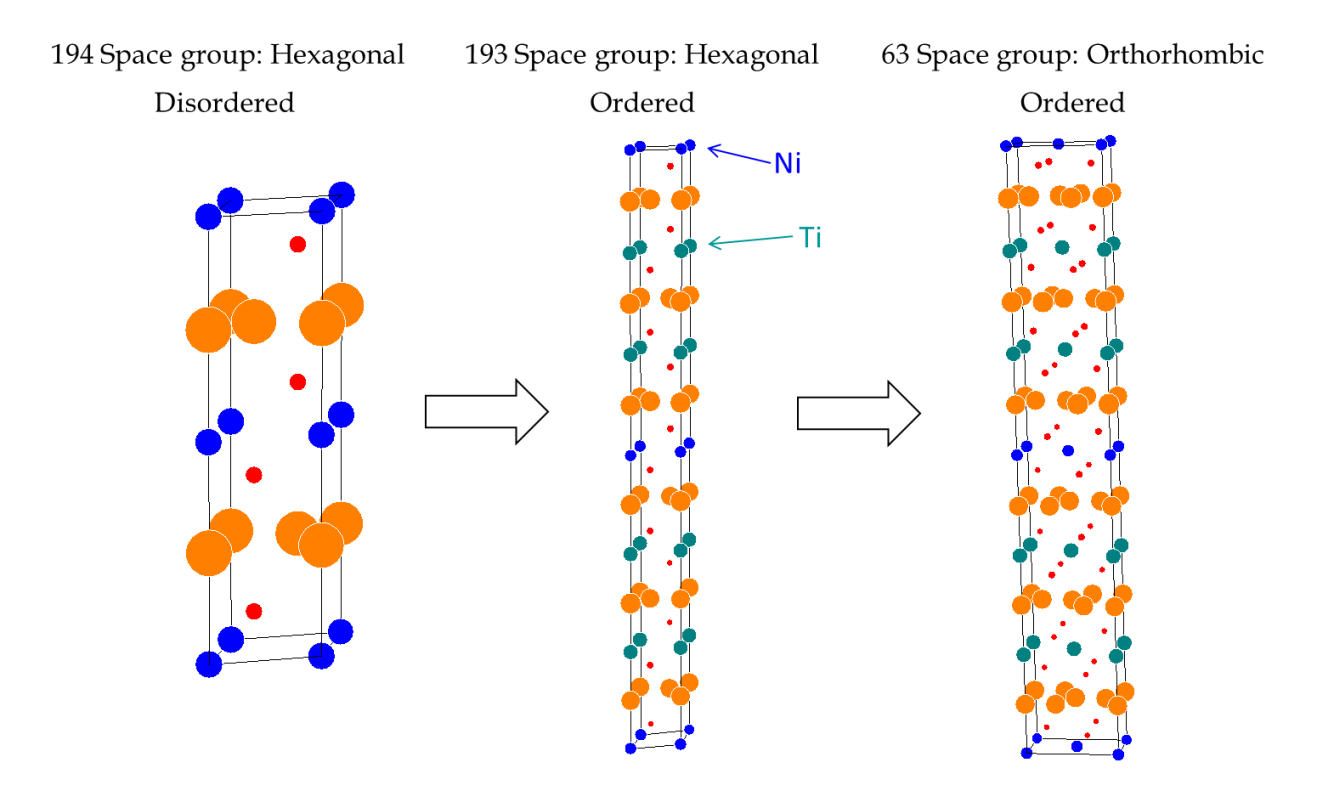


Figure 4.4 Space group transformation to generate through-plane ordered structure.

4.2.7 Simulation data interpretation and Pair Distribution Function (PDF) calculation

Data analysis includes generating nuclear probability density maps (.grd format) using the optimized structures using a MATLAB script. The nuclear probability density maps and isosurface levels were visualized using VESTA 3.1.8³¹ and Crystalmaker software.³² The pixel resolution was set at 0.1 Å for experimental and simulated density maps.

Experimental Pair Distribution Function (PDF) was obtained for the refined structure using PDFGUI software. ^{22,33–35} Simulated PDF patterns were calculated in GULP while incorporating phonon contributions that are not explicitly stated in the static calculations. The maximum cutoff radius was set at 20 Å, bin size at 1000 and 'shrink' value at 3.

4.3 Results and Discussion

4.3.1 Rietveld refinement: Neutron Diffraction

Rietveld refinement is performed with the high resolution Neutron Diffraction (ND) datasets to obtain the average structural information. Isotropic model (displacement parameters) was utilized for nickel and titanium atoms while the remaining atoms were left anisotropic during the refinement routine. A complete anisotropic model did not yield physically realistic displacement parameters for the transition metals. By setting the space group to 194, the structural model was able to simulate the experimental Bragg peak positions fairly accurately as seen in the difference plots in Figure 4.5 and Figure 4.6. The accuracy of the structure model and refined structural parameters is confirmed by relatively low goodness-of-fit parameter values (R_{wp} and R_F) as shown in Table 4.3 through Table 4.6. However, there are few extra features (bump at d-spacing of 4.2) that could not be predicted by the current structural model. These bumps could not be indexed by any impurity phase reflection with Na-Ni-Ti-O stoichiometry. We suspect that these small bumps might be due to weak local ordering of the sodium and/or transition metal atoms.

The estimated lattice parameters are consistent with the previous X-ray diffraction studies.³⁶ Irrespective of powder synthesis temperature (900 °C and 1000 °C), the sodium site occupancy increases for the '2b' sites (Na_f) at 300K compared to 15 K. The '2b' sites at the atomic coordinates (0, 0, 1/4) are positioned directly in-line with the transition metal '2a' sites at the location (0, 0, 0). This in-line arrangement contributes to a repulsive interaction and hence sodium prefers '2c' positions than '2b' positions. Higher thermal contribution at ambient conditions (300 K) offsets the energy penalty to some extent and consequently increasing the '2b' site occupancy. At low temperatures (15K), these energetically unfavorable '2b' sites remain relatively inaccessible.

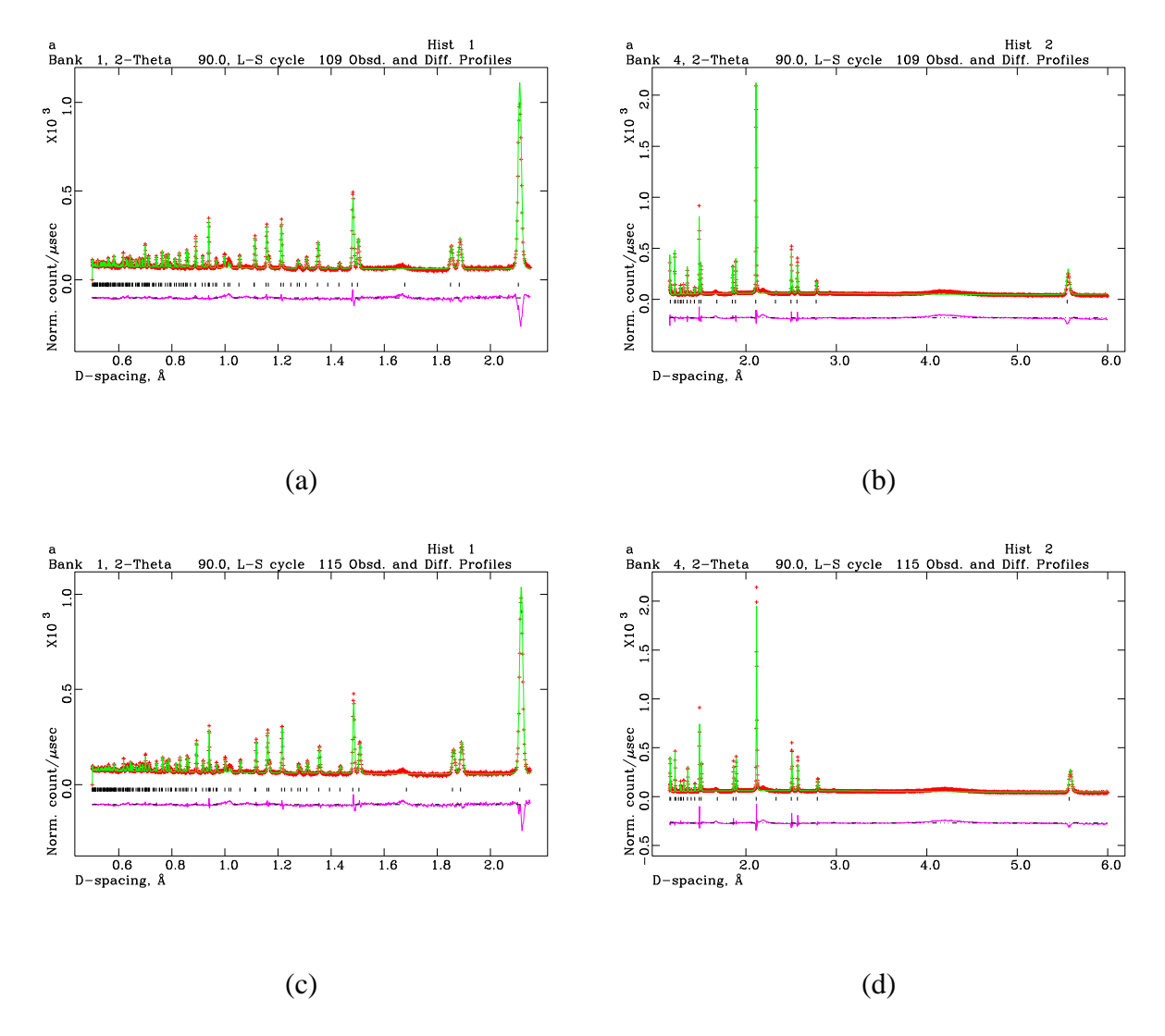


Figure 4.5 Rietveld refinement of P2-NT powders prepared at 900 °C and characterized at (a) 15K, bank 1, (b) 15K, bank 4, (c) 300K, bank 1, and (d) 300K, bank 4; red point indicates experimental data, green curve indicates simulated structure, and pink curve indicates difference curve; bank 1, bank 2 includes diffraction data in the d-spacing range of 0-2.2 Å, and 1.1-8 Å, respectively.

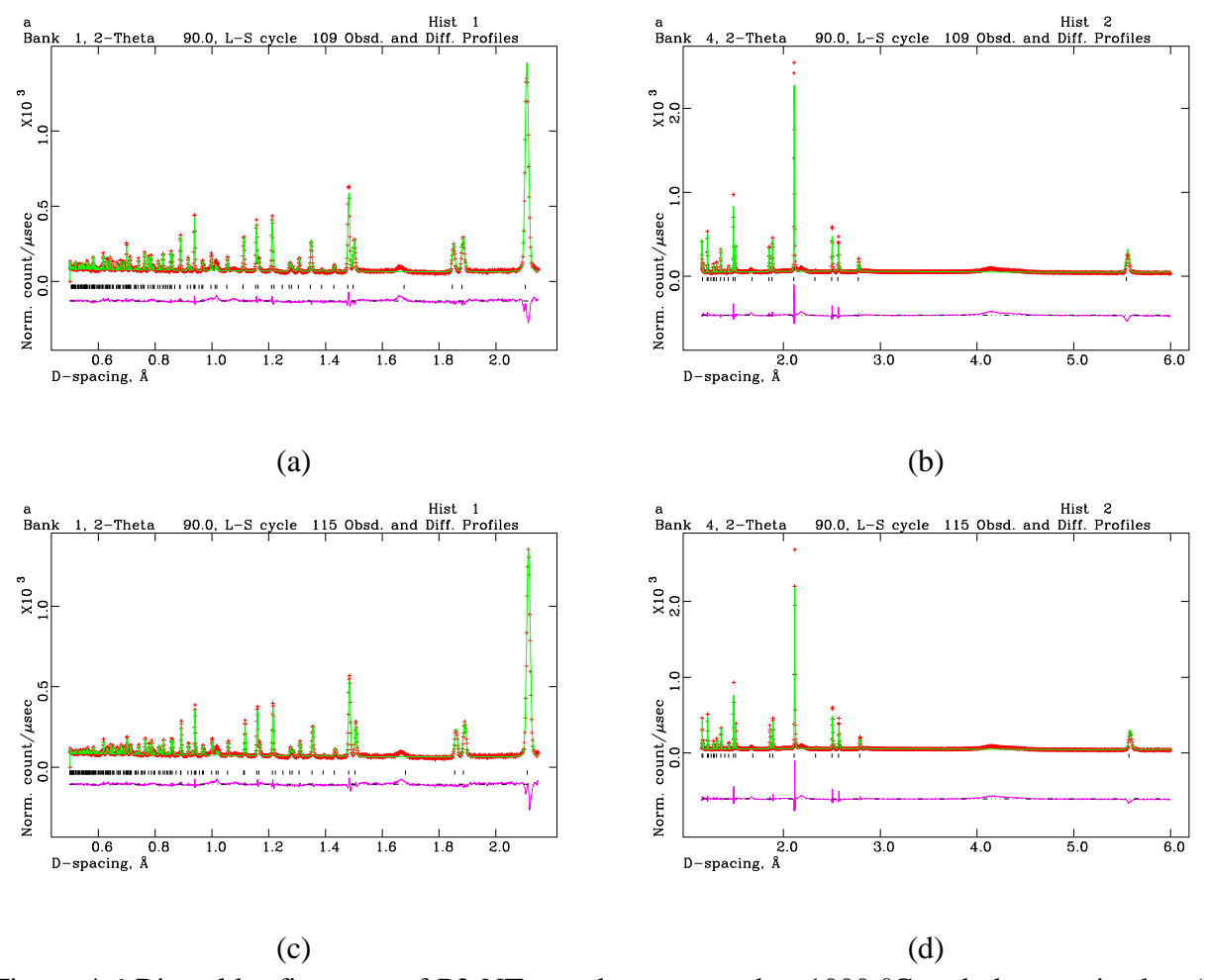


Figure 4.6 Rietveld refinement of P2-NT powders prepared at $1000\,^{\circ}$ C and characterized at (a) 15K, bank 1, (b) 15K, bank 4, (c) 300K, bank 1, and (d) 300K, bank 4.

Table 4.3 Structural information of P2-NT powders: Prepared at 900 °C and tested at 15K.

Element (Site)	X	у	Z	Occupancy	U_{11}	U_{22}	U_{33}	U_{12}
Na _f (2b)	0.0	0.0	0.25	0.1699	0.0094	0.0094	0.0022	0.0047
$Na_e(2c)$	0.3333	0.6667	0.25	0.4968	0.0161	0.0161	0.0063	0.0081
Ni (2a)	0.0	0.0	0.0	0.3333	0.0043	0.0043	0.0043	-
Ti (2a)	0.0	0.0	0.0	0.6667	0.0128	0.0128	0.0128	-
O (4f)	0.6667	0.3333	0.0957	1.0	0.0067	0.0067	0.0058	0.0034

Lattice parameters: a=b=2.9615 Å, c=11.1089 Å, $wR_p=0.089$, $R(F^2)=0.1650$, $\chi^2_{red}=50.07$

Table 4.4 Structural information of P2-NT powders: Prepared at 900 °C and tested at 300K

Element (Site)	X	у	Z	Occupancy	U ₁₁	U_{22}	U ₃₃	U_{12}
Na _f (2b)	0.0	0.0	0.25	0.1751	0.0286	0.0286	0.0022	0.0143
$Na_e(2c)$	0.3333	0.6667	0.25	0.4916	0.0333	0.0333	0.0110	0.0166
Ni (2a)	0.0	0.0	0.0	0.3333	0.0081	0.0081	0.0081	-
Ti (2a)	0.0	0.0	0.0	0.6667	0.0168	0.0168	0.0168	-
O (4f)	0.6667	0.3333	0.0952	1.0	0.0089	0.0089	0.0085	0.0044

Lattice parameters: $a = b = 2.9667 \text{ Å}, c = 11.1592 \text{ Å}, wR_p = 0.090, R(F^2) = 0.1580, \chi_{red}^2 = 49.41$

Table 4.5 Structural information of P2-NT powders: Prepared at 1000 °C and tested at 15K

Element (Site)	X	у	Z	Occupancy	U_{11}	U_{22}	U_{33}	U_{12}
Na _f (2b)	0.0	0.0	0.25	0.1623	0.0153	0.0153	0.0014	0.0076
$Na_e(2c)$	0.3333	0.6667	0.25	0.5044	0.0177	0.0177	0.0061	0.0089
Ni (2a)	0.0	0.0	0.0	0.3333	0.0029	0.0029	0.0029	-
Ti (2a)	0.0	0.0	0.0	0.6667	0.0078	0.0078	0.0078	-
O (4f)	0.6667	0.3333	0.0959	1.0	0.0074	0.0074	0.0046	0.0037

Lattice parameters: a = b = 2.9604 Å, c = 11.0951 Å, $wR_p = 0.1056$, $R(F^2) = 0.1630$, $\chi^2_{red} = 70.54$

Table 4.6 Structural information of P2-NT powders: Prepared at 1000 °C and tested at 300K

Element (Site)	X	y	Z	Occupancy	U_{11}	U_{22}	U_{33}	U ₁₂
Na _f (2b)	0.0	0.0	0.25	0.1761	0.0374	0.0374	0.0034	0.0187
$Na_e(2c)$	0.3333	0.6667	0.25	0.4906	0.0328	0.0328	0.0094	0.0164
Ni (2a)	0.0	0.0	0.0	0.3333	0.0040	0.0040	0.0040	-
Ti (2a)	0.0	0.0	0.0	0.6667	0.0069	0.0069	0.0069	-
O (4f)	0.6667	0.3333	0.0953	1.0	0.0097	0.0097	0.0080	0.0049

Lattice parameters: a=b=2.9654 Å, c=11.1470 Å, $wR_p=0.1096$, $R(F^2)=0.1663$, $\chi^2_{red}=77.38$

The calculated thermal expansion coefficients are: $\beta_a=1.83\times10^{-5}\text{Å/K}$, $\beta_c=17.65\times10^{-5}\text{Å/K}$ for powders prepared at 900°C and $\beta_a=1.75\times10^{-5}\text{Å/K}$, $\beta_c=18.21\times10^{-5}\text{Å/K}$ for powders prepared at 1000°C. These coefficients are fairly positive and a large anisotropy is noticeable, typical of isostructural layered oxides such as P2-Na_xMnO₂. This anisotropy is attributable to strong inplane bonding and relatively weak through-plane bonding in these layer-structured materials. Figure 4.7 depicts the nuclear density map of the refined structure at 15K calculated using JANA2006 crystallographic software. The Na_e density spots appear larger than Na_f due to the higher fractional occupancy as discussed before. Sodium thermal ellipsoids appear considerably oblate with the minor axis along the 'ab' plane in Figure 4.7a. and b. The transition metal density spots appear as perfect spheres due to the isotropic assumption (Figure 4.7c). In contrast, the oxygen density spots appear relatively more spherical (Figure 4.7d).

The degree of oblateness is quantified using displacement ratio parameter ($r = \sqrt{U_{33}/U_{11}}$ – 1) which quantitatively relates 'in-plane' deviation to the 'out-of-plane' deviation; 'plane' refers to region parallel to the 'ab' axis. At 15 K, Na_e and Na_f atoms have negative 'r' values of -0.37 and -0.52, respectively. These negative 'r' values are consistent with the oblate sodium ellipsoids. O3-NaCrO₂ has a more positive 'r' value of -0.18 and hence exhibits reduced oblateness.³⁹ The degree of oblateness correlates inversely to ionic conductivity; atoms with highly spherical displacement are likely to remain immobile in their lattice sites. The P2 compositions displays more pronounced 'in-plane' deviations and oblateness and hence support faster ion transport than O3 compositions. The oxygen atoms have a more positive 'r' value of -0.07 and are expected to remain fairly stationary.

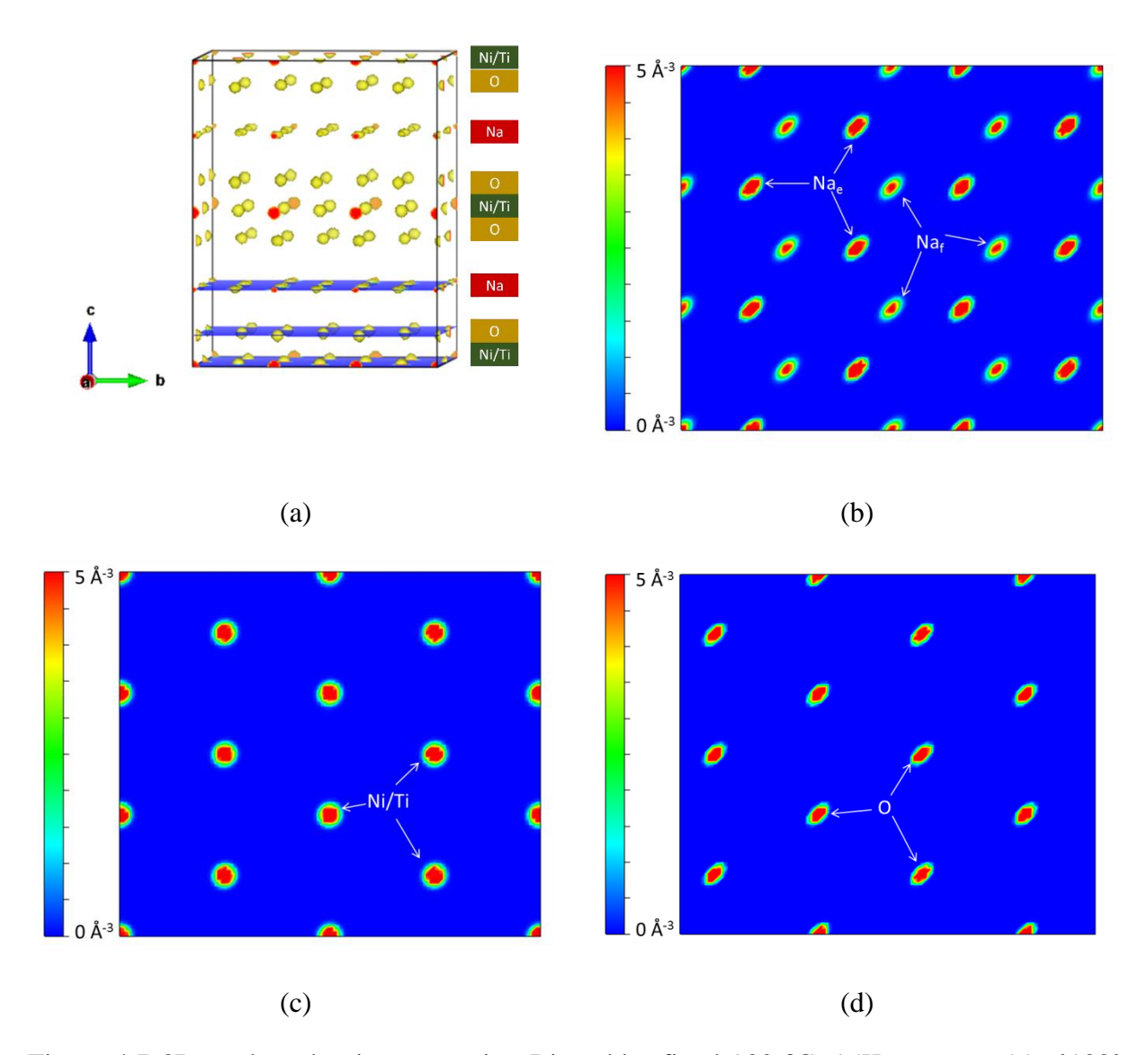


Figure 4.7 3D nuclear density map using Rietveld refined 900 °C, 15K structure (a), $\{100\}$ planar density describing sodium (b), transition metal (c) and oxygen atoms (d) with minimum and maximum saturation levels at 0 and 5 Å⁻³; atomic species legend is included on the right-side of 3D density map.

4.3.2 Interatomic potential sets: Selection and validation

The suitability and transferability of interatomic potentials to various binary and ternary oxides containing Na-Ni-Ti-O is evaluated in this section. The considered materials include structures with various space groups such as cubic, tetragonal, rhombohedral and monoclinic as shown in

Figure 4.8. The validity of the potential sets is evaluated by their ability to accurately replicate the experimental structural properties (lattice parameters). It should be noted that the bond character varies significantly from highly ionic in Na₂O to more covalent in TiO₂ and hence capturing the properties of these diverse materials with a single potential set is a challenging task. Nevertheless, various models have been proposed in the literature and several models were reviewed for their applicability.

Buckingham and Morse potential sets predicted the lattice parameters of binary and ternary oxides (containing Na-Ni-Ti) such as Na₂O (cubic), NiO (cubic), TiO₂ (tetragonal), NiTiO₃ (rhombohedral), Na₂Ti₃O₇ (monoclinic) and Na₈Ti₁₆O₃₂ (monoclinic) with reasonably good accuracy (ϵ_{buck} <2.6% and ϵ_{mors} <5.6%, respectively, where ϵ is the mean error in lattice parameter), demonstrating the general validity of the studied pairwise atomic interactions and transferability across various structure polytypes. The experimental and simulated lattice parameters are listed in Table 4.7-Table 4.10. All structures, except Na₂Ti₃O₇, yielded even lower error values (ϵ < 3.9% and ϵ <4.7%, respectively). Highly ionic structures such as Na₂O are well represented by Buckingham potential (ϵ =0.56%) than Morse potential (ϵ =3.27%) as the former predicts strong ionic interactions better. On the contrary, covalent structures such as rutile are modeled better by Morse potential (ϵ =1.0%) than Buckingham potential (ϵ =3.67%).

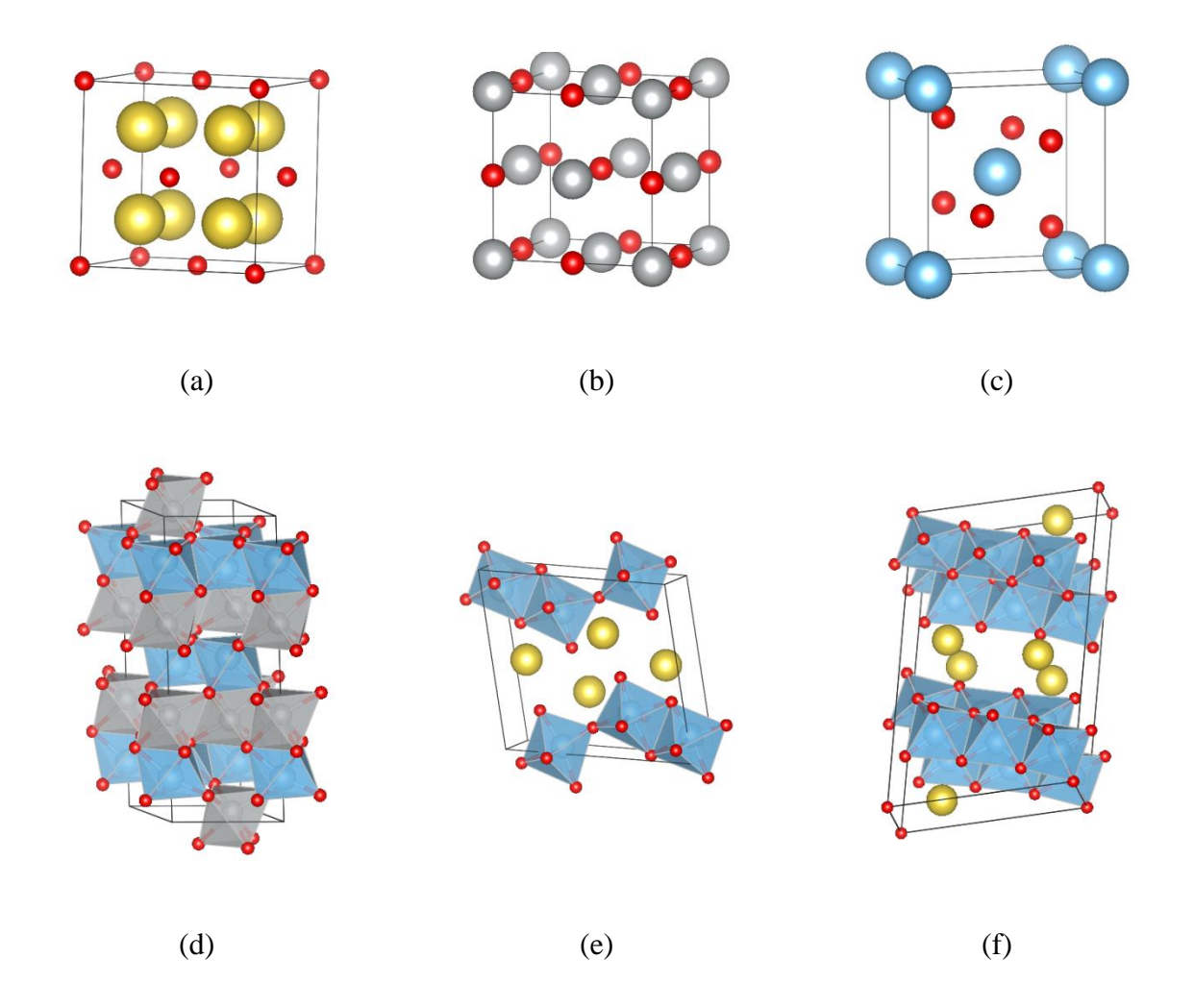


Figure 4.8 Crystal structure of (a) cubic sodium oxide (Na_2O), (b) cubic nickel oxide (NiO), (c) tetragonal titanium oxide (TiO_2), (d) rhombohedral nickel titanium oxide ($NiTiO_3$), (e) monoclinic sodium titanate-I ($Na_2Ti_3O_7$), and (f) monoclinic sodium titanate-II ($Na_2Ti_6O_{13}$); yellow, grey, red, and blue spheres represent sodium, nickel, oxygen, and titanium, respectively. colored polyhedra represent transition metals co-ordinated with oxygen atoms, sodium are left unbonded for clarity. $^{40-45}$

Good reproducibility of the lattice parameters were obtained for the studied oxide, $Na_{2/3}[Ni_{1/3}Ti_{2/3}]O_2$. Morse potential (ε =1.7%) provided better lattice parameter prediction than Buckingham potential (ε =3.6%) possibly due the large amount of titanium in this quaternary oxide.

Table 4.7 Transferability of Buckingham interatomic potential across binary oxides; $|\epsilon|$ is the modulus percentage error in lattice parameters.

Lattice		Na_2O			NiO			TiO_2		
	Cubic				Cubic			Tetragonal		
	Exp.	Calc.	3	Exp.	Calc.	3	Exp.	Calc.	3	
	(Å)	(Å)	(%)	(Å)	(Å)	(%)	(Å)	(Å)	(%)	
a	5.500	5.469	0.56	4.178	4.210	0.77	4.594	4.428	3.61	
b	-	-	-	-	-	-	-	-	-	
c	-	-	-	-	-	-	2.959	3.069	3.72	

Table 4.8 Transferability of Buckingham interatomic potential across ternary oxides.

		•	_					•		
Lattice		NiTiO ₃			$Na_2Ti_3O_7$			$Na_2Ti_6O_{13}$		
	Rhombohedral			ľ	Monoclinic			Monoclinic		
	Exp.	Calc.	8	Exp.	Calc.	3	Exp.	Calc.	ε	
	(Å)	(Å)	(%)	(Å)	(Å)	(%)	(Å)	(Å)	(%)	
a	5.032	5.011	0.42	9.133	9.073	0.66	15.131	15.566	2.87	
b	-	-	-	3.806	3.768	1.00	3.745	3.732	0.35	
c	13.792	13.921	0.94	8.566	9.096	6.19	9.159	9.048	1.21	

Table 4.9 Transferability of Morse interatomic potential across binary oxides.

		•			L		•			
Lattice		Na ₂ O			NiO			TiO_2		
	Cubic				Cubic			Tetragonal		
	Exp.	Calc.	3	Exp.	Calc.	3	Exp.	Calc.	3	
	(Å)	(Å)	(%)	(Å)	(Å)	(%)	(Å)	(Å)	(%)	
a	5.500	5.320	3.27	4.178	4.188	0.24	4.594	4.572	0.48	
b	-	-	-	-	-	-	-	-	-	
c	-	-	-	-	-	-	2.959	3.004	1.52	

Table 4.10 Transferability of Morse interatomic potential across ternary oxides.

Lattice	NiTiO ₃				Na ₂ Ti ₃ O ₇			Na ₂ Ti ₆ O ₁₃		
	Rhombohedral			ľ	Monoclinic			Monoclinic		
	Exp.	Calc.	3	Exp.	Calc.	3	Exp.	Calc.	8	
	(Å)	(Å)	(%)	(Å)	(Å)	(%)	(Å)	(Å)	(%)	
a	5.032	5.074	0.83	9.133	9.616	5.29	15.131	15.551	2.78	
b	-	-	-	3.806	3.605	5.28	3.745	3.577	4.49	
c	13.792	13.978	1.35	8.566	8.871	3.56	9.159	9.626	5.10	

4.3.3 Energetics of disordered structures: Atomic distribution effects

The effect of sodium allocation between the alkali layers on the overall energetics were investigated. Sodium atoms were distributed equally and disproportionately to the individual sodium layers, while still maintaining the overall composition using a randomization code. The plentiful vacant sites in the sodium layer offers large number of distribution possibilities. Disorder is maintained in the transition metal layer as well by a similar approach with equal and disproportionate allocation between the layers while keeping the net Ti: Ni ratio at 2:1.

By solving these randomized structures, we investigate the energy landscape for equal and unequal distribution using atomistic simulations with Buckingham and Morse potential models. Though Morse clearly predicted better than Buckingham potential, we make use of both models to understand scaling effects (unit cell to supercell) on model robustness. It was found that the structures with completely random distribution had the highest energy values while those with equal distribution had the least energy values. Structures with disproportionate distribution of one atomic species (sodium or transition metal) occupied intermediate energy values. This trend is consistent with Buckingham and Morse potential sets as shown in Figure 4.9a and b. It is also observed that fewer structures successfully optimized for completely randomized configurations as some of the initial structures were too far away from the global/local minimum. The normalized energy values of all the optimized structures are plotted in the energy distribution curve for analysis.

The plateaus in the energy distribution curve corresponds to structures with fairly identical energy levels and similar local structural environment. This provides a method of grouping structures with comparable energy values. It was found that equal allocation of atoms to all layers

results in a curve with single plateau for Buckingham and Morse potentials as shown in Figure 4.9 a and b. These structures exhibit a Gaussian distribution with energy values fairly close to the mean energy (E_{Buck} =-106.1 eV, E_{Morse} =-40.3 eV) as shown in Figure 4.9c and d. The absence of multiple plateaus in the energy distribution curve and multiple peaks in the histogram point demonstrates that the optimized structures possess similar local environment.

Likewise, structures with equal distribution of transition metal atoms have a single plateau in the energy distribution curve and a single Gaussian peak in probability distribution histogram (Figure 4.10a and b). On the contrary, the simulation with unequal distribution of transition metals and random allocation of atoms yielded two plateaus in the energy distribution curve and two distinct peaks in the histograms (Figure 4.10c and d, and Figure 4.11) due to the splitting of energy levels in the optimized structures.

It was found that the high energy peak (E_{Buck} =-105.6 eV/mol, E_{Morse} =-40.06 eV/mol) corresponds to structures with large deviation in the transition metal content per layer from their true stoichiometry; diff_{Buck}= 2.07, diff_{Morse}=2.02 for Ni species, where 'diff'= (n-mean)/total, 'n' is the atom count per layer, 'mean' is the average atom count per layer for equally distributed structures and 'total' equals the total number of optimized structures.

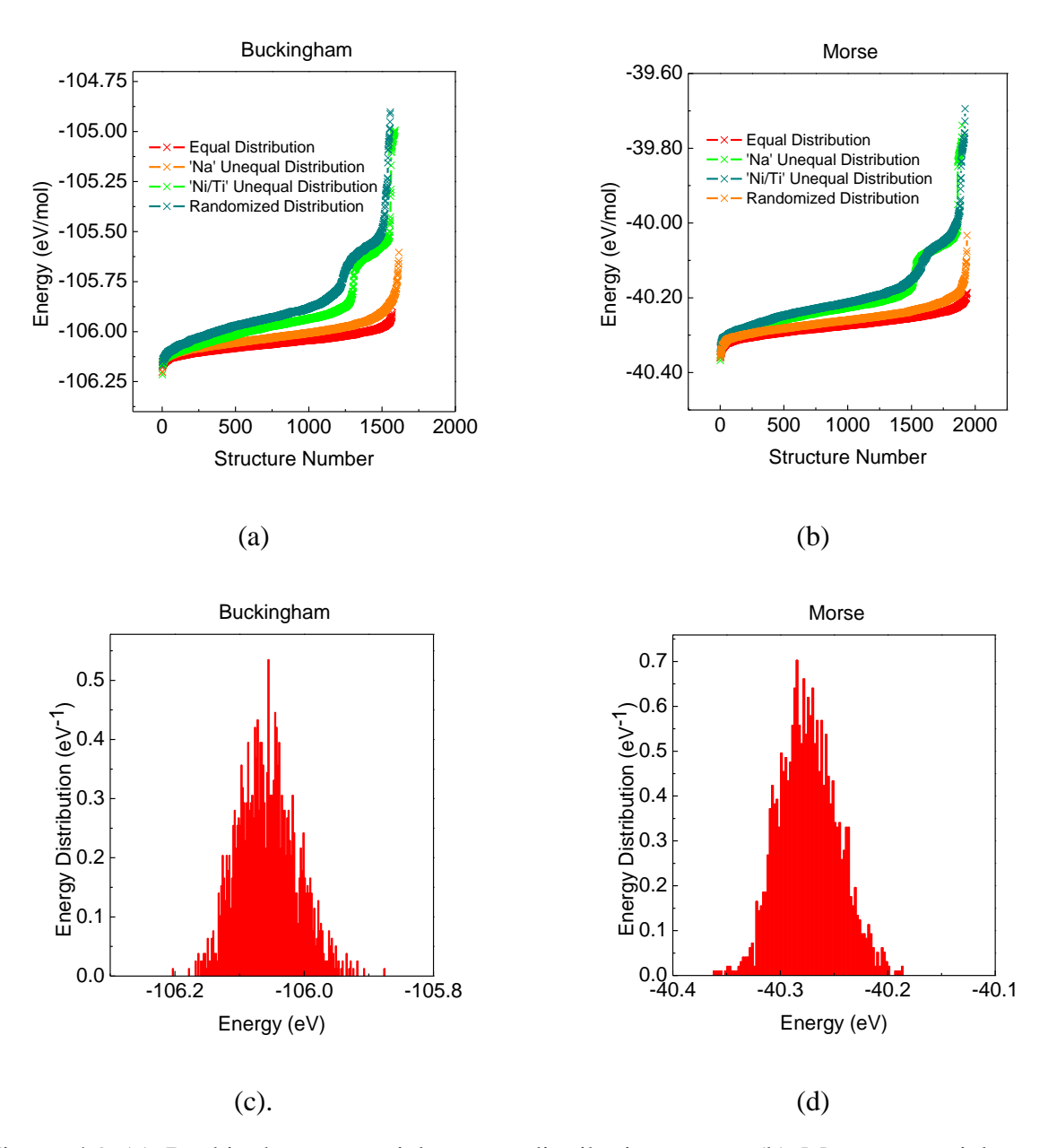


Figure 4.9 (a) Buckingham potential energy distribution curve, (b) Morse potential energy distribution curve, (c) probability distribution histogram of randomized structures with equal atomic distribution between layers using Buckingham potential, and (d) probability distribution histogram of randomized structures with equal atomic distribution between layers using Morse potential.

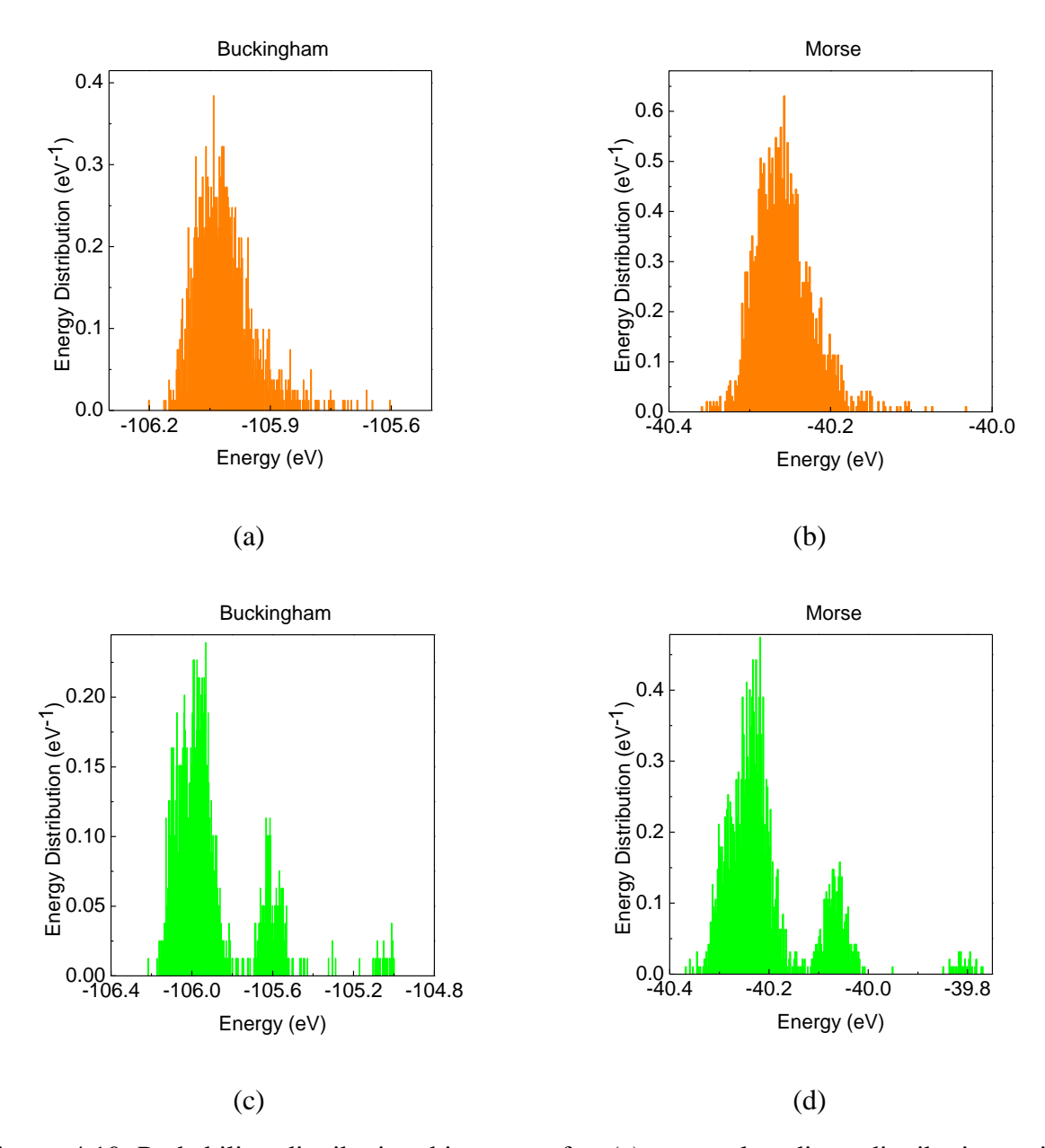
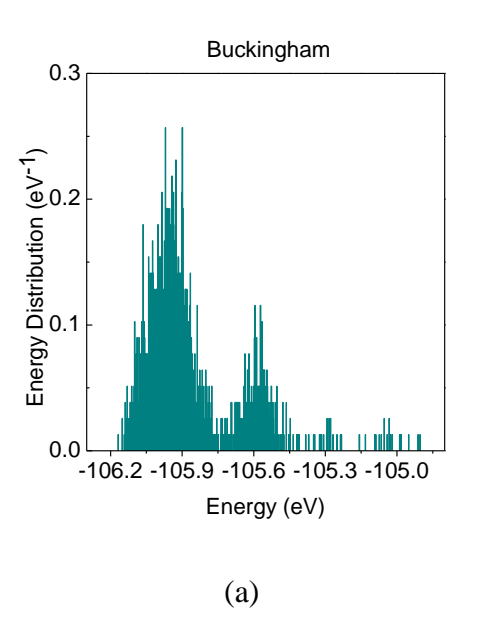


Figure 4.10 Probability distribution histogram for (a) unequal sodium distribution using Buckingham potential, (b) unequal sodium distribution using Morse potential, (c) unequal transition metal distribution using Buckingham potential, and (d) unequal transition metal distribution using Morse potential.



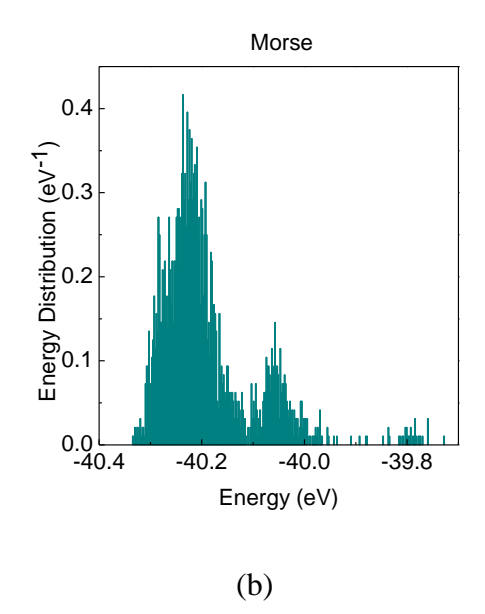


Figure 4.11 Probability distribution histogram for completely randomized structures using (a) Buckingham potential, and (b) Morse potential.

The structures that contribute towards the low energy peak (E_{Buck} =-105.95 eV/mol, E_{Morse} =-40.24 eV/mol) have transition metal content close to the stoichiometric value; diff_{Buck}= 0.84, diff_{Morse}=0.82 for Ni species. The peak splitting is clearly a consequence of unequal allocation of the transition metals between the layers and deviations from stoichiometry were found to be energetically unfavorable. On the other hand, sodium distribution study showed that the optimized structures contained fairly similar energy levels.

4.3.4 Energetics of ordered structures

The in-plane and thorough-plane ordered supercell structures were optimized to understand the energetics of these ordering schemes and disordered structures. The ordered structures failed to optimize with Buckingham potential due to unrealistically large core-shell separation distance. Highly unfavorable initial structures are likely to not optimize as the transition metal do not move significantly from their lattice positions during the structure optimization. This issue becomes

exacerbated in the presence of shells as titanium gets placed in the adjacent sites of the ordered structures. Morse potential yielded optimized structures for in-plane ordering and the energetics curve shows that the ordered structures consistently have higher energy values than disordered structures (ΔE =0.21 eV) demonstrating that long range ordering phenomenon is unfavorable for this composition (Figure 4.12).

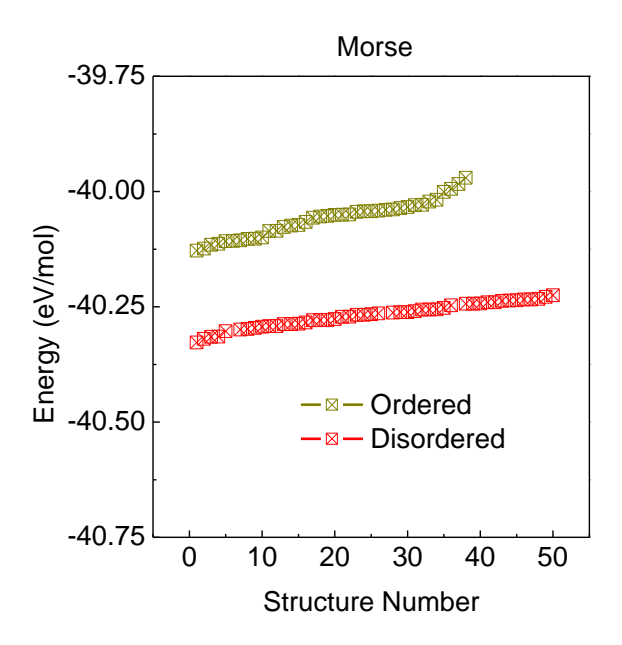


Figure 4.12 Energy distribution curve for ordered and disordered structures using Morse potential.

4.3.5 Simulated average structure

The supercell was sectioned into individual voxels and the probability of atomic distribution in each voxel was computed from all optimized configurations to generate the simulated nuclear density maps using MATLAB code. The density maps provide a graphical representation of the simulated average structures and are compared with the experimental density maps from Rietveld refinement. Figure 4.13a and b illustrates the 3D simulated nuclear density maps generated using

Buckingham and Morse potential sets. These maps show that the sodium density spots get compressed into oblate spheroidal form factor (minor axis in the 'ab' plane). Overall, the sodium density patterns are consistent with experimental nuclear density maps and the measured negative sodium displacement ratio. The spheroidal elongation aligns with the relative ease of in-plane sodium diffusion. 2D Isosurface sections are sliced along the {100} family of planes (Figure 4.13c and d) for distinguishing the sodium density spots in the two sites. The Na_f ellipsoids appear as low density spots (greenish), compared to Na_e ellipsoids (reddish) for both potential sets. This is consistent with the experimental site occupancy trend from Rietveld analysis and structural predictions.

The transition metal densities remain fairly spherical (Figure 4.14a and b) for both potential models, and confirms the validity of the isotropic model used in Rietveld refinement. Isosurface sections (Figure 4.14c and d) show that Morse potential yields more structures with offset transition metal atoms than Buckingham potential. Figure 4.15a and b confirms that oxygen density spots are also spherical. After energy minimization, the oxygen atoms still retain the AB|BA close-pack stacking sequence (typical of P2 structures), where | refers to sodium sheet, and do not deviate significantly from their equilibrium atomic positions for the majority of optimized structures. However, few structures did exhibit an overall displacement of all oxygen atoms while maintaining the P2 stacking sequence. This oxygen displacement also corresponded with shifts in transition metal and sodium atomic positions while maintaining the same crystal symmetry (identical space group). The offset oxygen density spots are evident in the isosurface cut-sections and occurs fairly readily for structures optimized with Morse potential. Since these offset structures retain the same overall symmetry and space group, this phenomenon cannot be attributed to any sort of phase transformations.

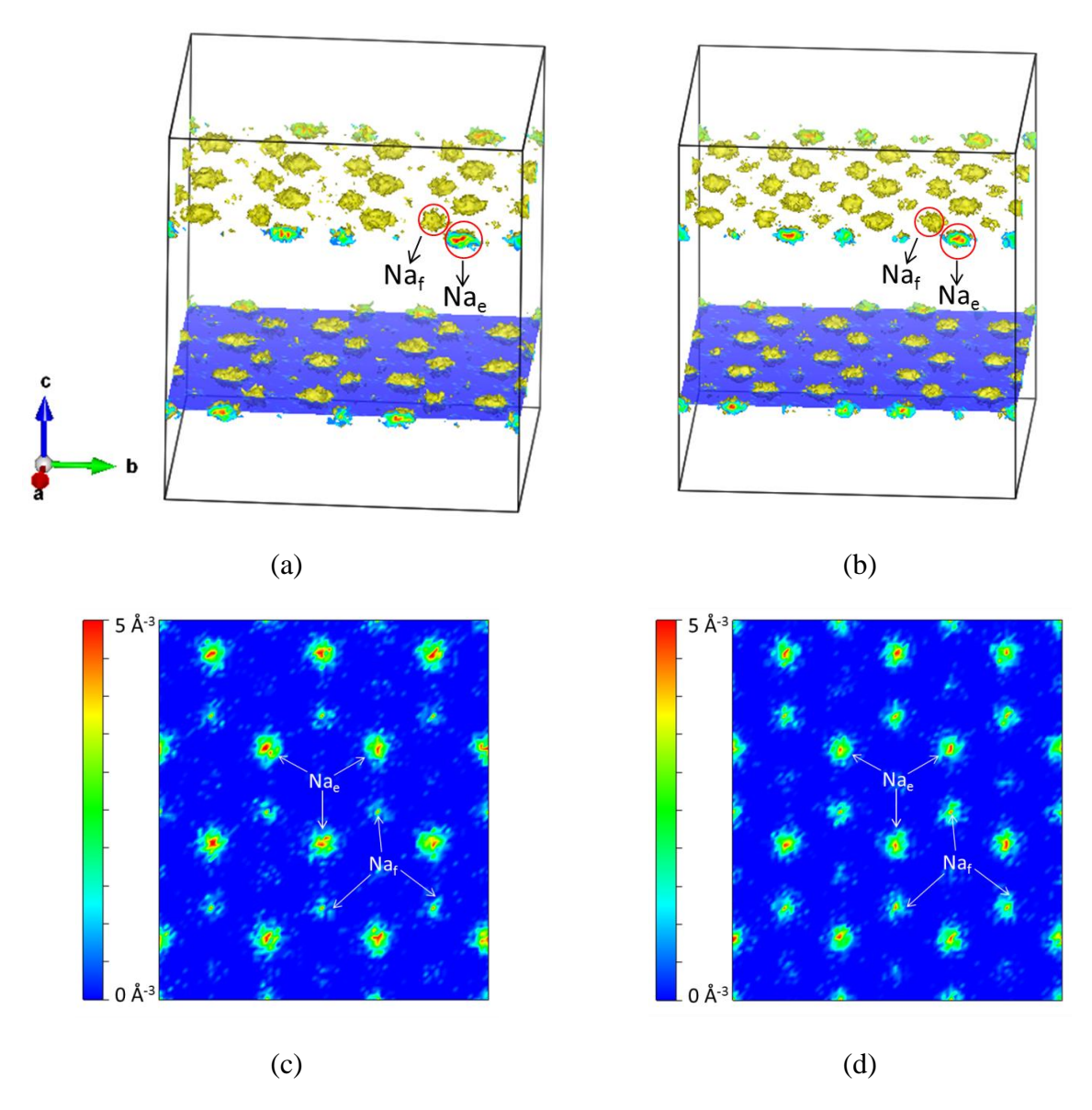


Figure 4.13 Simulated sodium probability density maps in (a) 3D using Buckingham potential and (b) 3D using Morse potential, (c) 2D along using Buckingham potential, and (d) 2D using Morse potential; selected 2D cut-sections are parallel to $\{100\}$ planes; minimum and maximum saturation levels set at 0 and 5 Å⁻³.

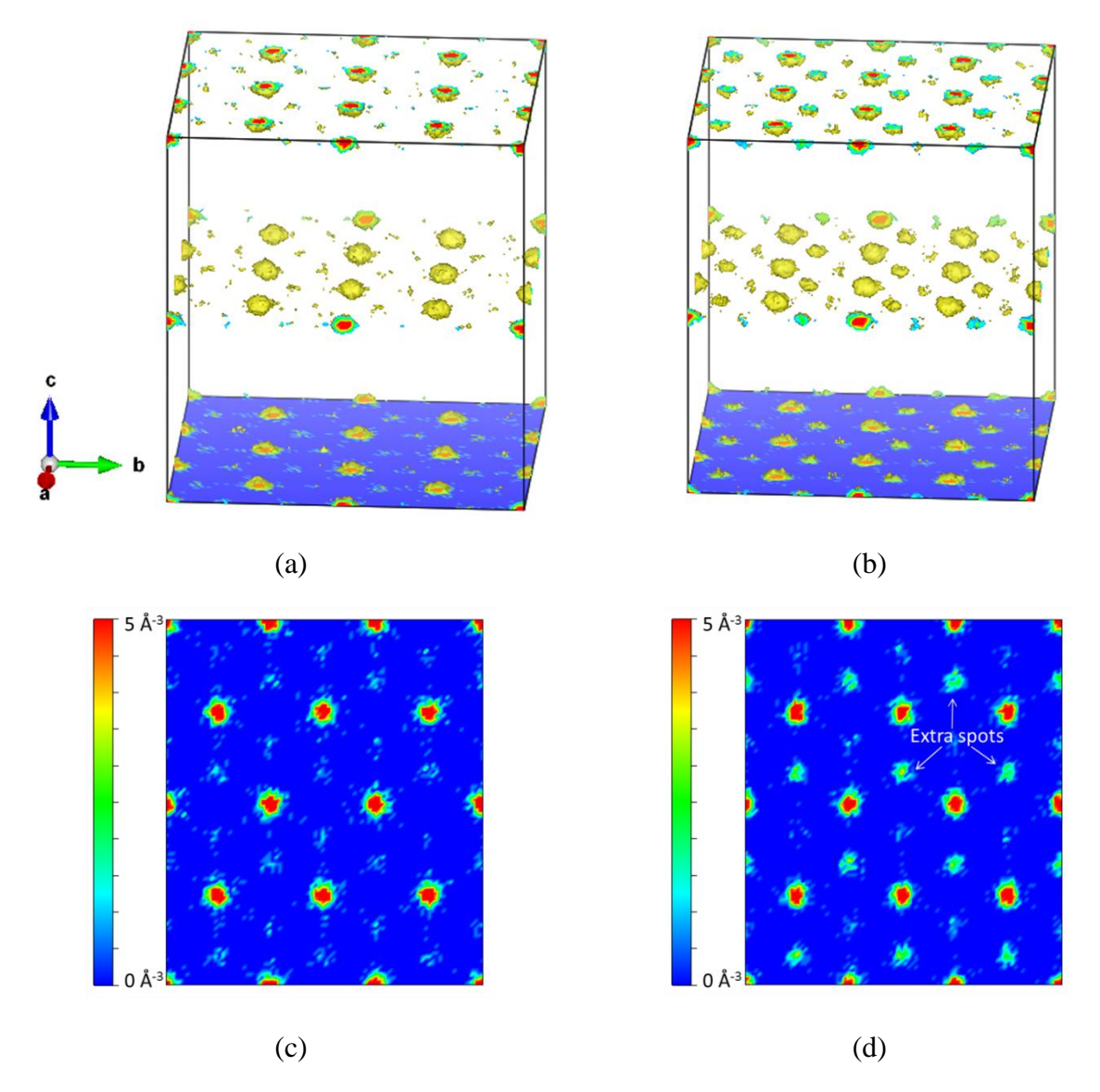


Figure 4.14 Simulated probability density maps for (a) sodium atoms in 3D using Buckingham potential and (b) sodium atoms in 3D using Morse potential, (c) sodium atoms in 2D using Buckingham potential, (d) sodium atoms in 2D using Morse potential; 2D cut-sections are parallel to {100} planes; minimum and maximum saturation levels set at 0 and 5 Å⁻³.

Evaluation of the energy distribution of these offset structures reveals that they have the same Gaussian distribution peak position as the non-offset structures showing that they have the same local environment. This also shows that the offset structures do not have a lower energy than non-offset structures to drive this structural re-organization. However, this phenomenon requiring a

concerted movement of all the atoms from their initial lattice positions poses an energy barrier and this restricts the extent of structural re-organization. This gets restricted by shell interactions in the Buckingham model. Morse model provides a stronger covalent bonding interaction and hence a higher tendency for the concerted motion.

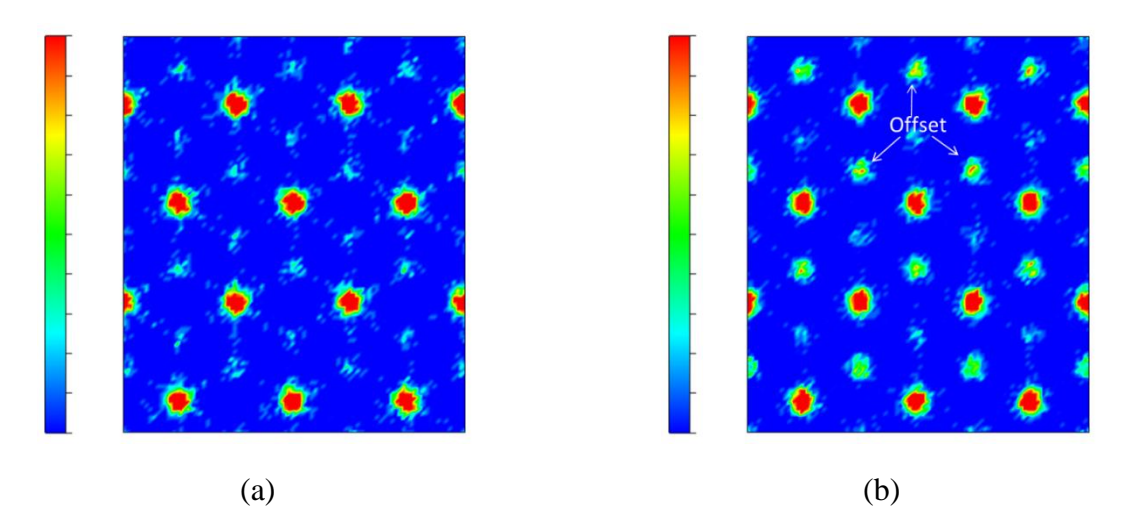


Figure 4.15 2D oxygen density maps using (a) Buckingham potential, and (b) Morse potential; 2D cut-sections are parallel to $\{100\}$ planes; minimum and maximum saturation levels set at 0 and 5 Å⁻³.

The displacement of close-packed oxygen atoms along the 'ab' plane can lead to lattice misalignments and create stacking faults in these layer-structured materials. These simulations are restricted to a domain size of roughly 1 nm (supercell size) to reduce computational time. The energy barriers for the displacive atomic movements would increases as the domains get larger in real materials and hence the extent of structures with stacking faults would eventually depend on the size of single crystalline domains. We anticipate that for sufficiently large crystallite size, the tendency for formation of stacking faults would be considerably hindered. Nevertheless, experimental studies report a tendency towards stacking fault formation in Na_xCoO₂, a layered oxide material. ⁴⁶ Future study would involve gathering experimental evidence for the presence

and extent of stacking fault in the investigated composition and their relevance to charge transport properties. The domain size can also be altered to match the percentage of stacking faults from the experiments to further increase the accuracy of the simulations.

4.3.6 Pair distribution function and probability density line-scans

Pair Distribution Function (PDF) analysis is a useful tool in the studying of local structure of disordered materials. PDF patterns would provide information on the presence and position of individual atoms in a predefined spherical radius. Given the lack of experimental PDF for the studied composition, we utilize PDFGUI to generate a pseudo-experimental PDF curve. It should be noted that the mean field approximation in the Rietveld refinement masks the local details and hence is referred to as 'pseudo-experimental' PDF curve. Nevertheless, it provides a decent baseline curve for comparison with simulation results.

PDF pattern of a typical mean energy structure (calculated in GULP) is compared with the Rietveld PDF pattern at 15K (Figure 4.16a and b). The peak positions of calculated patterns using Buckingham and Morse potentials are fairly comparable to those of the pseudo-experimental PDF pattern. This shows that the average structural features of the simulated structures are fairly consistent with the experimental data. The discrepancies in the PDF peak intensities are due to local structural details that are retained in the simulation experiments. The negative PDF peaks in the simulations are attributable to the titanium atoms with negative neutron scattering factor. Future work would involve collecting experimental PDF pattern without the mean field approximation for further analysis of the models.

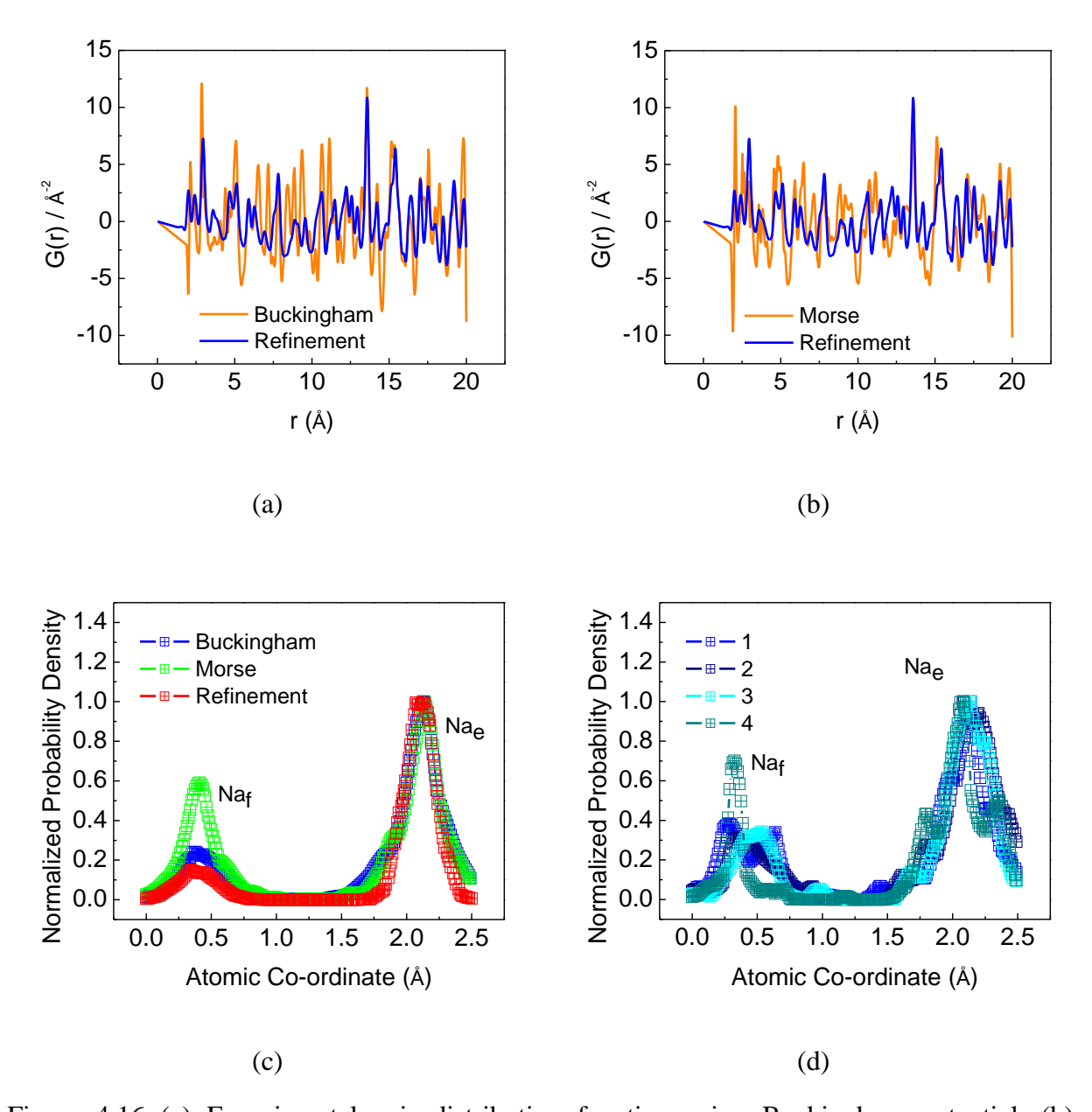


Figure 4.16 (a) Experimental pair distribution function using Buckingham potential, (b) experimental pair distribution function using Morse potential, (c) normalized probability density between Na_f and Na_e sites on the 'ab' plane comparing simulations with experiments, and (d) normalized probability density between four different Na_f-Na_e locations using Buckingham potential.

Figure 4.16c compares the averaged sodium probability density between Na_f and Na_e sites for simulated structures and refined structure (at 15K) along the 'ab' plane. This plot provides a semi-quantitative measure of comparing the simulated densities with experimental results and also

relates to the site occupancy ratio. The low temperature experimental data is compared as the thermal contributions are not explicitly captured in these static simulations. Overall, the Na_f peaks appear smaller than Na_e peaks due to their lower site occupancy. The Buckingham potential peak pattern is fairly consistent with the experiments while the Morse potential overestimates the Na_f site occupancy. We conclude that Buckingham potential provides a better description of the studied structure. Figure 4.16d. shows that the individual sodium probabilities do change considerably between different site pairs and is consistent with the fact that sodium atoms hop fairly readily between these sites.

4.4 Summary and future work

The average structural information of Na_{2/3}[Ni_{1/3}Ti_{2/3}]O₂ has been obtained using Rietveld refinement of neutron diffraction experiments at 15K and 300K. 194 space group (P63/mmc) structural model was found to adequate describe the Bragg reflections. Anisotropic thermal expansion co-efficients were calculated (β_a^{900C} =1.83×10⁻⁵Å/K, β_c^{900C} =17.65×10⁻⁵Å/K). While the Na_f site occupancy remained low (occ.=0.1699) at 15K due to repulsive transition metal interactions, they became more favorable (occ.=0.1751) at 300K due to higher thermal energy. The P2 ternary oxide displays considerable oblateness in sodium nuclear densities along the abplane as confirmed by the negative r-values (r_{Nae} =-0.37, r_{Naf} =-0.52), while oxygen nuclear densities remain fairly spherical (r_{O} =-0.07). Buckingham and Morse interatomic potentials were found to accurately predict the lattice parameters for the studied composition and model transferability was demonstrated for Na-Ni-Ti-O based oxide materials.

Equal distributed structures were found to be favored energetically while unequal distributed structures had considerably higher energy values. Equally distributed structures displayed a

Gaussian probability distribution showing that the most probable structures have mean energy values. The in-plane and thru-plane ordered structures were also found to be energetically unfavorable. Since the energy levels of the simulated structures were fairly identical, we predict that the local environment does not play a prominent role in the overall energetics.

We showed that the simulated density maps mirrored the experimental density maps fairly accurately for Buckingham and Morse potential models. However, few extra density spots were observed due to atomic displacement effects. Analysis of the offset structures confirm that they have the same crystallographic symmetry and hence identical space group as the non-offset structures. The offset structures were also found to have comparable mean energy value and Gaussian distribution as the non-offset structures. We anticipate that these structural reorganizations correlate with the simulation domain size and would result in stacking faults in real materials due to misalignment of lattice planes. Further experimental work is required to confirm the presence and extent of stacking fault in P2-NT phase. PDF curves revealed that Buckingham potential provides a better representation of sodium site occupancy than Morse potential. Future work would also require acquiring experimental PDF patterns for comparison with model results.

The learnings from the interatomic potentials, probability density maps and energy minimization technique from the atomistic simulations study can be further applied for more detailed investigations using Molecular Dynamics (MD) and Ab-initio calculations. This would also enable incorporation of electronic contributions that could not be explicitly accounted in these static simulations.

BIBLIOGRAPHY

BIBLIOGRAPHY

- 1. Islam, M. S. Ionic transport in ABO3 perovskite oxides: a computer modelling tour. *J. Mater. Chem.* **10**, 1027–1038 (2000).
- 2. Islam, M. S., Driscoll, D. J., Fisher, C. A. J. & Slater, P. R. Atomic-Scale Investigation of Defects, Dopants, and Lithium Transport in the LiFePO4 Olivine-Type Battery Material. *Chem. Mater.* **17**, 5085–5092 (2005).
- 3. Olson, C. L. & Nelson, J. Defect Chemistry, Surface Structures, and Lithium Insertion in Anatase TiO 2. *J. Phys. Chem. B* **110**, 9995–10001 (2006).
- 4. Lee, S. & Park, S. S. Atomistic Simulation Study of Mixed-Metal Oxide (LiNi1/3Co1/3Mn1/3O2) Cathode Material for Lithium Ion Battery. *J. Phys. Chem.* **116**, 6484–6489 (2012).
- 5. Tripathi, R., Wood, S. M., Islam, M. S. & Nazar, L. F. Na-ion mobility in layered Na2FePO4F and olivine Na[Fe,Mn]PO4. *Energy Environ. Sci.* **6**, 2257–2264 (2013).
- 6. Islam, M. S. & Fisher, C. A. J. Lithium and sodium battery cathode materials: computational insights into voltage, diffusion and nanostructural properties. *Chem. Soc. Rev.* **43**, 185–204 (2014).
- 7. Wang, Y., Huq, A. & Lai, W. Insight into lithium distribution in lithium-stuffed garnet oxides through neutron diffraction and atomistic simulation: Li7-xLa3Zr2-xTaxO12 (x=0-2) series. *Solid State Ionics* **255**, 39–49 (2014).
- 8. Pals, C. R. & Newman, J. Thermal Modeling of the Lithium/Polymer Battery. *J. Electrochem. Soc.* **142**, 3274–3281 (1995).
- 9. Doyle, M. & Newman, J. The use of mathematical modeling in the design of lithium/polymer battery systems. *Electrochem. Acta* **40**, 2191–2196 (1995).
- 10. Newman, J., Thomas, K. E., Hafezi, H. & Wheeler, D. R. Modeling of lithium-ion batteries. *J. Power Sources* **119-121**, 838–843 (2003).
- 11. Gomadam, P. M., Weidner, J. W., Dougal, R. a. & White, R. E. Mathematical modeling of lithium-ion and nickel battery systems. *J. Power Sources* **110**, 267–284 (2002).
- 12. Liao, Y. *et al.* Sodium Intercalation Behavior of Layered Nax NbS2 (0≤x≤1). *Chem. Mater.* **25,** 1699–1705 (2013).
- 13. Cabana, J. *et al.* Study of the transition metal ordering in layered NaxNix/2Mn1-x/2O2 (2/3 \leq x \leq 1) and consequences of Na/Li exchange. *Inorg. Chem.* **52**, 8540–8550 (2013).

- 14. Lee, D. H., Xu, J. & Meng, Y. S. An advanced cathode for Na-ion batteries with high rate and excellent structural stability. *Phys. Chem. Chem. Phys.* **15**, 3304–12 (2013).
- 15. Fielden, R. & Obrovac, M. N. Low Voltage Sodium Intercalation in NaxNix/2Ti1-x/2O2 $(0.5 \le x \le 1.0)$. *J. Electrochem. Soc.* **161**, A1158–A1163 (2014).
- 16. Shanmugam, R. & Wei, L. Na2/3Ni1/3Ti2/3O2: "Bi-Functional" Electrode Materials for Na-Ion Batteries. *ECS Electrochem. Lett.* **3,** A23–A25 (2014).
- 17. Shanmugam, R. & Lai, W. Study of Transport Properties and Interfacial Kinetics of Na2/3[Ni1/3MnxTi2/3-x]O2 (x = 0,1/3) as Electrodes for Na-Ion Batteries. *J. Electrochem. Soc.* **162**, A8–A14 (2014).
- 18. Yoshida, H. *et al.* P2-type Na(2/3)Ni(1/3)Mn(2/3-x)Ti(x)O2 as a new positive electrode for higher energy Na-ion batteries. *Chem. Commun.* **50**, 3677–3680 (2014).
- 19. Guo, S. *et al.* High-performance symmetric sodium-ion batteries using a new, bipolar O3-type material, Na0.8Ni0.4Ti0.6O2. *Energy Environ. Sci.* 1–8 (2015). doi:10.1039/C4EE03361B
- 20. Guo, H. *et al.* Na-deficient O3-type cathode material Na0.8[Ni0.3Co0.2Ti0.5]O2 for room-temperature sodium-ion batteries. *Electrochim. Acta* **158**, 258–263 (2015).
- 21. Larson, A. C. & Dreele, Von., R. General Structure Analysis System (GSAS), Los Alamos National Laboratory LAUR 86-748. (2004).
- 22. Toby, B. H. EXPGUI, A Graphical user interface for GSAS. *J. Appl. Crystallogr.* **34,** 210–213 (2001).
- 23. Ewald, P. P. Die berechnung optischer und elektrostatisher gitterpotentiale. *Ann. Phys.* **64**, 253–287 (1921).
- 24. Catlow, C. R. A. et al. Interatomic potentials for oxides. *Philos. Mag. A* 58, 123–141 (1988).
- 25. Dick, B. G. & Overhauser, A. W. Theory of the Dielectric Constants of Alkali Halide Crystals. *Phys. Rev.* **122**, 90–103 (1958).
- 26. Rønnau, A. A Closer Look at the TiO 2 (110) Surface with STM PhD thesis. 2, 17 (2003).
- 27. Pedone, A. *et al.* A New Self-Consistent Empirical Interatomic Potential Model for Oxides, Silicates, and Silica-Based Glasses. *J. Phys. Chem. B* **110**, 11780–11795 (2006).
- 28. Gale, J. D. & Rohl, A. L. The General Utility Lattice Program (GULP). *Mol. Simul.* **29**, 291–341 (2003).

- 29. MATLAB and Statistics Toolbox Release 2012b, The MathWorks, Inc., Natick, Massachusetts, United States.
- 30. Kraus, S, W. & Nolze, G. a program for the representation and manipulation of crystal structures and calculation of the resulting X-ray powder patterns. *J. Appl. Cryst.* **29,** 301–303 (1996).
- 31. Momma, K. & Izumi, F. VESTA 3 for three-dimensional visualization of crystal, volumetric and morphology data. *J. Appl. Crystallogr.* **44,** 1272–1276 (2011).
- 32. CrystalMaker. CrystalMaker. CrystalMaker Softw. Ltd (2013).
- 33. Proffen, T. & Billinge, S. J. L. PDFFIT, a program for full profile structural refinement of the atomic pair distribution function. *J. Appl. Crystallogr.* **32,** 572–575 (1999).
- 34. Cope, E. R. & Dove, M. T. Pair distribution functions calculated from interatomic potential models using the General Utility Lattice Program. *J. Appl. Crystallogr.* **40**, 589–594 (2007).
- 35. Juhás, P., Davis, T., Farrow, C. L. & Billinge, S. J. L. PDFgetX3: A rapid and highly automatable program for processing powder diffraction data into total scattering pair distribution functions. *J. Appl. Crystallogr.* **46**, 560–566 (2013).
- 36. Shin, Y. & Yi, M. Preparation and structural properties of layer-type oxides NaxNix/2Ti1-x/2O2. *Solid State Ionics* **132**, 131–141 (2000).
- 37. Shimono, T., Tanabe, D., Kobayashi, W. & Moritomo, Y. Structural Response of P2-Type NaxMnO 2 against Na+Intercalation. *J. Phys. Soc. Jpn.* **82**, 083601 (2013).
- 38. Petricek, V., Dusek, M. & Palatinus, L. Crystallographic Computing System Jana2006: General Features. *Z. Krist.* **229,** 345–352 (2014).
- 39. Tanabe, D., Shimono, T., Kobayashi, W. & Moritomo, Y. Temperature dependence of anisotropic displacement parameters in O3-type NaMO2 (M = Cr and Fe): Comparison with isostructural LiCoO 2. *Phys. status Solidi RRL* **8**, 287–290 (2014).
- 40. Zintl, B. & Baumbauch, H, H, V. Über Natriumoxyd. Zeitschrift für Anorg. und Allg. Chemie **198**, (1931).
- 41. Sasaki, S., Fujino, K. & Takeuchi, Y. X-ray Determination of Electron-density Distributions in Oxides: MgO, MnO, CoO, and NiO, and Atomic Scattering Factors of their Constituent Atoms. *Proc. Japan Acad. Ser. B* **21**, (1979).
- 42. Burdett, J, K., Timothy, H., Miller, G, J., Richardson Jr, J, W. & Smith, J, V. Structural-Electronic Relationships in Inorganic Solids: Powder Neutron Diffraction Studies of the Rutile and Anatase Polymorphs of Titanium Dioxide at 15 and 295 K. *J. Am Chem. Soc.* **109**, 3639–3646 (1987).

- 43. Liferovich, R. P. & Mitchell, R. H. Rhombohedral ilmenite group nickel titanates with Zn, Mg, and Mn: synthesis and crystal structures. *Phys. Chem. Miner.* **32**, 442–449 (2005).
- 44. Yakubovich, O, V. & Kireev, V, V. Refinement of the Crystal Structure of Na2Ti3O7. *Crystallogr. Reports* **48**, 24–28 (2003).
- 45. England, W. A., Goodenough, J. B. & Wiseman, P. J. Ion-Exchange Reactions of Mixed Oxides. *J. Solid State Chem.* **49**, 29–299 (1983).
- 46. Li, Q., Zhang, Y. & Xu, M. Unconventional Magnetic Transition in NaxCoO2 (x>0.7) Single Crystals. *J. Supercond. Nov. Magn.* **27**, 1235–1238 (2014).

5. SYNTHESIS, STRUCTURAL AND ELECTROCHEMICAL CHARACTERIZATION OF Na_{0.9}[Ni_{0.45}Ti_{0.55}]O₂, AN O-TYPE LAYER-STRUCTURED MATERIAL

5.1 Introduction

5.1.1 O3-type materials

The electrochemical and structural properties of P2-type titanate materials were investigated in the previous chapters. This chapter delves into characterizing the sodium intercalation/de-intercalation properties of O3-type titanate composition, $Na_{0.9}[Ni_{0.45}Ti_{0.55}]O_2$. Like P2-type materials, O3-type materials also possess layered structure with alternating stacking of sodium and transition metal sheets. O3-type materials have the prototypical α -NaFeO₂ structure, identical to the well-studied and commercialized LiCoO₂ chemistry. Quaternary O3-type oxides are attractive sodium intercalation electrode candidates due to High theoretical capacity due to higher sodium content

- i. High concentration of divalent transition metals (compared to P2 composition) enhancing the electron hopping and consequently electrical conductivity
- ii. Good ion transport properties facilitated by the 2D sodium slabs

However, the ion conductivity of O3-type are lower than the P2-type materials due to the sodium octahedral co-ordination and lower vacancy concentration. This has been established using computational and experimental studies. But, solid-state ion transport is often not the rate limiting step for titanate-based layered materials. The higher divalent transition metal concentration in the O3 materials promotes the formation of a percolating network and possibly ease limitations due to charge carrier transport processes.

5.1.2 Literature

O3-type materials are known to undergo multiple phase transitions, sodium/vacancy ordering during various stages of sodium deintercalation and these processes often lead to poor reversibility, and capacity retention. α-NaFeO₂ has an initial reversible capacity of 80 mAh/g but the capacity drops by 25% in 30 cycles with a relatively low charging voltage of 3.4 V. Extending the charging voltage to 4.0 V worsens the capacity fade to 80% at the end of 10 cycles. This large irreversible capacity loss has been attributed to the migration of iron to the sodium layers and subsequently blocking sodium transport. It is interesting to note that this migration issue is energetically favorable for O3 materials and unfavorable for P2 materials as the former structures retain octahedral co-ordination for both transition metal and sodium sites.

O3-NaCoO2 and O3-Na[Fe_{0.5}Co_{0.5}]O₂ shows a capacity decay of 7% in 30 cycles, and 16% in 50 cycles, respectively. O3-Na[Ni_{1/3}Co_{1/3}Fe_{1/3}]O₂ has 5% capacity drop in 20 cycles when cycled till 4.2 V with good electrochemical reversibility. The presence of large amount of cobalt promotes charge carrier mobility and hence this composition offers excellent high power performance. Further long-time cycling is required for this composition In 50 cycles, the capacity fade in O3-Na[Ni_{0.5}Mn_{0.5}]O₂ was reported to be 60% and it was further improved to 34% by electrolyte optimization by the addition of Fluorinated Ethylene Carbonate (FEC) additive. FEC additive effectively suppresses fade mechanisms by arresting side reactions as indicated by improved coulombic efficiency. Nevertheless, even with FEC additive, the intrinsic fade mechanism is still quite substantial. O3-Na[Ni_{1/3}Mn_{1/3}Co_{1/3}]O₂ cathodes (NMC) provide excellent capacity retention with no noticeable fade when cycled between 2-3.75 V for 50 cycles at C/5 rate.

From these literature reports, it becomes apparent that capacity fade is a common issue for many O3-type cathode materials and addressing this is crucial for further advancement of high-voltage, high-capacity cathode materials for Na-ion batteries. In addition to the aforementioned materials, several quaternary compositions were reported in light of growing interest in Na-ion battery chemistry. 8–11

5.1.3 Research Strategy

The focus of this research work is to investigate the influence of titanium on the electrochemical properties and phase transitions in Na_{0.9}[Ni_{0.45}Ti_{0.55}]O₂ composition using electroanalytical techniques such as impedance testing and step-potential technique, and ex-situ XRD testing. We anticipate that the presence of tetravalent titanium atoms provides a stabilizing influence in the transition metal layer due to the increased covalent bonding character (in Ti-O bonds) resulting in better cycleability than other O3-type transition metal oxides.

Recently, a titanate-based O3 material, Na[Ni_{0.5}Ti_{0.5}]O₂, was reported to have excellent capacity retention (only 6.8% drop in 100 cycles with 4.0 V charging voltage), high coulombic efficiency (96%), and good high-rate performance (90.5 mAh/g at 1C). However, this study lacks structural characterization to identify the presence and onset of phase transitions that are directly correlated with the reversibility of the sodium intercalation reactions and cycle-life performance. Also, the powders prepared in this study contained NiO impurity phase (electrochemically inert) that could be eliminated by optimized synthetic methods to achieve improved reversible capacitites. ¹²

5.2 Material synthesis & electrode fabrication

The O3NT oxide powders were prepared by firing the SPEX dry milled precursors at 1000 °C in a box furnace for 10 hours duration. The XRD pattern confirms that the synthesized powders are phase-pure (matches with the PDF reference code: 01-070-6690) without any impurity oxide phases as illustrated in Figure 5.1a. The reproduction of experimental XRD pattern by the predicted Bragg reflections confirms that this material crystallizes with space group R-3m. The calculated lattice parameters are: a=2.9983 Å, and c=16.1831 Å. The refined sodium occupancy value of 0.86 is fairly close to the target composition of 0.9.

The powders were comprised of agglomerates of micron-sized particles as shown by the SEM inset micrographs. The individual particles appear fairly dense and are micron-sized. The film electrodes consisted of the oxide particles embedded in a highly conductive network formed by carbon particles as depicted in the SEM and EDS mapped images (Figure 5.1b and c). The titanium is uniformly distributed in the individual particles demonstrating the absence of secondary titanium-rich phase/-depleted phases.

Composite electrode films were fabricated consisting of 80/10/10 weight ratio of active material, conductive carbon (Timcal C65) and Polyvinylidene fluoride binder. N-Methyl-2-pyrrolidone (NMP) was used as solvent for casting the film electrodes using the conventional doctor-blade technique. Aluminum was utilized as the substrate for casting the electrode films. After casting, the electrode films were dried using IR lamp overnight to remove the NMP with the same protocol as discussed in previous chapters. After overnight drying, the film electrodes were punched into 0.5" discs and transferred to glove box (<0.1 ppm H₂O and O₂) for storage before subsequent electrochemical testing.

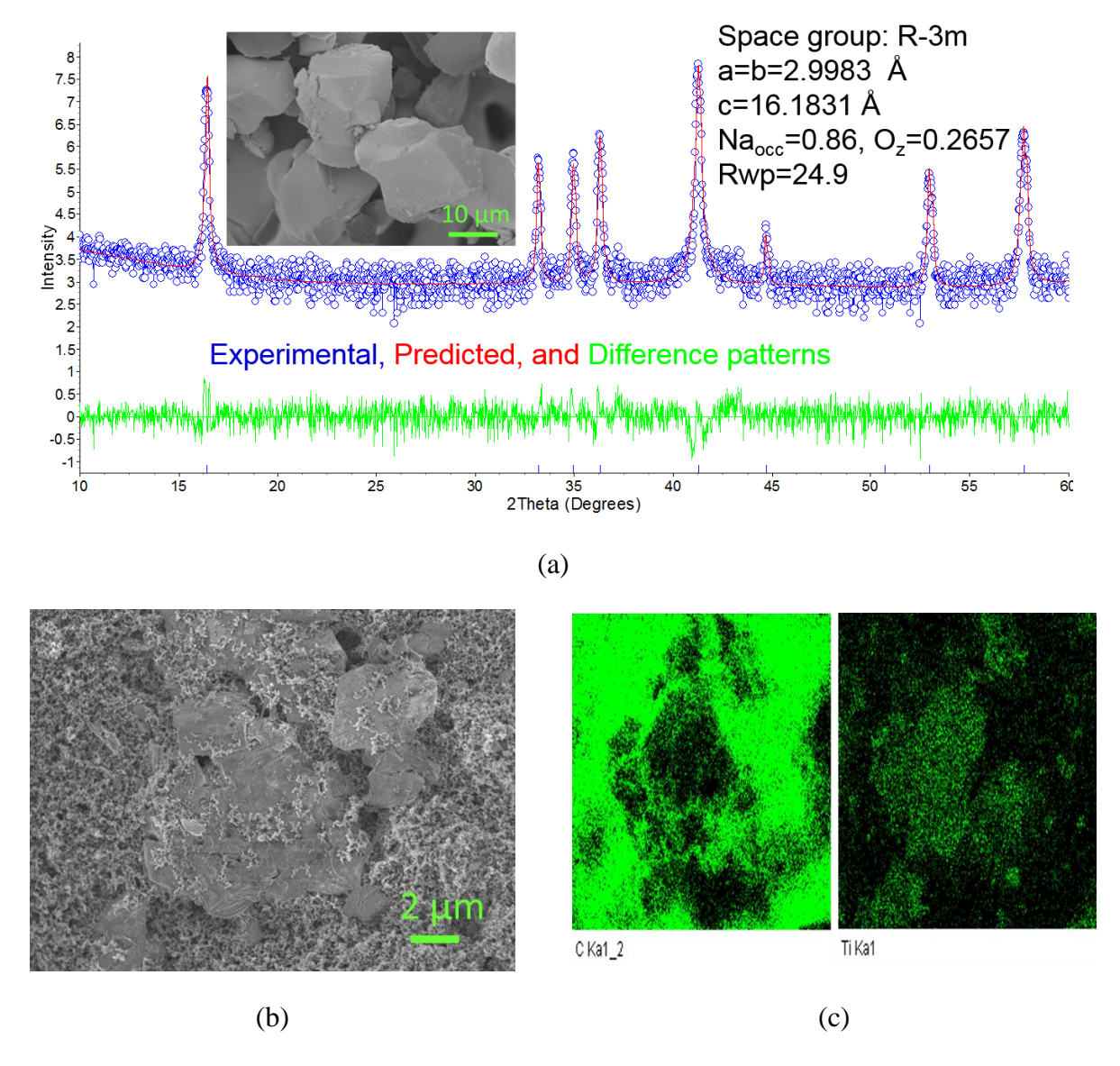


Figure 5.1 (a) Rietveld refinement of O3NT powders prepared by solid-state reaction at 1000 °C for 10 hours firing duration with inset figure showing powder morphology, (b) SEM morphology of composite film electrode showing O3NT particles embedded in a carbon network formed by conductive additive, and (c) EDS mapping of powders showing elemental distribution of carbon and titanium; refinement was performed with lab powder diffraction dataset using TOPAS software by Bruker Corporation. ^{13–16}

5.3 Electrochemistry

5.3.1 Voltage-composition curves: Galvanostatic Testing

O3NT has a high theoretical capacity of 229 mAh/g for complete removal of 0.9 moles of sodium per mole of the active material. Ideally, the sodium de-intercalation/intercalation reactions would follow a solid solution mechanism over a broad range of sodium content ($0 \le x \le 0.9$) with the activation of Ni^{2+/4+} redox couple as depicted in Equation 5.1.

$$Na_{0.9}[Ni_{0.45}^{II}Ti_{0.55}]O_2 \leftrightarrow Na_{0.9-x}[Ni_{0.90-}^{II}x_{/2}Ni_{x/2}^{IV}Ti_{0.55}]O_2 + xNa^+ + xe^- \qquad 5.1$$

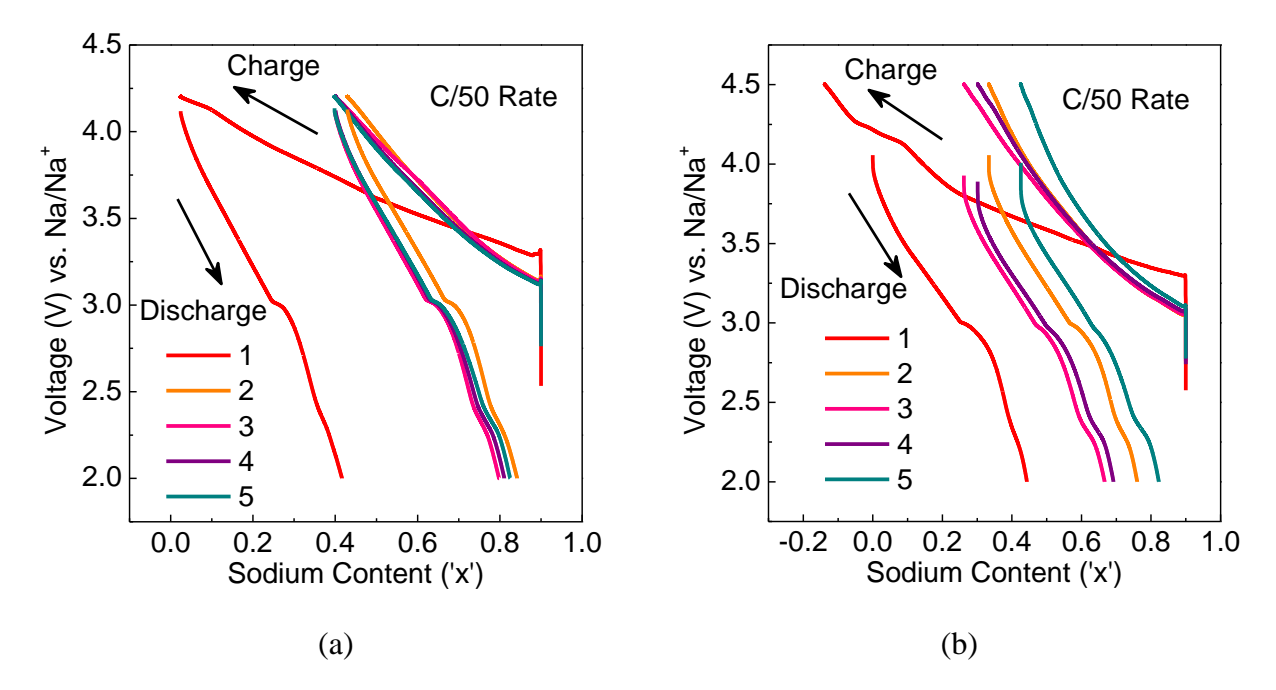


Figure 5.2 Voltage-composition curve of O3-Na_{0.9}[Ni_{0.45}Ti_{0.55}]O₂ under galvanostatic conditions of C/50 rate with (a) 4.2 V cutoff, and (b) 4.5 V cutoff; negative 'x' value during the 1st charging cycle is due to side reactions.

The charge/discharge curves of O3NT material tested under galvanostatic conditions of C/50 is shown in Figure 5.2 using the voltage-composition curves. The electrolyte utilized for this testing consisted of 0.5 M NaPF₆ salt dissolved in Ethylene Carbonate (EC)/Diethyl Carbonate (DEC)

(50/50 vol%). Anodized aluminum and copper rods function as current collectors for working electrode and metallic sodium, respectively. When the charging voltage is limited to 4.2 V, the 1st charge and discharge capacities are 222.7 mAh/g, and 99.7 mAh/g, respectively. The poor faradaic efficiency in the 1st cycle (44.8%) is due to electrolyte side reactions possibly facilitated by the active material. The 5th cycle charge and discharge capacities are 127.5 mAh/g, and 108. 4 mAh/g, respectively, with improved faradaic efficiency of 85%. The voltage profiles suggest that sodium intercalation/de-intercalation reactions can be sustained reversibly in the evaluated voltage window. Increasing the charging cutoff voltage to 4.5 V yields 1st charge and discharge capacities of 264 mAh/g, and 112.6 mAh/g, respectively. The first charging capacity is clearly higher than the theoretical capacity due to additional side reaction contributions. The discharge capacity improves slightly when the charging voltage is increased to 4.5 V due to the formation of more vacant sites in the charging step. However, the faradaic efficiency becomes slightly worse (1st cycle: 42.7%) in the highly oxidative potential regime. The voltage curves have small plateaus at 3.1 and 4.2 V, respectively, and a sloping profile in the remaining regions. The voltage plateaus and sloping regions are associated with two-phase and solid solution reactions, respectively, and are discussed further in the ex-situ XRD section.

5.3.2 Phase transitions: Ex-situ XRD

Experimental methods for ex-situ XRD characterization discussed in Chapter 3 were utilized for O3NT electrodes as well. The film electrodes were tested while exposed to ambient conditions for the preliminary trials. O3-type materials undergo phase transitions when sodium is extracted from the pristine composition and the crystal structure of the octahedral starting phase (O3) and prismatic low-sodium content phase (P3) are depicted in Figure 5.3. Due to the difference in the

oxygen stacking sequence, the O3 and P3 phases have different sodium co-ordination environments.

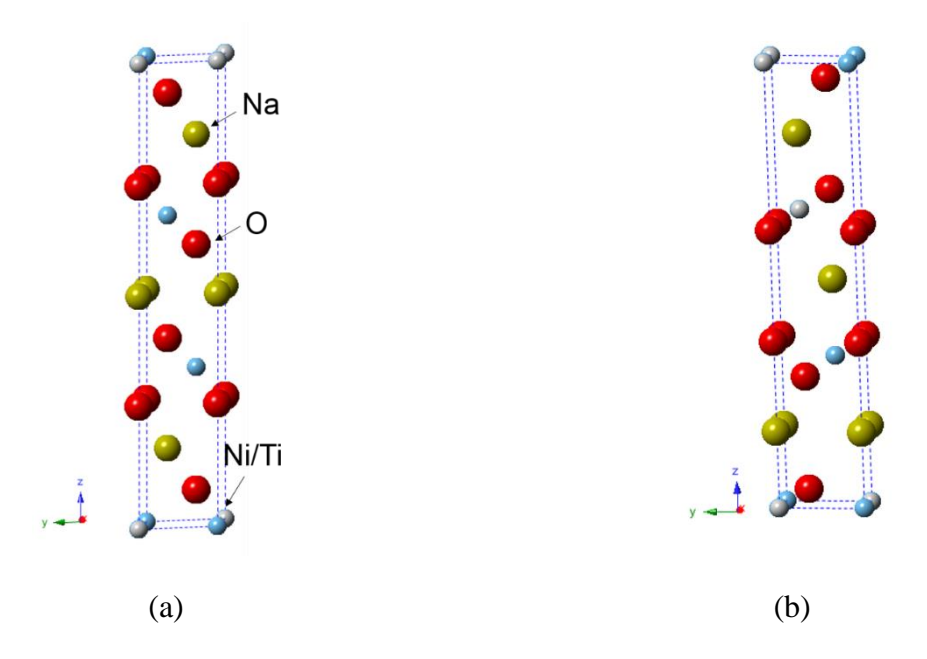


Figure 5.3 Crystal structure of (a) O3 phase with octahedral co-ordination of sodium, and (b) P3 phase with prismatic co-ordination of sodium demonstrating the different oxygen stacking sequence.

The initial O3NT phase with space group R-3m are depicted by 'x'=0.9 curve in Figure 5.4. Removal of small amounts of sodium (10%) causes the 16.5° peak intensity, characteristic of O3NT pristine phase, to drop considerably while a new peak forms at 15.8°. This peak splitting is associated with phase transformation from the initial O3 phase to P3 phase. This contrasts with other O3 compositions that have the phase transition sequence of O3 (hexagonal)-O3' (monoclinic)-P3 (hexagonal). At the measured compositions, there is no evidence of the formation of the low-symmetry O3' phase. The measured XRD reflections can be matched well with a two-phase mixture of O3+P3 as shown in Figure 5.5a. It is likely that the O3-O3' transition occurs in much smaller composition region of 0.9 > x > 0.81. Continued sodium extraction

results in higher amounts of P3 phase at the expense of O3 phase as indicated by decreasing intensities of 16.5° XRD peak.

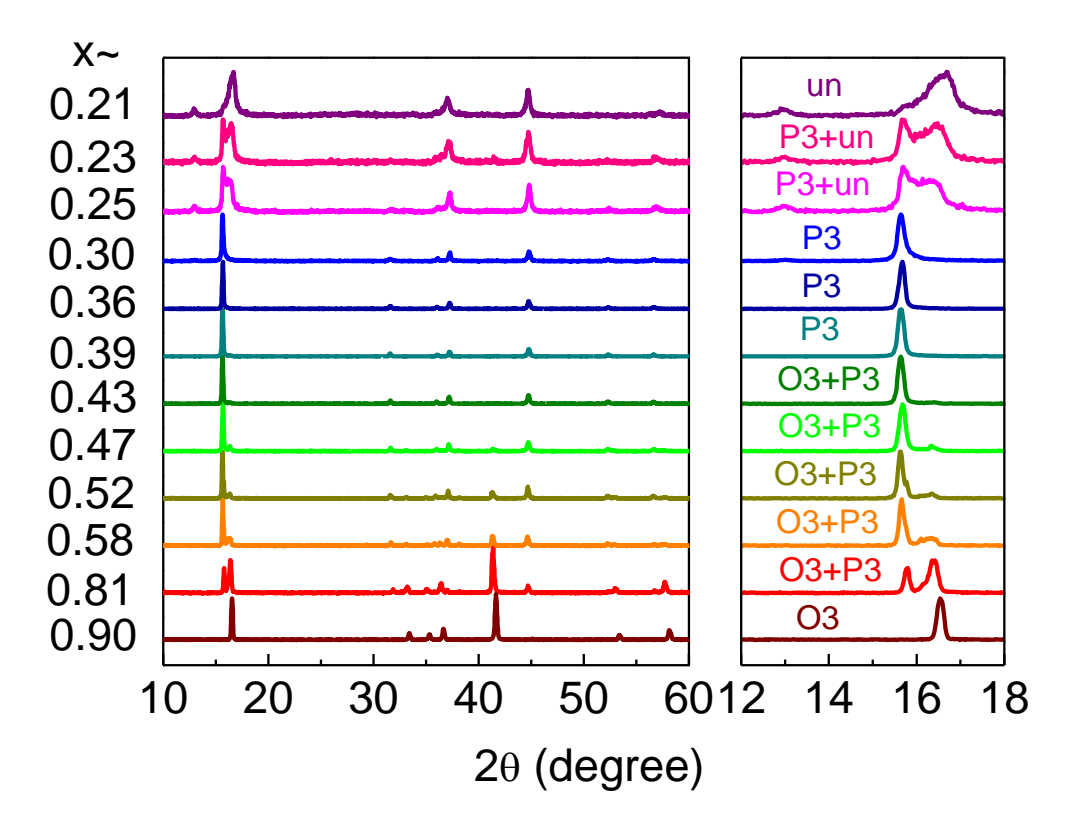


Figure 5.4 Ex-situ XRD characterization of O3NT phase at different sodium content; 'un' refers to the unidentified phase formed due to moisture intercalation of the low-sodium content phases.

The O3-P3 phase change involves gliding motion of oxygen layers to compensate the repulsive interactions between the closed-pack oxygen layers at low sodium contents. Hence, P3 phases are expected to have a higher Na-O bond length than the O3 phase. This is confirmed by longer average Na-O bond length in P3 phase (2.582 Å) than O3 phase (2.451 Å).

At sodium content (x) of 0.39, pure P3 phase is obtained and further sodium removal essentially leads to a solid-solution zone in the composition region of 0.39 > x > 0.30 and the refined patterns are shown in Figure 5.5b. When charging voltage is increased beyond 4.2 V, O3NT electrodes show

a splitting of the 15.6° peak and the resulting new peak has significant broadening. This peak splitting is not consistent with any P-related phases that were reported for other O3-materials. We suspect that this broadening is due to atmospheric interaction of the low sodium content P-phases (in composition zone of 0.30 > x > 0.21) that form at highly oxidative potentials. These phases can potentially accommodate water in the structure due to the large available spacing in the alkali slabs. Such water intercalation processes can result in loss of crystallinity due to exfoliation and this is consistent with the broadening of the XRD patterns. Efforts to mitigate moisture interaction by transferring the powders in inert atmosphere and limiting the atmospheric exposure to only a short time window (~10 minutes) with fast-scans were unsuccessful due to the extremely high moisture sensitivity of these phases. Future work to obtain structural information on the low-sodium content phases would require designing a hermetic in-situ electrochemical setup with XRD testing capability.

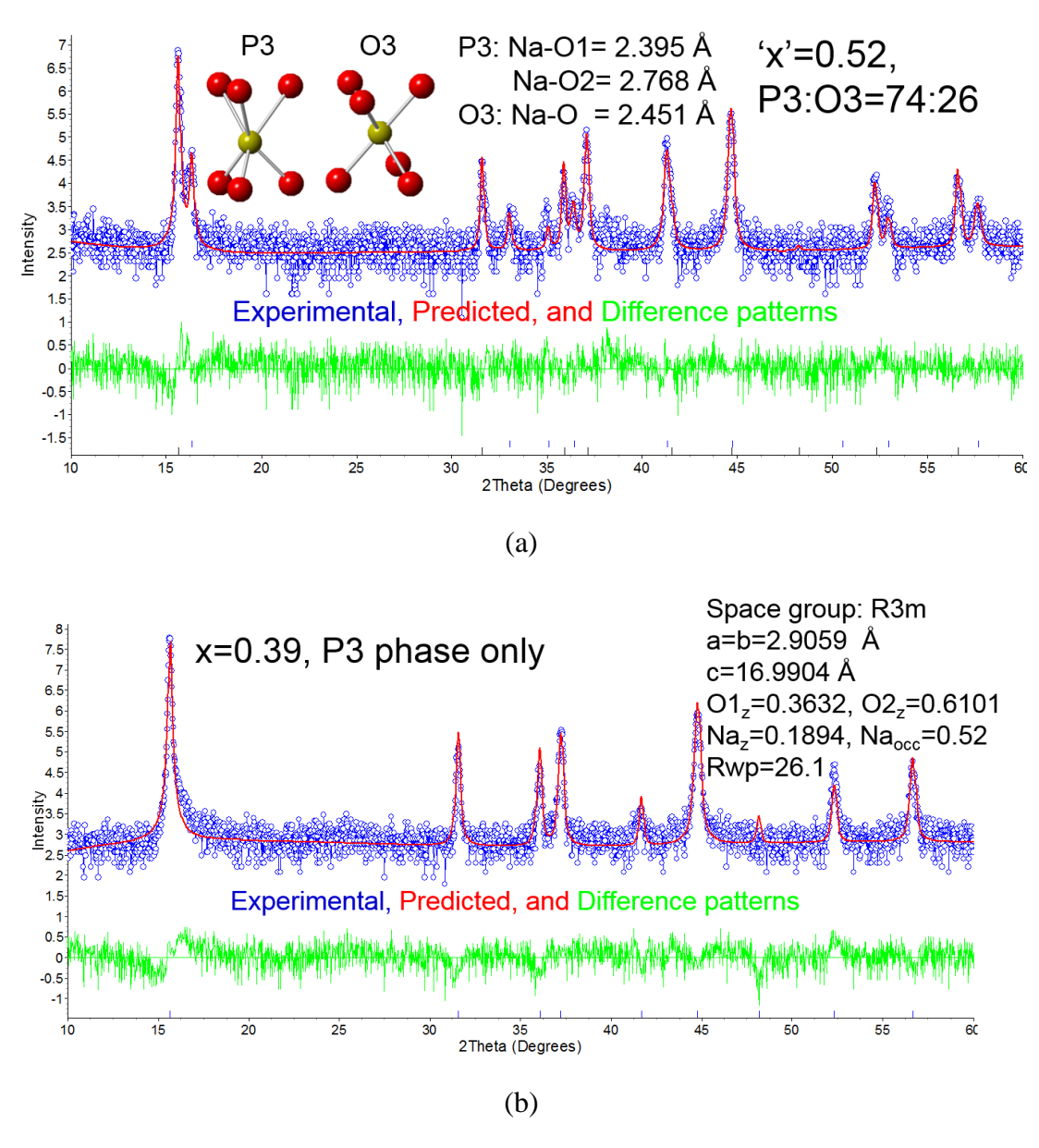


Figure 5.5 Rietveld refinement of O3NT electrode ($Na_x[Ni_{0.45}Ti_{0.55}]O_2$) prepared by electrochemical sodium extraction with (a) 'x'=0.52, and (b) 'x'=0.39; refinement performed using TOPAS software from Bruker Corporation, insert figures depict sodium co-ordination environment and Na-O bond lengths.

5.3.3 Equilibrium voltage profiles and solid-state diffusivity estimation: Potentiostatic Intermittent Titration Technique (PITT)

The PITT curves of O3NT material are depicted in Figure 5.6a and b. Overall, the voltage profile trends are consistent with the galvanostatic testing and show a smaller overpotential due to the low limiting current value (C/100). After the 1st cycle, the 4.2 V charge cutoff experiment has a very low voltage hysteresis between charge and discharge curves. However, the 4.5 charge cutoff experiment exhibits marked voltage hysteresis due to the insufficient reversibility of the low sodium content phases. The fairly good overlapping of the voltage profiles for both experiments, after the initial cycle, suggest that the O3NT material does not undergo deleterious structural changes due to repeated charge/discharge. The electrochemical stability for longer durations is further evaluated at faster charging rates in the cycling study.

The measured current transients while imposing the step potential in the PITT study are utilized for evaluating the solid-state diffusion co-efficient of sodium ions. Typically, an intercalation material undergoing phase transformation has two distinct current profiles and the rate of movement of the phase boundary essentially limits the diffusion process. However, the experimental current decays, shown in Figure 5.6c and d, do not match a phase separation material and is more consistent with an intercalation-type material. This is likely due to rapid movement of the phase boundary separating the O3 and P3 phases. We calculate the apparent chemical diffusion co-efficient using the theory discussed in chapter 3 for O3NT phase at various sodium contents. The fairly linear current regions further validate the applicability of this model.

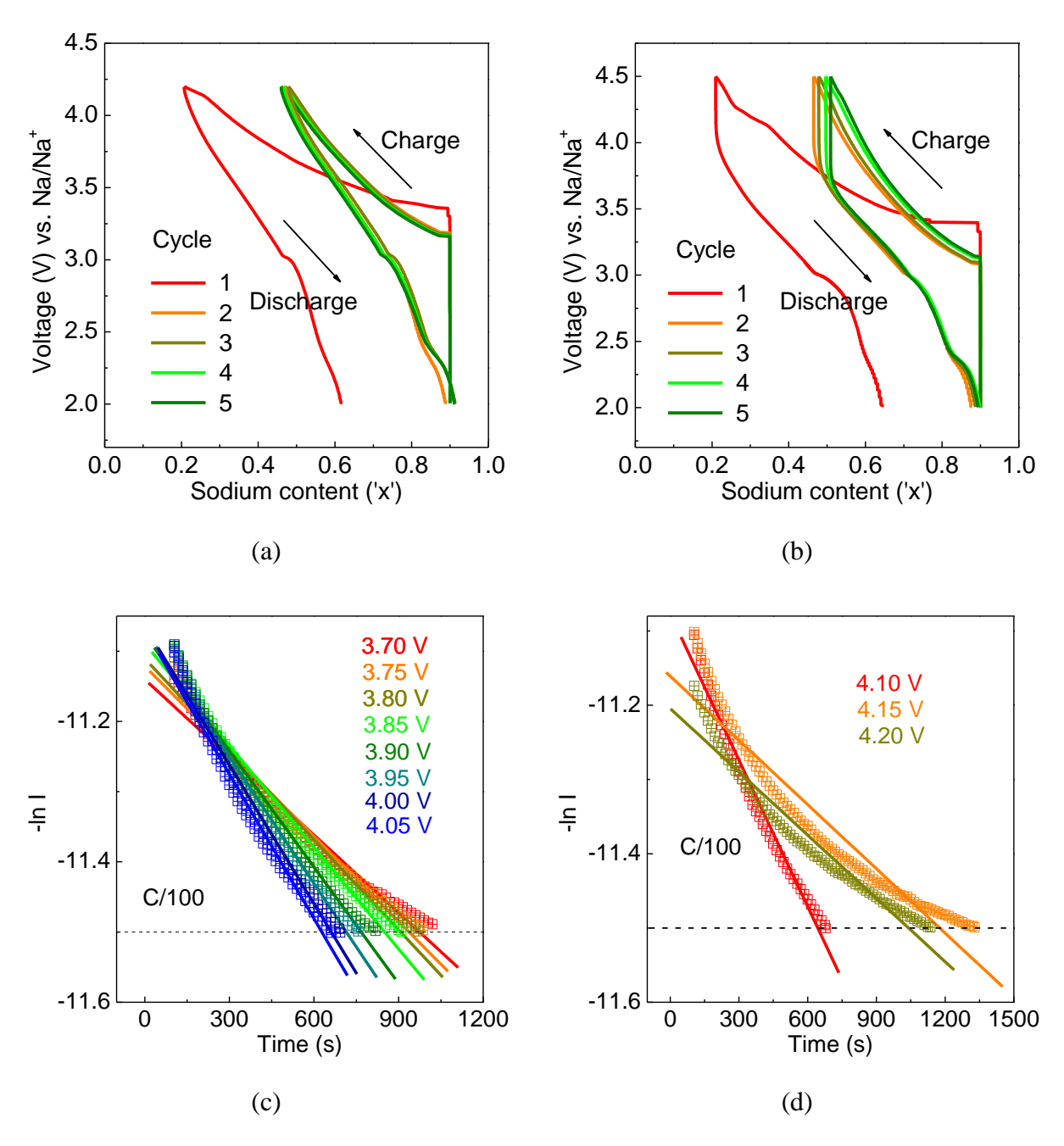


Figure 5.6 (a) Voltage profile of O3-Na_{0.9}[Ni_{0.45}Ti_{0.55}]O₂ using Potentiostatic Intermittent Titration Technique (PITT) with C/100 current and 4.2 V voltage limit, (b) Voltage profile using PITT with C/100 current and 4.5 V voltage limit, (c) current transient linear fitting with 4.2 V limit, and (d) current transient linear fitting with 4.5 V limit.

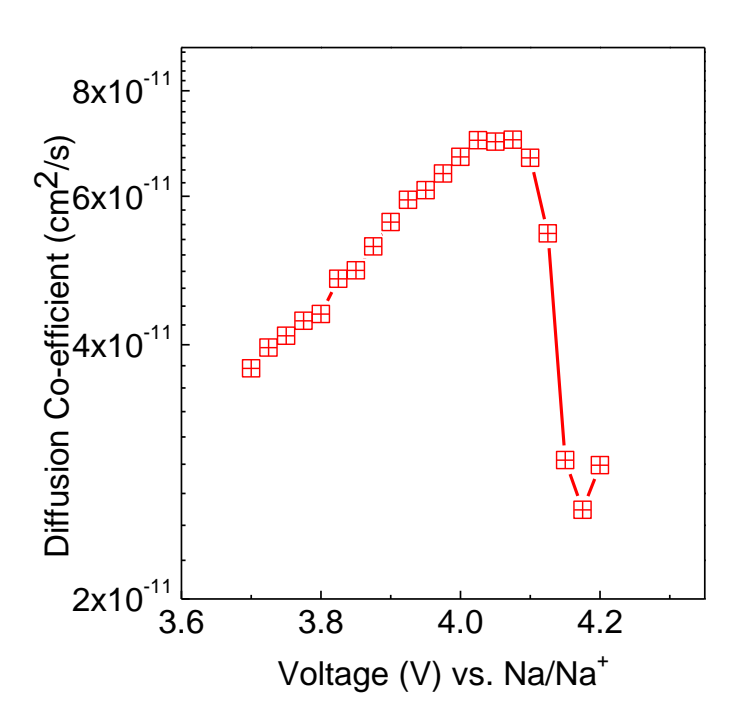


Figure 5.7 Solid-state diffusion co-efficient of sodium ions in O3NT material using potentiostatic intermittent titration testing.

The calculated sodium diffusion co-efficients are in the order of $5x10^{-11}$ cm²/s, considered reasonably fast for solid-state transport in intercalation materials as shown in Figure 5.7. The increase in diffusivity with voltage is consistent with the mechanism of faster ion hopping due to the creation of extra sodium vacant sites. The solid-solution model does not apply at high voltages as evidenced by non-linearity in current transient in Figure 5.6d.

5.3.4 Cycling study

5.3.4.1 Capacity retention at different voltage cutoffs

O3NT material was cycled between 2.0-4.0 V at C/10 rate for initial 10 cycles and C/2 rate subsequently as shown in Figure 5.8a. It is apparent that even with a relatively low voltage cutoff of 4.0 V, there is some irreversible side reactions in the initial cycles but the faradaic efficiency improves to 99% in the subsequent cycles at C/2 rate demonstrating excellent reversibility. The

discharge capacity values were measured to be 58.7 mAh/g, and 55.2 mAh/g at 25th and 115th cycle, respectively, corresponding to capacity decay of 6%. For the electrode cycled to 4.2 V, the faradaic efficiency remains at 54% in the 1st cycle showing that side reactions did not increase between 4.0 and 4.2 V experiments (Figure 5.8b). This results in a higher reversible capacity of 75.1 mAh/g, and 74.2 mAh/g at 25th and 115th cycle, respectively, with capacity retention of 99%. Typically, the capacity fade is directly correlated with the amount of extracted sodium ions due to strain induced failure mechanisms. However, the cycling trends do not match this theory and this discrepancy is likely due unaccounted random errors. Nevertheless, we show that the titanate-based O3NT material has excellent capacity retention. At charging voltages beyond 4.2 V, capacity values are still stable, contrary to other O3-materials, as shown in Figure 5.8c. But the practical discharge capacities are fairly restricted at these high operating voltages due to resistive contributions possibly from passivation films. This improved capacity retention is attributed to the stabilizing influence of titanium in the transition metal layer for this O3NT composition.

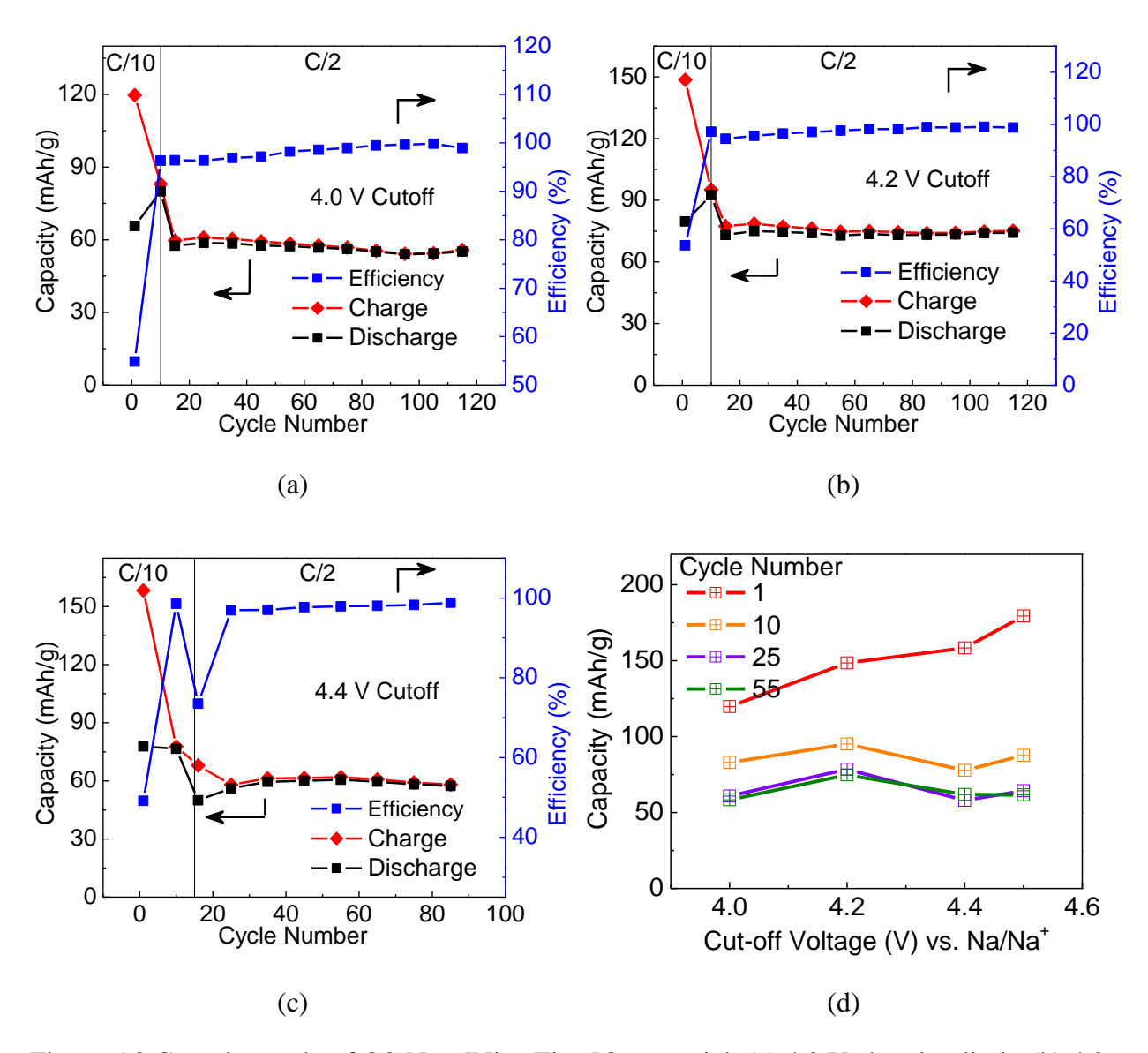


Figure 5.8 Capacity study of O3-Na_{0.9}[Ni_{0.45}Ti_{0.55}]O₂ material: (a) 4.0 V charging limit, (b) 4.2 V charging limit, (c) 4.4 V charging limit, and (d) Variation of charging capacity with different cut-off voltage limit.

The charging capacities are plotted as a function of cut-off voltage in Figure 5.8d. The 1st cycle charging capacities increase with charging cutoffs, as expected, with the maximum at 4.5 V charging voltage. However, 10th, 25th and 55th cycle charging capacity curves have a maximum at 4.2 V and the electrodes charged beyond 4.2 V have lower capacity. This suggests that the resistive

contributions possibly due to passivation films limit the capacity values at the high charging voltages (>4.2 V). Regardless of the passivation film effects, the presence of titanium in the O3NT material arrests the capacity fade significantly.

5.3.4.2 Impedance spectra evolution during cycling

The impedance spectra of the O3NT material collected after charging the films to 4.2 V during the cycling study are depicted in Figure 5.9a. The Nyquist plots have the following features: two overlapping arcs in the high frequency region, one arc in the medium frequency region and diffusional tail in the low frequency region. The Bode plot in Figure 5.9b provides the total impedance over the complete frequency domain and the arcs correspond to plateaus. The two high-frequency arcs are attributed to primary and secondary surface film resistance coupled with film capacitance in parallel RC circuit arrangement. The medium frequency arc is related to interfacial charge transfer reactions coupled with double layer capacitance. This equivalent circuit fitting approach is similar to P2NT phase impedance analysis discussed in Chapter 3. The circuit model, depicted in the inset Figure 5.9c, describes the physicochemical processes. Though Warburg component would adequately describe the linear tail at the low frequencies, it is not considered for diffusional analysis as the tail gets overshadowed during electrode cycling.

Repeated electrode cycling does not affect the interfacial kinetics and primary surface film resistances as shown in Figure 5.9c. This is consistent with the invariant high frequency arc and high frequency plateau in the Nyquist and Bode plots. However, the secondary surface film resistance increases gradually during cycling and this trend matches with the growing medium frequency arc that eventually overshadows the diffusional tail for a cycled electrode (n>80). The double layer capacitance (Cct), and secondary surface film capacitances (Csf2) are measured in mF range and the primary surface film capacitance (Csf1) fluctuates in mF-µF range (Figure 5.9d).

The latter fluctuation might be related to film instability. The demonstrated excellent capacity retention of O3NT phase is attributed to relatively minor changes in the physicochemical parameters that govern the sodium intercalation processes from impedance spectroscopy. The impedance parameters also show that interfacial charge transfer process is the slow rate-limiting processes for O3NT phase as it provides the largest resistive contribution. Quaternary compositions with cobalt, manganese substitutions can further promote the rate of charge carrier transport and further reduce the interfacial charge transfer resistance.

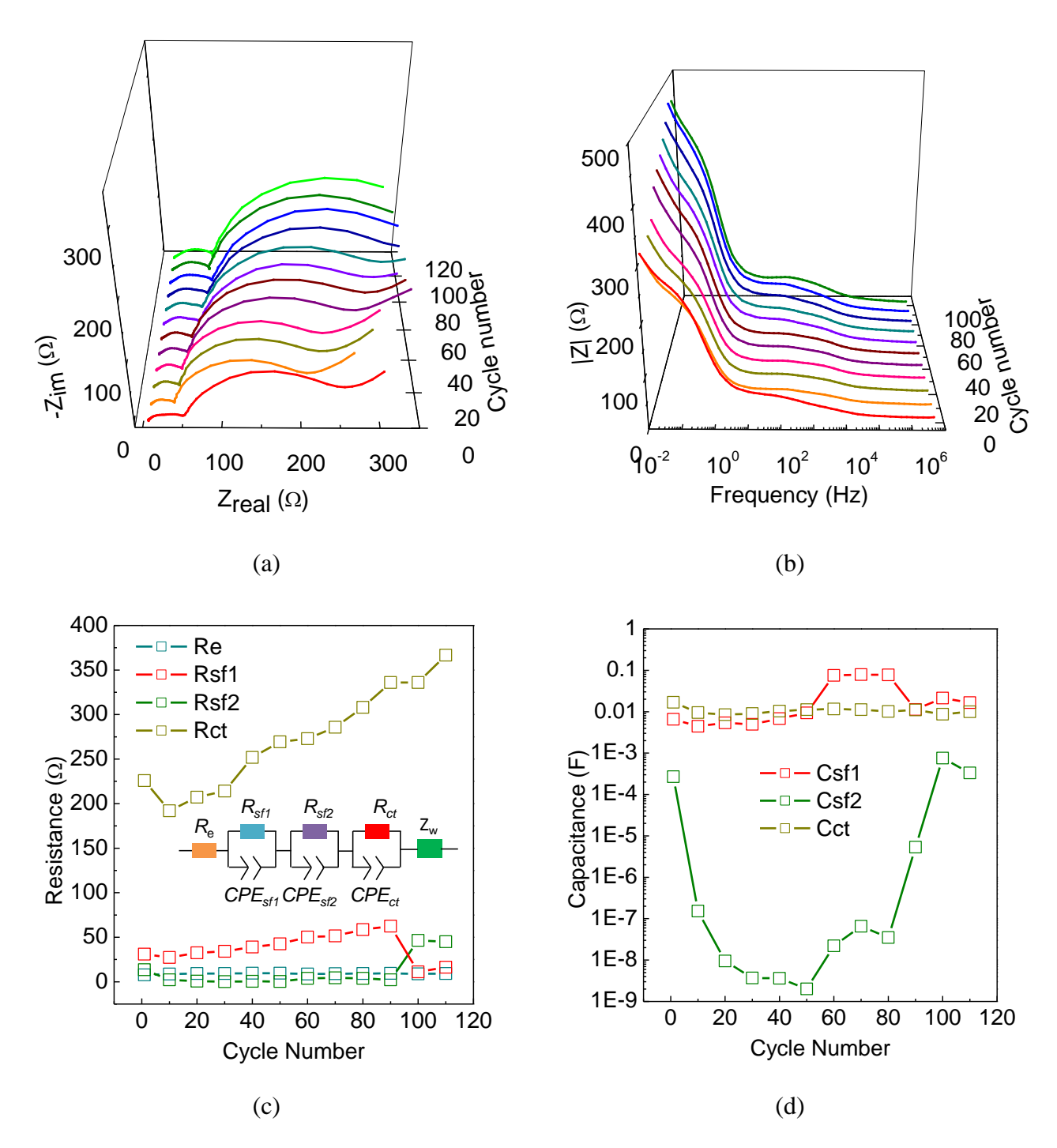


Figure 5.9 (a) Nyquist plot of O3NT electrodes charged to 4.2 V during cycling, (b) Bode plots of O3NT electrodes charged to 4.2 V during cycling, (c) Variation of electrolyte resistance (R_e), surface film resistances (Rsf1 and Rsf2), and charge transfer resistance (Rct) during cycling, and (d) Variation of double layer capacitance (Cdl) and surface film capacitances (Csf1 and Csf2).

5.3.4.3 Sodium metal deactivation: Prolonged cycling

Figure 5.10 represents the variation of the maximum counter electrode potential during each cycle with cycle number during the cycling study of O3NT electrode with 4.2 V cutoff. The counter electrode potential is measured with respect to the sodium reference electrode. Under open circuit conditions, the counter electrode potential would be the same as the reference electrode and the measured ΔV would read zero. At galvanostatic conditions, the voltage profile shows a small overpotential caused by kinetic or mass transport limitations at the counter electrode/electrolyte interface.

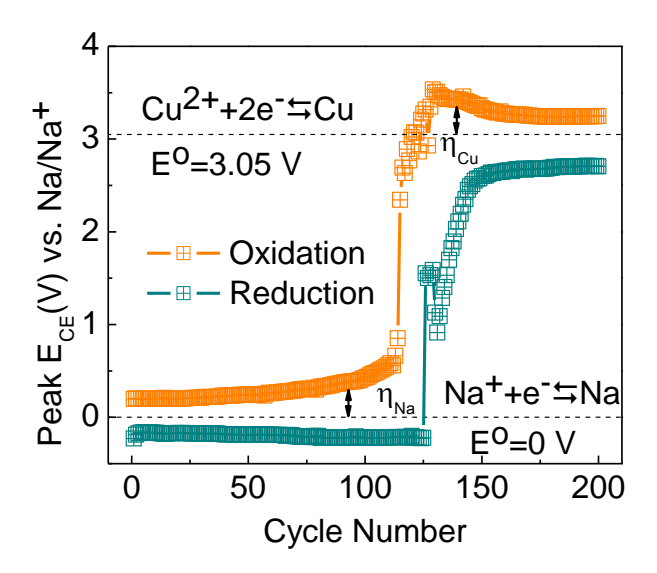


Figure 5.10 Variation of peak counter electrode potential with cycle number during galvanostatic cycling measured against Na/Na^+ reference electrode; ideally the measured voltage would be zero at the counter electrode as it has the same chemical potential as the reference electrode.

Upon repeated cycling, it is evident that the counter electrode peak voltage shifts drastically from zero towards 3 V. They measured voltage values are fairly close to the standard reduction potential of copper that is used as the current collector rod. During a discharge run, oxidation reaction needs to be supported at the counter electrode and this is typically through oxidation of

metallic sodium to sodium ions. When the sodium ions gets plated (reduction) during the subsequent charging run, the deposited sodium tends to be fairly powdery and has poor adhesion resulting in loss of active sodium metal. Repeated cycling leads to continual depletion of the active sodium metal surface due to this de-activation process. Further cycling leads to copper rods getting etched and large overpotential (typically beyond cycle number~120). This effect manifests as a capacity fade during the cycling studies when in actuality the issue is only due the counter electrode. The continual deactivation of the counter electrode has limited the cycling runs to ~100 cycles. One proposed method to avoid this is to directly use an intercalation-based anode and avoid sodium plating completely. However, this requires careful selection of a suitable anode intercalation material with good electrochemical stability and little irreversible capacity losses.

5.3.5 Rate testing

O3NT material provides discharge capacity values of 74.9 mAh/g, 71.2 mAh/g, 60 mAh/g, 47.8 mAh/g, and 30.4 mAh/g at C/10, C/5, C2, 1C, and 2C, respectively as shown in Figure 5.11a. The reduced capacities at high currents is linked to increasingly steeper sloping voltage curves (Figure 5.11b) at relatively long charge/discharge timescales. This is consistent with the impedance measurements that demonstrate interfacial charge transfer limitations at medium and low frequency regions. Nevertheless, O3NT phase has improved capacity values at higher currents than P2-NT phase due to the higher Ni/Ti ratio in the latter. The charge carrier transport (electron/holes) is facilitated primarily through the nickel atoms (Ni^{2+/3+} states) in the transition metal layer. Hence, a higher concentration of the nickel atoms results in the formation of a percolating network promoting facile movement of the charge carrier species.

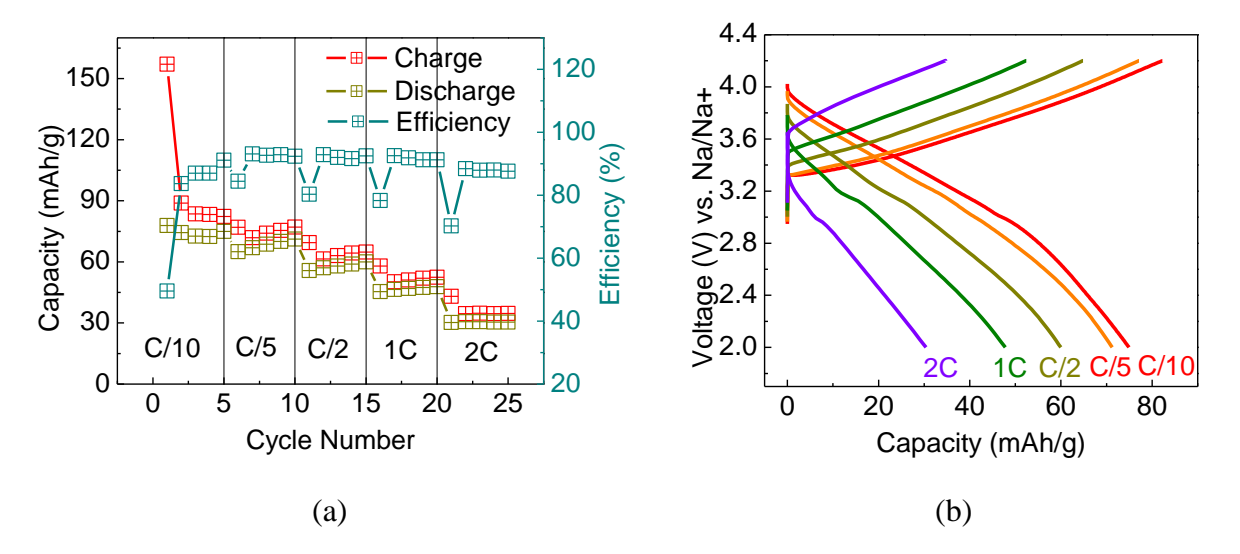


Figure 5.11 Rate performance testing of O3-Na_{0.9}[Ni_{0.45}Ti_{0.55}]O₂ material with 4.2 V cut-off voltage (a) capacity retention, and (b) voltage profiles.

5.4 Summary and future work

In this chapter, we study the electrochemistry of layered structured materials with octahedral coordination (O3) of sodium as they possess high theoretical capacity. These O3 materials suffer from capacity fade due to electrochemically driven phase separation and we characterize titanium based composition (O3NT) to impart structural stability by utilizing the covalent bonding character of titanium.

Phase-pure O3NT powders were prepared by solid-state reaction and characterized by XRD and SEM. Galvanostatic testing confirms that this composition supports reversible sodium intercalation/de-intercalation by activating the Ni^{2+/4+} redox couple while titanium remains invariant at 4+ valence state in the transition metal layer. PITT shows that a small voltage hysteresis between charge/discharge curves when the material is cycled with 4.2 V cutoff validating the electrochemical reversibility. The hysteresis becomes larger for films charged to 4.5 V due to irreversibility associated with newly formed phases. Ex-situ XRD shows that the O3

phase converts to P3 phase for small sodium removal resulting in the formation of a two-phase region and this region occurs for 0.81 > x > 0.39. This phase transformation involves gliding motion of the closed-pack oxygen layers due counteract the increasing repulsive interactions between oxygen layers. Pure P3 phase forms at 'x'=0.39 and a solid-solution domain is reported for 0.39 > x > 0.30. The quality of XRD pattern on powders with even lower sodium content were insufficient for structural analysis due to moisture interaction effects.

Cycling studies support that operating in the O3-P3 domain provides excellent capacity retention of 99% at the end of 115 charge/discharge cycles at C/2 rate. This confirms that titanium does provide a strong stabilizing influence by suppressing the capacity fade. The presence of P3 solid-solution regime over a broad voltage window allows for structural stability without significant capacity losses. Electrodes charged to high voltage of 4.5 V also have stable albeit lower capacity values. Impedance spectroscopy confirms that the rate of change of the physicochemical parameters that govern the sodium intercalation processes is relatively small supporting the excellent capacity retention characteristics. Rate study confirms that O3NT phase has improved performance compared to the P2NT phase due to the presence of higher nickel content in the transition metal layer aiding the charge carrier transport processes.

Structural characterization of the low-sodium content phases is essential to identify the phases and this requires further in-situ electrochemical-XRD testing. Given that the titanate-based composition provides stable capacity retention at high voltages (4.5 V) despite the phase transitions, future work can attempt at coating the oxide particles with an ion-conducting/inert passivation layer that can inhibit side reactions by limiting the electrolyte contact area. Potential coating materials include sodium zirconium silicophosphate, sodium yttrium silicate, β -alumina,

aluminum oxide, etc. ^{19–23} Alternatively, electrolyte additives such as FEC can also be employed to reduce the high-voltage side reactions. These approaches can potentially provide higher reversible capacities by allowing high voltage operation while utilizing the inherent stability effect provided by the titanate composition.

BIBLIOGRAPHY

BIBLIOGRAPHY

- 1. Yabuuchi, N., Yoshida, H. & Komaba, S. Crystal structures and electrode performance of alpha-NaFeO2 for rechargeable sodium batteries. *Electrochemistry* **80**, 716–719 (2012).
- 2. Lee, D. H., Xu, J. & Meng, Y. S. An advanced cathode for Na-ion batteries with high rate and excellent structural stability. *Phys. Chem. Chem. Phys.* **15**, 3304–12 (2013).
- 3. Yoshida, H., Yabuuchi, N. & Komaba, S. NaFe0.5Co0.5O2 as high energy and power positive electrode for Na-ion batteries. *Electrochem. commun.* **34,** 60–63 (2013).
- 4. Vassilaras, P., Toumar, A. J. & Ceder, G. Electrochemical properties of NaNi1/3Co1/3Fe1/3O2 as a cathode material for Na-ion batteries. *Electrochem. commun.* **38,** 79–81 (2014).
- 5. Komaba, S. *et al.* Study on the Reversible Electrode Reaction of Na1-xNi0.5Mn0.5O2 for a Rechargeable Sodium-Ion Battery. *Inorg. Chem.* **51**, 6211–20 (2012).
- 6. Komaba, S. *et al.* Fluorinated Ethylene Carbonate as Electrolyte Additive for Rechargeable Na Batteries. *ACS Appl. Mater. Interfaces* **3,** 4165–4168 (2011).
- 7. Sathiya, M., Hemalatha, K., Ramesha, K., Tarascon, J.-M. & Prakash, A. S. Synthesis, structure, and electrochemical properties of the layered sodium insertion cathode: NaNi1/3Mn1/3Co1/3O2. *Chem. Mater.* **24**, 1846–1853 (2012).
- 8. Huili, P., And, H. Y.-S. & Liquan, C. Room-Temperature Stationary Sodium-Ion Batteries for Large-Scale Electric Energy Storage. *Energy Environ. Sci.* (2013). doi:10.1039/C3EE40847G
- 9. Slater, M. D., Kim, D., Lee, E. & Johnson, C. S. Sodium-Ion Batteries. *Adv. Funct. Mater.* **23,** 947–958 (2013).
- 10. Palomares, V. *et al.* Na-ion batteries, recent advances and present challenges to become low cost energy storage systems. *Energy Environ. Sci.* **5**, 5884 (2012).
- 11. Ellis, B. L. & Nazar, L. F. Sodium and sodium-ion energy storage batteries. *Curr. Opin. Solid State Mater. Sci.* **16**, 168–177 (2012).
- 12. Yu, H., Guo, S., Zhu, Y., Ishida, M. & Zhou, H. Novel titanium-based O3-type NaTi(0.5)Ni(0.5)O2 as a cathode material for sodium ion batteries. *Chem. Commun.* **50**, 457–459 (2014).
- 13. TOPAS V4: General Profile and structure analysis software for powder diffraction data.-User's Manual, Bruker AXS, Karlsruhe, Germany. (2008).

- 14. Cheary, R. W. & Coelho, A. A. A fundamental parameters approach to X-ray line-profile fitting. *J. Appl. Cryst.* **25**, 109–121 (1992).
- 15. Cheary, R. W., Coelho, A. A. & Cline, J. P. Fundamental parameters line profile fitting in laboratory diffractometers. *J. Res. Natl. Inst. Stand. Technol.* **109**, 1–25 (2004).
- 16. Kern, A., Coelho, A. A. & Cheary, R. W. Convolution based profile fitting- Diffraction analysis of the microstructure of materials. 17–50 (2004).
- 17. Saadoune, I., Maazaz, A., Menetrier, M. & Delmas, C. On the NaxNi0.6Co0.4O2 System: Physical and Electrochemical Studies. *J. Solid State Chem.* **117,** 111–117 (1996).
- 18. Lai, W. & Ciucci, F. Thermodynamics and kinetics of phase transformation in intercalation battery electrodes -phenomenological modeling. *Electrochim. Acta* 531–542 (2010). doi:10.1016/j.electacta.2010.09.015
- 19. Clearfield, A., Jerus, P. & Cotman, R. N. Hydrothermal and solid state synthesis of sodium zirconium silicophosphate. *Solid State Ionics* **5**, 301–304 (1981).
- 20. Shannon, R. D., Taylor, B. E., Gier, T. E., Chen, H.-Y. & Berzins, T. Ionic Conductivity in Na5YSi4012-Type Silicates. *Inorg. Chem.* 17, 958–964 (1978).
- 21. Whittingham, M. S. & Huggins, R. A. Measurement of Sodium Ion Transport in Beta Alumina Using Reversible Solid Electrodes. *J. Chem. Phys.* **54**, 414 (1971).
- 22. Cho, J., Kim, Y. J. & Park, B. Novel LiCoO2 Cathode Material with Al2O3 Coating for a Li Ion Cell. *Chem. Mater.* 3788–3791 (2000).
- 23. Scott, I. D. *et al.* Ultrathin Coatings on Nano-LiCoO2 for Li-Ion Vehicular Applications. *Nano Lett.* **11,** 414–418 (2011).

6. CONCLUSIONS

Designing low-cost, long cycle life battery devices remains a prime challenge for stationary and grid-sector applications. Na-ion batteries are actively researched to address the gaps in these market areas and is anticipated to provide a low-cost, sustainable solution as they are based on inexpensive, plentiful and geographically widespread sodium resources. Characterization of novel functional intercalation-type materials remains a research challenge for device development. Availability of multiple electrode material choices would diversify the product performance specifications and address a larger market segment with different performance metrics. In this research work, inorganic materials with various structure types such as tunnel- and layer-related phases were investigated as novel sodium intercalation electrodes.

Using impedance spectroscopy, we show that perchlorate based electrolyte (1M NaClO₄ in EC/DMC) had a continual growth of surface films contributing to increasing film resistance at open circuit conditions. Fluorine based electrolyte (0.5M NaPF₆ in EC/DEC), on the other hand, had a lower film resistance with a gradual growth rate of the surface films demonstrating better passivation stability. Cyclic voltammetric testing showed that anodized aluminum (with exposed aluminum cross-section to contact film) provided excellent corrosion resistance as indicated by lower oxidative peak currents than nickel, stainless steel, graphite, titanium, and plain aluminum. Electrochemical methods were validated using well-studied Na_{0.7}CoO₂ and LiFePO₄ electrode materials using in-lab synthesized materials. The electrochemistry of novel, tunnel-type materials: sodium nickel phosphate (SNP) and sodium cobalt titanate (SCT) were evaluated. Reversible sodium de-intercalation/intercalation reactions were shown in SNP using Ni^{2+/4+} redox couple with average voltage of 2.0 V vs. Na/Na⁺ with 50% of theoretical capacity (~50 mAh/g). A large voltage

hysteresis of 1V was obtained between charge/discharge curves. Ex-situ XRD testing confirmed that the material retained the starting structure due to the inherent structural stability of polyanionic material classes. PITT testing of SCT shows sloping, symmetric charge/discharge curves between 3.6-4.2 V indicative of intercalation-type reactions with good faradaic efficiency of 86%. The voltage hysteresis is 1.4 V in fluorine based electrolyte when tested at 70 °C and increases to 1.6 V in perchlorate based electrolyte when tested at room temperature. The voltage hysteresis is reported to be inherent to the material chemistry and a thermally activated process. We conclude that the slow solid state diffusion of sodium ions in SNP and SCT causes the large voltage polarization and further improvements would require significant particle size reduction to reduce the diffusional length scale.

Layer-structured titanate materials with prismatic (P2) and octahedral co-ordination (O3) of sodium atoms were investigated as potential sodium intercalation electrodes. P2-NT and P2-NMT materials were prepared by optimal solid state reaction techniques to obtain reasonably phase pure powders. High cathodic redox potential of 3.7 V vs. Na/Na⁺ for Ni^{2+/4+} and low redox potential of 0.7 V vs. Na/Na⁺ for Ti^{4+/3+} is reported for P2-NT phase demonstrating its bifunctional nature. Using P2-NT as cathode and anode ('bifunctional') would provide significant cost benefits in large-scale manufacturing. The sloping voltage profile between 2-4.2 V, and ex-situ XRD testing confirms that the P2-NT phase retains the initial structure without any phase change. Good reversibility is demonstrated in P2-NMT phase as well with few additional peaks at E>4.0 V possibly due to sodium ordering processes. AC and DC testing on sintered pellets show a wide separation between the electronic and ionic conductivity curves with the former being ~4 orders faster. Impedance spectroscopy of film electrodes show a decreasing interfacial resistance with charging voltage from equivalent circuit modeling. P2-NMT electrodes were shown to possess

faster interfacial reaction kinetics than P2-NT electrodes over the complete voltage range. PITT and EIS data supports relatively fast solid state diffusion of sodium ions (10⁻¹²-10⁻¹³ cm²/s), as expected for the prismatically co-ordinated layered oxides. P2-NMT electrodes were found to provide significantly improved capacity retention than P2-NT electrodes at higher currents due to the faster interfacial kinetics and enhanced charge-carrier transport processes. These materials are shown to possess good capacity retention in the cathodic regime. However, P2-NT phase has a pronounced capacity fade in the anodic regime and this is likely associated with electrocatalytic reduction induced by nickel species. This can potentially be avoided by forming a protective surface film to limit electrolyte exposure. Attempts to incorporate calcium and potassium in the P2 structure by traditional solid-state synthetic routes to stabilize the structure for improved performance were unsuccessful due to the formation of perovskite- and framework-related impurity phases.

The structural properties of P2-NT material was evaluated using experimental neutron diffraction and computational studies. Rietveld refinement provided average structural information while computational methods based on atomistic simulations provided both average and local structural details. The Bragg reflections of space group P63/mmc (# 194) reproduced the experimental patterns fairly accurately and utilized as a good structural model. The measured anisotropy in thermal expansion co-efficient values: β_a^{900C} =1.83×10⁻⁵Å/K, β_c^{900C} =17.65×10⁻⁵Å/K was reported to be due to the layered configuration with weaker through-plane bonding. Na_f sites were found to contain lower occupancy than Na_e sites due to higher repulsive interaction with the in-line transition metal atoms. The Na_f site occupancy was found to gradually increase (0.1699 \rightarrow 0.1751) as the testing temperature is raised from 15 \rightarrow 300K. The higher thermal contribution at ambient conditions was found to make the unfavorable sodium sites slightly more

accessible. The experimental sodium nuclear densities displayed considerable oblateness along the ab-plane while oxygen nuclear densities remained fairly spherical. Buckingham and Morse-type interatomic potential models provided fairly accurate structural representation of various binary and ternary oxides, and the target phase. Energetics study confirmed that equally distributed structures had the lowest energy for both potential models. The simulated nuclear densities matched the experimental patterns fairly well. The simulated patterns were also found to contain additional density spots due to displacive movements and this effect is attributed to the formation of stacking faults. The simulated and pseudo-experimental PDF patterns showed some differences due to the averaging effect in Rietveld refinement and further analysis would require experimental PDF measurements. These potential models would act as a good framework for further model improvement using Ab-initio energy hypersurface fitting approaches and MD studies to investigate the dynamics of sodium transport.

The electrochemical and structural properties of O3NT material was characterized with the potential of realizing higher reversible capacities than P2 materials. The stabilizing influence of titanium to reduce the capacity fade was evaluated. Galvanostatic testing and PITT confirm the excellent electrochemical reversibility with small voltage hysteresis with charging voltage of 4.2 V. However, higher voltages were found to lead to affect the reaction reversibility. Ex-situ XRD testing show that the O3 phase transforms to P3 phase in composition range of 0.81 > x > 0.39. We predicted that the intermediate O3' phase occurs in a smaller domain of 0.90 > x > 0.81. Further extraction of sodium results in the formation of an unknown phase possibly with high moisture sensitivity. We show that cycling the electrode in the O3-P3 domain provides for an excellent capacity retention of 99% in 115 cycles at C/2 rate. Impedance spectroscopy confirms that the physicochemical parameters such as surface film resistance and interfacial charge transfer

remains fairly invariant during cycling contributing to the excellent capacity retention. We also report that O3NT phase has good capacity retention when cycled in higher charging voltages (>4.2 V) and these enhanced capacity retention is attributed to stronger bonding character of titanium. However, the capacity values become reduced in these high voltage cutoff studies possibly due to the formation of resistive surface films by electrolyte breakdown at highly oxidative potentials. Future work involving masking the surface of the active particles can potentially inhibit these side reactions and provide improved capacity retention. Rate studies confirm that O3NT electrodes provide improved capacity retention than P2NT electrodes due to the presence of higher nickel providing a percolating network for fast transport of charge carrier species.